Measurement of the Charged-Hadron Multiplicity in Proton-Proton Collisions at LHC with the CMS Detector

by

Yen-Jie Lee

M.S., National Taiwan University (2004)

Submitted to the Department of Physics
in partial fulfillment of the requirements for the degree of

Doctor of Philosophy

at the

MASSACHUSETTS INSTITUTE OF TECHNOLOGY

April 2011

[June 20

Author .....
Department of Physics
April 30th, 2011

Certified by .....
Wit Busza
Francis Friedman Professor of Physics
Thesis Supervisor

Accepted by .....
Krishna Rajagopal
Associate Department Head for Education

Measurement of the Charged-Hadron Multiplicity in Proton-Proton Collisions at LHC with the CMS Detector

by

Yen-Jie Lee

Submitted to the Department of Physics
on April 30th, 2011, in partial fulfillment of the
requirements for the degree of
Doctor of Philosophy

Abstract

Charged-hadron pseudorapidity densities and multiplicity distributions in proton-proton collisions at $\sqrt{s} = 0.9,\ 2.36,\ 7.0$ TeV were measured with the inner tracking system of the CMS detector at the LHC. The charged-hadron yield was obtained by counting the number of hit-pairs (tracklets). The charged-particle multiplicity per unit of pseudorapidity $dN_{\rm ch}/d\eta\,|_{|\eta|<0.5}$ at $\sqrt{s} = 7.0$ TeV is $5.78 \pm 0.01(\text{stat.}) \pm 0.23(\text{syst.})$ for non-single-diffractive events, higher than predicted by commonly used models. The relative increase in charged-particle multiplicity from $\sqrt{s} = 0.9$ to 7 TeV is $66.1\% \pm 1.0\%(\text{stat.}) \pm 4.2\%(\text{syst.})$ and strong KNO violation is observed in the multiplicity distributions. Results are compared with low energy measurements.

Thesis Supervisor: Wit Busza

Title: Francis Friedman Professor of Physics

Contents

Outline

On 20 Nov 2009, the Large Hadron Collider (LHC) [1], the world's largest particle accelerator, successfully delivered the first p+p collision at $\sqrt{s} = 900$ GeV. In 2010, the LHC also delivered collisions at 2.36 TeV and 7.0 TeV, which were the highest energy collisions ever achieved by any particle accelerator and opened a new era of high energy physics research. The LHC was designed to deliver high energy p+p and Pb+Pb collisions to cover a very wide range of research topics, from the discovery of the Higgs boson, or super-symmetric particles, to the studies of the quark-gluon plasma.

In my field, the medium created in Pb+Pb collisions is particularly interesting. In order to understand the Pb+Pb collisions, it is crucial to understand the particle production in p+p collisions, such as the angular distribution of the produced particles, average abundance, and event-by-event multiplicity distributions. These measurements provide an essential reference for Pb+Pb collisions in order to study the properties of the quark-gluon plasma. It is also crucial to understand the bulk of the particle production in the case of p+p collisions in order to discover new phenomena. p+p collisions are primarily governed by the soft processes, which involve non-perturbative QCD and can only be modeled phenomenologically. Therefore the studies of the particle production not only provide valuable background knowledge to the new discoveries, but also are intriguing in themselves and provide crucial guidance to the commonly used event generators and analytical models.

In this thesis, two studies of the particle production in p+p collisions with the Compact Muon Solenoid (CMS) experiment [2] are described. The first is the study of the pseudorapidity distribution of charged particles ($dN_{\mathrm{ch}}/d\eta$). It involves the measurement of the average abundance of particles produced in different emission angles, and can be performed in the early stage of the experiment. Although this measurement averages over different events and different processes, it can already provide good separation between models. The second is the study of the event-by-event multiplicity, which gives information about the fluctuation in the particle production process and provides more details about the particle production mechanism. The analyses in both studies are based on the tracklet method (hit-pairs in the CMS pixel detector), which is a proven technique from the PHOBOS experiment [3]. The technique developed and improved in this thesis was applied to the first collision data and led to the first publication of the CMS experiment.

The increase of the pseudorapidity particle density from 0.9 to 2.36 (to 7.0) TeV is found to be much larger than the predictions from the commonly used event generators

and models. This means that the energy dependence of the predictions from multiple parton interaction models are not accurate. Modifications and tunings are necessary. The pseudorapidity distribution measurement also provides crucial information during the detector commissioning phase because the occupancy and the distribution of the particles which pass through the detector is the starting point in the understanding of all data.

The outline of this thesis is the following: Chapter 1 gives the theoretical framework, related to the understanding of particle production in p+p collisions. A review of the $dN_{\mathrm{ch}}/d\eta$ and multiplicity distribution measurements performed in previous experiments is compiled in the Chapter 2. Chapter 3 and 4 give an introduction to the LHC and the CMS detector. Chapter 5 discusses the event triggering and selection. The tracklet reconstruction and pseudorapidity distribution measurement are described in Chapter 6. Chapter 7 extends the application of the tracklet analysis technique to the multiplicity distribution measurement, and the systematic uncertainty studies. In the last chapter, the results from the p+p collision studies at $\sqrt{s} = 0.9$, 2.36 and 7.0 TeV are summarized and discussed.

1. Introduction

As mentioned in the outline, the main goal of this thesis is to provide a useful p+p reference for the study of the Pb+Pb collisions. The lead ions contain 208 nucleons and the first step of the Pb+Pb collisions involve many nucleon-nucleon scatterings. Since so many collisions happen at the same time in a small space, they create a medium with extremely high energy density and may lead to the state known as the quark-gluon plasma, consisting of deconfined quarks and gluons. However, the nucleon-nucleon scattering is not simple itself. The nucleons are extended objects which contain structure. Moreover, the scattering involves the soft processes, which cannot (yet) be calculated reliably from first principles. The description of the soft processes has to rely on phenomenological models.

In order to understand the first steps of Pb+Pb collisions, it is important to measure the particle production in p+p collisions and provide inputs to the models. The results in p+p can also be compared to Pb+Pb collisions to study the property of the produced medium. Furthermore studies of particle production in p+p collision are interesting in themselves. They can be used to improve our understanding of soft processes and the incalculable part of the hadronic interaction. In this thesis, the pseudorapidity density and charged hadron multiplicity distributions are measured and discussed. The pseudorapidity density contains the space and time information of the particle production, while the multiplicity distributions give information about fluctuations and correlations.

This chapter briefly discusses theoretical and experimental concepts which are related to the multi-particle production in p+p collisions. The chapter begins with an introduction to the building blocks of matter and the Standard Model which describes the interactions between the elementary particles.

Since the proton is a complicated system, the inelastic collision events can be classified into several event classes, such as diffractive and non-diffractive events. The event classification of the p+p collisions will be introduced, and the connection to the physical picture will be described. The theoretical and phenomenological description of the

multiplicity distributions and charged hadron spectra will also be discussed.

Experimentally, simulations of the detector response to the p+p collision rely on event generators. An introduction to the common used generators, PHOJET [4, 5] and PYTHIA [6], for event simulation will be presented. Calculations and predictions at LHC energies from these generators will also be presented. In Chapter. 8, they are compared with the experimental results presented in this thesis.

1.1. The Standard Model

What are the building blocks of matter? How do they interact with each other? These are the questions that drive the development of science. There are four known interactions in nature: the gravitational force which is responsible for the falling of apples; the electromagnetic force which enables us to touch and to grab objects around us; the strong force which is the source of the nuclear power, and is responsible for the interaction between the hadrons; finally the weak force which governs the transitions from one quark flavor to another and the interaction between neutrinos and other elementary particles. The Standard Model is so far the most successful gauge theory that describes the interaction between fundamental particles, including electromagnetic, weak and strong interactions. Gravitational force is not yet integrated in the Standard Model.

In the Standard Model, the building blocks of matter are point-like particles, which carry a spin of 1/2. They are usually grouped into three families; each family consists of two leptons and two quarks. The properties of these elementary particles are summarized in Table. 1.1. For each particle, there is an associated antiparticle with the same mass but opposite quantum numbers. Leptons participate in weak and electromagnetic (if it carries electromagnetic charge) interactions. Quarks carry "color charges", which means that quarks also participate in the strong interaction. Color charges are the strong interaction version of charges, which have no relation to the real colors of daily life. There are three color charges, usually denoted by blue (B), red (R) and green (G). Experimentally, all particle states observed in nature are "colorless" or "*white*". This is called the *color confinement*. The quarks cannot appear freely and have to group together in the form of *hadrons*, which are colorless. Hadrons observed in the lab can be classified into *baryons* and *mesons*. Baryons consist of three quarks (qqq), or three anti-quarks ($\bar{q}\bar{q}\bar{q}$). The colors of the quarks inside a baryon are RGB (R+G+B=white), which satisfies the requirement of color confinement. Mesons consist of a quark and an anti-quark ($q\bar{q}$). The colors of the quarks inside a meson are $B\bar{B}$, $G\bar{G}$ and $R\bar{R}$ (The sum

of the color and anti-color is white).

The interactions between particles are mediated by gauge bosons. The photons are responsible for the electromagnetic interaction between charged particles, which is formulated as Quantum Electrodynamics (QED). The weak interactions, mediated by th $W^{\pm}$ and Z^0 bosons, are described by the electroweak theory. The strong force between hadrons is mediated by gluons, which is described by Quantum Chromodynamics (QCD). The forces and the mediators are summarized in Table. 1.2. The coupling constants of the weak and electromagnetic forces are small, and enabled the application of the perturbation techniques to perform accurate calculations. However, in the case of strong interaction, the coupling constant in soft processes (low momentum transfer) is large such that calculation based on perturbation theory is not reliable. Since the direct calculation can not (yet) be carried out, the studies of the general property of hadron-hadron collision, such as p+p collisions, are of fundamental importance and provide necessary guidance to the development of the theoretical models.

Generation	Quarks				Leptons			
	Name	Symbol	Charge	Mass	Name	Symbol	Charge	Mass
First	Up	u	+2/3	1.5 - 4.5 MeV	Electron	e^-	-1	0.511 MeV
	Down	d	-1/3	5.0 - 8.5 MeV	Electron neutrino	ν_e	0	$< 2 \times 10^{-6}$ MeV
Second	Charm	c	+2/3	1.0 - 1.4 GeV	Muon	μ^-	-1	105.7 MeV
	Strange	s	-1/3	80 - 155 MeV	Muon neutrino	ν_μ	0	< 0.19 MeV
Third	Top	t	+2/3	174.3 ± 5.1 GeV	Tau	τ^-	-1	1777 MeV
	Bottom	b	-1/3	4.0 - 4.5 MeV	Tau neutrino	ν_τ	0	< 18.2 MeV

Table 1.1.: The properties of the quarks and leptons. [7]

	Strong	Electromagnetic	Weak	Gravitational
Mediator	Gluon (g)	Photon (γ)	$W^\pm, Z$	Graviton
Spin-Parity	1^-	1^-	$1^-, 1^+$	2^+
Range [m]	$< 10^{-15}$	∞	10^{-18}	∞
Relative Strength	1	10^{-2}	10^{-13}	10^{-38}

Table 1.2.: The fundamental force carriers and properties.

1.2. p+p collisions

1.2.1. Physics picture of p+p collisions

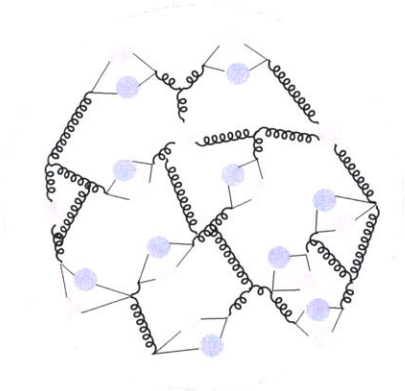

Figure 1.1.: Schematic view of the proton in the parton model.

From e+p scattering [8, 9], we know that protons are extended objects. In the study of the p+p scattering, the structure of the proton should be taken into account. In the framework of the parton model, the constituents of the proton, when it is probed by a hard scattering at virtuality scale Q^2, can be described by the structure function ($F(x,Q^2)$, x is the momentum fraction of the parton). The structure function of the proton is determined by fits to e+p and p+$\bar{\text{p}}$ collision data. From this point of view, the p+p collisions are actually interactions between two bags of partons. Assuming the factorization of the proton structure holds, the $2 \to 2$ differential cross-sections of the p+p scattering can be written in the following form:

$$\frac{d\sigma_{ij}}{dt} = \int dx_1 \int dx_2 F_i(x_1,Q^2) F_j(x_2,Q^2) \frac{d\hat{\sigma}_{ij}}{dt} \tag{1.1}$$

where t is one of the the Mandelstem variable which describes the interaction involving the exchange of an intermediate particle through *t-channel* with squared four-momentum t. The definition of t can be found in Section. A.4, i, j are the index of the parton species (quarks and gluons) and $\hat{\sigma}$ is the cross-section from matrix element calculations. However, this is not the whole story. The first problem of this equation is that the differential cross-section diverges in the $t \to 0$ limit, and regularization is needed. Secondly, the scattered partons have to be translated to hadron level to be

compared with the experimental results. This involves branching / showering (splitting of the partons) and *hadonization* (picking up another parton to make a final state particle which is colorless). However, the hadronization process of the scattered partons is not yet understood from the first principle and can only be modeled phenomenologically. Moreover, in the high-energy p+p collisions, the initial momenta of the protons are high enough such that many partonic interactions can occur in one collision, which makes the picture even more complicated. The high-energy collisions also involved the interactions between low x partons ($x < 10^{-4}$) where the uncertainty of the structure function is large from the current knowledge of the collision data.

Apart from some theoretical insights that describe the general properties of the collisions, there is no straightforward analytical calculation, starting from first principles, which can give a complete description of the p+p collision. Practically, the description of the particle production relies on the Monte Carlo generator based on factorization and phenomenological models. A further discussion of event generators will be given in Sec. 1.5. Based on these reasons, the measurements of the charged particle production will be important tests on the physics picture we have and provides useful guidence to the model building.

1.3. Experimental observables

In the study of the particle production in p+p collisions, the abundance of the charged particles and their angular distributions are the simplest observables. The coordinate system and kinematic variables are summarized in Appendix. A. Instead of the angle (θ), the rapidity y is a better variable because it is an additive quantity in the Lorentz transformation (relativistic version of velocity). However, it is difficult to measure the energy (or the mass) of each charged particle in the experiment. The pseudorapidity (η) is usually used to characterize the emission angle of the charged particles because it is closely related to rapidity (y). To justify this, the $dN_{\rm ch}/dy$ and $dN_{\rm ch}/d\eta$ from PYTHIA generator are plotted together and shown in Fig. 1.2. A short introduction to the PYTHIA generator is given in Sec. 1.5.1. There is a dip at mid-rapidity, which is due to the Jacobian transformation from rapidity to pseudorapidity. This transformation also widens the distribution. The generated $dN_{\rm ch}/d\eta\ |_{|\eta|\sim 0}$ is roughly 16%(18%) lower than the $dN_{\rm ch}/dy\ |_{|y|\sim 0}$ at $\sqrt{s} = 53$ (7000) GeV and the ratio of the two distributions at mid-rapidity ($|\eta| < 1.0$) is only weakly dependent on the collisional energy.

The pseudorapidity density ($dN_{\rm ch}/d\eta$) is an averaged quantity over all kinds of dif-

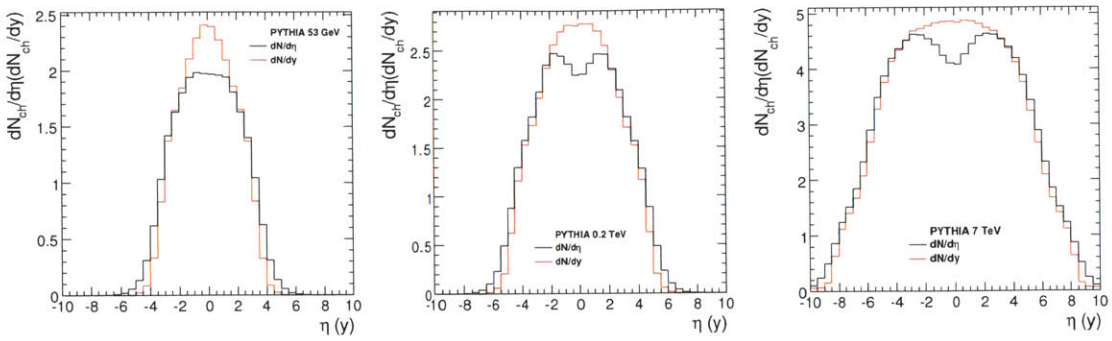

Figure 1.2.: The comparison between $dN_{\mathrm{ch}}/d\eta$ and dN_{ch}/dy from PYTHIA D6T Tune [10] at $\sqrt{s} = 53, 200$ and 7000 GeV.

ferent events created in the p+p collisions. It shows the averaged event shape of the collisions. The pseudorapidity density at $\eta \sim 0$ increases as a function of $\sqrt{s}$ and can be described by a 1(or 2) degree polynomial of $\log s$. Sudden changes in the trend may indicate new phenomena in low P_T particle production.

The distribution of the event-by-event multiplicity N_{ch} characterizes the fluctuation of the charged hadron abundance. The multiplicity distribution $P(N_{ch})$ characterizes the amount of correlation in the particle production. If there is no correlation between the creations of final-state charged hadrons, the distribution is Poissonian. A wider distribution implies positive correlations.

1.3.1. Particle production processes

The bulk of the particle production in p+p collisions arises from the soft interactions, which contains elastic and inelastic scatterings. The elastic scattering involves the exchange of virtual mesons or virtual photons. Experimentally, due to the small momentum transfer and high beam energy, the scattered proton usually passes through the very forward region of the detector and is undetected. In this thesis, the elastic processes are not further discussed.

The soft inelastic interactions are typically classified into diffractive processes and non-diffractive scattering. In Good and Walker's picture [11], one can expand the initial-state proton in terms of a complete set of states. During the proton-proton scattering, the large number of states of the projectile is absorbed by the target and diffractively dissociates into a collection of particles. This diffractive system has the same intrinsic quantum numbers as the original proton, i.e. the same charge, isospin, baryon number

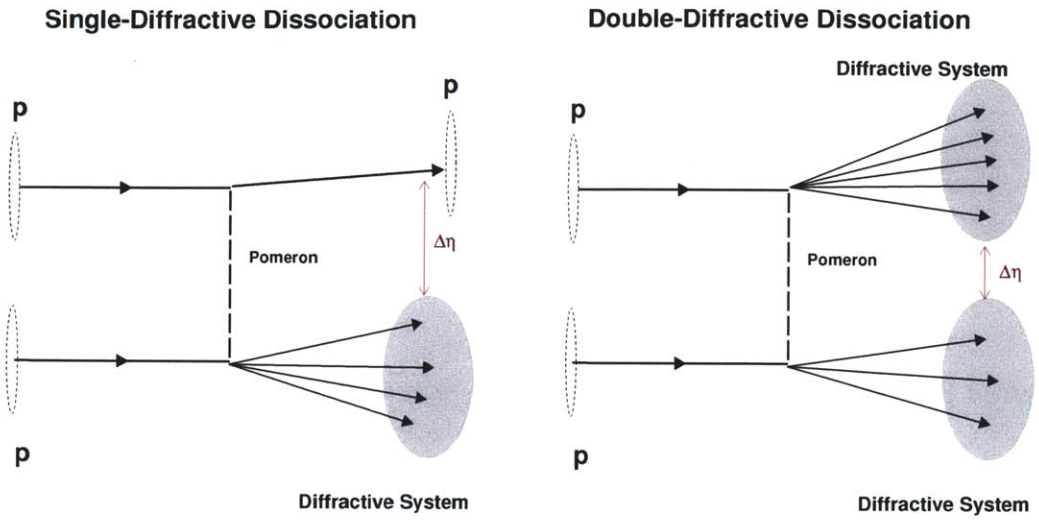

Figure 1.3.: The schematic view of single-diffractive dissociation (SD) and double-diffractive dissociation (DD).

and etc. The target receives a small momentum transfer from the projectile proton and remain unchanged, as shown in Fig. 1.3. Between the diffractive system and the target a large gap in rapidity is created and devoid of particles. This is called a single-diffractive (SD) collision. In some cases, both of the protons are turned into diffractive systems as shown in Fig. 1.3. This is called the double-diffractive dissociation (DD). In the non-diffractive (ND) collisions, there are parton-parton interactions with larger momentum transfer as well as the exchange of quantum numbers. No diffractive systems are created. Usually, non-diffractive collisions create more particles and lack rapidity gaps.

Fig. 1.4 shows the charged hadron pseudorapidity distributions of those processes at 7 TeV predicted by PYTHIA [6] and PHOJET [4, 5]. Short descriptions of these generators are in Section. 1.5. The single-diffractive distribution features an asymmetric pseudorapidity distribution, which has a peak around the initial pseudorapidity of the proton beam and the contributions of the particles emitted from the diffractive system. Usually, the emitted particles only appear on one side of the detector and a requirement of coincident in both side of the detector will lead to suppression of the single diffractive component. The double-diffractive distribution is more symmetric and has a dip in the mid-rapidity. The non-diffractive distribution has many particles produced in the mid-rapidity and the density decreases in the high pseudorapidity region. The PYTHIA and

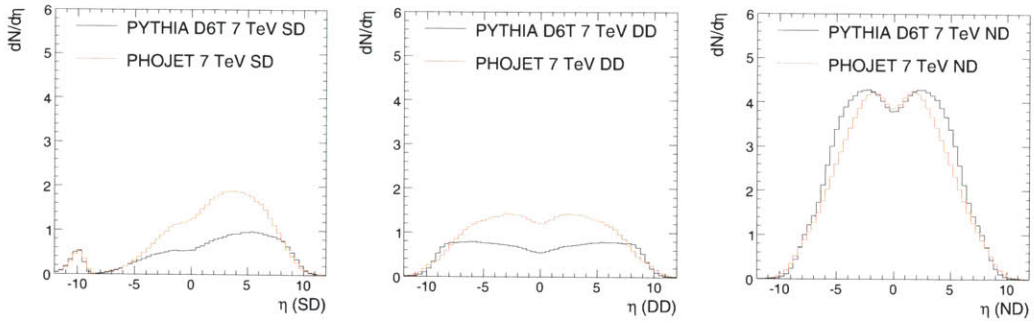

Figure 1.4.: The $dN/d\eta$ distributions from single-diffractive (SD), double-diffractive (DD), and non-diffractive (ND) processes generated by PYTHIA and PHOJET generator. The parameter used in PYTHIA is the D6T tune [10].

PHOJET gives quite different predictions on the properties of the diffractive processes, including the diffractive fractions and average multiplicity.

Although these generators are tuned with the data from low energy measurements, the uncertainty of the $dN_{\rm ch}/d\eta$ due to the parameters used in the generator is still large. Fig. 1.5 shows the predictions from different parameter tunes and generators. The predicted $dN_{\rm ch}/d\eta\,|_{\eta\sim 0}$ is 3.5 - 5.6. The measurement from LHC will be able to eliminate the unsuitable tunes.

In this thesis, we present the results from the inelastic non-single-diffractive (NSD) interactions, which are based on an event selection that retains a large fraction of the ND and DD events, while SD processes are suppressed.

1.4. Theoretical concepts related to p+p collisions

1.4.1. Fermi-Landau Model

In 1950, Fermi and Landau proposed a statistical way for the description of high energy collisions of hadrons [12, 13]. The main assumption is that the interactions between the hadrons are so strong such that the incident hadrons stopped each other. All the energy carried by the hadrons are deposited in a small volume and produce a fireball. A statistical equilibrium is reached during the collision.

When two nucleons collide with very high energy in their centre-of-mass frame, this energy will suddenly be released in a small volume surrounding the two nucleons. Since the interactions of the pion field are strong, the energy W which is deposit in this vol-

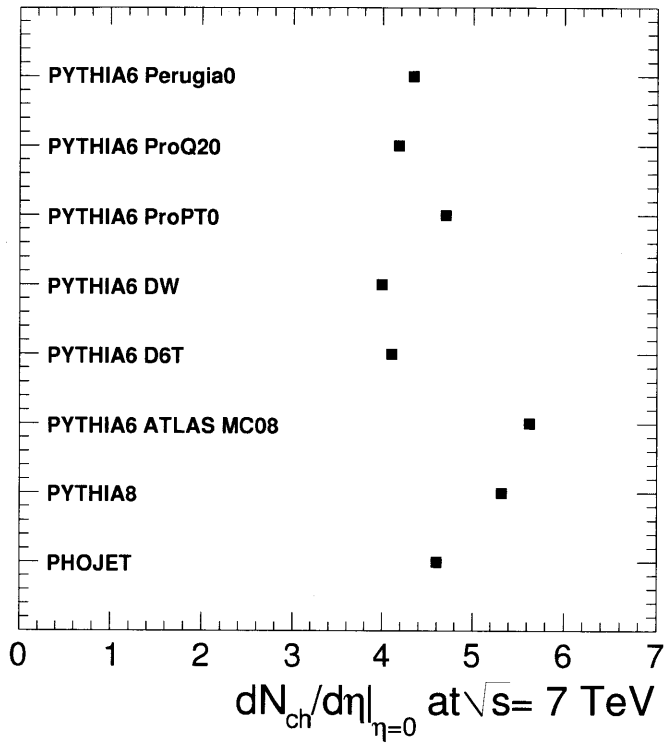

Figure 1.5.: The predicted $dN/d\eta\ |_{|\eta|\sim 0}$ at $\sqrt{s} = 7.0$ TeV from PYTHIA and PHOJET generator

ume will be distributed among the various degrees of freedom present in this volume according to the statistical laws. Then this concentration of energy will rapidly dissolve and produce particles [12].

The volume Ω, in which the energy of the two colliding nucleons is dumped, is assumed to be energy dependent because of the Lorentz contraction:

$$\Omega = \frac{\Omega_0}{\gamma} \tag{1.2}$$

$$= \Omega_0 \frac{2Mc^2}{W} \tag{1.3}$$

where M is the nucleon mass. In the extremely high energy collisions, the energy density is expected to be proportional to the fourth power of the temperature, T:

$$\frac{W}{\Omega} \propto T^4 \tag{1.4}$$

From Eq. 1.2 we have:

$$\frac{W}{\Omega} = \frac{W^2}{2MC^2\Omega_0} \propto T^4 \tag{1.5}$$

$$W \propto T^2 \tag{1.6}$$

According to the standard calculation of statistical mechanics, the density of the particles turns out to be proportional to the third power of the temperature:

$$n \propto T^3 \tag{1.7}$$

From Eq. 1.5 and Eq. 1.7, the number of particles produced is

$$N = n \times \Omega \tag{1.8}$$

$$\propto W^{1/2} \tag{1.9}$$

This means that the total number of particles produced in the collisions will be proportional to $W^{1/2}$ (or $s^{1/4}$).

Fermi-Landau's picture is an extreme case which assumes that the interaction between the two proton is so strong such that a thermalized state is created. However, it is found experimentally that the particle abundance is actually growing slower than this power law (Eq. 1.9). The transverse momentum distribution is found to be much narrower than the longitudinal momentum distribution which suggests that the interaction between the protons is weak. These experimental results imply that the interaction between two protons is not strong enough to create a fully thermalized system.

1.4.2. Feynman Scaling

In 1969, Feynman predicted the character of the hadron production in very high-energy collisions of hadrons [14] from phenomenological arguments. The conclusion was that the total number of particles created in the collision rises logarithmically with $\sqrt{s}$.

$$\langle N \rangle \propto \ln \sqrt{s} \propto \ln W \tag{1.10}$$

where $W = \sqrt{s}/2$, which is the total energy of the incoming particle in the center-of-mass frame. He suggested that the ratio of longitudinal momentum p_z to the total available W ($x = p_z/W$) and the transverse momenta p_T are the appropriate variables to use

for the various outgoing particles in comparing experiments at various values of W in the c.m. system.

Two-body interaction involved in the exchange of currents carry quantum numbers such as the isospin. The fields, which are connected to those currents, are expected to radiate and produce particles (analogous to bremsstrahlung). In the limit of $W \to \infty$, by Lorentz transformation, the fields to be radiated are becoming a δ function in the z direction. This means that the field energy is uniform in p_z and the mean number of particles of fixed p_T is distributed as dp_z/E for not too large x.

From the argument above, the probability of finding a particle of kind i with transverse momentum p_T and mass m can be expressed in this form:

$$P(p_T, x) \propto f_i(p_T, x) \frac{dp_z}{E} d^2 p_T \tag{1.11}$$

where

$$E = \sqrt{m^2 + p_T^2 + p_z^2} \tag{1.12}$$

$$= W\sqrt{x^2 + (\frac{m_T}{W})^2} \tag{1.13}$$

where $m_T = \sqrt{m^2 + p_T^2}$. Since p_T/E becomes dx/x in the large W limit, $P(p_T, x)$ becomes independent of W. The $f_i(p_T, x)$ factorizes approximately (found experimentally) and can be expressed as

$$f_i(p_T, x) = g_i(p_T) f_i(x) \tag{1.14}$$

with a normalization of g_i chosen to be:

$$\int g_i(p_T) d^2 p_T = 1 \tag{1.15}$$

The mean total number of particles produced is:

$$\langle N_i \rangle = \int f_i(p_T, x) \frac{dp_z}{E} d^2 p_T \tag{1.16}$$

$$= \int_{-1}^{1} f_i(x) \frac{dx}{\sqrt{x^2 + (\frac{m_T}{W})^2}} \tag{1.17}$$

Feynman assumed that for $x_F = 0$, a finite limit(C) is reached. Therefore:

$$\int_{-1}^{1} f_i(x) \frac{dx}{\sqrt{x^2 + (\frac{m_T}{W})^2}} \leq 2 \int_{0}^{1} C \frac{dx}{\sqrt{x^2 + (\frac{m_T}{W})^2}} \tag{1.18}$$

$$= 2C \ln \left(x + \sqrt{x^2 + (\frac{m_T}{W})^2} \right) \Big|_0^1 \tag{1.19}$$

$$= 2C \left[\ln \left(1 + \sqrt{1 + (\frac{m_T}{W})^2} \right) + \ln \frac{m_T}{W} \right] \tag{1.20}$$

In the large W limit, $\langle N_i \rangle \propto \ln W \propto \ln \sqrt{s}$. Since the width of the rapidity distribution is also a proportional to $\ln \sqrt{s}$ and assume that the produced particles are evenly distributed in rapidity, it follows that the dN/dy near the mid-rapidity is independent of $\sqrt{s}$ as shown in Fig. 1.6.

In 1971, the first hadron collider, the Intersecting Storage Rings (ISR) commenced operation, colliding p+p($\bar{\text{p}}$) at $\sqrt{s}$= 30.4 to 62.2 GeV. However, it was observed at ISR energies that the pseudorapidity density at the mid-rapidity ($\eta \sim 0$) increased as a function of $\sqrt{s}$ and the results implied that the interaction between hadrons can not be explained by wee parton interactions. A review of the pseudorapidity density is given in Section. 2.2.

Feyman's picture is another extreme case which assumes that the interaction between partons are weak. Compared to Fermi-Landau model, this picture is closer to the experimental data. The missing ingredients are the contributions from gluon radiations (which was not known at that time).

1.4.3. Limiting fragmentation

While Feynman scaling gave some insights to the particle production in the mid-rapidity, the hypothesis of limiting fragmentation of the target and of the projectile is proposed by Benecke *et al.* [11] which focuses on the fragmentation region. The authors suggest the rest frame of the projectile (P) and of the target (L) give more insight for the

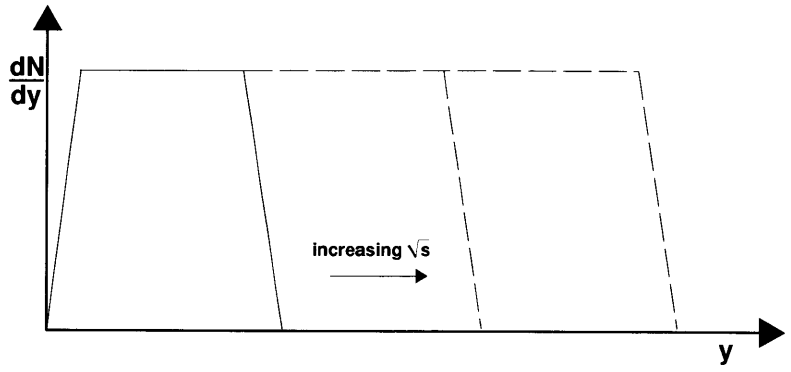

Figure 1.6.: Demonstration of the Feynman scaling of the inclusive particle production $A + B \rightarrow X$ in the rest frame of B.

description of a collision. In the L system, the projectile passes through the target and turns the target into an excited state. The excited state then breaks into several pieces. This is quite similar to the picture which Good and Walker proposed in the diffractive process. In the rest frame of the target, the projectile is highly relativistic. Due to the time dilation, the fast components (the projectile) can't change. The only part which start to radiate particles is the slow components in the collision (the target). The distributions of the *broken-up fragments of the target* reach a limiting distribution, based on kinematical arguments. One obvious example is that the target proton is turned into a Δ particle and emits a pion. Clearly, conservation laws limit the kinematic distribution of the pion. The same discussions can apply to the projectile in the P system. The particles created in the *pionization process* that are slow in the centre-of-mass frame, which correspond to the particles produced in the mid-rapidity, do not contribute to the limiting distributions. A schematic plot of the limiting fragmentation is shown in Fig. 1.7.

The limiting fragmentation is observed in p+p(p+$\bar{\text{p}}$) and heavy-ion collisions experimentally. The $dN/d\eta$ distributions from different energies in the rest frame of the target line up in a common curve before reaching the central plateau. Moreover, it was first observed in p+A collisions [15, 16] and later in Au+Au collisions [17] that this scaling continues to hold in a larger rapidity range (for instance, Fig. 1.8). The origin of this scaling effect is not understood. It was later called "*Extended Longitudinal Scaling*" by Mark Baker of the PHOBOS Collaboration [18].

The results of limiting fragmentation and extended longitudinal scaling in p+p(p+$\bar{\text{p}}$) collisions are reviewed in Section. 2.2.1.

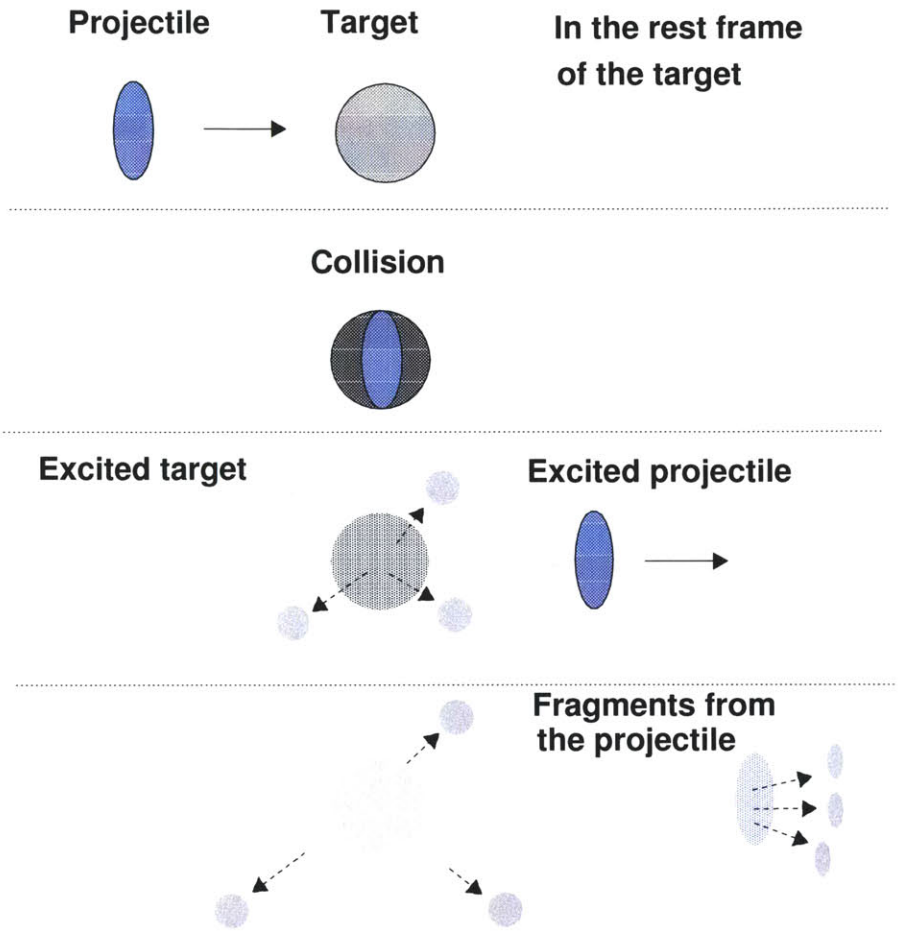

Figure 1.7.: Demonstration of the limiting fragmentation of the inclusive particle production $A + B \rightarrow X$ in the rest frame of B.

1.4.4. Koba-Nielsen-Olesen (KNO) Scaling

Inspired by the Feynman scaling and early data, the KNO scaling was suggested by Koba, Nielsen, and Olsen [19] for the description of the multiplicity distribution. They suggest that if the multiplicity distribution is expressed in the variable $z = N_{ch}/ < N_{ch} >$, the distribution $\Psi(z) = < N_{ch} > P(z)$ is a universal function in the high energy limit.

Although the original assumption of Feynman scaling turned out to be wrong, KNO scaling is found to hold at NAL and ISR energies [20–22] (See Section 2.3.1). In high-energy collisions at Sp$\bar{p}$S and Tevatron, the KNO scaling is found to be violated. Comparisons of the multiplicity distributions in KNO variable are reviewed in Section. 2.3

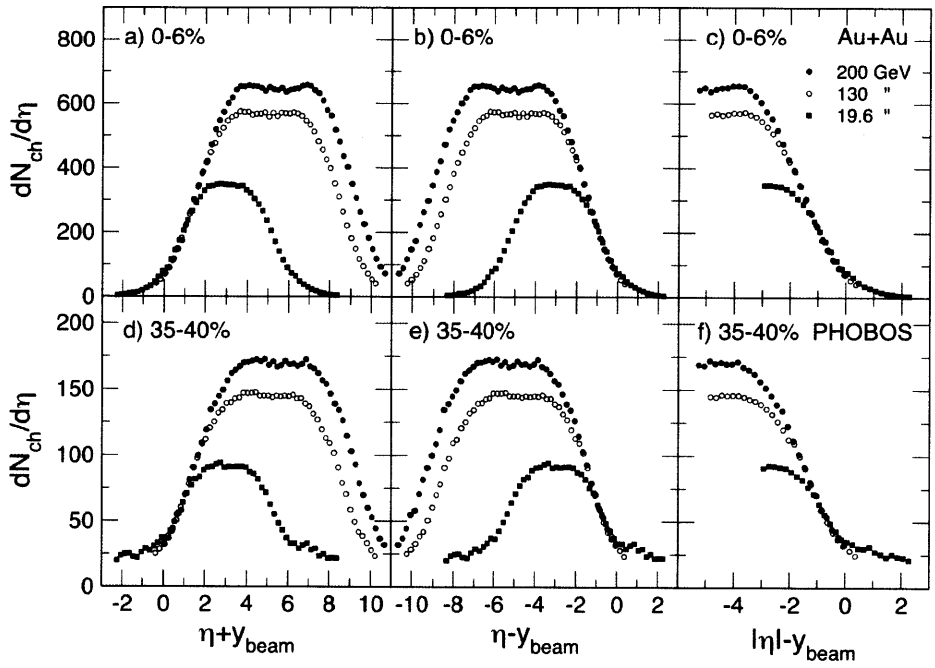

Figure 1.8.: Example of Extended Longitundinal scaling in the 0-6% and 35-40% centrality Au+Au collisions from the PHOBOS collaboration [17].

1.4.5. Negative binomial distributions

From the p+p collision data taken at the NAL [20], ISR [22] and Sp$\bar{p}$S [24] energies, it is found that the charged particle multiplicity distributions in p+p collisions deviates from the Poisson distribution. The widths of the distributions are larger than Poisson distribution indicates positive correlation between charged particles. For instance, the decay of the unstable particles and the showering of the partons. Further analyses show that the distributions can be described by a negative binomial distribution (NBD), which is defined as:

$$f(n) = \begin{pmatrix} k+n-1 \\ k-1 \end{pmatrix} p^n (1-p)^k \tag{1.21}$$

which gives the probability number of n fails in a sequence of independent Bernoulli trials before a specified number k success occurs. Further discussions of the negative binomial distribution are given in Appendix. B. In the study of the charged hadron multiplicity, the NBD is usually expressed as

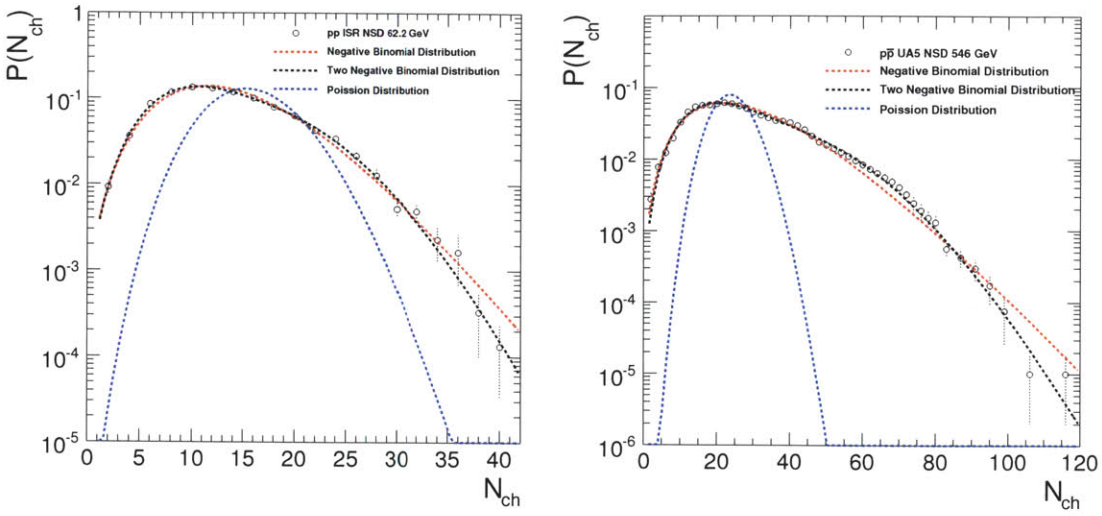

Figure 1.9.: The multiplicity distributions in the full phase space from the SFM experiment at the ISR [22] and the UA5 collaboration at Sp$\bar{p}$S [23]. The distributions are fit with a negative binomial distribution (NBD), a Poisson distribution or two NBDs.

$$f(n)=\frac{\Gamma(k+n)}{\Gamma(n+1)\Gamma(k)}\left(\frac{\bar{n}}{k}\right)^{n}\left(1+\frac{\bar{n}}{k}\right)^{-n-k} \tag{1.22}$$

where the average multiplicity of the distribution is ($\bar{n}=k/p-1$). Fig. 1.9 shows that the NBD distribution describes the ISR data reasonable well, while the Poisson distribution doesn't describe the data.

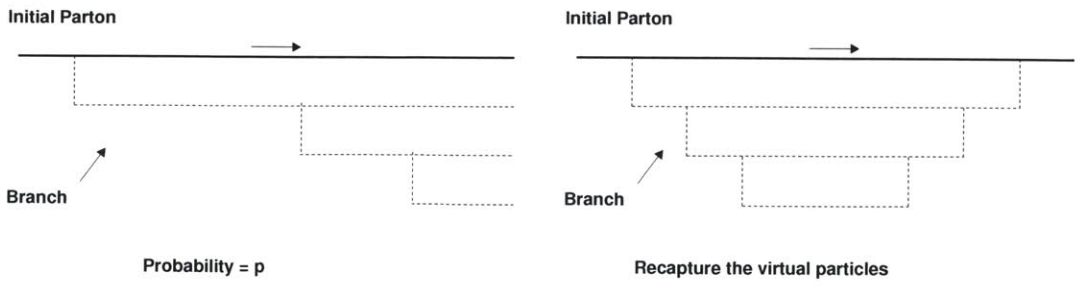

Figure 1.10.: Schematic view of the parton evolution

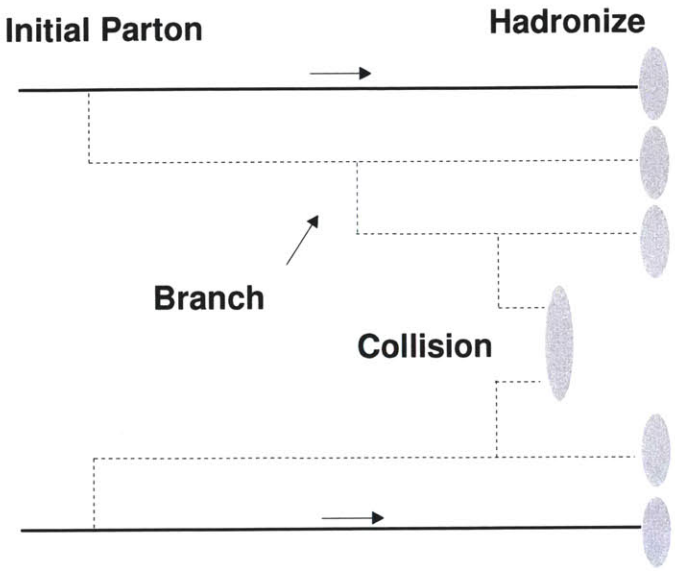

Figure 1.11.: Collision between soft partons

The origin of a charged multiplicity distribution following the NBD distribution is not fully understood. A phenomenological explanation is the following: The partons in the hadron undergo parton branching as shown in Fig. 1.10. If there is no collision happen, the parton absorbs the virtual particles. If the probability of branching is p, then the number of out going partons is a negative binomial distribution. In the p+p collisions, the lowest energy partons interact and the each out-going partons hadronize and produced the observed charged particles.

Another phenomenological explaination was provided by the *Clan Model.* Inspired by the cascade processes and jet fragmentation studies, the Clan Model [25] was proposed. The model describes the particle production by a cascading mechanism. In a collision, *clans*(clusters) are assumed to be produced independently in the collision and can be described by the Poisson distribution $\tilde{F}(n_c, \bar{n}_c) \propto {\bar{n}_c}^{n_c}/n_c!$, where n_c is the number of clans and $\bar{n}_c$ is the average number. The probability to produce another particle (p) is assumed to be proportional to the number of existing particles. The probability of

producing N_{ch} particles in a clan $F(N_{ch})$ is characterized by the following relations:

$$F(0) = 0 \tag{1.23}$$

$$(N_{ch}+1)F(N_{ch}+1) = p \times N_{ch}F(N_{ch}) \tag{1.24}$$

Eq. 1.23 corresponds to the fact that a cluster contains at least one particle. $F(N_{ch})$ can be expressed as:

$$F(N_{ch}) = \frac{F(1)p^{N_{ch}-1}}{N_{ch}} \tag{1.25}$$

And the multiplicity distribution is:

$$P(N_{ch}) = \sum_{x=0}^{N_{ch}} \tilde{F}(x, \bar{n_c}) \sum^{*} F(N_1)F(N_2)...F(N_x) \tag{1.26}$$

where $\sum^{*}$ denotes the sum over all partitions with $N_{ch} = n_1+n_2+...n_x$. It is shown in [25] that Eq. 1.26 is a negative binominal distribution. The average number of particles per clan $\bar{n}_{ch}$ and the average number of clans $\bar{n_c}$can be directly derived from the negative-binomial parameters:

$$\bar{n}_{ch} = \frac{\bar{n}}{k} / \ln(1+\frac{\bar{n}}{k}) \tag{1.27}$$

$$\bar{n}_c = sk\ln(1+\frac{\bar{n}}{k}) \tag{1.28}$$

From the experiments at Sp$\bar{p}$S collider, it is found that the multiplicity distribution deviates from the NBD distribution [23]. Fig. 1.9 shows the measurement at $\sqrt{s} = 546$ GeV [23], there are additional structures found around the peak when the distribution is compared with NBD fit. It is clear that a fit with two NBDs works much better in the description of the high-energy collisions. Also in the fit of the lower energy data, the two-components fit also works better. It has to be noted that each NBD distribution describes one kind of event class or production mechanisms so that there is no interference between the two components. Fits with two NBDs can be performed without constraints (as shown in the Fig. 1.9), or with constrains in the parameters which characterize the *soft* and *semi-hard* components [26]. The soft component which doesn't contain mini-jets follows the KNO scaling. The semi-hard component violates the KNO scaling. Experimental efforts are also made for the investigation of the relative fraction of the two different components [27].

Another possible explanation to this deviation is the contribution from the multiple parton interaction. The events with two parton-parton scatterings form another event class which extend the tail part of the multiplicity distribution. This can also explain why the deviation from a single NBD distribution increases as a function of collisional energy because the probability of multiple parton interaction increases.

1.4.6. Saturation model

In the framework of parton model as described in Sec. 1.2.1, the proton are bags of partons and the distributions of the partons are described by the parton distribution function. The violation of the Feynman scaling shows the importance of the gluon contribution in the low x region. To get the full description of the proton-proton collision, one must include the lowest x partons in the picture.

At small x, by the uncertainty principle the interaction develops over large longitudinal distance $z \sim 1/(mx)$, where m is the nucleon mass [28]. When the x is sufficiently small, z becomes larger than the nucleon diameter. The incident probe interacts with all the partons within the transverse area $\sim 1/Q^2$ determined by the momentum transfer Q. Since the probe interacts with partons with cross-section $\sigma \sim \alpha_s/Q^2$, the number of partons (N) is proportional to Q^2:

$$N \sim \frac{S_p}{\sigma} \sim \frac{1}{\alpha_s(Q^2)} Q^2 R^2 \tag{1.29}$$

where S_p is the transverse area of the nucleon $S_p \sim \pi R^2$. The density of the parton is given by:

$$\rho \sim \frac{x F(x,Q^2)}{\pi R^2} \tag{1.30}$$

In case of $\sigma\rho \gg 1$, we deal with a dense parton system. At very high gluon density, the anniliation process of the gluons limits the growth of the gluon density and the number of gluon is related to the geometry of the nucleon. The saturation scale Q_s^2 which defines the scale of the gluon saturation can be determined by the condition $\sigma\rho \sim 1$:

$$Q_s^2 \sim \alpha_s(Q_s^2) \frac{x F(x,Q_s^2)}{\pi R^2} \tag{1.31}$$

Therefore the number of gluons is given by:

$$xF(x,Q_s^2) \sim c\frac{Q_s^2}{\alpha_s(Q_s^2)} \tag{1.32}$$

where c is a constant. Assuming the number of hadrons in the system is proportional to the number of the scattered partons (detailed discussions can be found in [29]), we get:

$$\frac{dN}{d\eta} \propto xF(x,Q_s^2) \tag{1.33}$$

$$\propto \frac{Q_s^2}{\alpha_s(Q_s^2)} \tag{1.34}$$

From $\gamma^* p$ scattering data at HERA, it is found that the saturation scale Q_s^2 is proportional to $\sqrt{s}^{\lambda}$ [30–32], where $\lambda \sim 0.27 - 0.29$ [32]. Therefore we get:

$$\frac{dN}{d\eta}(\sqrt{s}) \sim As^{\lambda/2} \tag{1.35}$$

It would be interesting to check if this parametrization describe the data and the extracted λ parameter can be compared with the values obtained from the HERA data [33].

1.5. Event Generators

From the discussions in the last section, there are two important missing pieces which are needed to explain the experimental results. (1) The inclusion of the gluon radiation is necessary in order to explain the raising pseudorapidity density. (2) Implementation of the multiple parton interaction models is necessary to explain the measured charged hadron multiplicity fluctuations. Other than those missing elements, the discussions and calculations usually stay in the parton level. The translation from partons to hadron level is also needed in order to compare the theoretical prediction to the experimental observables. Those complications make the calculation directly from first principles difficult.

To describe the p+p collisions, Monte Carlo technique is usually used to generate events with the best guess from models. The goal is to produce the events at the hadron level as the input to the full detector simulation. This helps to understand the expected

signal and possible background components in the collisions. The hard collisions involve high momentum transfer can be described by perturbative QCD (pQCD). However, the majority of the events come from soft interactions in the minimum-bias events triggered by the detector. The coupling constant α_s of the strong force is $O(1)$ in scattering with low Q^2 and the perturbation method is not valid. Usually, additional phenomenological models are added to the generator for the description of the soft component

Due to the color confinement, the out-going partons *hadronize* and produce colorless final state particles. This transition is not yet understood from first principle calculations and has to be described by phenomenological models. In this section, we will give a brief introduction to the event generators used in this thesis.

1.5.1. The PYTHIA Generator

The PYTHIA [6] generator tries to combine calculations from the pQCD to phenomenological models in order to provide a complete description of the soft and hard processes in the p+p collisions. In the $A + B \rightarrow X$ process, total cross-section is divided according to:

$$\sigma_{\text{tot}}^{AB} = \sigma_{\text{el}}^{AB} + \sigma_{\text{SD}}^{AB} + \sigma_{\text{DD}}^{AB} + \sigma_{\text{ND}}^{AB} \tag{1.36}$$

The total cross-section σ_{tot} is calculated by the Reggeon based method which is described in Appendix C.2 and Eq. C.10. The elastic cross-section σ_{el} is estimated by optical theorem and subtracted from the total cross-section. The inelastic collisions are classified into the single-diffractive (SD), double-diffractive (DD) and non-diffractive (ND) processes. Higher order diffractive processes such as central diffraction with double Pomeron exchange are not included in the PYTHIA (version 6.4) simulation. The diffractive cross-sections are described by parametrizations motivated by the Regge theory [34]. The non-diffractive cross-section is given by Eq. 1.36 with elastic and diffractive components subtracted.

The non-diffractive process is described phenomenologically, but closely related to the pQCD. Starting from Eq. 1.1, the QCD cross-section for hard $2 \rightarrow 2$ processes, as a function of the p_T^2 scale is given by [34]:

$$\frac{d\sigma}{dp_T} = \sum_{i,j,k} \int dx_1 \int dx_2 \int dt\, F_i(x_1, Q^2) F_j(x_2, Q^2) \frac{d\hat{\sigma}_{ij}^k}{dt} \delta\left(p_T^2 - \frac{tu}{s}\right) \tag{1.37}$$

Since the differential cross-section diverge roughly like dp_T^2/p_T^4, a parameter $p_{T\min}$ is introduced. The hard-scattering cross-section above a given $p_{T\min}$ is

$$\sigma_{\text{hard}}(p_{T\min}) = \int_{p_{T\min}^2}^{s/4} \frac{d\sigma}{dp_T^2} dp_T^2 \tag{1.38}$$

The σ_{hard} can be larger than the total non-diffractive cross-section σ_{tot}, which means there are several parton-parton interactions in a single event. This is the concept of the *multiple parton interaction.* The event multiplicity is sensitive to the $p_{T\min}^2$. The number of the parton-parton interactions is given by:

$$N_{\text{int}} = \frac{\sigma_{\text{hard}}}{\sigma_{ND}} \tag{1.39}$$

There are two models which describe the fluctuation of the N_{int}. The old model assumes that there is no correlation between the parton-parton interactions and the N_{int} is assumed to be Poissonian. A fit to the UA5 data [35] gives $p_{T\min} \sim 1.6$ GeV. In the new model, the N_{int} is characterized by the overlap of two disks (the incoming protons) with varying impact parameter. The density of the partons $\rho(r)$ in each disk is described by a exponential form ($\rho(b) \propto \exp(-b^d)$) or a double Gaussian($\rho(b) \propto \frac{1-\beta}{\alpha_1^3}\exp\left(-\frac{b^2}{a_1^2}\right) + \frac{\beta}{\alpha_2^3}\exp\left(-\frac{b^2}{\alpha_2^2}\right)$). The width and the relative fraction of the two Gaussian are tunable parameters. For each impact parameter, the fluctuation of the N_{int} is assumed to be a Poisson distribution.

Starting from the hard interaction, initial- and final-state radiation corrections are added. In PYTHIA, the branching of the outgoing parton is modeled by a parton shower approach. A shower may be viewed as a sequence of $1 \to 2$ branchings. In the PYTHIA, those sequence includes $q \to qg$, $g \to gg$, $g \to q\bar{q}$, $q \to q\gamma$ and $l \to l\gamma$. In those branching processes $a \to bc$, the mother a branches into two daughter, with parton b carrying a fraction z and parton c carrying a fraction $1-z$. The branching probabilities $P_{a\to bc}(z)$ are given by DGLAP evolution equations [36, 37]. The energy and momentum are conserved at each step of the showering process and the shower cut off is at a mass scale of 1 GeV.

In order to compare with experimental observable, PYTHIA uses *the Lund model* [38] to describe the *hadronization* process. The Lund model describes the transition from a scattered parton to final state hadrons with a string fragmentation model. Starting with a $q\bar{q}$ pair, as the distance between the quarks increases, another $q_1\bar{q}_1$ pair may be created from the vacuum fluctuation. The $q\bar{q}_1$ pair hadronizes and creates a meson, while

q_1 continues the fragmentation process. The q_1 may (or may not) pair off with a $\bar{q}_2$. The algorithm continues iteratively. In the Lund string fragmentation model, the tunneling mechanism is assumed to create each new $q_i\bar{q}_i$ pair. The fragmentation function which describe how $q_i\bar{q}_i$ pairs are creates and the hadronization of multiparton systems are proposed in the model. Details of the model can be found in [38]. If a produced particle is unstable, it decays into stable particles by the decay table implemented in the PYTHIA generator.

Since PYTHIA gives reasonable description of the existing data, especially the hard scattering part, the PYTHIA generator is used as the main generator for trigger efficiency and correction studies.

1.5.2. The PHOJET Generator

Compared to PYTHIA, whose starting point is a hard scattering and tries to extend the model to describe soft interactions, PHOJET focuses on the soft part of the p+p collision and approaches the question from a different angle.

The PHOJET generator is based on the ideas of the Dual Parton Model (DPM). A review of the DPM can be found in [39]. The DPM is a phenomenological model of large number of charge (N_c) and flavor (N_f) expansion of QCD. This model relates the parameters used to describe the cross-sections directly to multi-particle production. In DPM, the proton proton scattering can be described by the exchange of *Pomerons* and *Reggeons*. Some short discussions are given in Appendix C.2. In DPM, Pomerons are virtual quasi-particle which carried quantum numbers of vacuum. A Pomeron exchange diagram corresponses to exchange of several gluons between the partons, with total quantum numbers equal to the vacuum quantum numbers. The p+p scattering is dominated by single Pomeron scattering, which includes elastic or diffractive scattering. PHOJET also tries to implement the hard scattering in the language of Pomeron in order to give a consistent description between hard and soft scattering processes.

The hadronization process from partons to hadrons is also based on the Lund string fragmentation model. The PHOJET generator has been tuned to give good description of the charged hadron multiplicity and diffractive processes. Comparison between PHOJET and previous measurements is summarized in Sec. 2.2.3.

In this thesis, the Monte Carlo simulated events with PHOJET generator are used as a cross-check on the trigger and efficiency corrections.

2. Previous Measurements

Charged-hadron production has been studied extensively, from cosmic ray, fixed target experiments to hadron colliders. It has to be noted that although those experiments were trying to measure the same quantity, there were different techniques, triggers and kinematic reaches involved. These differences should be taken into account when results are compared.

In this chapter, the multiplicity measurements from experiments are reviewed. The techniques and detectors, which were used for those measurements, are summarized.

2.1. Experiments

2.1.1. Cosmic ray experiments

Charged particle production was first studied with cosmic rays (for instance, [40]) to understand the property of the hadronic interaction. The analysis methods and variables proposed in the cosmic ray studies were adapted in the later hadron collider experiments.

Due to the nature of the cosmic ray studies, there was less control on the incident particle. It was difficult to determine the initial energy and the type of the incident particle. Careful event selections are needed to select hadronic interaction. Moreover, most of the data were from emulsion experiment and the target was usually a mixture of different nuclei. This made the interpretation of the results non-trivial. In this data review, we focus on the results from fixed target and collider experiments.

2.1.2. Experiments at the National Accelerator Laboratory (NAL)

Inclusive p+p collisions were studied by **the 30-in. hydrogen bubble chamber** at the National Accelerator Laboratory (NAL). The chamber had been exposed to proton beams with $p_{\text{Beam}} = 102, 205, 303, 405$ GeV/c, which corresponded to $\sqrt{s} =$ 13.8,19.6,23.8,27.6 GeV/c [20]. About $(1-7)\times 10^3$ pictures were taken in each energy,

which corresponded to 3-10k events. The bubble chamber had a 4π solid-angle acceptance and was used to study the inclusive particle production in the collisions.

The multiplicity distributions were shown to satisfy the KNO scaling. The experiment also measured the pseudorapidity and rapidity distribution of the pion at $\sqrt{s} = 205$ GeV. The $dN/d\eta$ showed a dip at $\eta \sim 0$ in the center-of-mass frame while dN/dy was found to be *flat* [20]. The experiment also measured inclusive cross-section measurement.

2.1.3. Experiments at the Intersecting Storage Rings

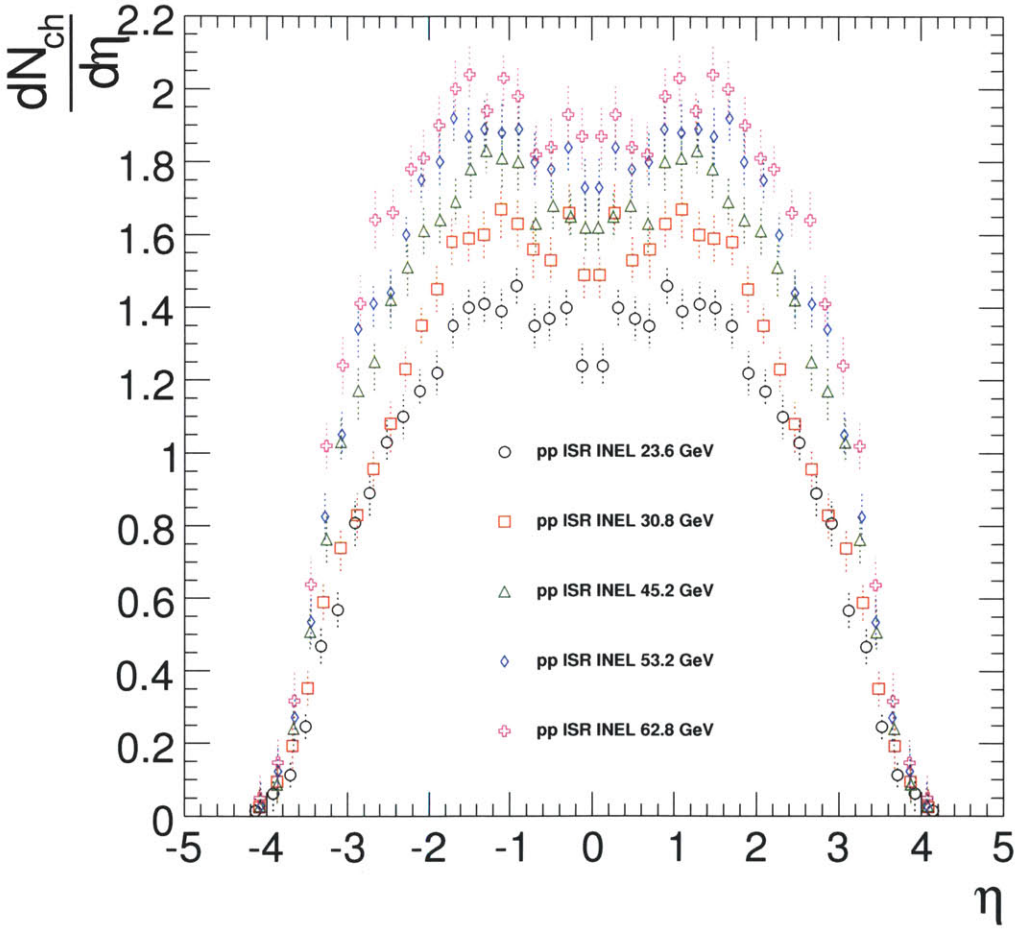

Figure 2.1.: Inclusive inelastic $dN_{\mathrm{ch}}/d\eta$ from ISR energies with statistical errors.

A detector based on streamer chamber (SCD) at the CERN-ISR measured the inelastic charged particle multiplicity at $\sqrt{s} = 23.6$, 30.8, 45.2, 53.2 and 62.8 GeV. This ex-

periment contained two streamer chambers which covered a range of $|\eta| < 4$ which corresponded to ~ 90% of the total solid angle. The measurement was performed without magnetic field, which is sensitive to pions with $p_T > 45$ MeV/c. A good rejection of charged secondaries not pointing to the production vertex could also be achieved. Data taking was triggered by a coincidence between large scintillator hodoscopes on each side of the interaction region. A total of 2300 to 7400 events, were taken in the five ISR-energies and used for further analysis. The most interesting results from this experiment were the evidence for a violation of Feynman scaling [21]. KNO scaling of the multiplicity distribution in the range $|\eta| < 1.5$ was found to be valid in the ISR energies and the distributions significantly deviated from Poisson distribution. The experiment also confirmed the increasing p+p total cross section as a function of $\sqrt{s}$.

The Split Field Magnet detector (SFM) at the CERN-ISR measured the NSD and inelastic p+p collisions at $\sqrt{s} = 30.4$, 44.5, 52.6 and 62.2 GeV. In SFM, an inclusive trigger was used instead of a left-right coincidence from counters in the forward direction. Triggered events were classified as SD and NSD events if there was a track with a Feynman $x > 0.8$, or there was no track in one of the two rapidity hemispheres. If the number of reconstructed multiplicity was larger than 7, the event was also treated as a non-diffractive event. The measurements were also corrected for the secondaries, contaminations from leptons and the geometrical acceptance. The experiment also demonstrated the KNO scaling holded in the NSD events at the ISR energies.

2.1.4. Experiments at the Spp̄S

The UA1 (Underground Area 1) experiment measured the NSD p+p̄ collisions at $\sqrt{s}$ = 200 - 900 GeV during the Pulsed Collider run at the Spp̄S in March 1985 [41]. There were a total of 188k events collected, 18% at the lowest energy $\sqrt{s} = 200$ GeV, and 34% at the highest energy $\sqrt{s} = 900$ GeV. The minimum-bias trigger used was a two-arm trigger that required at least two charged particles in opposite rapidity hemispheres in the range $1.5 < |\eta| < 5.5$. Only tracks with $p_T > 0.15$ GeV/c were retained for analysis. Corrections on track finding efficiency, detector acceptance, secondaries and photon conversion were applied. The overall systematic errors including luminosity, event selection and corrections were 15 %. UA1 also measured the $dN/d\eta$ distribution at $\sqrt{s} = 540$ GeV which used 8000 events taken without magnetic field [42]. This setup reduced the amount of the particles lost at low-momenta to about 1%. A systematic error of 5% was quoted for this measurement.

The UA5 (Underground Area 5) experiment was operated at the ISR and the Spp̄S

collider. UA5 performed detailed $dN_{ch}/d\eta$ measurements, including inelastic and NSD results from p+p collisions at $\sqrt{s} = 53, 200, 546, 900$ GeV [23, 23, 24]. UA5 also compared p+p and p+$\bar{p}$ collisions at $\sqrt{s} = 53$ GeV [43]. UA5 had two large streamer chambers which provided large solid angle coverage. The low momentum reach for pions was ~ 45 MeV/c such that smaller than 1% of the charged particles were lost. However, there were no systematic errors assigned in those measurements.

UA5 also measured the multiplicity distributions with different η-regions. The result was also extrapolated to full phase space. There were 4000 events used for analysis at $\sqrt{s} = 200$ GeV, and 7000 events each for 540 and 900 GeV [35, 44, 45]. The most interesting results from the UA5 measurement were the *violation of the KNO scaling* in the full phase space, and the multiplicity distributions *deviated from a single negative binomial distribution.*

A Forward Silicon Micro-Vertex detector (P238) was a forward geometry silicon micro-vertex detector which was proposed as a part of a hadronic B-physics experiment (P238) [46]. The minimum-bias trigger was a coincidence of the 2 scintillation counter in the forward region. The collaboration reported the $dN_{ch}/d\eta$ of charged particles produced in 630 GeV p+$\bar{p}$ collisions at CERN Sp$\bar{p}$S collider in the range $1 < |\eta| < 6$. The results were based on 3×10^6 triggers. The correction for fake tracks and secondaries were each about 2%. The single diffractive interaction correction was about 0.5%. The corrections were obtained from a PYTHIA simulation which was tuned with UA5 data. The biggest uncertainty was the overall normalization error (5%) which was from the inconsistency when x, y data were used simultaneously in tracking compared to the results where only the x or y information was used. The result from P238 gave a complementary check on the UA5 results obtained at similar collisional energies.

2.1.5. Experiments at the Tevatron

The CDF (Collider Detector at Fermilab) experiment at the Tevatron collider measured the $dN_{ch}/d\eta$ within $|\eta| < 3.5$ in p+$\bar{p}$ collisions at $\sqrt{s} = 630$, 1800 GeV during the 1987 run [47]. The study used data from the vertex time-projection chamber (VTPC), which provided charged-particle tracking. The beam-beam counter (BBC) was used to trigger the detector readout. The BBC consisted of two sets of scintillation counters which covered the pseudorapidity range $3.2 < |\eta| < 5.9$. The VTPC was sensitive to particles with transverse momentum greater than 50 MeV/c. The detector trigger required at least one hit in each set of BBC counters in coincidence with the beam crossing. There were 30000 triggers at 1800 GeV and 9400 triggers at 630 GeV collected for this analysis.

The event selection retained events that pass either of the following tests: (1) a minimum of four tracks in the VTPC with at least one in each of the forward and backward hemispheres (2) an interaction point derived from VTPC information within 16 cm of that determined from BBC time of flight. Those trigger and event selections were relative insensitive to SD events. The CDF result showed that the increase of $dN_{\mathrm{ch}}/d\eta$ at $\eta \sim 0$ is faster than $\ln\sqrt{s}$. However, the authors did not correct for events missed by the trigger or selection procedure, which is quite surprising because this procedure can change the results dramatically. This choice makes it hard to compare CDF results to other experiments.

CDF also measured the multiplicity distribution at both energies with a large sample [48]. The tracks were reconstructed with a central tracking chamber (CTC). However, the study considered only tracks with a p_T greater than 400 MeV/c. The measurement was also done with two separate samples [27], where a *hard* event had a jet which deposited at least 1.1 GeV in the calorimeter towers and a *soft* event was the one that contained no jets. The results showed that the KNO scaling holded in the "soft" sample while violated in the "hard" sample.

The E735 experiment at the Tevatron collider measured the multiplicity distribution of NSD events in p+$\bar{\mathrm{p}}$ collisions at $\sqrt{s} = 300$, 546, 1000 and 1800 GeV [49]. The multiplicities were determined from the number of hits in an array of 240 scintillators which covered the range of $|\eta| < 3.25$. Time of flight counters covered a range of $1.6 < |\eta| < 3.25$ were used for trigger. The results were extrapolated to full phase space by UA5 simulation, which was tuned to the UA5 data, and PYTHIA. Sample size and corrections were not mentioned in the paper.

2.1.6. Experiments at the Relativistic Heavy Ion Collider

The PHOBOS experiment at RHIC had a charged particle multiplicity detector covering a large fraction of the total solid angle. The charged particle reconstruction in this experiment was based on the silicon detector. The PHOBOS experiment measured inclusive p+p collision at $\sqrt{s} = 200$ and 410 GeV in the range $|\eta| < 5.4$. The charged particle multiplicity was reconstructed with a *Hit Counting* method, which used the segmentation of the silicon multiplicity detector. The large acceptance also provided checks on the existing measurements at $\sqrt{s} = 200$ GeV. The results were consistent with UA5 measurement on p+$\bar{\mathrm{p}}$ collisions.

The STAR experiment measured the NSD p+$\bar{\mathrm{p}}$ collisions at $\sqrt{s} = 200$ GeV at RHIC. The main detector of the STAR experiment was the time projection chamber which

covered a pseudorapidity range of $|\eta| < 1.8$. The trigger used was a coincidence of the signals from the zero degree calorimeters and beam-beam counters. A data set of 3.9 million was collected during 2002. Tracks with $p_T > 0.2$ GeV/c are retained for analysis. Corrections on tracking efficiency, secondaries and SD contribution were based on PYTHIA simulation.

Table 2.1.: Summary of the experiments before the startup of the LHC. The symbol ∘ indices that measurements of $dN_{ch}/d\eta$ (or multiplicity distributions) is available in this experiment.

Exp.	$\sqrt{s}$ (GeV)	Type	$dN_{ch}/d\eta$	Multi.	Trigger	N_{ev}	p_T reach	η	Ref.
NAL	13.8,19.6,23.8,27.6(p+p)	INEL	∘	∘	incl.	26k		Full	[20, 50]
SCD	23.6,30.8,45.2,53.2	INEL	∘	∘	incl.	2k-7k	45 MeV		[21]
SFM	30.4,44.5,52.6,62.2	INEL/NSD		∘	incl.				[22]
UA1	200,500,900(p+$\bar{p}$)	NSD		∘	2-arm		150 MeV	$\|\eta\| < 5.5$	[41]
	540(p+$\bar{p}$)	NSD	∘						[42]
UA5	53(p+p p+$\bar{p}$)	INEL	∘	∘	2-arm	4k	45 MeV	$\|\eta\| < 3.5$	[43]
	53,200,546,900 (p+$\bar{p}$)	INEL/NSD	∘						[24]
	546(p+$\bar{p}$)	INEL/NSD	∘	∘					[23]
	540(p+$\bar{p}$)	NSD		∘					[35]
	200,900(p+$\bar{p}$)	NSD		∘	2-arm	4k, 7k		$\|\eta\| < 5.0$	[44, 45]
P238	630(p+$\bar{p}$)	NSD	∘		2-arm	3M		$1 < \|\eta\| < 6$	[46]
CDF	630,1800(p+$\bar{p}$)	Uncor.	∘		2-arm	9k, 30k	50 MeV	$\|\eta\| < 3.5$	[47]
	630,1800(p+$\bar{p}$)	NSD		∘	2-arm	9k, 30k	50 MeV	$\|\eta\| < 2.5$	[48]
	630,1800(p+$\bar{p}$)	NSD		∘	2-arm	3M, 4M	400 MeV	$\|\eta\| < 1.0$	[27]
E735	300,500,1000,1800(p+$\bar{p}$)	NSD		∘	2-arm			$\|\eta\| < 3.25$	[49]
	1800(p+$\bar{p}$)	NSD		∘	2-arm	5M		$\|\eta\| < 3.25$	[51]
PHOBOS	200,410(p+p)	INEL/NSD	∘		1(2)-arm			$\|\eta\| < 5.4$	[52]
STAR	200(p+p)	NSD	∘						[53]

2.2. $dN_{ch}/d\eta$ distributions

The measurement of charged hadron angular distribution was first carried out in the studies of cosmic rays and later performed in the collider experiments. The pseudo-rapidity distributions of p+p($\bar{p}$) collisions had been measured from NAL to Tevatron energies, which spaned almost three orders of magnitudes. The results from different energies were similar in shape, but with width and height increased as a function of $\sqrt{s}$. It has been observed from the NAL data that the distributions consisted of a flat plateau near the mid-rapidity and decreased to 0 in the forward region. There was a dip near $\eta = 0$, which was from the Jacobian transformation from the rapidity to the pseudorapidity (See Sec. 1.3 for more details).

Fig. 2.1 shows the $dN_{ch}/d\eta$ from ISR energies. It is clear the the $dN_{ch}/d\eta$ at mid-rapidity is increasing, which indicates that Feynman scaling is violated. The authors also confirmed the substantial violation by converting the observed $dN_{ch}/d\eta$ to dN_{ch}/dy [21]. The data didn't show an increase in width and the distributions stops at $\eta \sim 4$, which could be from the effect of limited detector sensitive to very forward particles. Although the correction on geometrical acceptance was apply, the correction factor due to the acceptance for $|\eta| > 3.5$ was 1-10 [21] which may lead to larger systematic error.

Fig. 2.2 and 2.3 show the $dN_{ch}/d\eta$ distributions of inclusive and NSD p+p (p+$\bar{p}$) collisions from ISR to Tevatron energies. At several center-of-mass energies, the distributions were measured by several experiments and the results were found to be consistent with each other. The data showed a clear trend of widening in η, which was proportional to the rapidity of the beam (y_{Beam}).

The CDF data showed a large central dip in the mid-rapidity. It has to be noted that the results were uncorrected for the events which missed the trigger and there were large systematic uncertainties quoted by the authors for the data in the range of $|\eta| > 1$.

2.2.1. Fragmentation region

In order to test the limiting fragmentation hypothesis, the distributions are plotted in the lab frame of the incoming proton beam, which is shown in Fig. 2.4 for inclusive p+p($\bar{p}$) collisions and in Fig. 2.5 for NSD events. The distributions from higher energies tend to join an universal curve at the region of low $\eta - y_{Beam}$, which suggest that the limiting fragmentation holds in the forward region. It seems that the limiting fragmentation distribution follows a straight line. It is also found that the scaling continues to

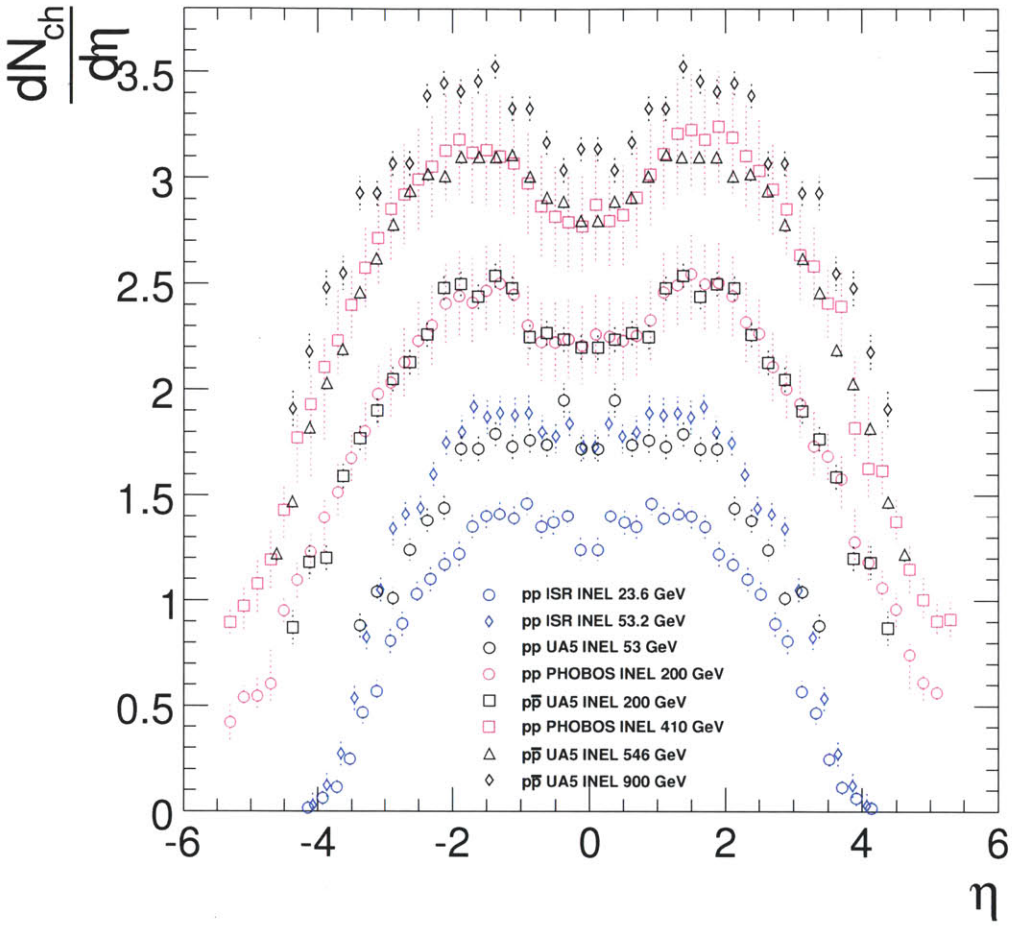

Figure 2.2.: Inclusive inelastic $dN_{ch}/d\eta$ from ISR to Tevatron energies.

hold in larger $\eta - y_{Beam}$ where the produced particles are not expect to come from the fragmentation of the projectile. This phenomenon is called *the extended longitudinal scaling* [18]. The cause of the scaling is not yet understood. Busza [18] interpreted it as direct evidence of some kind of saturation, akin to that in the Color Glass Condensate picture of particle production.

The spread of the data points in the fragmentation region is roughly 20% for inclusive distributions and 10% for NSD distributions. In the collider experiments, the fragmentation region corresponds to very forward region of the experiment, where large acceptance corrections were applied to the raw data. Part of the large variation can also come from the difficulty of event triggering.

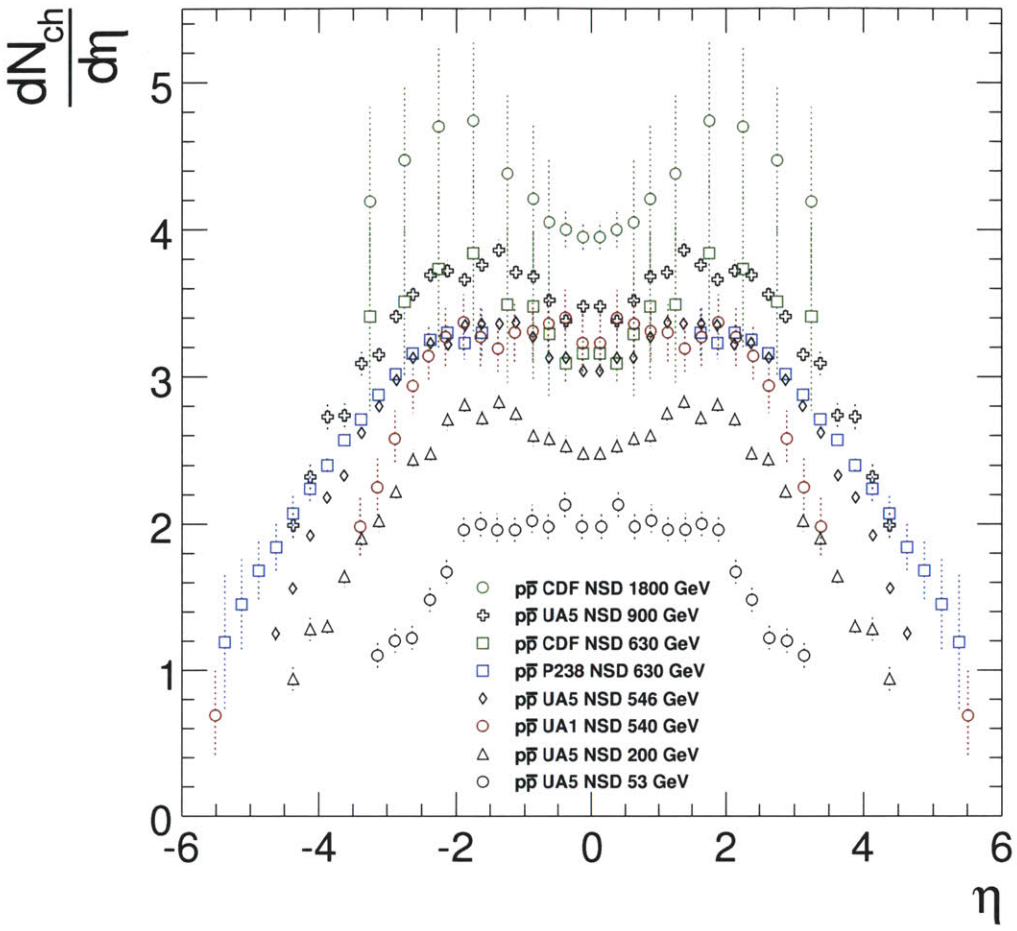

Figure 2.3.: Non-single-diffractive inelastic $dN_{\mathrm{ch}}/d\eta$.

2.2.2. Energy dependence of the pseudorapidity density at the mid-rapidity

Fig. 2.6 shows the $dN_{\mathrm{ch}}/d\eta$ at $|\eta| \sim 0$ as a function of $\sqrt{s}$. Note that there is no systematic errors for the UA5 data. The closed symbols are NSD data while open symbols are inelastic data.

The raising $dN_{\mathrm{ch}}/d\eta$ can be fit with two different parameterizations: $a + b\ln s$ and $a + b\ln s + c\ln s^2$. Both fits give reasonable description to the observed data. The measurement at $\sqrt{s} = 1.8$ TeV from CDF showed deviations from the linear fit [47] and the second-order fit gives a better χ^2. This suggests that $dN_{\mathrm{ch}}/d\eta\,|_{\eta=0}$ increases fast than $\ln s$.

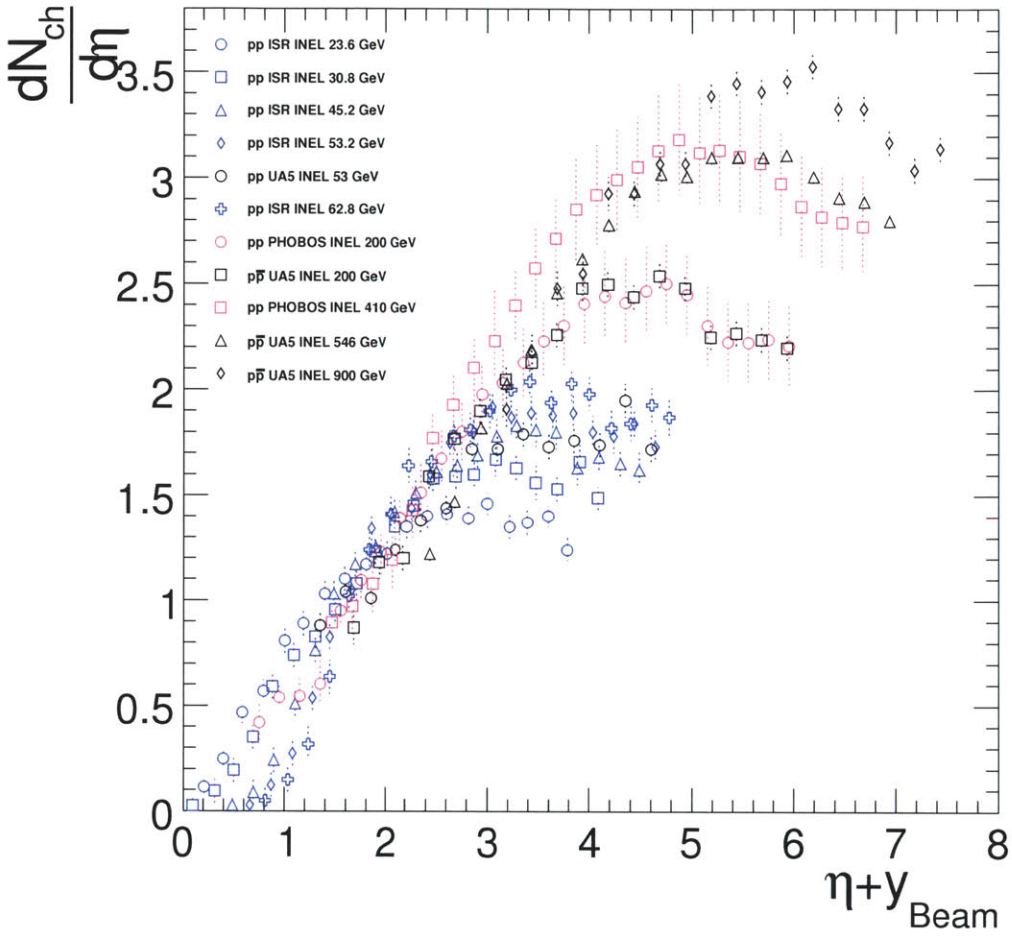

Figure 2.4.: Inclusive inelastic $dN_{ch}/d\eta$ in the rest frame of the proton beam.

Since the two empirical fits gives quite different extrapolations at LHC energies (up to 25%), the measurement at high energy will help to identify the correct parameterization.

2.2.3. Comparison between data and PHOJET

Fig. 2.7 shows the comparison between NSD $dN_{ch}/d\eta$ and the results from the PHOJET generator. The PHOJET generator describes the $dN_{ch}/d\eta$ reasonably well up to $\sqrt{s} =$ 1800 GeV. The consistency between data and MC is at the 5% to 10% level except the CDF data in the range of $|\eta| > 1$. The generated $dN_{ch}/d\eta$ from PHOJET is higher than data at $\sqrt{s} = 53$ - 630 GeV and lower than the CDF measurement at $\sqrt{s} = 1800$ GeV. The dip structure at mid-rapidity is also reproduced by the PHOJET generator.

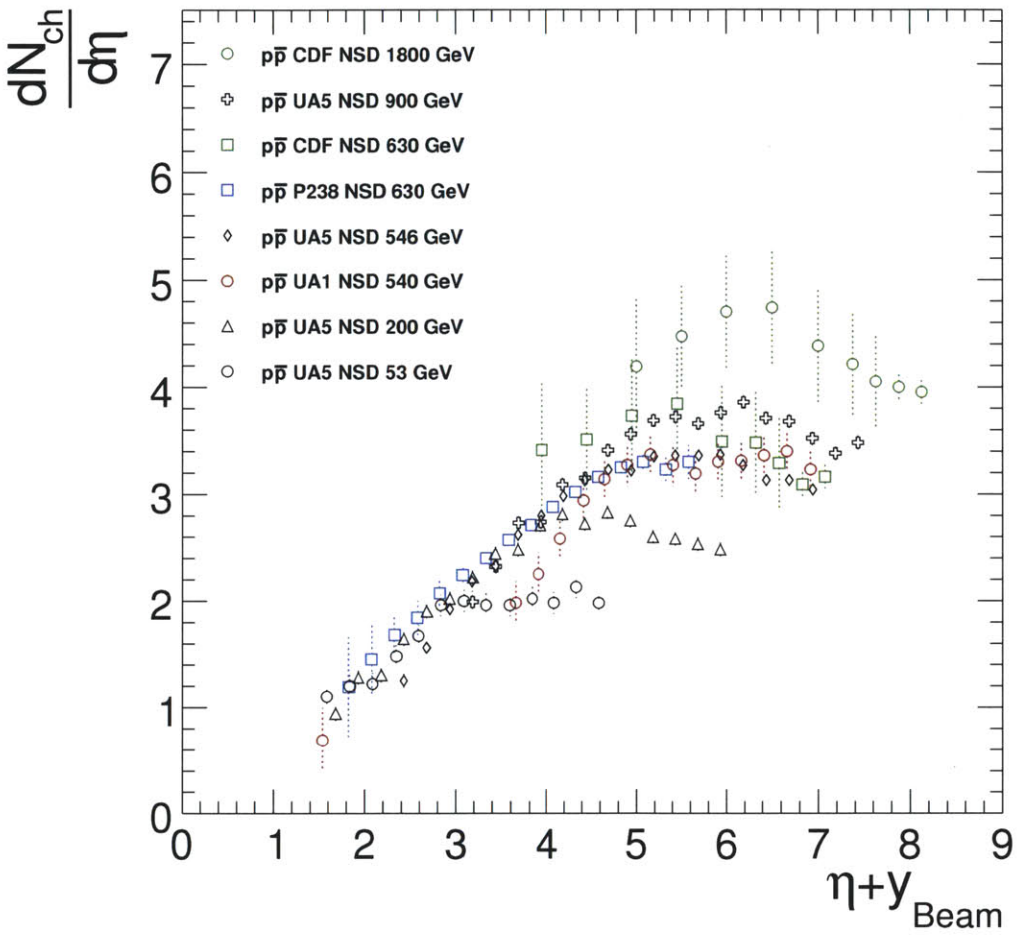

Figure 2.5.: Non-single-diffractive inelastic $dN_{ch}/d\eta$ in the rest frame of the proton beam.

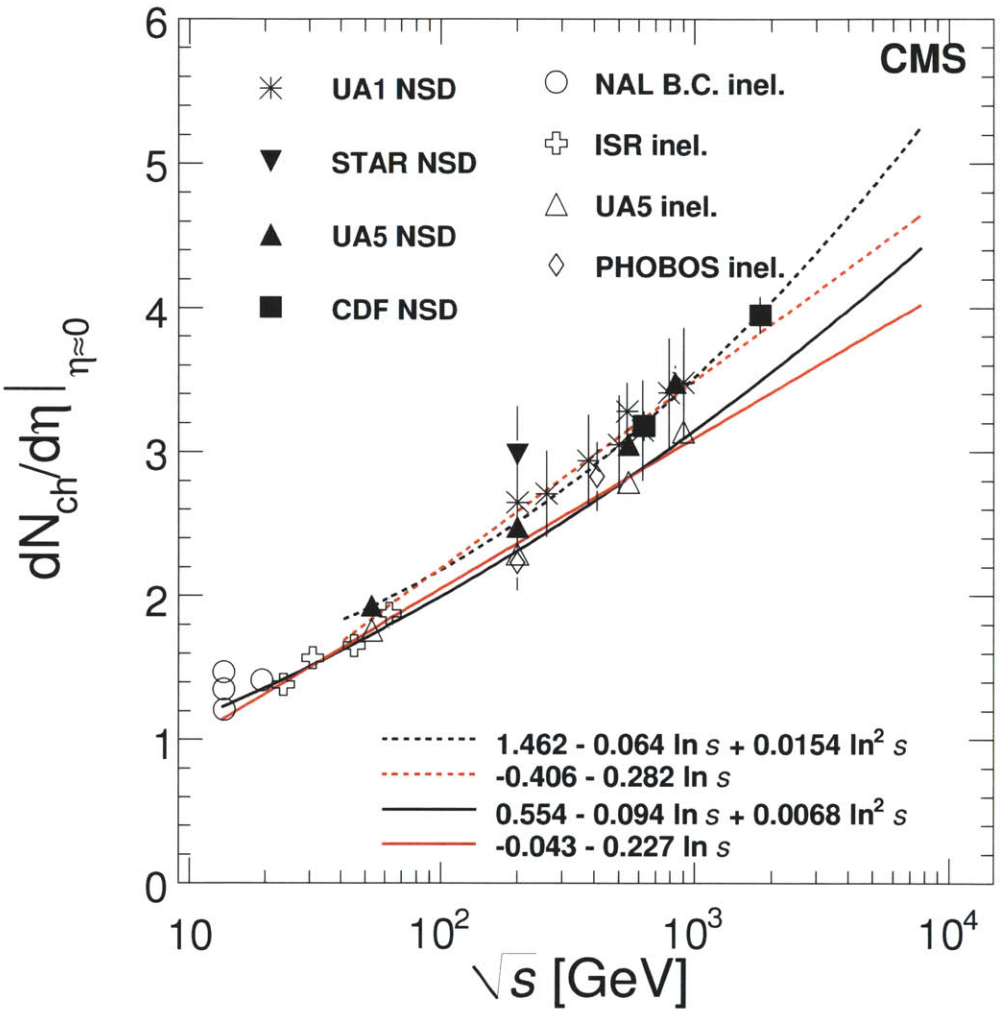

Figure 2.6.: $dN_{ch}/d\eta$ as a function of $\sqrt{s}$. The solid lines are fits to the inclusive data while dashed lines are fits to the NSD data. The systematic errors are shown when available.

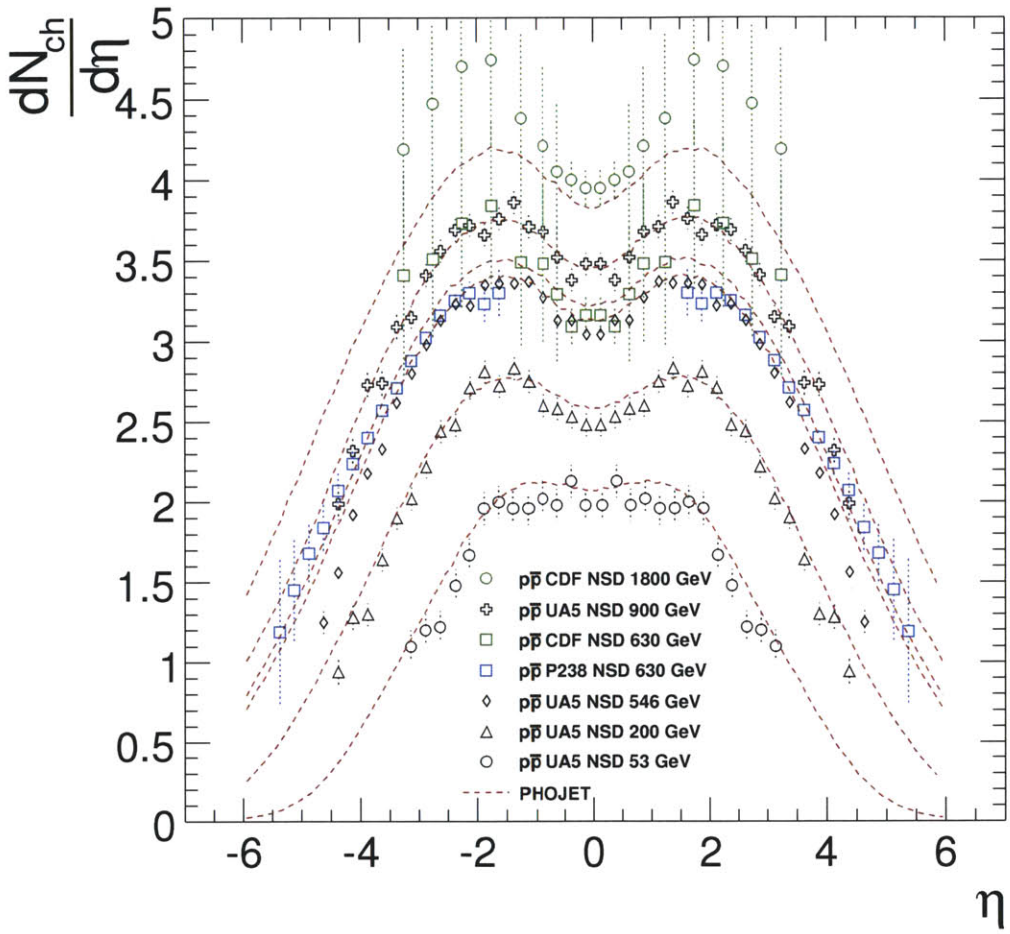

Figure 2.7.: Non-single-diffractive inelastic $dN_{\mathrm{ch}}/d\eta$ compared with PHOJET generator.

2.3. Multiplicity distributions

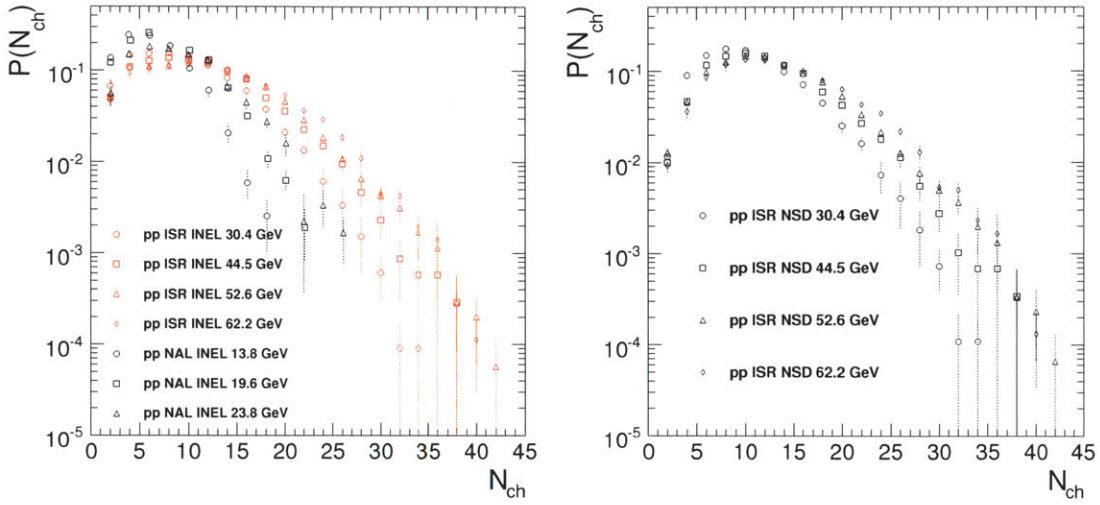

Figure 2.8.: The multiplicity distributions measured in the NAL and ISR energies. (Left Panel) The distributions from inclusive events. (Right Panel) The distributions from NSD events.

Multiplicity distributions measured in full phase space from NAL and ISR are shown in Fig. 2.8. Increasing the energy resulted in an increase in total multiplicity. Studies were done in inclusive events and NSD events. By comparing the distributions from both event selections, one can see that the single-diffractive events are populated in low multiplicity region of the distribution.

2.3.1. Validity of KNO scaling

To assess the validity of KNO, the multiplicity distributions are expressed using KNO variable $z = N_{ch}/ < N_{ch} >$, which is shown in Fig. 2.9. The distributions from different energies ($\sqrt{s} < 63$ GeV) and different experiments join an universal curve, which can be described as a negative binomial function. Although the Feynman scaling is broken, it is clear that the KNO scaling is hold in the ISR and NAL energies.

Fig. 2.10 shows the multiplicity distributions before the startup of the LHC, including Sp$\bar{p}$S and Tevatron data. It is evident that the KNO scaling is violated between lowest energy and highest energy dataset. The data with $\sqrt{s} > 100$ GeV show a extended high multiplicity tail which can not be described by a single NBD. The extended high multiplicity tail seems to grow smoothly as a function of $\sqrt{s}$.

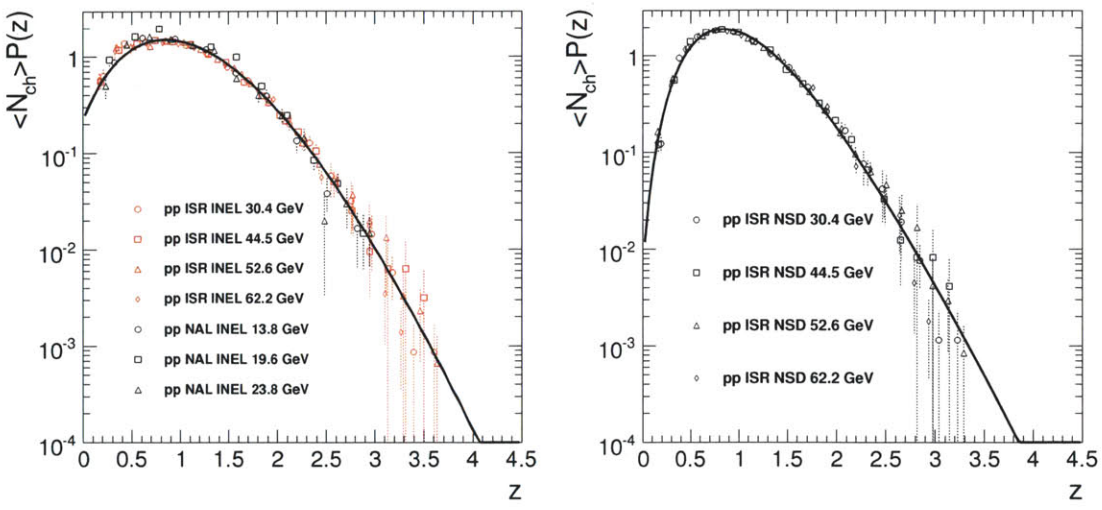

Figure 2.9.: The multiplicity distributions measured in the NAL and ISR energies and fit by a negative binominal function. The distributions are normalized and expressed using KNO variables. (Left Panel) The distributions from inclusive events. (Right Panel) The distributions from NSD events.

For the low z region, the height of the peak from higher energies is lowered because $< N_{ch} >$ is increasing faster due to the high multiplicity tail. In E735 data, a large uncertainty was shown in the low multiplicity region which was due to the correction and rejection of the beam background.

The distributions in UA5 can be described by a fit with two NBD (Fig. 1.9). This indicates that there are two *independent* classes in the multiplicity distribution. Each of the class follows a NBD. But the origin of the shoulder structure is not yet understood. Possible explanations are the contributions from mult2iple parton interactions, or increasing contributions from the hard processes involve in the production of high p_T jets.

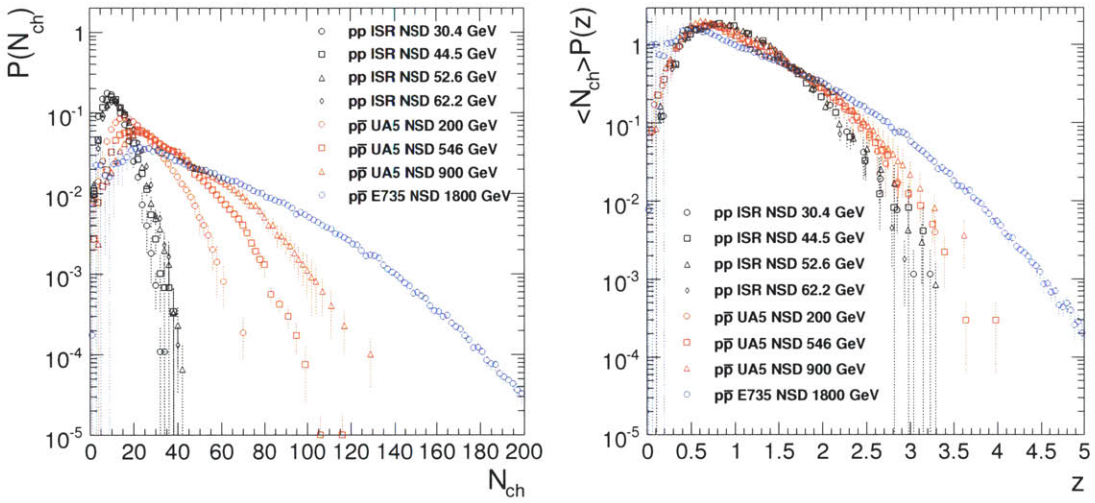

Figure 2.10.: The multiplicity distributions measured in multiplicity variables (left panel) and in KNO variables (right panel).

3. The Large Hadron Collider

The Large Hadron Collider (LHC) [1] is a two-ring-superconducting-hadron accelerator and collider installed in the existing 26.7 km tunnel that was constructed between 1984 and 1989 for the CERN LEP accelerator. It is designed to collide proton beams with a center-of-mass energy of 14 TeV and luminosity of $10^{34}\text{cm}^{-2}\text{s}^{-1}$. It also collides lead ions with an energy of 2.76 TeV per nucleon and a peak luminosity of $10^{27}\text{cm}^{-2}\text{s}^{-1}$. In this chapter, a brief description of the LHC is presented.

3.1. Design and Layout of LHC

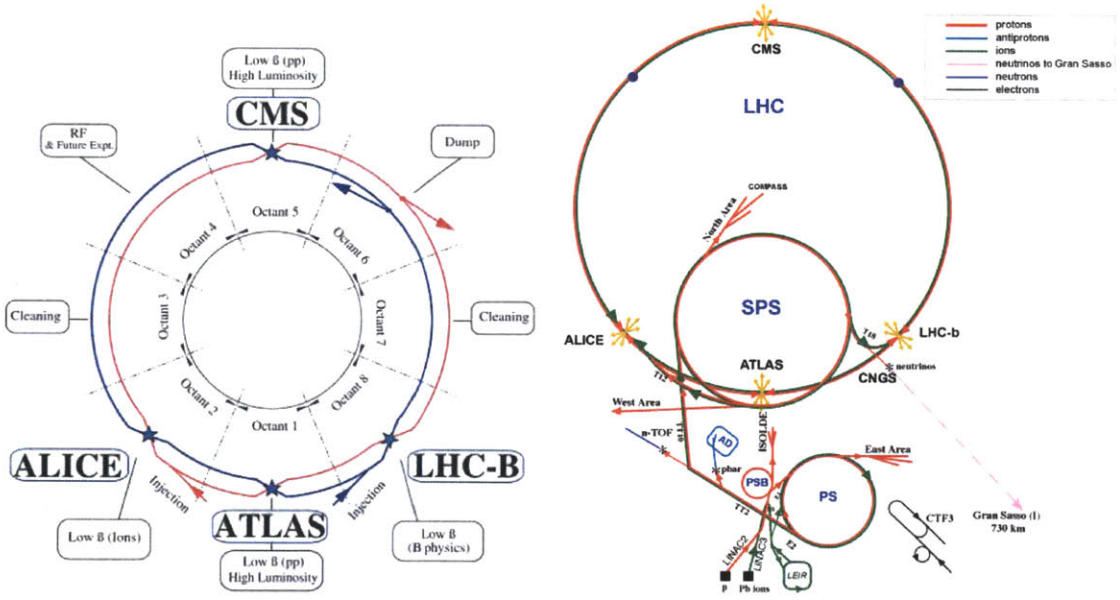

Figure 3.1.: Schematic layout of the LHC (Beam 1 - clockwise, Beam 2 - anticlockwise)

The LHC is a synchrotron that accelerates two counter-rotating beams in separate beam pipes. It has eight arcs and eight straight sections and the basic layout is shown in Fig. 3.1. There are 4 beam crossing points which contain the experiments (point 1, 2,

5 and 8). The injection systems from SPS to LHC for Beam 1 and Beam 2 are located at Point 2 and Point 8. Insertions at Points 3 and 7 each contain two collimation systems for beam cleaning. The RF systems which accelerate the particles are located at Point 4.

There are 1232 superconducting dipole magnets that bend the beam trajectories and 392 quadrupole magnets that are used to keep the beams focused. The superconducting magnets are kept at the operating temperature of 1.9 K with liquid helium. The dipole magnets are operated with a current of 11.85 kA and provide a field of 0.54 T during injection and a nominal field of 8.33 T during nominal collisions with beam energy of 7 TeV. RF systems provide a RF voltage of 8 - 16 MV/beam which accelerates the particle, compensate the synchrotron radiation loss (7 keV/turn).

The protons(lead ions) are grouped in cylindrical bunches with a radius of 16.6(15.9) μm and a length of 7.55(7.94) cm with a bunch spacing of 25(100) ns in the nominal operation. The design bunch intensity is 1.15×10^{11} for protons and 7×10^{7} for lead ions. The maximum bunches per ring is 2808(592) for nominal proton-proton(Pb+Pb) runs.

3.2. Experiments at the LHC

There are six experiments that operates at the LHC:

1. CMS (Compact Muon Solenoid) [54] and ATLAS (A Toroidal LHC Apparatus) [55] are two general-purpose detectors that are built to study both p+p and Pb+Pb collisions. The focus of the two experiments are the verification of the Standard Model, search for the Higgs boson, physics beyond the Standard Model, and heavy ion physics. The detector is optimized for high-p_T physics to enhance the discovery potential of new heavy particles postulated by various of models such as the supersymmetric extensions (SUSY) of the Standard Model, and the use of the high-p_T probes in the study of the quark-gluon plasma. The analysis in this thesis is based on the CMS detector and the details are described in Chap. 4

2. ALICE (A Large Ion Collider Experiment) [56] is a dedicated heavy-ion which is optimized to study heavy ion collisions. The strength of the detector is in the low-p_T observables such as the particle multiplicity measurement, particle identification.

3. LHCb (The Large Hadron Collider beauty experiment) [57] studies the CP-violation in the b-quark systems produced in the proton-proton collisions.

4. TOTEM (TOTal Elastic and diffractive cross section Measurement) [58] is designed for the measurement of total cross section, elastic scattering and diffractive proecsses in the p+p collisions, which is located in the forward region of the CMS detector.

5. LHCf (Large Hadron Collider forward) [59] is a special-purpose detector to study the particles generated in the forward region of collisions which is located close to the ATLAS experiment. The LHCf is designed to measure the energy and number of π^0, which will help explain the origin of high energy cosmic rays.

3.3. Startup

On 10th September 2008, the proton beam at LHC was successfully circulated in the main ring of the LHC for the first time. The machine is ready for collisions at $\sqrt{s} = 900$ GeV. However, during the 10 TeV magnet commissioning, a short circuit occurred and resulted damage of magnets. The repairing of the magnet and installation of additional protection features was done during 2009. On 20th November 2009, the proton beams were successfully circulated with injection energy 450 GeV per beam again, with the first proton-proton collisions at 900 GeV.

On 30 November 2009, the LHC became the highest-energy particle accelerator in the world with 1.18 TeV per beam, which was a record held by the Tevatron at Fermilab in the Unite States. After the 2009 winter shutdown, the accelerator ramped up the beam energy to 3.5 TeV on 19th March 2010 and delivered the first collisions at 7.0 TeV on 30th March 2010.

During the startup, the initial collision rate was 5 - 50 Hz (corresponds to $L \sim 1 - 10 \times 10^{26}$ cm^{-2}s^{-1}) and the expected number of pile-up is less than 0.3%.

4. The CMS detector

The CMS detector is a multi-purpose detector which provides capability to study p+p and heavy-ion collisions. A detailed description of the CMS experiment can be found in Ref. [60]. An important aspect driving the detector design and layout is the choice of the magnetic field configuration in order to measure precisely the momentum of charged particles. A compact design is chosen and this results in a choice of high magnetic field which provides a large bending power.

In the multiplicity analysis, the crucial parts of the CMS detector is the pixel tracker, which is used to reconstruct the charged particles, forward calorimeter (HF) and Beam Scintillator Counters (BSCs) [60, 61] in the forward region, which are used for triggering and event selection. In this chapter, the design and performance of the CMS detector will be described.

4.1. CMS design concept

The overall layout of CMS is shown in Fig. 4.1. The central feature of the CMS apparatus is a superconducting solenoid of 6 m internal diameter, providing a uniform magnetic field of 3.8 T. Immersed in the magnetic field are the pixel tracker, the silicon-strip tracker (SST), the lead-tungstate crystal electromagnetic calorimeter (ECAL) and the brass/scintillator hadron calorimeter (HCAL). In addition to barrel and end-cap detectors for ECAL and HCAL, the steel/quartz-fibre forward calorimeter (HF) covers the region of $|\eta|$ between 2.9 and 5.2. Muons are measured in gas-ionization detectors embedded in the steel return yoke. Two elements of the CMS detector monitoring system, the Beam Scintillator Counters and the Beam Pick-up Timing for the eXperiments (BPTX) devices [60, 62], were used to trigger the detector readout. In the following sections, the sub-detectors will be described in detail.

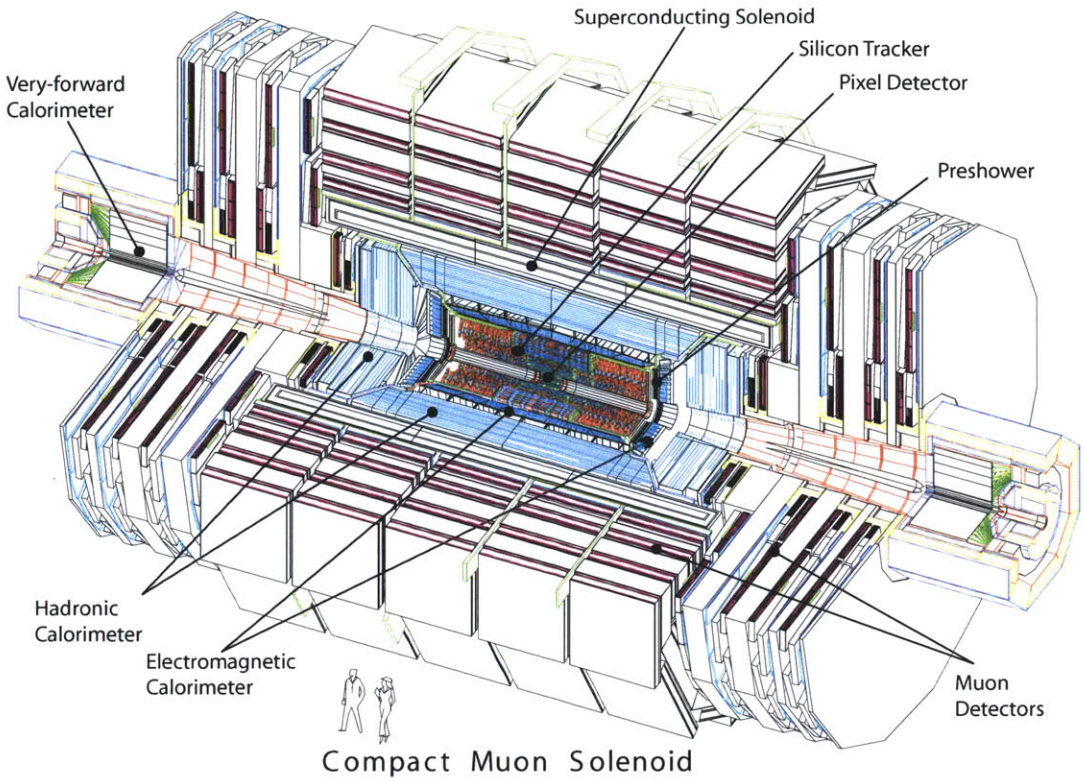

Figure 4.1.: The overall layout of the CMS detector. The beam monitoring system in the forward region is not shown.

4.2. Magnet

In order to provide unambiguous determination of the sign of the muons with a momentum up to 1 TeV/c in the reconstruction of the decaying new particles, it requires a momentum resolution of $\Delta p/p \sim 10\%$ at $p = 1$ TeV/c [63]. CMS chose a large superconducting solenoid, the design parameters of which are given in Table 4.1 [64]. A large bending power can be obtained for a modestly-sized solenoid, albeit a high-field superconducting one, as the bending starts at the primary vertex. The main feature of the CMS solenoid are the use of a high-purity aluminum-stabilised conductor and indirect cooling (by thermosyphon) together with full epoxy impregnation.

During the data taking in 2009-2010, the magnetic field was set to 3.8 T for the most of the beam time. A small data set was also taken with $B = 0$ at $\sqrt{s}$= 7 TeV.

Field	4 T (3.8 T during the data taking)
Inner Bored	5.9 m
Length	12.9 m
Number of Turns	2168
Current	19.5 kA
Stored energy	2.7 GJ
Hoop stress	64 atm

Table 4.1.: Parameters of the CMS superconducting solenoid.

4.3. Inner tracking system

The CMS tracker system which covers a pseudorapidity range of $|\eta| < 2.4$, comprises 66 million silicon pixels and 9.6 silicon strips [65]. The occupancy of the pixel detector is about 10^{-4} at high luminosity p+p data taking. Even in heavy-ion (Pb+Pb) running, the occupancy is at the level of 1% in the pixel detector and less than 20% in the silicon strip detector, which permits the reconstruction in the high multiplicity environment. The tracker is designed to provide an impact-parameter resolution of about 100 μm and a transverse-momentum resolution of about 0.7 % for 1 GeV/c charged particles at normal incidence (η=0) [63]. The layout of the CMS tracker is shown in Fig. 4.2.

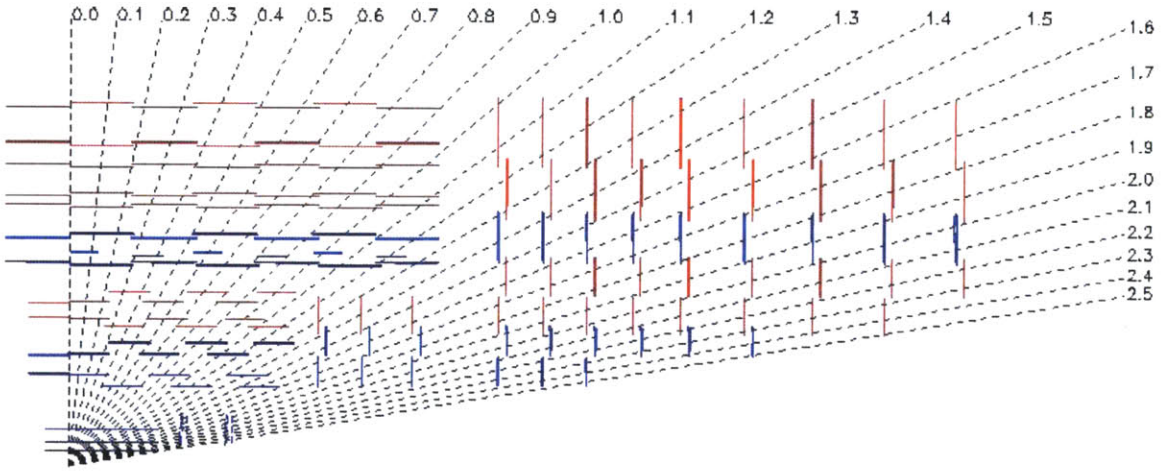

Figure 4.2.: The CMS tracker layout (1/4 of the z view).

4.3.1. Pixel tracker

The pixel detector consists of 3 barrel layers with 2 endcap disks on each side on them (Fig.4.3) [65]. The 3 barrel layers are located at mean radii of 4.4 cm, 7.3 cm and 10.2 cm, and have a length of 53 cm. This means that CMS is capable to detect charged pions with transverse momentum greater than $\sim$ 50(70) MeV/c with the first(second) pixel barrel layer with a magnetic field of 3.8 Tesla. The 2 end disks, extending from 6 to 15 cm in radius, are placed on each side at $|z| = 34.5$ cm and 46.5 cm. The recorded hits in the barrel layers are used for tracklet reconstruction for charged multiplicity study. The details are described in Chap. 6.

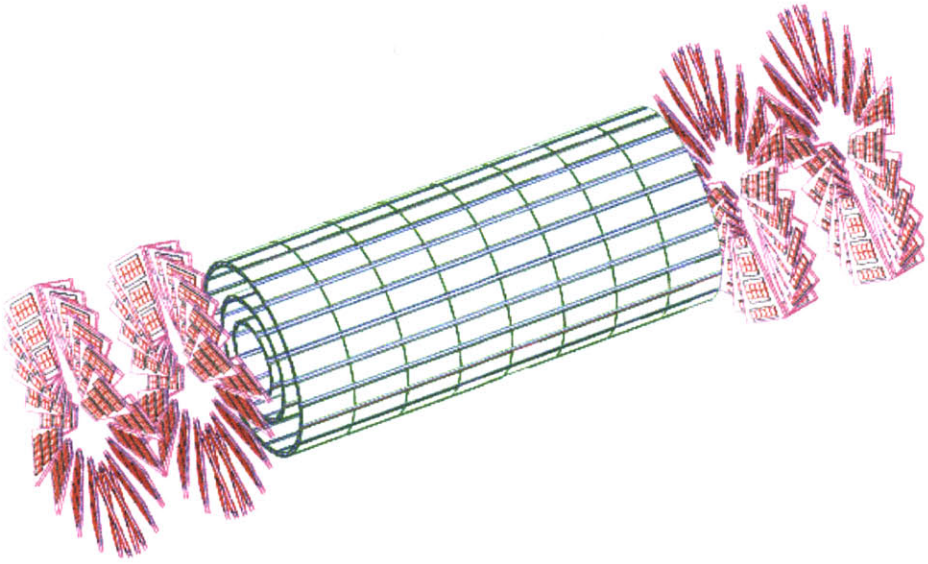

Figure 4.3.: The CMS Pixel Detector layout .

4.3.2. Silicon Strip tracker(SST)

The barrel tracker region is divided into 2 parts: a TIB (Tracker Inner Barrel) and a TOB (Tracker Outer Barrel) [63, 65]. The TIB is made of 4 layers and covers up to $|z| < 65$ cm and The TOB comprises 6 layers with a half-length of $|z| < 110$ cm. The first 2 layers of TIB and TOB are made with "stereo" modules in order to provide a measurement in both $r-\phi$ and $r-z$ coordinates. A stereo angle of 100 mrad has been chosen.

The endcaps are divided into TEC (Tracker End Cap) and TID (Tracker Inner Disks). Each TEC comprises 9 disks that extend into the region 120cm $<$ |z| $<$ 280cm, and each TID comprises 3 small disks that fill the gap between the TIB and the TEC. The TEC

and TID modules are arranged in rings, centered on the beam line, and have strips that point towards the beam line, therefore have a variable pitch. The first 2 rings of the TID and the inner most 2 rings and the fifth ring of the TEC have "stereo" module. The spec and performance of the silicon sensors used in the strip detectors are summarized in Table. 4.2.

During the data-taking period, 98.4% of the pixel and 97.2% of the SST channels were operational. The fraction of noisy pixel channels was less than 10^{-5}. The signal-to-noise ratio in the SST depends on the sensor thickness and was measured to be between 28 and 36, consistent with the design expectations and cosmic-ray measurements [63, 66]. The tracker was aligned as described in Ref. [67] using cosmic ray data prior to the LHC commissioning. The precision achieved for the positions of the detector modules with respect to particle trajectories is 3-4 μm in the barrel for the coordinate in the bending plane. This allowed us to perform the first physics measurement with an already aligned detector.

part	No. detectors	thickness (μm)	mean pitch (μm)	$r-\phi(z)$ resolution (μm)
TIB	2724	320	81/118	23-34(23)
TOB	5208	500	81/183	35-52(52)
TID	816	320	97/128/143	
TEC	2512	320	96/126/128/143	
TEC(2)	3888	500	143/158/183	

Table 4.2.: Detector types in the silicon tracker.

The CMS tracker gives a transverse momentum resolution of 0.5-7.0% and 95% reconstruction efficiency for muons with P_T of 1-100 GeV/c. [63]

4.4. Muon system

The Layout of the muon system is shown in Fig. 4.4. Three types of gaseous detectors are used to identify and measure muons [63, 68]. The choice of the detector technologies has been driven by the very large surface to be covered and by the different radiation environments. In the barrel region ($|\eta| < 1.2$), where the neutron induced background is small, the muon rate is low and the residual magnetic field in the chamber is low, drift tube (DT) chambers are used. In the 2 endcaps, where the muon rate as well as the neutron induced background rate is high, the magnetic field is also high, cathode strip chambers (CSC) are deployed and cover the region up to $|\eta| < 2.4$. In addition

to this, resistive plate chambers (RPC) are used in both barrel and the endcap regions. The RPCs are operated in avalanche mode to ensure good operation at high rates (up to 10kHz/cm^2). The typical momentum resolution of the muons is from 0.7% ($p \sim$10 GeV) to 10% ($p \sim 1$ TeV). [63]

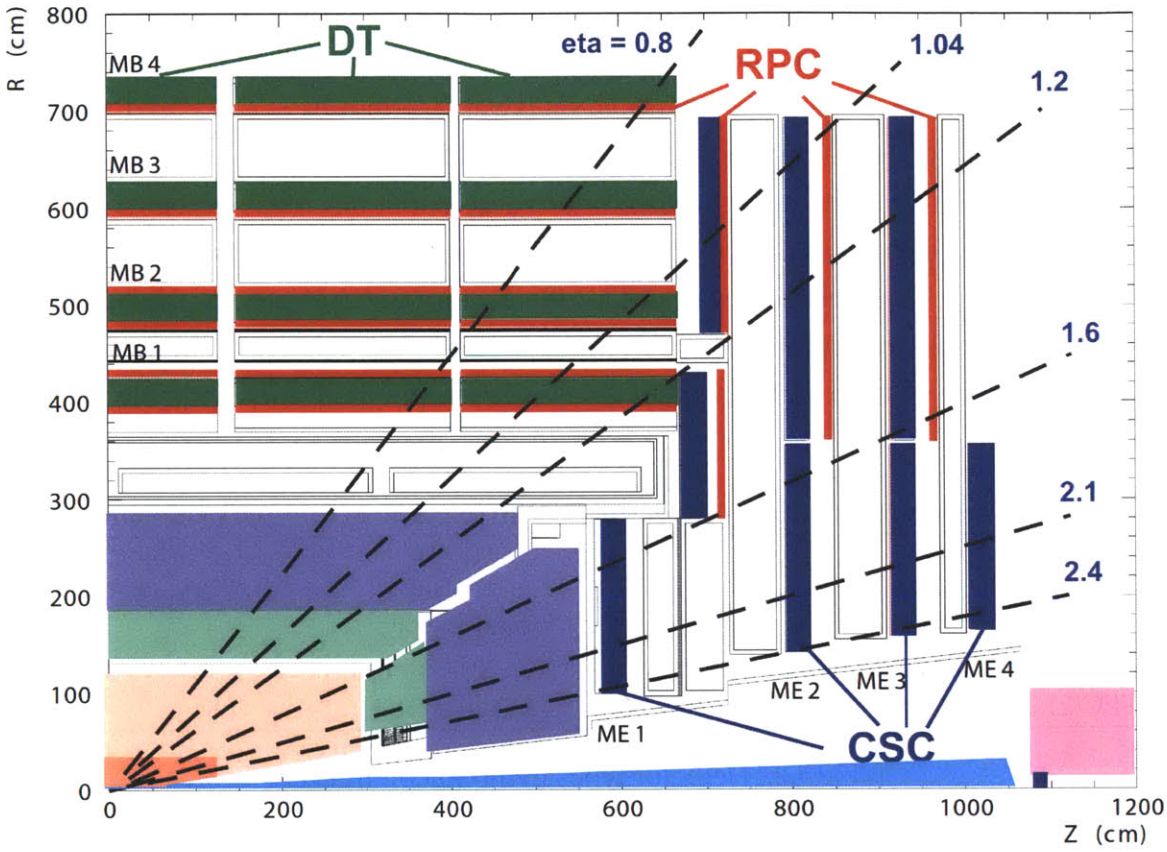

Figure 4.4.: The Layout of the CMS Muon system.

4.5. Electromagnetic calorimeter

The Electromagnetic Calorimeter (ECAL) is a hermetic, homogeneous calorimeter comprising 61200 lead tungstate ($PbWO_4$) crystals mounted in the central barrel part, closed by 7324 crystals in each of the 2 endcaps. [69] The goal of the ECAL to reconstruct the electromagnetic objects such as electrons and photons, as well as the EM component of the jets. Lead tungstate scintillating crystals are chosen in order to have short radiation ($\chi_0 = 0.89$ cm) and Moliere (2.2 cm) lengths, are fast (80% of the light is emitted within 25 ns) and radiation hard (up to 10 Mrad). Silicon avalanche photodiodes (APDs) and

vacuum phototriodes (VPTs) are used for signal amplification. The layout of the CMS ECAL is shown in Fig. 4.6.

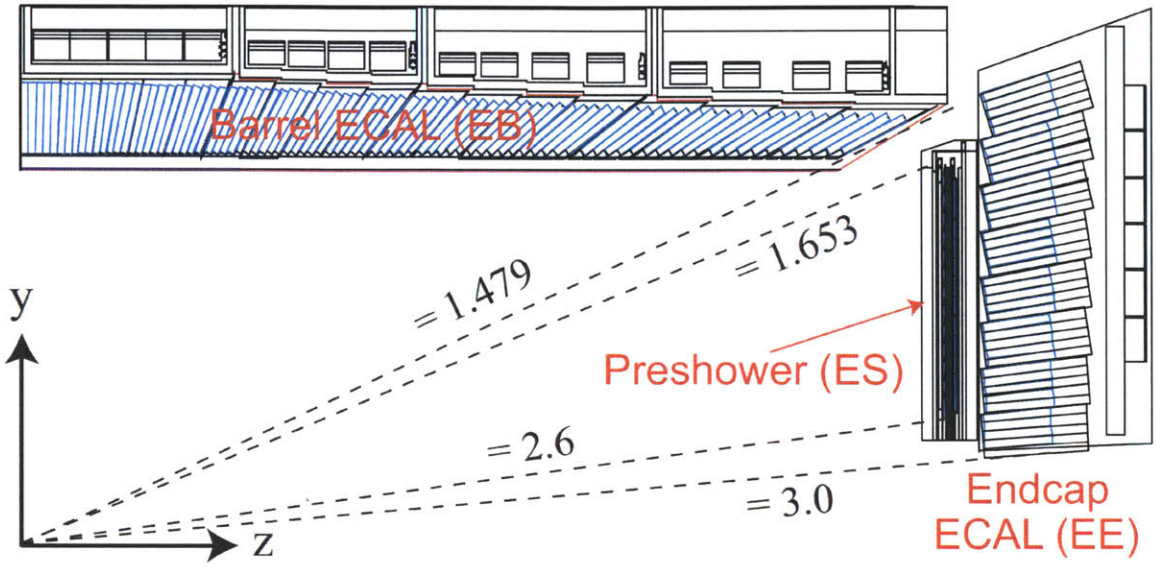

Figure 4.5.: The Layout of the CMS Electromagnetic Calorimeter system.

The ECAL Barrel (EB) covers a pseudorapidity interval of $0 < |\eta| < 1.479$. The inner radius is 129 cm, which means that a charged particle should have a p_T of at least ~1.5 GeV/c to reach the EB [63, 69]. Each crystal have a front face cross-section of $\sim 22 \times 22\text{mm}^2$, which covers 0.0174 in $\Delta\phi$and $\Delta\eta$, and a length of 230 mm, corresponding to 25.8 χ_0.

The ECAL Endcaps (EE) are two "Dees" at a distance of 314 cm from the center of the CMS and covering a pseudorapidity range of $1.479 < |\eta| < 3.0$. The endcap crystals are all identical and have a front face cross section of $28.6 \times 28.6\text{mm}^2$ and a length of 220 mm ($24.7\chi_0$). A preshower device is placed in front of the crystal calorimeter over much of the endcap pseudorapidity range in order to provide better separation power between π^0 and photons. The active elements of this device are 2 planes of silicon strip detectors, with a pitch of 1.9mm, which lie behind disks of lead absorber at depths of 2 χ_0 and $3\chi_0$.

4.6. Hadron calorimeter

The goal of the hadron calorimeter (HCAL) [70] is to minimize the non-Gaussian tails in the jet energy resolution and to provide good containment and hermetricity for the

missing transverse energy (E_T^{miss}) measurement. Due to the choice of the CMS magnet, the HCAL design maximizes material inside the magnet coil in terms of interaction lengths.

In the pseudo-rapidity range of $|\eta| < 3.0$, brass/scintillator sampling calorimeter is chosen. Brass has a reasonably short interaction length and is non-magnetic and the scintillator tiles with wavelength-shifting (WLS) fiber minimize the space devoted to the active medium. The photodetection readout is based on multi-channel hybrid photodiodes (HPDs). The hadron barrel (HB) part of HCAL consist of 32 towers covering the pseudorapidity range of $|\eta| < 1.4$, resulting in 2304 towers with a segmentation of $\Delta\eta \times \Delta\phi = 0.087 \times 0.087$. The hadron endcap (HE) of HCAL covers the pseudorapidity region $1.3 < |\eta| < 3.0$. For the 5 outermost towers at smaller η), the ϕ segmentation is 5°.and the η segmentation is 0.087. For the 8 innermost towers the ϕ segmentation is 10°, whilst the η segmentation varies from 0.09 to 0.35 at the highest η. The total number of HE tower is 2304. In order to sample the energy from penetrating hadron showers leaking through the rear of the calorimeters and improve the E_T^{miss} resolution, the hadron outer (HO) detector is placed outside the magnet. It contains scintillators with a thickness of 10 mm and covers the pseudorapidity region $|\eta| < 1.26$.

In the forward region, the hadron forward (HF) calorimeter covers the pseudorapidity range $3.0 < |\eta| < 5.0$. The HF is located 11.2 m from the interaction point and is made of steel absorber and embedded radiation hard quartz fibers, which provide a fast collection of Cherenkov light. There are 13 towers in η, all with a size given by $\Delta\eta \sim 0.175$, except for the lowest-η tower with $\Delta\eta \sim 0.1$ and the highest-η tower with $\Delta\eta \sim 0.3$. The ϕ segmentation of all towers is 10°, except for the highest-η tower which has $\Delta\phi \sim 20°$. The hadron forward detector served as an important detector in the $dN/d\eta$ analysis which provides good selection on the collisional events.

4.7. Beam monitoring system

4.7.1. Beam Pick-up Timing for the eXperiments (BPTX)

In order to monitor the beam condition, the two Beam Pick-up Timing for the eXperiments (BPTX) devices, located around the beam pipe at a distance of ±175 m from the IP on either side, are designed to provide precise information on the bunch structure and timing of the incoming beam, with better than 0.2 ns time resolution [62]. The BPTX detector uses two standard LHC beam position monitors (BPM) each comprising

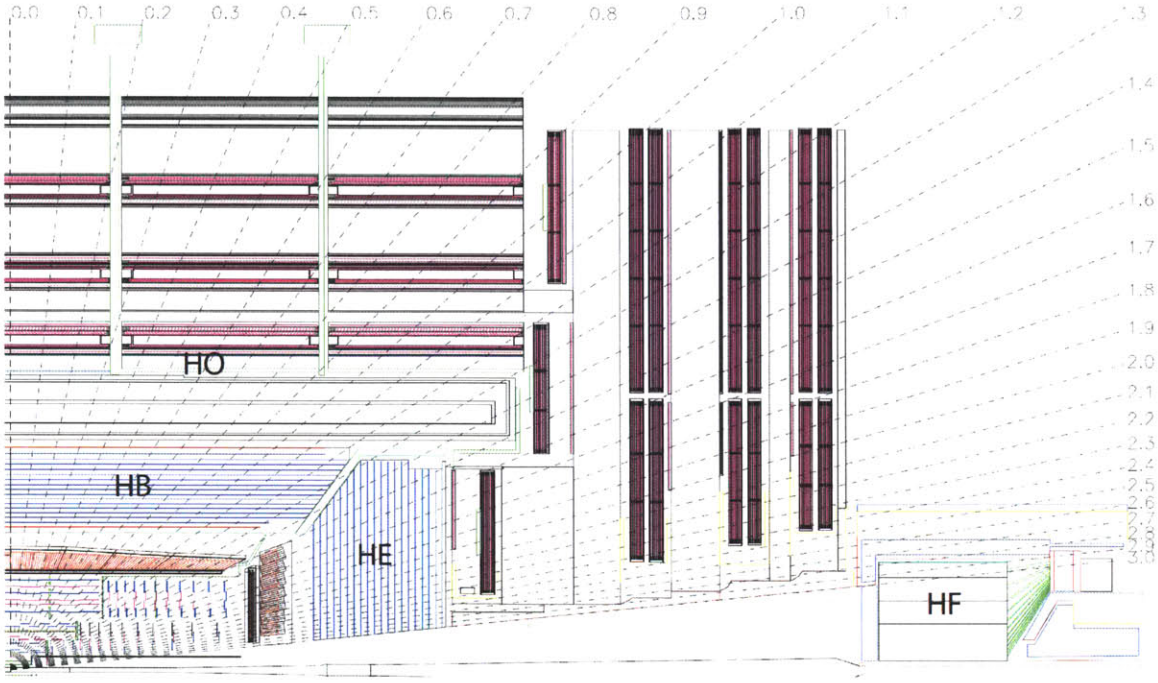

Figure 4.6.: The Layout of the CMS Hadronic Calorimeter system.

of four electrostatic button electrodes positioned symmetrically around the beam-pipe.

The BPTX is measured to be fully efficiency in detecting the beam with bunch intensity greater than 10^9 which provides valuable inputs to the Level 1 trigger.

4.7.2. Beam Scintillator Counters (BSC)

The two Beam Scintillator Counters (BSCs) are located at a distance of ± 10.86 m from the nominal interaction point (IP) and are sensitive in the $|\eta|$ range from 3.23 to 4.65 [61]. The scintillators for the BSC1 station are mounted on the inner surface of the HF detectors on both sides of the IP. The flight time between the IP and BSC1 is 36.5 ns. Each BSC is a set of 16 scintillator tiles. The structure and location of the BSC are shown in Fig. 4.7.

The four segments in each *outer* petal are grouped to two PMTs (PMT = photomultiplier tube), providing a segmentation in two halves, one for each end. The scintillator rings provide eight signals on each side. This gives in total $2 \times (8+8) = 32$ BSC1 channels.

Earlier measurements have shown a time resolution around 3 ns for these scintillators taken from the OPAL mini-plug detector. With the routing of the signal cables to the

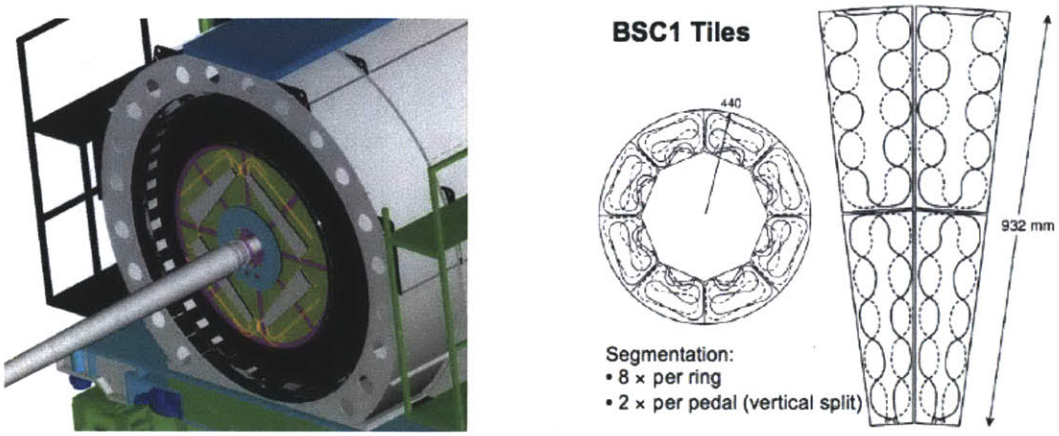

Figure 4.7.: Location and schematic of BSC detector. [61]

readout in USC55, a resolution around 5 ns is expected. The scintillators (BC408), read out through photo-multipliers via wavelength shifting fibers, are expected to provide 14 photo-electrons per traversing MIP.

The readout of the BSC counters is implemented using commercial electronics located in NIM and VME crates in rack S1E08. Signals from the PMT-s are discriminated and then combined using off-the-shelf logical NIM units (e.g. LeCroy) to implement the required coincidence logic and delays. This requires NIM to LVDS units for signal conversion in the end. The LVDS signals are routed to the GT rack via 4x2 wire commercial Ethernet cables.

The BSC elements have an average minimum-ionizing-particle(MIP) detection efficiency of 95.7%. The signal from BSC are also designed to provide hit and coincidence rates as inputs to the Level 1 trigger. The efficiency of the BSC segments was measured based on the MIP peak in the scintillators. The details of the efficiency determination can be found in Appendix. D.

4.8. Trigger system

The bunch crossing rate at LHC is 40 MHz which leads to $\sim 10^9$ interactions/sec at design luminosity, which makes full event recording impossible. The trigger system is designed to provide filter with a rejection factor of nearly 10^6 to select interesting events. The CMS trigger system can be divided into two parts: The Level 1 Trigger (L1), which use custom electronics, provides fast decision. The High Level Trigger (HLT) system, which relies upon commercial processor, perform reconstruction on the L1 accepted

events and make decisions from more detailed information [2, 63]. The triggers used in this analysis will be discussed in Chapter 5.

4.8.1. Level 1 Trigger

The CMS L1 trigger electronics itself is pipelined and deadtimeless, and can render a decision on every bunch crossing (40 MHz), synchronised to the LHC clock. The L1 trigger involve calorimetry and muon systems as well as some correlation of information from these systems. The L1 decision is based on the presence of local objects such as photons, electrons, muons and jets, using information from the calorimeters and muon systems. Detailed description of the L1 Trigger system can be found in Ref. [2]. During the startup, the *Zero-Bias* and *Minimum-Bias* Triggers are also implemented based on the BPTX coincidence or activities in BSCs which will be described in Sec. 4.8.3.1.

The L1 pipeline data storage time is 3.2 μs which included the signal propagation delays. This means that the L1 trigger calculations must be done in many cases in less than 1 μs. The schematic plot of the L1 Trigger is shown in Fig. 4.9. The L1 Global Trigger (GT) collects and synchronises the information from the calorimeters and muon systems and make a decision to keep or reject an event. Once the L1 trigger generates an accept, all data which used as input to the L1 trigger system are moved to the DAQ along with the event readout data for storage and will be processed by the High Level Triggers [2]. Typically, the event rate is reduced by a factor of $O(1000)$.

4.8.2. High Level Trigger

Events which pass the L1 trigger are processed by the High-Level Trigger system(HLT) [2]. Only data accepted by the HLT are recorded for offline physics analysis. The rate of events accepted by the HLT should be within limits allowed by the data recording technology ($O(100)$ Hz) and thus a rejection factor of $O(1000)$ is needed. In traditional 3-level trigger systems, this is achieved in two stages: a hardware/software-based Level-2 trigger which quickly provides the large rejection factor and a Level-3 processor farm which makes decisions based on more sophisticated algorithms. The CMS HLT hardware consist of a single processor farm called the "Event Filter Farm". The farm comprises PCs mounting 2.66 GHz dual quad-core Intel processors and a total of 16 GB RAM (as of 2010). The CMS HLT combines the rejection power and speed of a Level-2 trigger with flexibility and sophistication of Level-3 in a single processor farm [2].

The full detector data ($\sim$1 MB) accepted by the L1 Trigger are read out by the DAQ

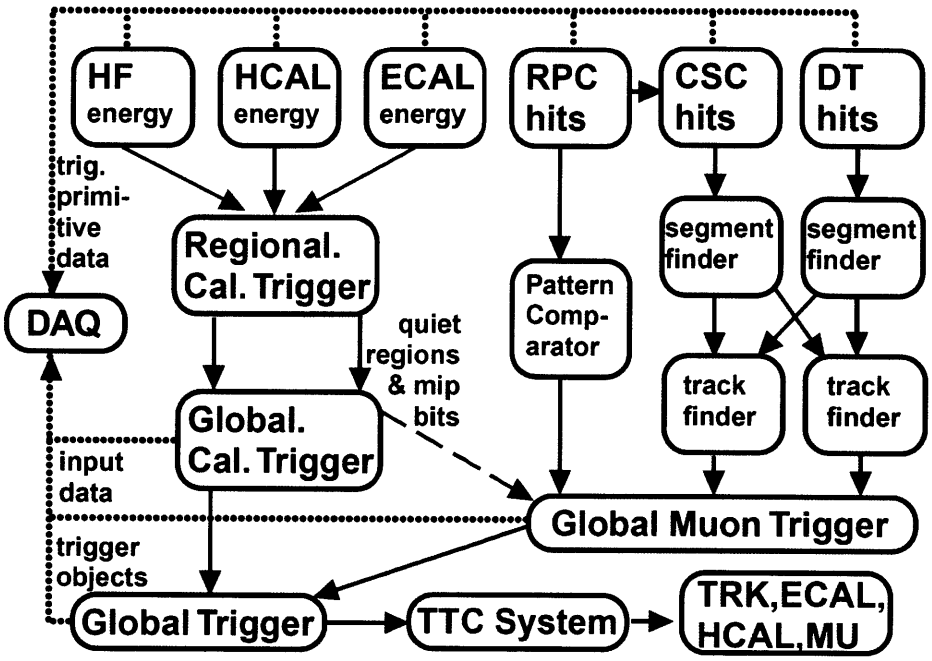

Figure 4.8.: Overview of Level 1 Trigger [2]

system at a rate up to 100 kHz. The assembling of the event fragments coming from each detector front-end module takes place in two stages. First, the front end data are assembled into larger fragments (super-fragments) which are then delivered to Read-out Units (RU) in eight different and independent sets (DAQ slides) in a round-robin scheme, such that all super-fragments of an event are delivered to the same DAQ slice. In each DAQ slice the super-fragments are managed by the Event Builder where they are finally assembled into complete events. From the BU, the events are handed to the Filter Units (FU), the applications which runs the actual High Level Trigger reconstruction and selection. Events accepted by the HLT are forward to the Storage Managers(SM) and then stream event data on storage [71]. In the FU, the high level objects such as ECAL clusters, jets and muons are reconstructed for event filter determination.

The CMS HLT is highly flexible. The HLT Triggers can be as simple as "mark and pass", or involved in complicated physics object reconstruction. For the MinBias triggers used in the thesis, the HLT paths are seeded by BPTX and BSC-based L1 triggers and no further event reconstruction are needed in the HLT stage.

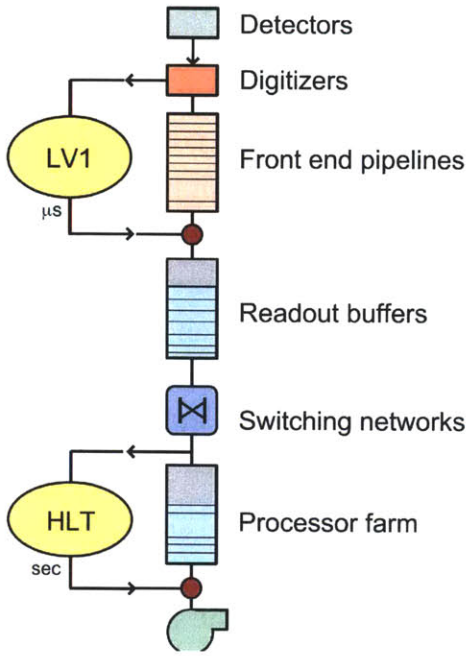

Figure 4.9.: Overview of Level 1 Trigger [72]

4.8.3. Triggers used at the startup

In this section contains information concerning the triggers used at startup for minimum-bias studies, which are based on BPTX and BSCs. The goal of those triggers is to provide Zero-Bias / 'Empty-Target'/ minimum-bias data sets which can be used to understand the trigger efficiencies and beam background.

4.8.3.1. BPTX-based triggers

During the commissioning in 2009, the BPTX is found to be fully efficient for the detection of the crossing of the filled proton bunches with an intensity $> 10^9$. This enables us to use the readout of the BPTX signal as L1 trigger.

The most important trigger based on the BPTX is the Zero-Bias trigger, which is the crossing of two filled proton bunches. There is also a trigger that requires only one filled and one empty bunch crossing; this is sometimes called 'empty target' trigger and will be used for corrections for beam gas and halo.

4.8.3.2. BSC-based triggers

The main purpose of the BSC system is to provide collision/background monitoring information for CMS. Besides the monitoring goals, signal pulses are also extracted from the readout of the BSC and BPTX detectors for triggering.

The Global Trigger (GT) has 64 so-called technical trigger inputs (LVDS) to which simple signals (pulses) from the BSC and BPTX are routed. The required logic (fanning in the 32 individual BSC signals in logical "or"s and "and"s) for these signals before entering the GT is fully implemented. There are 8 technical and 4 extra algo trigger bits from the BSC, and 7 technical and 4 algo bits from the BPTX provided for the General Trigger.

The relevant trigger bits for this analysis are listed in table 4.3. The BSC halo trigger use the timing information of the BSC inner ring or outer paddle. The trigger bit 36-39 fires if the timing between the signals from both side of the BSC detector is consistent with beam halo passing through the CMS. The single-sided BSC MinBias trigger bit fires if there is a hit in the BSC (bit 34). The coincidence BSC MinBias trigger bits fires if there is at least one hit in both side of the BSC detector in time coincidence.

The BSC halo bits are used for beam gas and beam halo tagging and rejection, while the BSC MinBias triggers are used to select collisional events.

4.9. Simulations

The detailed Monte Carlo (MC) simulation of the CMS detector response is based on GEANT4 [73]. The position and width of the beam spot in the simulation were adjusted to that determined from the data. Simulated events were processed and reconstructed in the same manner as collision data.

Table 4.3.: BSC L1 bit assignments.

Bit number	Bit Name	Description
Technical bits		
34	L1Tech_BSC_minBias_OR	there is at least one hit in the BSC
36	L1Tech_BSC_halo_beam2_inner	beam 2 halo, inner
37	L1Tech_BSC_halo_beam2_outer	beam 2 halo, outer
38	L1Tech_BSC_halo_beam1_inner	beam 1 halo, inner
39	L1Tech_BSC_halo_beam1_outer	beam 1 halo, outer
40	L1Tech_BSC_minBias_threshold1	at least one hit in time coincidence
41	L1Tech_BSC_minBias_threshold2	at least two hits in time coincidence
Algorithm bits		
124	L1_BscMinBiasOR_BptxPlusORMinus	at least one BSC hit in time with one BPTX

5. Event selection

During the data taking, three different data sets are taken for the studies. The first sample is a *Zero-Bias* sample which is taken whenever a collision is possible, i.e., two filled bunches. This sample has no bias due to the online trigger. However, it also contains empty events and beam backgrounds. The second sample is an *Empty-Target* sample, which require only one filled bunch. The empty-target sample will only contain empty events and beam background. The third sample is a *Minimum-Bias* (MinBias) sample based on a 1-arm trigger. This trigger requirement rejects most of the beam backgrounds, while retains most of the collisional sample.

With the three different samples, one can estimate the contamination from the beam gas and beam halo in order to develop useful strategy for the background rejection. The Zero-Bias sample is used for trigger efficiency validation. Those studies are detailed and discussed in this chapter.

In this chapter, the details of the event selections are presented. The online trigger is discussed first, followed by event vertex reconstruction and beam background rejection.

5.1. Online Trigger

As discussed in Chapter. 1, the p+p scattering we focus on is the NSD collisions in order to reduce the uncertainty due to the modeling of the SD event and reduce the contamination from the beam background. To minimize the bias imposed on such an analysis by the trigger strategy it is essential to optimize the trigger to accept a large fraction of the NSD cross section while reject most of the SD cross-section. Furthermore, it is essential to study the relative contributions of single-diffractive, double-diffractive and non-diffractive collisions as well as the admixture of non-collisional background such as beam gas interactions and beam halo.

In order to study collisional and beam-gas events, it is important to have a Zero-Bias trigger and an Empty-Target trigger in the Level 1 Trigger menu. The Zero-Bias trigger is based on the coincidence of the BPTX signal which triggers on the crossing of two filled

colliding bunches, therefore contains collision sample and beam background contribution. The empty-target trigger requires only one filled and one empty bunch crossing based on BPTX. No collisional events are expected in the empty-target sample.

To achieve high trigger efficiency on the MinBias sample, the CMS readout is triggered by a signal in any of the BSC segments(see Fig. 4.7), coincident with a signal from either BPTX indicating a beam or a bunch crossing the IP. The three data sets are summarized in Table. 5.1.

Table 5.1.: The three different data sets used in this thesis.

Name	Event content	Trigger selection
Zero-Bias	Empty, beam gas, collisions	Coincidence of BPTX
Empty-target	Empty, beam gas	BPTX XOR signal
Min-Bias	Empty, beam gas, collisions	Coincidence of BPTX, any hit in the BSC

5.2. Event Vertex Reconstruction

A valid primary vertex is useful for beam-background rejection and provide the reference point for the tracklet reconstruction. In this analysis, there are three different methods used for the event vertex determination. The *cluster vertex* method uses information from single layer, which is a simple algorithm without using correlation between different detector layers. The *tracklet vertex* method is a quick algorithm which correlates two layers of the pixel detector. This algorithm works also on data taken without magnetic field. The *agglomerative vertex* reconstruction [74] uses fully reconstructed tracks, which provides robust and accurate vertex positions. This method is also used in the final analysis on data taken with magnetic field. With different complexity in algorithm and different vertexing efficiency and resolution, the three methods are used for various of cross-checks.

5.2.1. Cluster Vertex reconstruction

When a charged particle pass through the pixel detector, the width of the cluster along the beam line (w) is proportional to the amount of material it passes through (Fig. 5.1. The expected width (w_v) can be calculated with the following relation:

$$w_v(v_z) = 2 \times |z - v_z|/r + 0.5 \tag{5.1}$$

where z is the z position of the cluster, r is the radial coordinate of the cluster and v_z is the z position of the primary vertex.

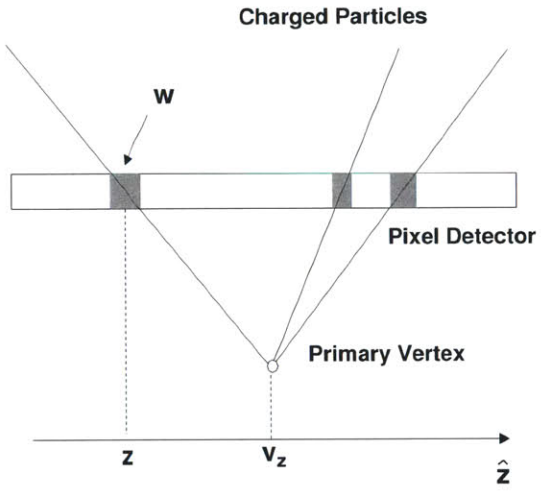

Figure 5.1.: Demonstration of the cluster vertex algorithm.

In this algorithm, a scan along the -15.9 cm $< |v_z| < 15.9$ cm with a step of 0.1 cm is performed. For each assumed v_z, we calculate the number of compatible hits ($N(v_z)$) with $|w_v - w| < 1$. The vertex position which has the highest number of compatible hits is selected as the primary vertex candidate.

If there are two vertex candidates which has equal amount of compatible hits, a χ estimator is defined to estimate the compatibility of the cluster size to the assumed vertex position:

$$\chi(v_z) = \sum_{i=2}^{N_{cluster}} |w - w_v(v_z)| \tag{5.2}$$

The vertex candidate which the lowest $\chi(v_z)$ is selected as a final primary vertex.

5.2.2. Tracklet Vertex reconstruction

In order to have a better vertex position resolution while keeping the algorithm relatively simple, a tracklet-based vertex reconstruction technique is introduced. This algorithm is used for magnetic field off analysis.

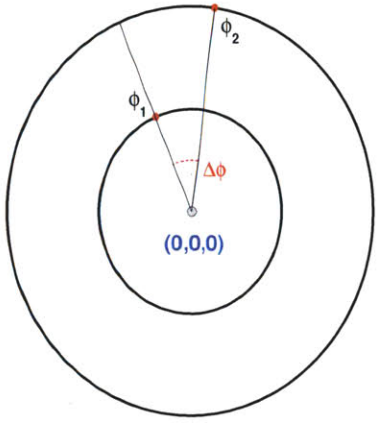

Figure 5.2.: The definition of $\Delta\phi$ of the proto-tracklet in vertex reconstruction. The ϕ angle is calculated with respect to the center of the CMS detector (0,0,0).

The first step in reconstructing the primary vertex is to take a first layer hit and loop over the second layer hits. If the difference in azimuthal angle ($\Delta\phi$) between the two hits is smaller than $\Delta\phi_{cut}$, this pair is saved as a proto-tracklet. This procedure is repeated for each first layer hit to get a collection of proto-tracklets. The algorithm is demonstrated in Fig. 5.3

The expected z vertex position of such proto-tracklets is given by the following expression:

$$z = z_1 - \rho_1 \times (z_2 - z_1)/(\rho_2 - \rho_1) \tag{5.3}$$

where $z_{1(2)}$ is the z position of the first (second) layer hit in the proto-tracklet, and $\rho_{1(2)}$ is the radius in cylindrical coordinates. The calculated z positions are saved to a collection of vertex candidates.

The second step is to determine the primary vertex position from the vertex candidates. Looping through the vertex candidates in the collection, the z position of each

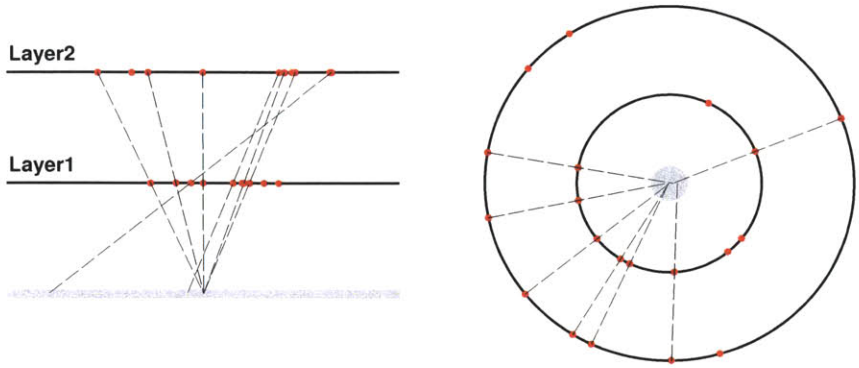

Figure 5.3.: *Left*: The reconstructed proto-tracklets in the X-Z plane. *Right*: The reconstructed proto-tracklets in the r-ϕ plane.

is compared to all other candidates. If the difference $|\Delta z|$ between two candidates is smaller than Δz_{cut}, they are grouped together into a vertex candidate cluster. The cluster with the highest number of candidates is selected as the primary vertex; its z position is determined from the average z position of the cluster.

In this analysis, the optimized parameters were found to be $\Delta\phi_{cut} = 0.08$ and $\Delta z_{cut} = 0.14$.

The resolution of the pixel tracklet method is found to be only slightly worse than the pixel triplet method and significantly better than the cluster method.

5.2.3. Agglomerative Vertex reconstruction

The x and y positions of the luminous region where protons of both beams interact, from here on referred to as beam spot, are constant within a given data set. The beam spot for each data set is obtained from three-dimensional vertex fits based on tracks reconstructed with $p_{\mathrm{T}} > 0.9$ GeV/c, using the full event sample. The tracks are reconstructed as described in [74]. The RMS of the beam spot in both directions was found to be less than 0.1 mm.

The z position and shape of the beam spot is obtained in a similar manner, using the event-by-event primary vertex reconstructed as described below. Due to the low collision rate, the probability for more than one inelastic collision to occur in the same bunch crossing is less than 0.5%.

To reconstruct the z coordinate of the primary vertex for each event, tracks consisting

of triplets of pixel hits are formed. The minimal transverse momentum of these tracks is ≈ 75 MeV/c. The tracks are required to originate from the vicinity of the beam spot with a transverse impact parameter (d_T) smaller than 0.2cm. Of these, only tracks with $d_T < 4\sigma_T$, where σ_T is the quadratic sum of the uncertainty of d_T and the RMS of the beam spot in the transverse direction, are used in the vertex reconstruction.

The vertex-reconstruction algorithm uses the z coordinate of the tracks at the point of closest approach to the beam axis and the corresponding estimated measurement uncertainty (σ_z). It performs an agglomerative clustering by adding tracks to form groups. These groups (denoted the i^{th} and j^{th} group) are then merged based on their normalized distance, $d_{ij}^2 = (z_i - z_j)^2/(\sigma_i^2 + \sigma_j^2)$ where σ_i and σ_j are the uncertainties of the z_i and z_j positions, with a fast nearest-neighbor search algorithm [74]. The z position and its uncertainty σ_z for the newly joined group are calculated using a weighted average. The clustering process stops when the smallest normalized distance between the remaining groups gets larger than 12, where the stopping condition was optimized using simulated events. Only vertices formed from at least two tracks are considered further except when there is only one track reconstructed in the event. In this case the vertex position is given by the point of closest approach of the track to the beam axis. The fraction of single-track vertices in the data sample is 1.7% at 0.9 TeV, 1.3% at 2.36 TeV and 0.9% at 7 TeV. The overall vertex reconstruction efficiency, evaluated from the data after all other event selection cuts, is 99.2% and the probability of reconstructing more than one primary vertex candidate is 5.0% (7.4%) at 0.9 TeV (2.36 TeV). When more than one vertex candidate is reconstructed, the vertex composed of the largest set of tracks is chosen. This selection is safe since in the startup, the average number of collisions per bunch crossing is $\ll 1$ which no event pile-up is expected.

The distribution of the reconstructed vertex positions along the beam axis is shown in Fig. 5.4, and compared with that obtained from the simulation, adjusted to the measured beam spot in three dimensions.

5.3. Performance

The performance of vertex resolution as a function of hit multiplicity among the three available vertexing methods are shown in Fig. 5.5. The agglomerative vertexing gives the best resolution in sample with magnetic field on, but doesn't work in the magnetic field off case. This method is used in the final analysis of the magnet field on sample. The tracklet vertexing also works in the sample without magnetic field, and has a better

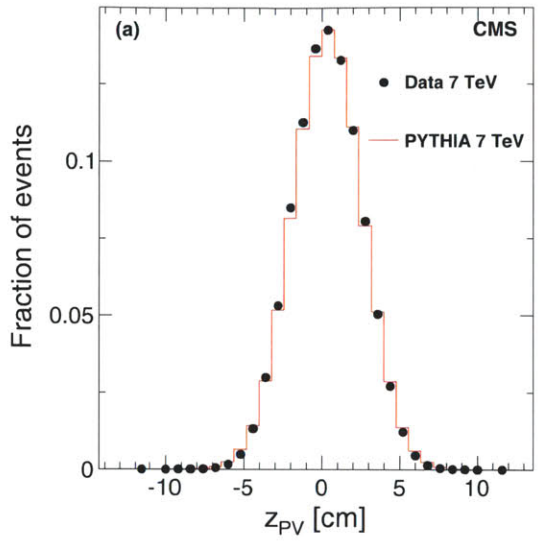

Figure 5.4.: The distribution of the reconstructed z position of the primary vertex in the 7 TeV data (symbols), compared to the same distribution from PYTHIA simulation (lines).

performance compared to Cluster vertexing. This algorithm is used for B=0 analysis. Cluster vertexing has less sensitivity to the detector condition or misalignment and it was used for cross-checks and systematic studies.

5.4. Event Selection

This analysis uses LHC collision data sets collected at LHC startup. The collision rate with p+p collision are about 11, 3, and 50 Hz at $\sqrt{s}$ =0.9, 2.36, 7.0 TeV respectively. The fraction of events with two or more collisions is negligible (< 0.3%). After all event selections described in the following section, there are 40320 (0.9 TeV) 10837 (2.36 TeV) and 55100 (7.0 TeV) events which enter the analysis.

5.4.1. Selecting Collision Events

To select valid collisions, we select events with a BPTX coincidence, indicating a filled bunch from either beam crossing the IP at the same time based. Events which have at least 1 hit in all of the BSC segments are selected, which pass the Level 1 trigger.

In order to suppress the single-diffractive component and keep most of the non-

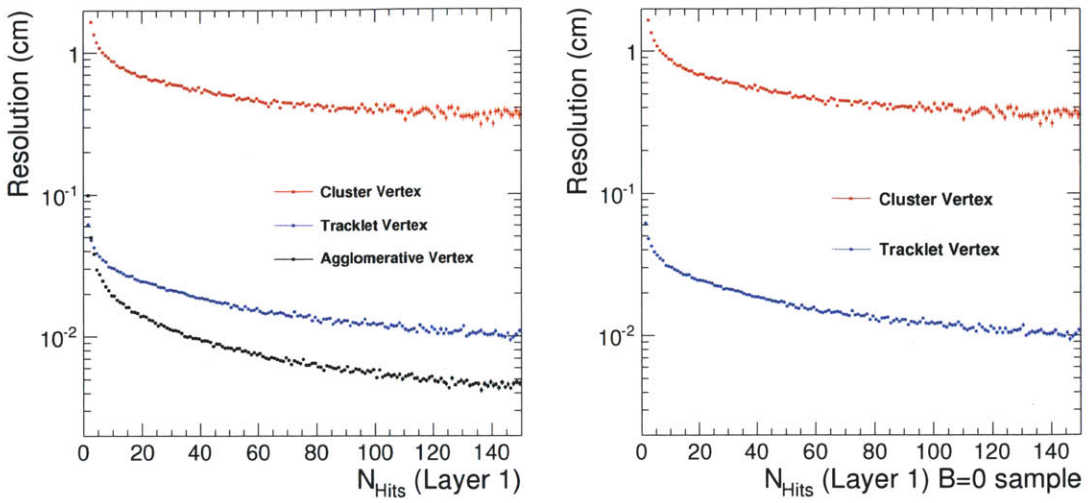

Figure 5.5.: The vertex resolution as a function of hit multiplicity in the 7 TeV PYTHIA Monte Carlo sample.

single diffractive events, we select events that contain a coincidence of at least one calorimeter tower containing a total energy great than 3 GeV in the positive and negative HF, i.e on either side of the IP.

A valid vertex is required for this analysis. The main analysis uses the agglomerative vertex which is described in 5.2.3. Data sample reconstructed with cluster vertexing and tracklet vertexing are used for cross-checks.

5.4.2. Rejecting beam halo events

The selected collision candidate events still contain a contribution from beam induced background events that can pass the collision trigger. Beam halo events were rejected based on the BSC beam halo bits (Techical Bit 36, 37, 38, and 39) as described in Section. 4.8.3.2.

5.4.3. Rejecting high occupancy events

Another type of beam background events are very high pixel multiplicity events present in the data set. The number of pixel hits in one pixel layer can go up to several thousands, however, in non-collisional like distributions. An example event is shown in Figure 5.6 that looks like a shower traversing the full longitudinal extent of the pixel system

at one transverse location. Those events are created by beam particles directly hitting the detector structure.

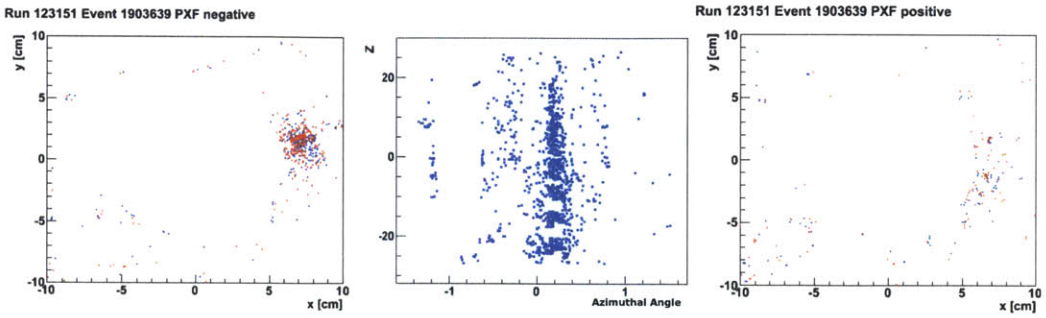

Figure 5.6.: An example high hit multiplicity event. The transverse position of all pixel hits the negative-side (left) and positive-side (right) disks. The ϕ-z distribution for the 2nd barrel layer is shown in the center. A transversely isolated shower develops from +z to -z, incidentally also leaving much more energy in the negative-side HF than the positive-side.

Most of these background events can be removed by requiring an HF hit coincidence and a BPTX coincidence. As the primary signature of these high occupancy pixel events is the preponderance of extremely long clusters along the beam direction, this is the natural quantity for event-by-event discrimination. As done in the cluster vertex algorithm (Section. 5.2.1), this is achieved by plotting all clusters according to their z-position and cluster size along the beam. Since the cluster length of the hits from primary tracks are proportional to the z distance with respect to the primary vertex, they will leave a characteristic V-shaped pattern in this space. Non-primary hits (e.g. loopers, secondaries) mostly fall outside this V-shape (see Figure 5.7).

To judge how compatible the primary vertex position is with the cluster-shape information, we define the *Cluster Vertex Compatibility* (Q) as the ratio of clusters that fall within the V-shape (N^{V}_{Hits}) to the average number of clusters inside the same V-shape when it is displaced by ± 10 cm ($N^{\pm V}_{Hits}$) along the beam (z-axis in the CMS coordinate system).

$$Q = \frac{N^{V}_{Hits}}{(N^{+V}_{Hits} + N^{-V}_{Hits})/2} \tag{5.4}$$

For collisional events with only primary tracks and a properly reconstructed vertex, the Q will be a large number. In the high pixel multiplicity events, we get $Q \sim 1$.

Fig. 5.8(a) shows the correlation of Q and the number of pixel hits (N_{hits}) from the MinBias sample at $\sqrt{s} = 0.9$ TeV. This can be compared to Monte Carlo simulations where only collisions are present (Figure 5.8(c)) and empty-target sample where only beam background is present (Figure 5.8(b)). The collisions typically have good cluster vertex compatibility (large Q). On the other hand, the high hit multiplicity beam background events are populated around $Q \sim 1$. It is clear that a simple diagonal cut can be effective in cleaning up the sample in data without cutting much at all into the overall efficiency.

It should be noted that the HF coincidence requirement itself is also effective in removing beam background, as another prominent feature of the background is significant asymmetry in the energy deposits between the forward and negative hemispheres. The vertex quality distributions in 0.9 TeV MinBias sample after all other selections have been applied (including the HF coincidence) are shown in Figure 5.9(a) for the collision bunches and Figure 5.9(b) for the empty-target bunches. Only a few high-multiplicity beam-background events remain in the collision events, which are clearly removed with the diagonal cut (indicated by the red line). Furthermore, it is evident from the very few entries to the left of the cut in Figure 5.9(b) that only a tiny fraction (per mille level at 0.9 and 2.36 TeV; less than $2x10^{-5}$ at 7 TeV) of beam-gas events survive the complete event selection.

The implementation used in the event selection for the $dN/d\eta$ and dN/dp_{T} analyses at $\sqrt{s} = 7$ TeV differs slightly from the cut used at 0.9 and 2.36 TeV to accommodate higher multiplicity real collision events. The definition of quality events, indicated by the lines in Figure 5.9(a) and Figure 5.9(c), is as follows:

$$Q > (a \times N_{Hits}) \,||\, N_{Hits} < b \,||\, Q > c. \tag{5.5}$$

In case of 7 TeV collisions, the parameters are set to $a = 0.0045$, $b = 150$ and $c = 2$.

In addition to the higher multiplicity reach of 7 TeV collisions that is evident in Figure 5.9(c), it is also apparent that the beam conditions are 'cleaner' than at the lower energies, i.e. there are proportionately fewer events in the low-quality tail than in Figure 5.9(a). This is because of the much higher collision rate in 7 TeV data taking compared to low energy runs.

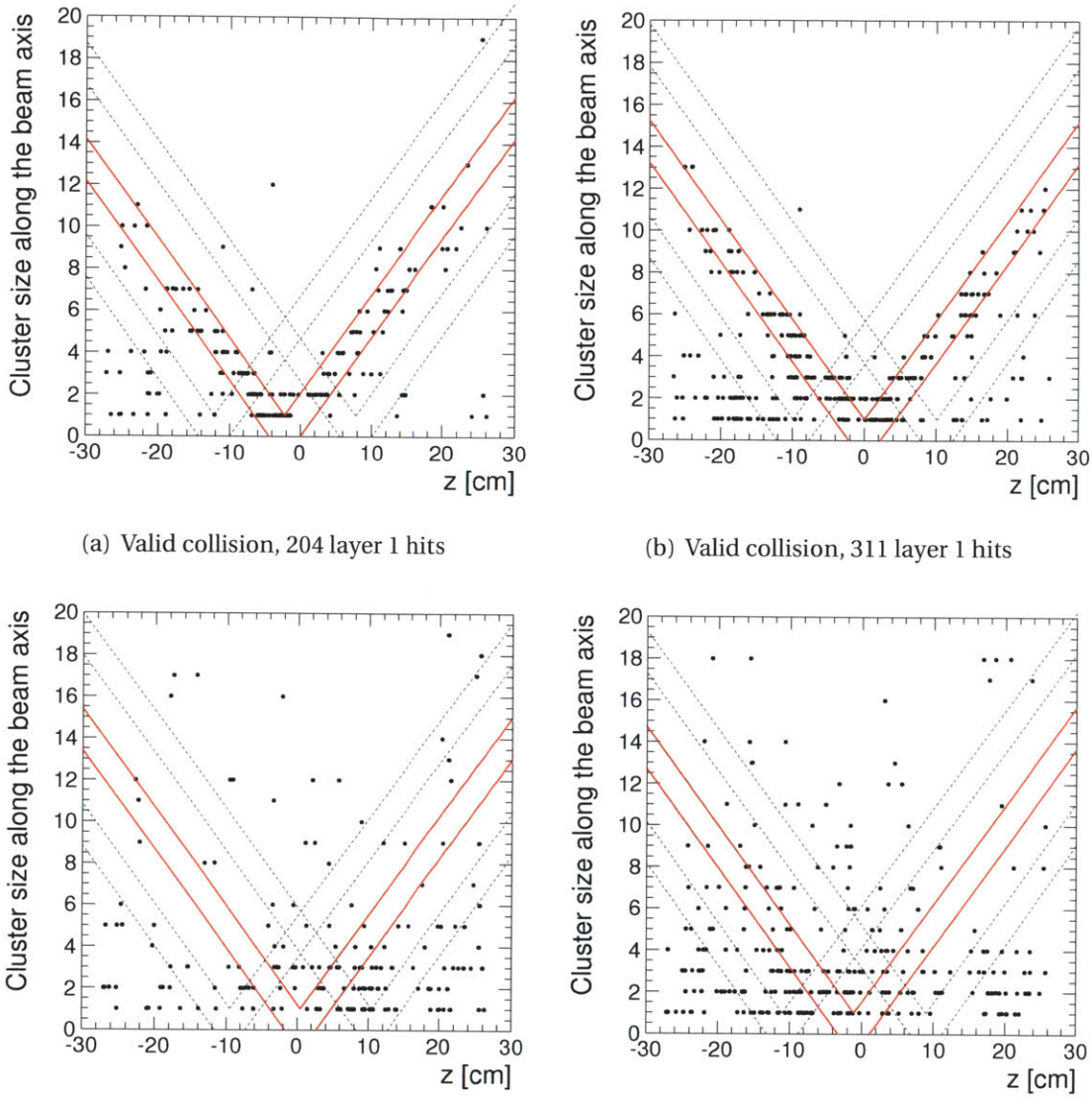

(a) Valid collision, 204 layer 1 hits

(b) Valid collision, 311 layer 1 hits

(c) Beam background, 204 layer 1 hits

(d) Beam background, 311 layer 1 hits

Figure 5.7.: The example distribution of pixel clusters according to their z-position and cluster length along the beam, shown with the V-shaped selection of clusters compatible with primary particles coming from the collision vertex. The dashed lines show the shifted V-shape for compatibility estimation. (a) A 7 TeV Collision with 204 hits in the first pixel barrel layer.(b) A 7 TeV collision with 311 hits in the first pixel barrel layer. (c) Beam background event with 204 hits in the first pixel barrel layer.(d) Beam background event with 311 hits in the first pixel barrel layer.

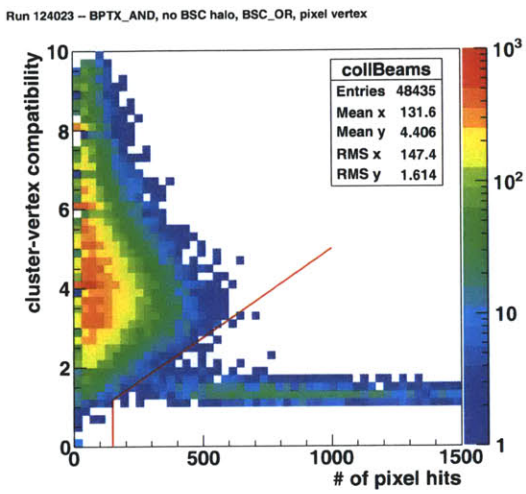

(a) 0.9 TeV MinBias sample

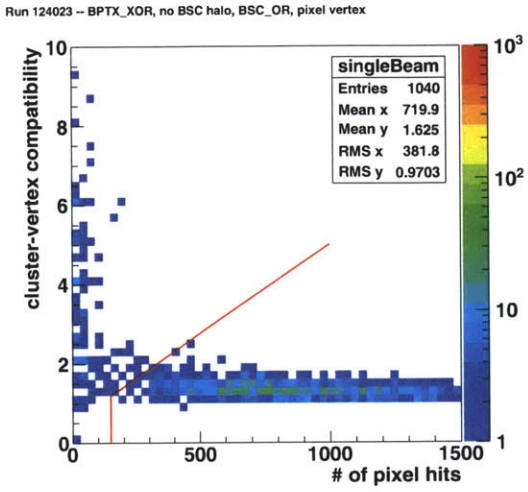

(b) Empty-target sample

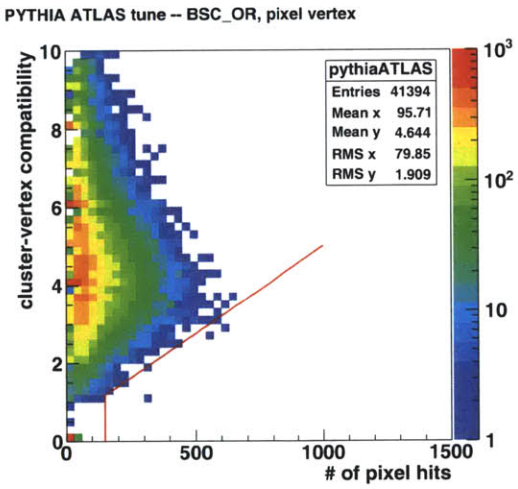

(c) 0.9 TeV PYTHIA MC events

Figure 5.8.: (a) The distribution of vertex compatibility (Q) versus hit multiplicity after applying all the selections from Table 5.2 except the HF coincidence. The quality selection cut is indicated by the red line. (c) The same quantity for PYTHIA Monte Carlo simulated events and (b) data events triggered by empty-target trigger.

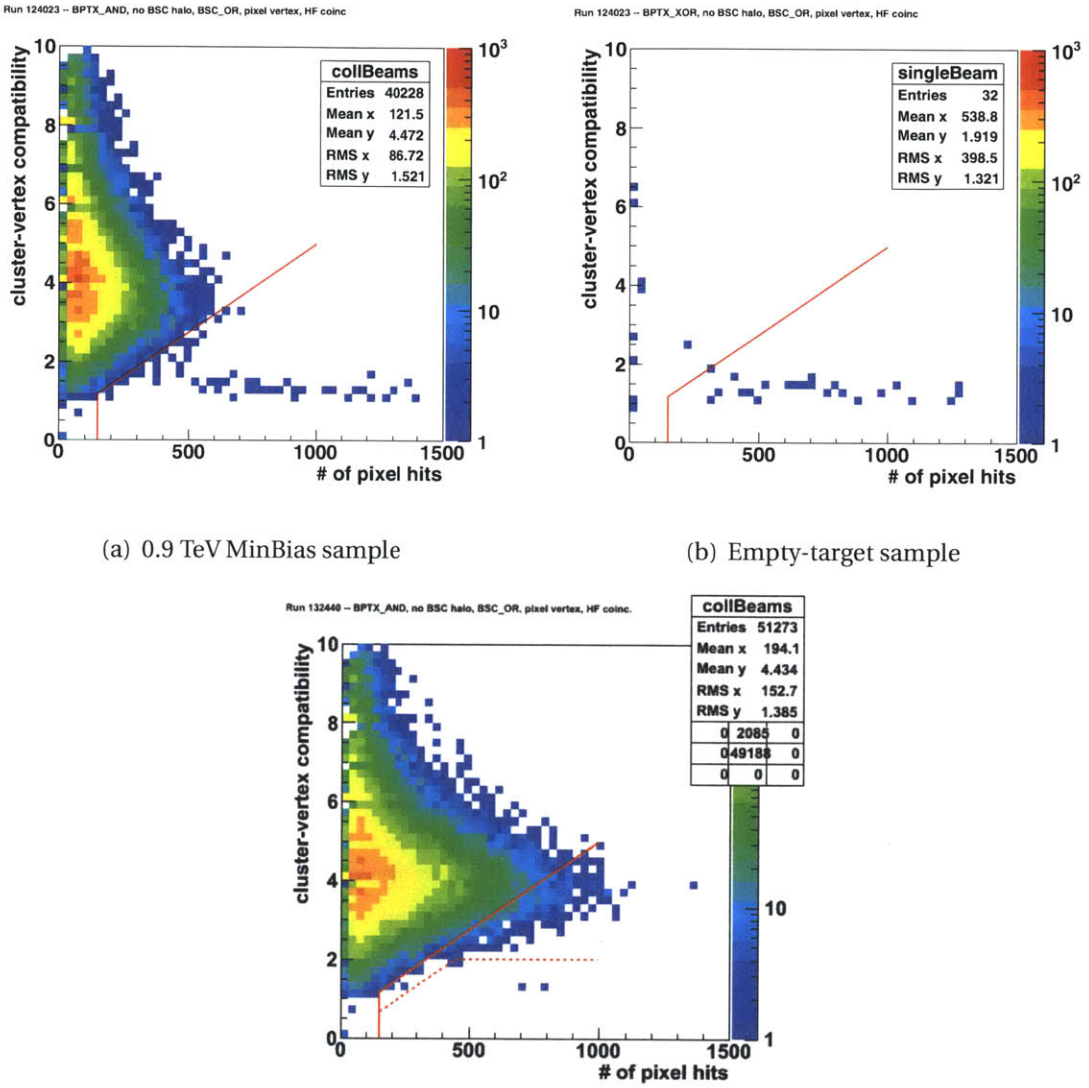

(a) 0.9 TeV MinBias sample

(b) Empty-target sample

(c) 7 TeV MinBias sample

Figure 5.9.: (a) The distribution of vertex compatibility (Q) versus hit multiplicity after applying all the selections from Table 5.2 including the HF coincidence at $\sqrt{s} = 0.9 TeV$. The quality selection cut is indicated by the red line. (b) The same selection applied to data events triggered in empty-target bunch crossings (i.e. those when only one beam was crossing the IP). (c) The same selection applied to 7 TeV collision events, where the dashed line indicates the updated cut position.

5.5. Trigger and selection efficiency studies

The efficiency of the event selection used in this analysis is estimated from a MC study. MC events are generated using the Pythia event generator and then processed by a full GEANT 4 simulation [75] including detector response simulation. For each data run a separate set of simulated events is generated with matching energy and beam spot parameters.

The total number of collision events and the number of collision events passing each subsequent requirement are listed in Table 5.2.

Table 5.2.: Number of events per data sample used in this analysis. The offline event selection criteria are subsequently applied, i.e. each line includes the selection of the lines above.

Beam Energy	0.9 GeV	2.36 TeV	7.0 TeV
Run Number	124023	124120	132440
Magnetic Field	3.8 T	3.8 T	3.8 T
Selection			
BPTX Coincidence + one BSC Signal	72 637	18 074	68 512
One Pixel Track	51 308	13 029	62 097
HF Coincidence	40 781	10 948	55 322
Beam Halo Rejection	40 741	10 939	55 309
Beam Background Rejection	40 647	10 905	55 301
Valid Event Vertex	40 320	10 837	55 100

Table 5.3.: Check on the non-collisional events. The offline event selection criteria are subsequently applied, i.e. each line includes the selection of the lines above.

Beam Energy	7.0 TeV
Selection	
BPTX XOR + one BSC Signal	3 167
One Pixel Track	336
HF Coincidence	15
Beam Halo Rejection	10
Beam Background Rejection	5
Valid Event Vertex	0

5.5.1. Event selection efficiency

Inelastic p+p collisions at 7 TeV simulated by PYTHIA consist of an admixture of 19.2% SD, 12.9% DD and 80.8% NSD processes. The efficiency of the event selection for the different processes is determined to be 26.7% for SD, 33.6% for DD and 86.3% for NSD. Based on our cross checks with data (looking at diffraction signals in the HF), we assign a relative 20% error on these SD and DD efficiencies. The event selection efficiency for NSD and SD events (symbols) is shown in Fig. 5.10 as a function of simulated charged particle multiplicity in the $|\eta| < 2.5$ range, together with the distribution of the same multiplicity (lines).

The magnitude of the correction of the measurements to the NSD part of the p+p cross section depends on the fraction of SD processes accepted by the event selection. Based on the PYTHIA process composition we estimate the fraction of selected SD events relative to selected events to be 5.8% at 7 TeV.

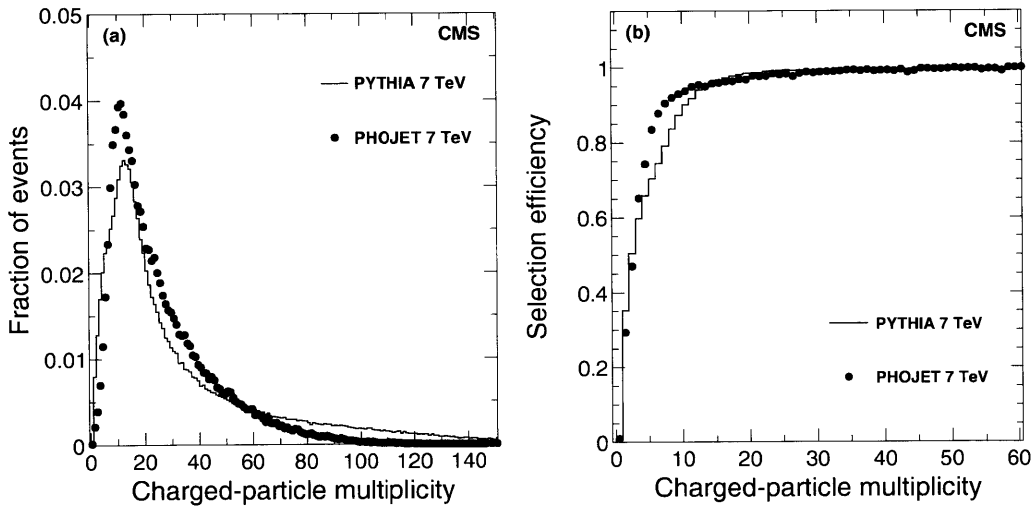

Figure 5.10.: (a) Generated multiplicity distributions of primary charged hadrons in the range $|\eta| < 2.5$ for $\sqrt{s} = 7$ TeV after the event selection is applied to the reconstructed events, using inelastic events from the PYTHIA (histogram) and PHOJET (symbols) event generators. (b) The event selection efficiency expected for NSD events from the PYTHIA (histogram) and PHOJET (symbols) event generators as a function of generated charged hadron multiplicity in the region $|\eta| < 2.5$.

5.5.2. MC event selection efficiencies

The MC event selection efficiencies are shown in Table. 5.4. The SD fraction is dropping as a function of $\sqrt{s}$ in both generator, while the DD and ND fraction is increasing. Since the event multiplicity is increasing, the event selection efficiency increases as a function of center-of-mass energy. The selected SD fraction in PYTHIA is higher than PHOJET, and the difference is up to 1.8%. This difference is from the ways of modeling the SD events and is taken into account in the systematic uncertainty.

Table 5.4.: Expected fractions of SD, DD, ND and NSD processes ("Frac.") obtained from the PYTHIA and PHOJET event generators before any selection and the corresponding selection efficiencies ("Sel. Eff.") determined from the MC simulation.

PYTHIA									
Energy	0.9 TeV			2.36 TeV			7.0 TeV		
	Frac.	Sel. Eff.	Sel. Frac.	Frac.	Sel. Eff.	Sel. Frac.	Frac.	Sel. Eff.	Sel. Frac.
SD	22.5%	16.1%	5.2%	21.0%	21.8%	6.3%	19.2%	26.7%	6.8%
DD	12.3%	35.0%	6.2%	12.8%	33.8%	5.9%	12.9%	33.6%	5.8%
ND	65.2%	95.2%	88.7%	66.2%	96.4%	87.8%	67.9%	96.4%	87.4%
NSD	77.5%	85.6%	94.8%	79.0%	86.2%	93.6%	80.8%	86.3%	93.1%
PHOJET									
Energy	0.9 TeV			2.36 TeV			7.0 TeV		
	Frac.	Sel. Eff.	Sel. Frac.	Frac.	Sel. Eff.	Sel. Frac.	Frac.	Sel. Eff.	Sel. Frac.
SD	18.9%	20.1%	4.9%	16.2%	25.1%	5.0%	13.8%	30.7%	5.0%
DD	8.4%	53.8%	5.9%	7.3%	50.0%	4.5%	6.6%	48.3%	3.8%
ND	72.7%	94.7%	89.2%	76.5%	96.5%	90.5%	79.6%	97.1%	91.2%
NSD	81.1%	90.5%	90.9%	83.8%	92.4%	89.5%	86.2%	93.4%	95.0%

6. Pseudorapidity distribution measurement

The pseudorapidity distributions are measured by three different methods with the CMS detector: pixel counting technique, tracklet reconstruction from this thesis, and full tracking [76, 77]. The pixel counting method uses pixel hits from a single pixel layer has good sensitivity to low p_T particles, but it's more sensitive to the background contamination. The full tracking method involves a more complicated algorithm and is insensitive to background hits and low p_T loopers. The three methods are complementary to each other and are useful for the understanding of systematic uncertainties. In this thesis, the tracklet method will be presented and the results will be compared with other methods in Chapter. 8.

In this chapter, the measurement of the charged hadron pseudorapidity distribution in NSD p+p collisions with the CMS pixel detector is presented. The reconstruction of hit-pairs (tracklets), which is used to characterized the event multiplicity, is described in Sec. 6.1. The corrections of detector effects, such as the reconstruction efficiency, contributions from the secondary particles which comes from the weak decays, δ ray and photon conversions have to be applied to the raw spectra. The effect of triggering efficiencies, contribution from the SD process and MC model dependence are also studied.

6.1. Tracklet method

Tracklets are *two hit combinations* in consecutive layers of the pixel detector consistent with a track originating at the primary vertex. In the CMS experiment, the pixel hits are reconstructed from the clusters of energy deposit in the pixel detector, which is described in [66]. The *reconstructed hits* are used in the tracklet reconstruction. The tracklet analysis makes use of the correlation between hit positions in the first two layers of the pixel detector. Pairs of hits produced by the same charged particle will have only

small differences in the pseudorapidity (η) and the azimuthal angle (ϕ) with respect to the primary vertex.

This analysis uses the first three tracker layers in the CMS silicon pixel barrel [66]. The first layer is located at a distance between 3.6 and 5.2 cm from the beam line, the second layer is between 6.6 and 8.0 cm and the third layer is between 9.4 and 10.8 cm. For a homogeneous magnetic field of 3.8 Tesla, charged pions with transverse momentum greater than ~50(70) MeV/c can reach the first(second) pixel layer. That allows the reconstruction of tracklets from all but the lowest p_T particles.

With the three layers of the pixel detector, there are three possible combinations: 1st+2nd, 1st+3rd and 2nd+3rd layers. The combination of 1st+2nd layer provides the lowest p_T reach, but it's more sensitive to the beam-pipe induced background. The combination of 2nd+3rd have a higher p_T threshold and less sensitive to the possible low P_T background, however, it needs a larger correction on the strangeness content and secondary production. The three combinations are complement to each other and the results are useful for layer-by-layer systematic checks.

For each tracklet, the pseudorapidity is calculated from the hit position in the first layer. The differences in pseudorapidity ($\Delta\eta$) and azimuthal angle ($\Delta\phi$) are important for characterizing the tracklet and are calculated by:

$$\Delta\eta = \eta_1 - \eta_2 \tag{6.1}$$

$$\Delta\phi = \phi_1 - \phi_2 \tag{6.2}$$

where $\eta_{1(2)}$ is the pseudorapidity of the first(second) hit with respect to the primary vertex, and $\phi_{1(2)}$ is the azimuthal angle.

In addition to primary charged particles, the tracklet collection will also include contributions from low-p_T "loopers", secondary interactions in the beam-pipe, and particles from weak decays. We do not apply a hit selection on the reconstructed hits, i.e. all pixel hits are used in the analysis. This design is to minimize the systematics due to detailed pixel detector simulation. "Combinatorial background tracklets" are defined as combinations from looper hits, secondary hits and hits from different primary tracks. The background fraction can be estimated by a data driven method, which will be described in Sec. 6.1.3. The looper contribution can be suppressed by a selection on $\Delta\eta$. The tracklets from secondary particles cannot be removed, and the correction for this contribution relies on MC simulation. In the following sections, we describe the details of the tracklet analysis.

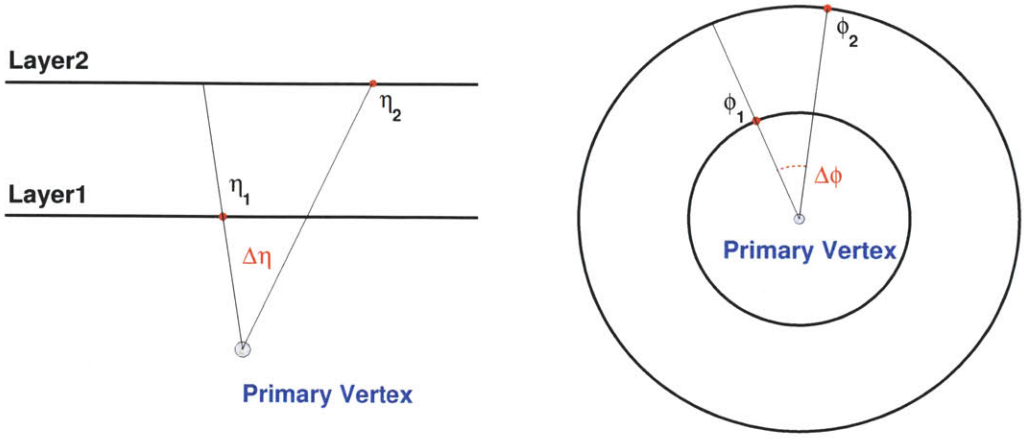

Figure 6.1.: The definition of $\Delta\eta$ and $\Delta\phi$ of the tracklet.

6.1.1. Tracklet reconstruction

Tracklets are pairs of pixel hits in each of the first two pixel layers. In this analysis, tracklets are reconstructed in four steps:

1. The primary vertex is reconstructed with the method described in Chapter 5.2.3. An event is used only if there is at least one reconstructed primary vertex. If more than one is found, the vertex with more associated tracks is chosen. To ensure this analysis to be insensitive to acceptance correction, all reconstructed vertices lie within $|v_z| < 20$cm (see Fig. 5.4).

2. For each reconstructed hit, we calculate the pseudorapidity, $\eta_{1(2)}$, for the first (second) layer using the primary vertex location. This design gives a better resolution on the pseudorapidity.

3. Starting with a reconstructed hit in the first pixel layer and looping over the reconstructed hits in the second layer we save all possible combinations as proto-tracklets.

4. We sort the proto-tracklets by $\Delta\eta = (\eta_1 - \eta_2)$, which is the difference in pseudorapidity of the first and second layer hits. If a second layer hit is matched several times, the proto-tracklet with the smallest $\Delta\eta$ is kept. The selected proto-tracklets are final reconstructed tracklets. (Fig. 6.2)

5. To ensure the reconstructed tracklets are consistent with the primary vertex, tracklets with $|\Delta\eta| < 0.1$ are selected in the multiplicity analysis.

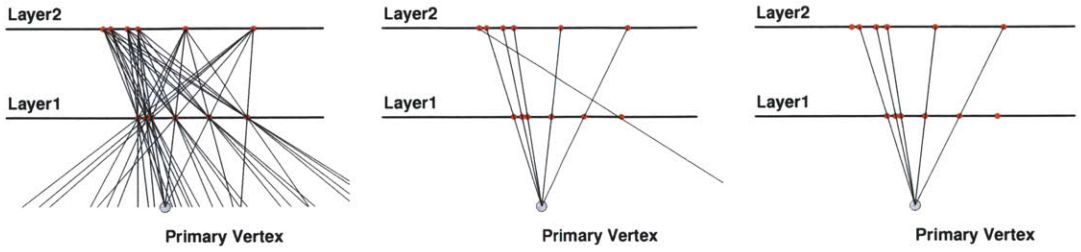

Figure 6.2.: Demonstration of the tracklet reconstruction algorithm. (Left pannel) Reconstructed proto-tracklets. The red dots are the reconstructed hits in the pixel detector and the lines show all possible combinations between the hits in the two pixel layers (Proto-tracklets) (Central panel) Reconstructed tracklets after cleaning. Now all the hits are only used once. Sometimes there are still hits with large $\Delta\eta$ reconstructed as the cleaned tracklets. Therefore, further selections are needed to reject those tracklets. (Right panel) Reconstructed tracklets with $|\Delta\eta| < 0.1$ requirement.

The reason that the tracklets are ranked by $\Delta\eta$ is because the magnetic field in the CMS detector bends the trajectory of the charged particles in the ϕ direction which makes the $\Delta\phi$ width much larger than the $\Delta\eta$ width. The $\Delta\eta$, $\Delta\phi$ distribution of the reconstructed tracklets is shown in Figure 6.3 and Figure 6.4. From Monte Carlo study, the typical widths of the $\Delta\eta$ and $\Delta\phi$ from the charged particle are 0.004 and 0.05 if the distribution is fit by a Gaussian distribution.

6.1.2. Event Multiplicity

Since the event selection efficiency, tracklet reconstruction efficiency and background level are dependent on the event multiplicity, a event multiplicity variable (M) is important for this analysis. Several possible multiplicity variables are

1. pixel hit multiplicity in the first layer (N_{hit1})
2. Number of reconstructed tracklets ($N^{Raw}_{Tracklet}$)
3. Number of background subtracted tracklets ($N_{Tracklet}$)

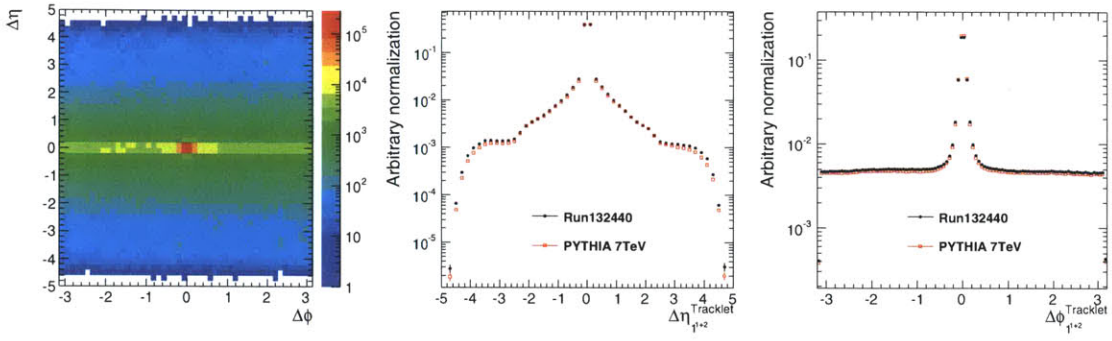

Figure 6.3.: (Left pannel) The scatter plot of $\Delta\eta$ and $\Delta\phi$ from Run 132440. (Central panel) The comparison of $\Delta\eta$ spectrum between Run 132440 and PYTHIA ATLAS 7 TeV sample. (Right panel) The comparison of $\Delta\phi$ spectrum between Run 132440 and PYTHIA ATLAS 7 TeV sample.

The number of background subtracted tracklets is a good variable because it's less sensitive to the background hits, while the other two methods are more sensitive to the combinatorial background. In this analysis, $N_{Tracklet}$ is selected to give the main results while N_{hit1} and $N^{Raw}_{Tracklet}$ are used for cross-checks.

6.1.3. Combinatorial background subtraction

Background tracklets can be created from incorrectly associated hits. The main source of the background tracklets are the hits from the low p_T loopers, secondary produced particles, and hits from beam background (Fig. 6.5). Also when the hit density is high, the possibility to associate hits from different charged particle increases. The fraction of background tracklets depends on the event multiplicity. A naïve event mixing will not give a correct background shape because the signal-to-background ratio is different and the looper contribution cannot be reproduced. To estimate the background fraction (β), a sideband method is used to reproduce the shape of the combinatorial background, which will be described below.

The difference in pseudorapidities and azimuthal angles between the first layer hit (η_1,ϕ_1) and second layer hit (η_2,ϕ_2) of a tracklet is very useful for signal tracklet identification. In the two-dimensional plot of $\Delta\eta = \eta_1 - \eta_2$ and $\Delta\phi = \phi_1 - \phi_2$ shown in Figure 6.3, we see that the combinatorial background tracklets have no correlation in ϕ, i.e. the spectrum of $\Delta\phi$ is flat. A slight decrease in the background level, as shown in the figures, at $|\Delta\phi| \sim 2.2$ is because the looper tracklet contribution with large $\Delta\phi$ is cre-

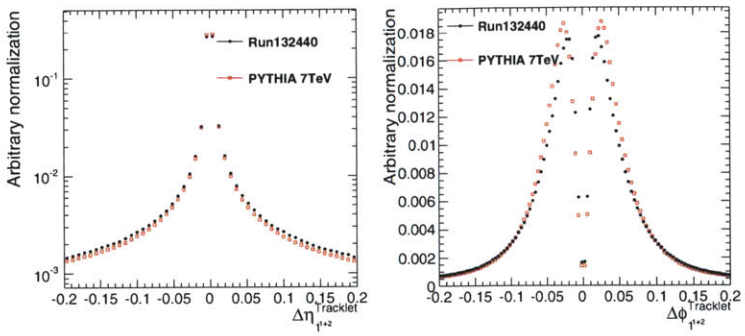

Figure 6.4.: (Left panel) The comparison of $\Delta\eta$ spectrum between Run 132440 and PYTHIA ATLAS 7 TeV sample. (Right panel) The comparison of $\Delta\phi$ spectrum between Run 132440 and PYTHIA ATLAS 7 TeV sample. The agreement between data and MC is at 10% level. Since the $\delta\eta$ and $\delta\phi$ cuts we apply is loose, the systematic uncertainty due to the difference between data and Monte Carlo is small.

ated by particles with high transverse momentum. On the other hand, signal tracklets exhibit a correlation peak around $\Delta\phi = 0$. This enables us to introduce a data-driven method to estimate the background fraction.

The $1 < |\Delta\phi| < 2$ region is chosen to be the sideband region and $|\Delta\phi| < 1$ to be the signal region. Because those regions cover the same amount of $\Delta\phi$ phase space, there is no additional normalization factor applied when we estimate the background level from the sideband region. The $|\Delta\eta|$ spectra for different pseudorapidity regions are shown for MC in Fig. 6.6 and for data in Fig. 6.7, which demonstrates that the combinatorial background can be described fairly well by the spectrum obtained from the $\Delta\phi$ sidebands. Using this sideband method, one can estimate the fraction of the combinatorial background (β) with $|\Delta\eta| < 0.1$ by the ratio of the counts of tracklets in the signal region (N_S) and the sideband region (N_{SB}), i.e. $\beta = \frac{N_{SB}}{N_S}$.

Because the background fraction is dependent on the event multiplicity variable M, Fig. 6.8(a)), pseudorapidity (η_1 in Fig. 6.8(b)), and the position of primary vertex v_z, the data samples are divided into bins of (M, η_1, v_z) to obtain $\beta(M, \eta_1, v_z)$. The typical background fraction is on the order of 0.5% to 30%. Even if the background fraction is wrong by 10%, the systematics due to the background subtraction will be in the range 0.05%-3%. The background subtracted number of tracklets can be calculated by $N_{Tracklet} = (1-\beta) \times N^{raw}_{Tracklet}$.

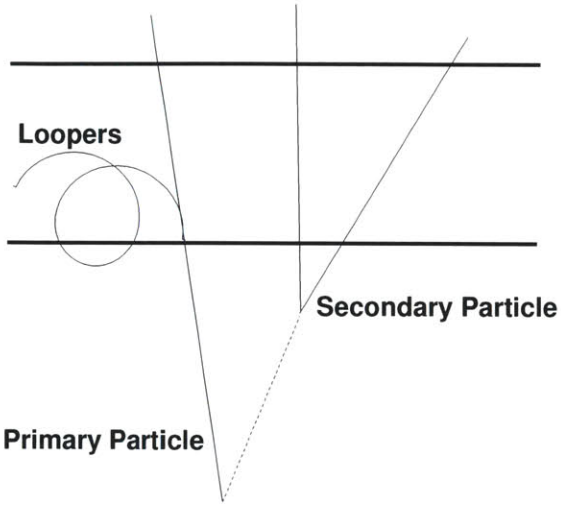

Figure 6.5.: Demonstration of difference sources of pixel hits.

6.1.4. Efficiency and Acceptance Correction

To calculate the number of hadrons, an efficiency correction has to be applied. To correct for the reconstruction efficiency and detector acceptance, the correction factor $\alpha(M,\eta,v_z)$ is introduced and defined as:

$$\alpha(M,\eta,v_z)=\frac{N^{Truth}_{Hadron}(M,\eta,v_z)}{(1-\beta(M,\eta,v_z))N^{raw,MC}_{Tracklet}(M,\eta,v_z)}. \tag{6.3}$$

where $N^{Truth}_{Hadron}(M,\eta,v_z)$ is the number of charged hadrons in the simulated sample (Monte Carlo Truth). The $\alpha(M,\eta,v_z)$ is evaluated by a large number of simulated events and is used to calculate the charged hadron spectra from the measured background subtracted tracklets. The typical correction factors are close to 1 because of the high hit reconstruction efficiency. For high pseudo-rapidity region, the correction factors start to increase due to the limited acceptance. The extrapolation to $p_T = 0$ is also included in this α correction. The calculated α correction factors are shown in Fig. 6.9 and 6.10.

The η acceptance range as a function of the primary vertex position is shown in Fig. 6.11 and the range of the primary vertex position used in different pseudo-rapidity bins are summarized in Table. 6.1.

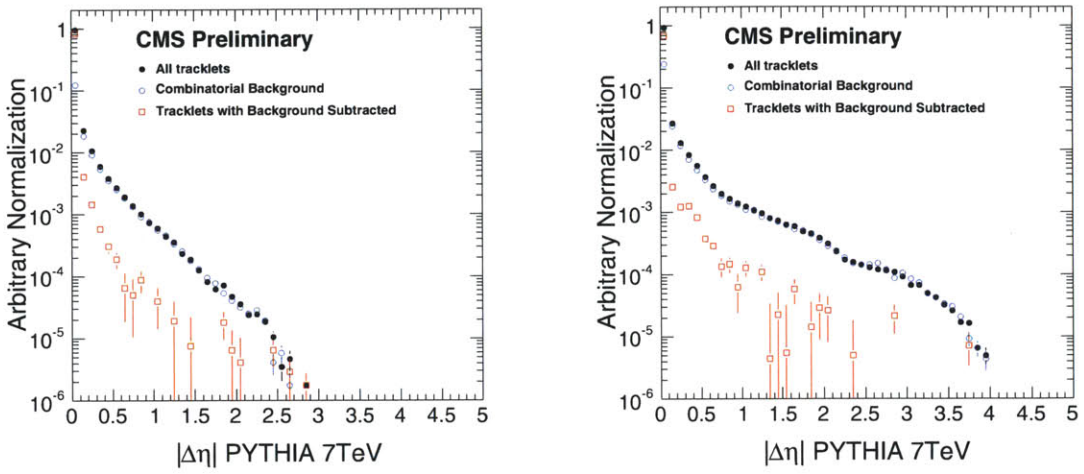

Figure 6.6.: The $\Delta\eta$ spectra for $|\eta| < 0.5$ (left) and $1.0 < |\eta| < 1.5$ (right) in the 7 TeV PYTHIA sample from the 1st+2nd layers.

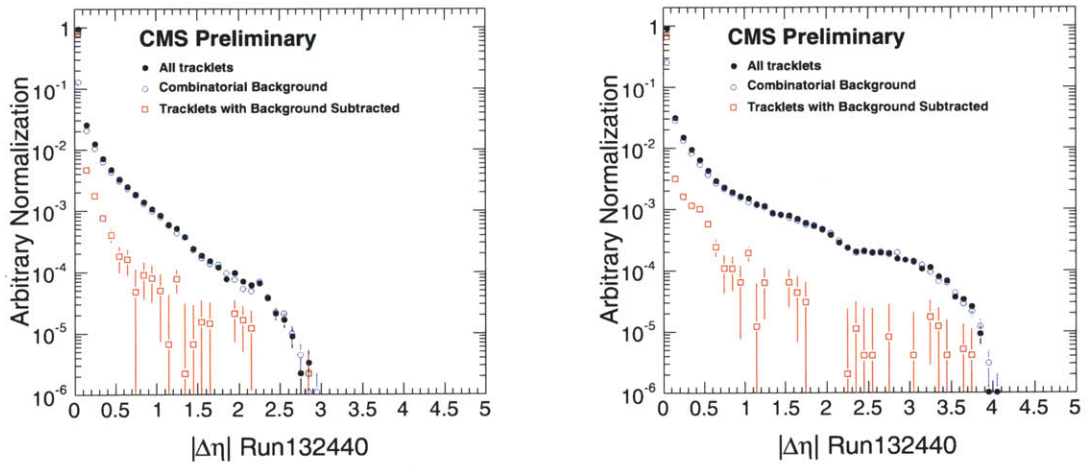

Figure 6.7.: The $\Delta\eta$ spectra for $|\eta| < 0.5$ (left) and $1.0 < |\eta| < 1.5$ (right) in the data sample (Run 132440) from the 1st+2nd layers.

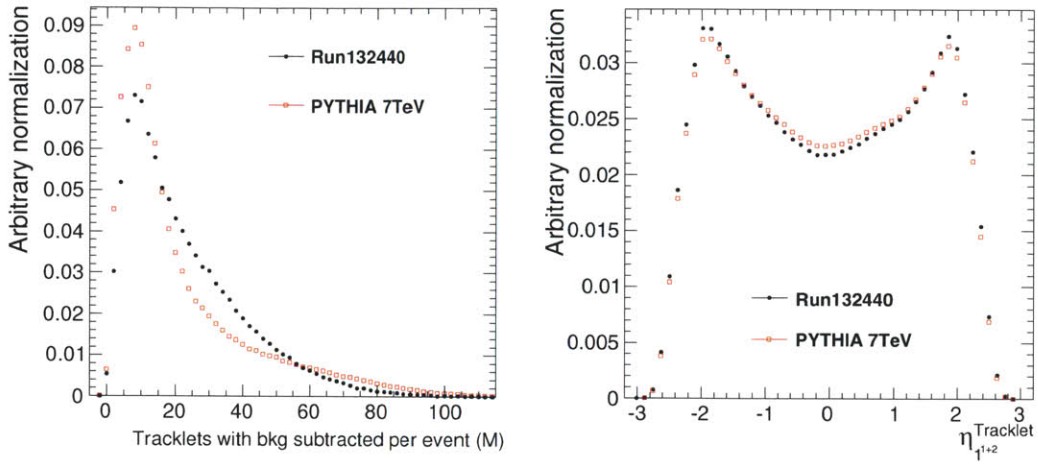

(a) (b)

Figure 6.8.: (a) Number of background subtracted tracklets per event. The background fraction is estimated by a sideband method which is described in the text. (b) Pseudorapidity distribution of raw tracklets from the data sample (Run 132440) and PYTHIA ATLAS 7 TeV.

6.2. $dN/d\eta$ study

The pseudo-rapidity distribution of charged particles is obtained from the measured number of tracklets ($N^{raw}_{Tracklet}$) after background subtraction, efficiency and acceptance correction and normalization to the number of selected events.

Using the correction factor α and background fraction β, the $dN_{ch}/d\eta$ of the selected events can be calculated by:

	η bins	$[-2.0,-1.5]$	$[-1.5,-1.0]$	$[-1.0,-0.5]$	$[-0.5,0.0]$
1st+2nd	V_z range (cm)	[-10,12]	[-16,12]	[-16,12]	[-16,12]
1st+3rd	V_z range (cm)	[-2,12]	[-14,12]	[-16,12]	[-16,12]
2nd+3rd	V_z range (cm)	[-2,12]	[-14,12]	[-16,12]	[-16,12]
	η bins	$[0.0,0.5]$	$[0.5,1.0]$	$[1.0,1.5]$	$[1.5,2.0]$
1st+2nd	V_z range (cm)	[-16,12]	[-16,12]	[-16,12]	[-16,10]
1st+3rd	V_z range (cm)	[-16,12]	[-16,12]	[-16,12]	[-16,2]
2nd+3rd	V_z range (cm)	[-16,12]	[-16,12]	[-16,12]	[-16,2]

Table 6.1.: The selected V_z range of the primary vertex for different pseudo-rapidity bins for tracklets from three different combinations.

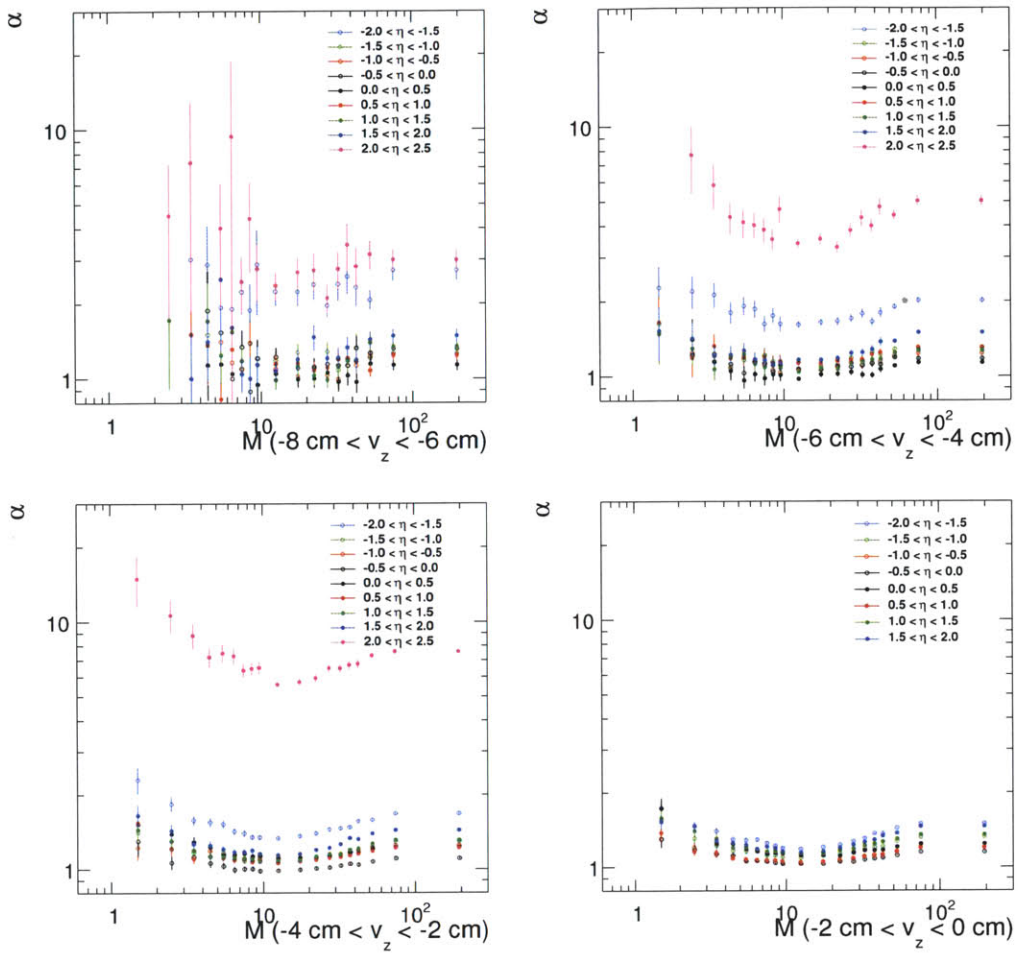

Figure 6.9.: The calculated correction factors (α) with 2M 7.0 TeV MC in bins of v_z for -8<$|V_z|$<0.

$$\frac{dN_{ch}}{d\eta}(\eta) = \frac{\sum_{(M,V_z)} \alpha(M,\eta,V_z)(1-\beta(M,\eta,V_z))N^{raw}_{Tracklet}(M,\eta,V_z)w(M)}{(1+f^0_{NSD})\sum_M N_{selected}(M)(\eta)\delta\eta w(M)} \tag{6.4}$$

where $N_{selected}(\eta)$ is the number of selected events used in each η bin and $\delta\eta$ is the bin width. Due to the requirement that there has to be a reconstructed primary vertex, the events with no activity in the pixel detector are essentially lost and the event selection efficiencies $\epsilon(M)$ should also be accounted. To get the total NSD $dN/d\eta$, corrections on the event weighting ($w(M)$) and fraction of events with $M = 0(f^0_{NSD})$ for the effect of the event selection is necessary, where $w(M)$ and f^0_{NSD} are defined as:

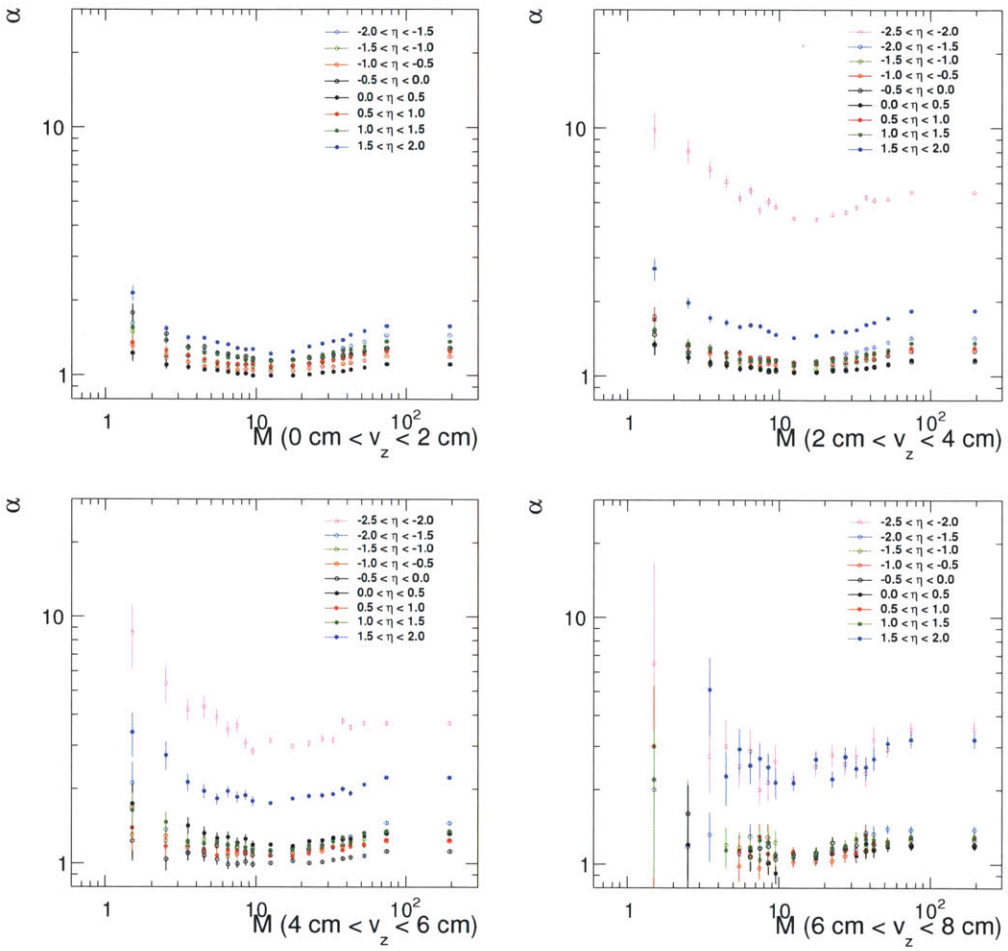

Figure 6.10.: The calculated correction factors (α) with 2M 7.0 TeV MC in bins of v_z for $0<|V_z|<8$.

$$w(M) = \frac{(1 - f_{SD}(M))}{\epsilon_{NSD}(M)} \tag{6.5}$$

and

$$f^0_{NSD} = \frac{N^0_{NSD}}{N_{NSD}} \tag{6.6}$$

$w(M)$ and f^0_{NSD} are estimated from PYTHIA D6T sample and the size of those correc-

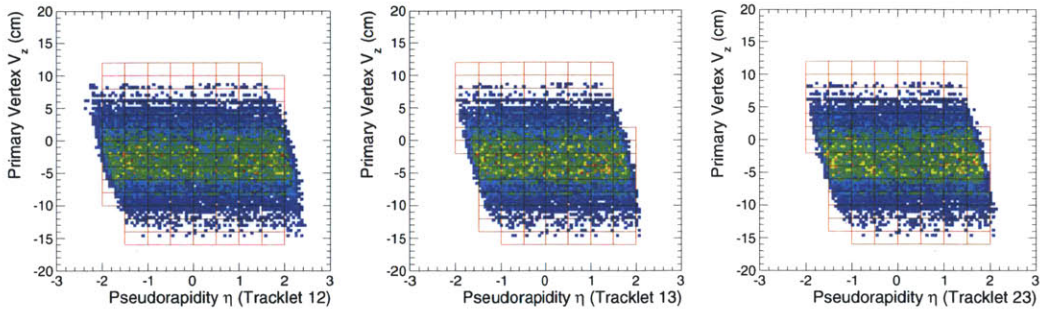

Figure 6.11.: The selected V_z range of the primary vertex as a function of pseudorapidity bins with the reconstructed tracklet spectrum overlapped from Run 123596 from the pixel layer combinations of 1st+2nd (left), 1st+3rd (middle) and 2nd+3rd (right). The stripes shown in the plot are gaps in the pixel detector. The boxes show the selected phase space in this analysis.

tion is $\sim 7\%$.

6.3. Results

The data samples are reconstructed and corrected with the tracklet method. For each data sample, $dN_{\mathrm{ch}}/d\eta$ measurements are done with three different combinations of pixel layers ($1^{st}+2^{nd}$, $1^{st}+3^{rd}$, $2^{nd}+3^{rd}$). The results from different combinations are corrected separately. Fig. 6.12 shows the results from the three combinations obtained from 7 TeV sample. The results from different pixel layers have different sensitivity to secondaries and detector acceptance effect. The results from the three combinations agrees to each other at the 2% level, and are symmetric in η. Finally, the three measurements are averaged to give the final results.

Fig. 6.14 shows the final results from the three different energies. The distributions are averaged over negative and positive values of η. The systematic uncertainties will be described in Section. 6.4. The statistical error is in 0.5-1% level which is small compared to the systematic uncertainties.

The reconstructed $dN/d\eta$ is also compared with the generator truth we used for correction. The result is shown in Fig. **??**. There is a reasonable agreement between the PYTHIA tune we choose and the reconstructed result from 7 TeV data which gives us more confidence on the MC correction procedure.

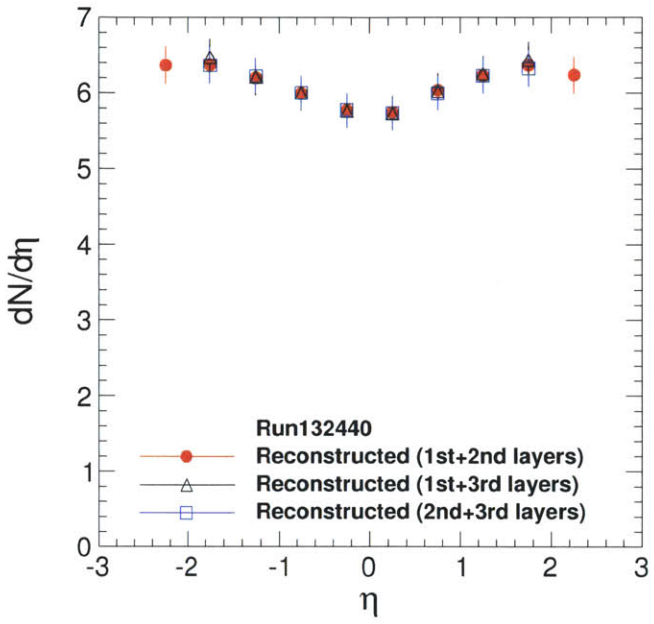

Figure 6.12.: The reconstructed $dN/d\eta$ from three different combinations of pixel layers ($1^{st}+2^{nd}$, $1^{st}+3^{rd}$, $2^{nd}+3^{rd}$) from Run 132440 ($\sqrt{s}=7$ TeV). The errors shown in the figure are dominated by the systematic uncertainties.

6.4. Systematic Uncertainties

6.4.1. Systematic error of the trigger efficiency

To estimate the systematic error of the Monte Carlo based trigger efficiency evaluation we performed a series of studies.

6.4.1.1. Variation of the diffractive component

To understand the effect of the diffractive component, we vary the fraction of the diffractive process in the Monte Carlo sample. If we decrease the single-diffractive fraction, the correction factor $f_{SD}(M)$ will be smaller and lead to a larger $dN_{\mathrm{ch}}/d\eta$. The same trend also applies to the double-diffractive component. If we remove the single-diffractive component completely, the effect is found to be 6%.

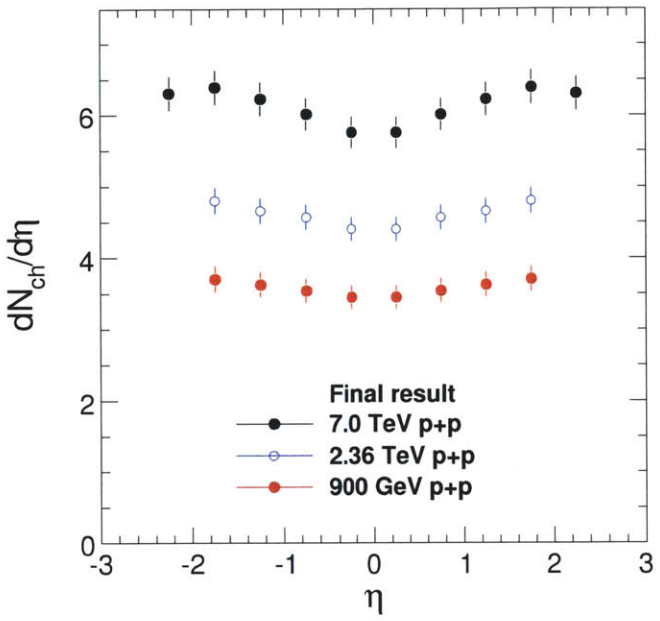

Figure 6.13.: The reconstructed $dN/d\eta$ from tracklet method with the final systematic uncertainty. The results are symmetrized in η. The error shown in the figure is dominated by the systematic uncertainties.

6.4.1.2. Different event selection

We selected the NSD enriched events by requiring a coincidence of energy deposit in the HF towers (See Section. 5.4). One can change this requirement to BSC based trigger, i.e. selection on the BSC tirgger bit 40. This requires at least one hit in the both side of the BSC counter. The selected events are analyzed and corrected with the same procedure as the HF based analysis.

Fig. 6.15 shows the results from this study. The results are consistent with each other within 2%.

6.4.2. Systematic uncertainties from algorithmic efficiency correction

The scale factor α which corrects for the reconstruction efficiency, secondary particle production and acceptance. There are two factors which change the algorithmic efficiency: event mean transverse momentum and tracklet multiplicity.

Events with low mean transverse momentum contain less particles which arrive the pixel layer and need higher α correction. The effect of the event mean P_T is studied

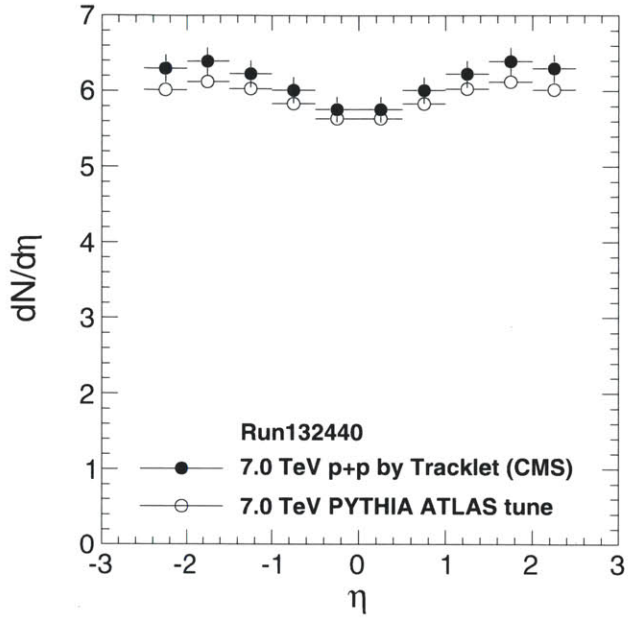

Figure 6.14.: The reconstructed $dN/d\eta$ from tracklet method with the final systematic uncertainty compared with the generator truth from PYTHIA ATLAS tune at 7 TeV.

by comparing MC samples with different mean P_T and samples produced by different generators (PHOJET and PYTHIA). If the mean P_T is changed by 10%, the effect is found to be 0.7%.

Events with high tracklet multiplicity tend to have lower tracklet reconstruction efficiency because the probability to connect hits from different charged hadron increases. A proper multiplicity variable is necessary to characterize the event multiplicity. However, different multiplicity variables have different event-by-event resolution and different sensitivities to background hits. To study the systematics due to the choice of multiplicity variable, the results are checked by using different event multiplicity definitions: (1). number of first layer hits, (2). number of tracklets, and (3). number of background subtracted tracklets. The effect is estimated to be 1.0%.

The effect due to the event topology is checked by HYDRO events, which generates random particles and provides events with different topology compared to PYTHIA generator. The generated events are corrected by PYTHIA MC and the effect due to the event topology is found to be 0.2%.

We sum the systematic uncertainties due to the algorithmic efficiency linearly and a

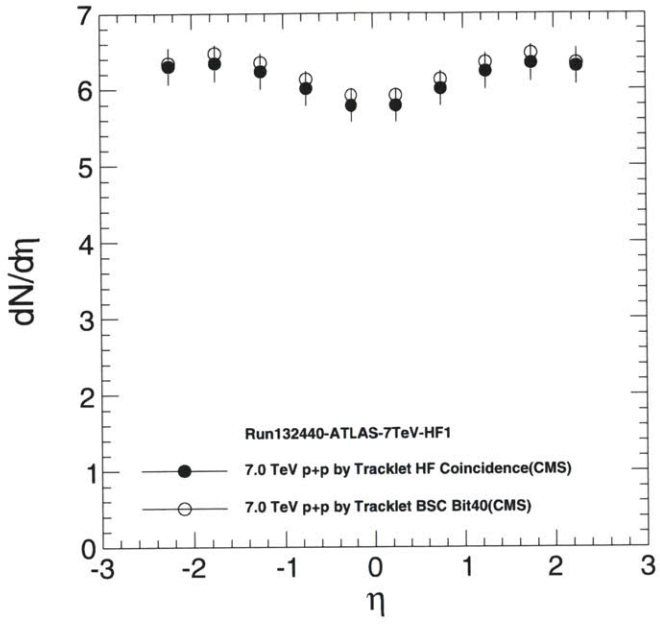

Figure 6.15.: The reconstructed $dN/d\eta$ from tracklet method on MC samples using BSC bit 40 selection vs using HF coincidence selection. The difference is in 2% level.

1.9% uncertainty is assigned for this. The 0.9 and 2.36 TeV analysis were performed in an earlier stage of the experiment and a larger uncertain was quoted for the efficiency correction (3%).

6.4.3. Systematic uncertainties due to the extrapolation to low p_T

The extrapolation correction is included in the α correction factor. The agreement between results from different pixel layer combinations is at the 2% level as shown in Fig. 6.12. Since the corrections of the p_T extrapolation for different combinations are different, this give us confidence that the systematics due to this extrapolation is small.

We estimate the systematic uncertainties due to the extrapolation to low p_T by comparing the results from different MC. We quote a 0.2% systematic uncertainty for the correction.

6.4.4. Systematic uncertainties due to vertex resolution

In this analysis, a valid primary vertex is essential and the systematic uncertainty due to the vertex resolution is checked by smearing the vertex z position by a Gaussian with a width of 20 microns. The effect is found to be negligible. ($< 0.5\%$)

6.4.5. Systematic uncertainties from MC efficiency correction and single diffractive fraction

The event selection correction factors w, f^0_{NSD} are obtained from the MC. The uncertainty due to event selection and SD fraction is estimated by varying the SD fraction($f_{SD}(M)$) and cross-checked by PHOJET generator. A 3.0%(3.5%) uncertainty is assigned for this in 0.9 and 2.36 TeV (7 TeV) analysis.

6.4.6. Systematic uncertainties due to the tracklet selection

The effect of the signal region definition is checked by varying the $\Delta\eta$ and $\Delta\phi$ selection criteria. The effect is found to be $< 0.1\%$ for changing $\Delta\eta$ cut from 0.1 to 0.2. The effect of signal region and sideband region definition is studied by changing the selection criteria. If the signal region definition is changed to $|\Delta\phi| < 1.5$ and sideband region definition is changed to $1.5 < |\Delta\phi| < 3.0$, the reconstructed $dN/d\eta$ is changed by 0.5%. A 0.5% systematic uncertainty is assigned for this.

6.4.7. Systematic uncertainties from secondary contribution

The systematic uncertainties from secondary contribution is checked in two ways. The effect of secondary produced particle from the interaction between charged hadrons and pixel detectors is checked by changing the GEANT production cut off. The effect is found to be negligible. ($< 0.5\%$)

The effect of secondary particles from strange particles are checked by varying the fraction of the strange particles. Increasing the strangeness content by 40% will change the reconstructed $dN/d\eta$ by 1%.

From those studies, we assign a 1% uncertainty for this.

6.4.8. Systematic uncertainties from misalignment

The η and ϕ correlations between the first and second layer hits of the pixel detector are used in the tracklet reconstruction, thus the effect of misalignment becomes more important, i.e. the width of the signal correlation peak will be dependent on the misalignment.

Uncertainty due to the misalignment is estimated by comparing the hit distributions between data and MC. The difference in acceptance is found to be in 2% level and we quote this difference as the systematic uncertainty. The uncertainty due to the widening of the correlation peak is estimated to be in 1% level.

6.4.9. Systematic uncertainties from low p_T loopers, beam halo and event pile-up

To test the effect from the hits of low p_T loopers and beam halo, 10 random hits were added to the first layer (flat as a function of η). This increases the average number of hits in the first layer by 30%. The effect on the final measurement is at the 1% level. The monitoring of the hit multiplicity as a function of time is important for us to understand the effect from the beam background.

6.4.10. Systematic uncertainties from pixel hit reconstruction

There is a chance that the pixel reconstruction efficiency in data is actually different from that of the Monte Carlo simulation. To study this effect, we remove reconstructed hits with a probability of 0.5%. The difference in the result is found to be at the 1% level.

For tracks with a very shallow angle, there is a non-negligible probability that the pixel hit will be split into two separate hits. This effect is studied by artificially splitting the pixel hits with a probability of 1%. The effect is found to be 0.4%.

We also check the systematic uncertainty from the hit reconstruction algorithm. We tune the pixel hit reconstruction algorithm with different templates and thresholds. The difference is found to be 0.1%.

6.4.11. Cross-checks from magnetic field off sample

We checked the tracklet reconstruction performance in Run 133242, which is collected without magnetic field at 7 TeV. PYTHIA MC with ATLAS tune is generated with the same

condition for correction. This check allows us to investigate the systematics due to the loopers and P_T extrapolation.

The reconstructed tracklet spectra are shown in Fig. 6.16. We now see a narrow correlation peak in $\Delta\phi$. The data and MC are in good agreement.

We follow the same procedure to reconstruct $dN/d\eta$ from this sample Fig. 6.17 shows the results from this run. The results are consistent with Run 132440 which is taken with magnetic field B = 3.8 T at 2% level.

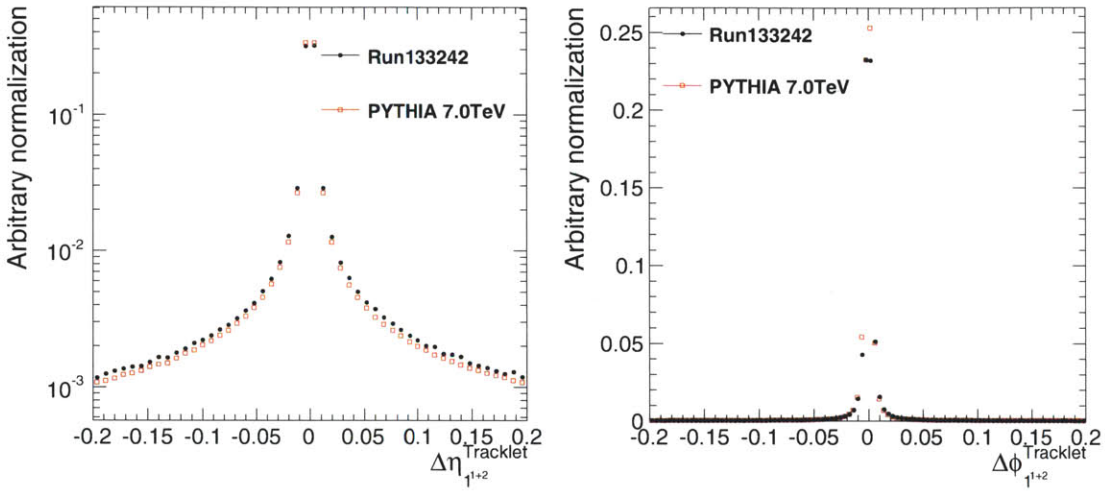

Figure 6.16.: (Left panel) The comparison of $\Delta\eta$ spectrum between Run 133242 and PYTHIA ATLAS 7 TeV sample. (Right panel) The comparison of $\Delta\phi$ spectrum between Run 133242 and PYTHIA ATLAS 7 TeV sample.

The systematic uncertainties discussed in this section are summarized in Table 6.2. The estimated total systematic uncertainty for the $dN/d\eta$ measurement is 4.6%.

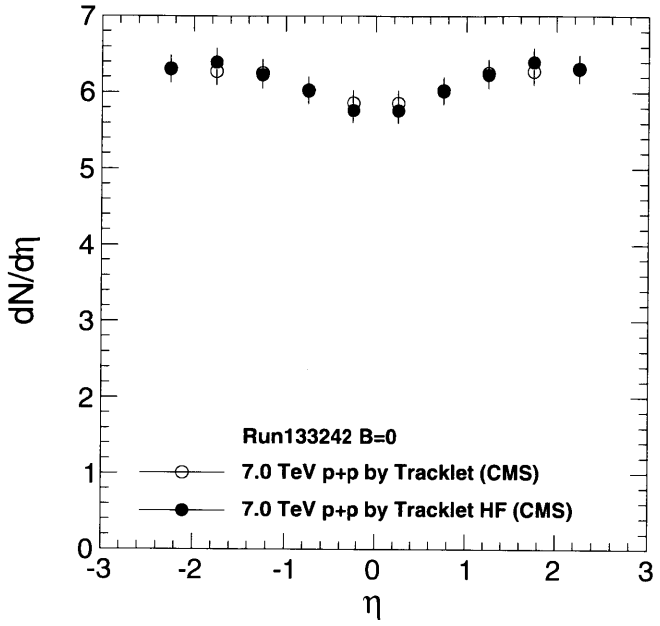

Figure 6.17.: The comparison between magnetic field on (3.8T) and magnet field off results. The reconstructed $dN/d\eta$ from Run132440 (B=3.8T) are shown as black dots while the results from Run 133242 (B=0) are shown as the black circles.

Source	Correction	0.9 TeV	2.36 TeV	7 TeV (%)
Algorithmic efficiency	α	3.0	3.0	1.9
P_T extrapolation	α	0.3	0.3	0.3
Pixel hit reconstruction efficiency	α	1.0	1.0	1.0
Pixel hit splitting	α	0.4	0.4	0.4
Acceptance uncertainty	α	1.0	1.0	1.0
Correction of secondary particles	α	1.0	1.0	1.0
Selection and background subtraction	β	0.5	0.5	0.5
Misalignment	α, β	1.0	1.0	1.0
Correction of looper hits	α, β	1.0	1.0	1.0
Random hit from beam halo	α, β	0.2	0.2	0.2
Effect of event pile-up	α, β	0.1	0.1	0.1
Correction on event selection	w, f^0_{NSD}	3.0	3.0	3.5
Total		4.9	4.9	4.6

Table 6.2.: Summary of systematic uncertainties.

7. Multiplicity distribution measurement

The multiplicity distributions are measured by tracklet (in this thesis) and tracking methods with the CMS tracker [78]. The tracklet method has lower p_T reach such that the extrapolation correction to zero p_T is small. Due to the statistical nature of the tracklet method, the event-by-event multiplicity resolution is worse than the tracking method. The tracking method has low fake rate and better resolution on the event multiplicity. But the requirement of hits in the strip detector limits the low p_T reach to ~ 100 MeV/c such that it has larger uncertainty due to the extrapolation.

This chapter describes a tracklet-based analysis method for the measurement of the charged hadron multiplicity distribution. In this analysis, the same event selection and tracklet reconstruction algorithm as the pseudorapidity distribution measurement are used for the selecting and reconstructing NSD events in p+p collisions. Details can be found in Section 6.1. Compared to pseudorapidity density analysis which is an measurement of the integrated quantity over all events with different charged hadron multiplicity, this analysis provides a more detailed information about the multiplicity fluctuation. In order to correct the observed raw spectrum to the multiplicity distribution, an unfolding procedure which use the information from the Monte Carlo simulation is necessary.

This analysis contains three major steps:

1. Raw spectrum reconstruction

2. Bayesian unfolding

3. Event selection correction and single-diffraction component subtraction.

They will be discussed in detail in the following sections. The systematic uncertainty studies are detailed in Section 7.4.

7.1. Raw spectrum reconstruction

The multiplicity distribution requires a multiplicity variable for each event in order to extract the multiplicity fluctuation. For each event, reconstructed tracklets with $|\Delta\eta|$<0.1 are selected for analysis. In order to estimate the background contribution, the $1 < |\Delta\phi| < 2$ region is chosen to be the sideband region for combinatorial background estimation and $|\Delta\phi| < 1$ to be the signal region. Using this sideband method, one can estimate the uncorrected event by event multiplicity(M) by:

$$M = N_S - N_{SB} \tag{7.1}$$

where $N_{S(SB)}$ is the number of tracklets in the signal(sideband) region. The event by event multiplicity M is used as an input to the unfolding process to get the correct multiplicity distributions.

Fig. 7.1 shows the uncorrected tracklet multiplicity spectrum with the first and second pixel layers for the three different energies. The raw spectrum needs to be corrected for the effects due to the detection.

7.2. Correction of detection effects

In order to correct the effect of tracklet reconstruction efficiency, contribution from the secondaries and detector acceptance, Bayesian unfolding technique is selected to correct the tracklet multiplicity distributions to the true multiplicity distributions. Since this method is an iterative process and unfolded results usually converge very quickly, it can avoid complicated matrix inversion procedure as well as computing intensive fitting (such as χ^2 unfolding method). However, due to its iterative nature, one needs to check the statistical uncertainty carefully.

7.2.1. General concept of unfolding problem

The ultimate goal of the physics measurement is to get the physics quantity with detector effect removed. If one has a true spectrum (T) as a function of physics quantity (t), the observed spectrum (M) as a function of detection variable (m) is recorded in the detector level. The observed spectrum is usually convoluted by detector effects such as detector efficiency, detector resolution, and transportation which is demonstrated in Fig. 7.2. The relation between the true spectrum and observed can be written as the

following:

$$M_m = \sum_t R_{mt} T_t \tag{7.2}$$

where R_{mt} is the response matrix which accounts for the detector effects. From the expression above, the true spectrum can be calculated by:

$$U_t = \sum_m R^{-1}_{mt} M_m \tag{7.3}$$

However, the inverse matrix may not exist because R_{mt} can be singular. Even if the response matrix can be inverted, the unfolded result (U_t) from Eq. 7.3 usually exhibit oscillation behavior due to the amplification of the statistical fluctuation during the calculation.

Another option is to use numerical approach to solve this problem. For example, one can use a χ^2 minimization method to obtain the unfolded results. A χ^2 function can be defined by

$$\chi^2(U) = \sum_t (M_m - \sum_m R_{mt} U_t) \tag{7.4}$$

and a minimization program is used to tune the U_t until the minimum χ^2 is found. If the U_t is the same as T_t, the χ^2 will be 0. This approach is usually computing intensive because of the large number of the tunable parameters. If the χ^2 minimization is performed without proper regularization, the unfolded distribution will still exhibit strong oscillation behavior.

In the following sections, an unfolding method which is based on the Bayes' theorem will be discussed. The advantage of this method is that it is an iterative algorithm which is not involved in numerical minimization or matrix inversion. Usually, the convergence of the result is very quick, and limited number of iterations provides an implicit regularization.

7.2.2. Bayes' Theorem

Bayes' theorem expresses the conditional probability in terms of the prior probabilities (or called unconditional probabilities), which is widely used to calculate the *inverse probability* from a known conditional probability. For example, there is a measurement (M) and a physics input (T). If M has a non-zero probability, the conditional probabilities satisfies the following relation:

$$P(T|M) = \frac{P(M|T)P(T)}{P(M)} \tag{7.5}$$

where $P(M)$ and $P(T)$ are the prior probabilities of M and T, $P(M|T)$ is the conditional probability of M given T, $P(T|M)$ is the conditional probability of T given M.

As shown in Fig. 7.3, the conditional probabilities can be expressed as:

$$P(T|M) = \frac{P(M \cap T)}{P(M)} \tag{7.6}$$

$$P(M|T) = \frac{P(M \cap T)}{P(T)} \tag{7.7}$$

By using Eq. 7.6 and Eq. 7.7, we can derive the Bayes' theorem:

$$P(T|M)P(M) = P(M \cap T) = P(M|T)P(T) \tag{7.8}$$

$$P(T|M) = \frac{P(M|T)P(T)}{P(M)} \tag{7.9}$$

In case of several independent physics inputs (T_t, $t = 1, 2, \ldots, n_t$) and several measured values (M_m, $m = 1, 2, \ldots, n_m$), the Bayes' theorem can be stated as:

$$P(T_t|M_m) = \frac{P(M_m|T_t)P(T_t)}{P_0(M_m)} \tag{7.10}$$

$$= \frac{P(M_m|T_t)P(T_t)}{\sum_{t'} P(M_m|T_t')P(T_t')} \tag{7.11}$$

However, the $P(T_t)$ is the unknown which is to be extracted, as suggested in [79, 80], an unfolding procedure is introduced as follows. If we assume that $P(T_t)$ is known in the beginning ($P_0(T_t)$), then based on the Eq. 7.12 the conditional probability $P(T_t|M_m)$ can

be calculated by:

$$P(T_t|M_m) \sim \frac{P(M_m|T_t)P_0(T_t)}{\sum_{t'} P(M_m|T'_t)P_0(T'_t)} \tag{7.12}$$

where $P_0(T'_t)$ is the initial prior probability, which can be an uniform distribution or a distribution predicted by generator. The unfolded distribution after the first iteration can be calculated by

$$P_1(T_t) = \sum_m P(T_t|M_m)P(M_m) \tag{7.13}$$

One can repeat this procedure to calculate the unfolded distribution P_n for the nth iteraction. From the Monte Carlo study, it is shown that $P_n(T_t)$ is moving closer to the real spectrum $P(T_t)$.

7.2.3. Unfolding procedure

In this analysis, the physical quantities t is the charged hadron multiplicity, the measurement m is the event by event tracklet multiplicity. From the discussion in the last section, one can recognize that $P(T)$ is the charged hadron multiplicity distribution(T_t) and $P(M_m)$ is the raw spectrum(M_m). $P(M_m|T_t)$ is the response matrix(R_{mt}) which describes the physics and detector effects. This unfolding procedure contains the following four steps:

1. Start with the PYTHIA generator multiplicity distribution (or a flat distribution for cross-check) as a prior distribution (P_t), calculate the smearing matrix ($\tilde{R}_{tm}$) by

$$\tilde{R}_{tm} = \frac{R_{mt}P_t}{\sum_{t'} R_{mt'}P_{t'}} \tag{7.14}$$

2. Calculate the unfolded distribution with the smearing matrix by using the measured tracklet multiplicity spectrum (M_m):

$$U_t = \sum_m \tilde{R}_{tm}M_m \tag{7.15}$$

3. Replace the prior distribution P_t by U_t and go back to step 1 for several iterations.

4. After the unfolded distribution converges (changes between iterations are much smaller than statistical error), the event selection efficiency(ϵ_t) and single-diffractive fraction(f_t^{SD}) corrections are applied to get the final multiplicity distributions U_t':

$$U_t' = \frac{(1 - f_t^{SD})}{\epsilon_t} U_t \tag{7.16}$$

Fig. 7.4 shows the event selection efficiency ϵ_t and single-diffractive fraction f_t^{SD}. The event selection efficiency is mainly driven by the vertex reconstruction efficiency. The single-diffractive fraction correction only affects the low multiplicity part and the typical correction factor is 0 - 20%.

7.3. Multiplicity distribution measurement

Tracklet multiplicity spectra from the 1st+2nd, 2nd+3rd and 1st+3rd layers are corrected and averaged to obtain the final multiplicity distributions. The charged particle multiplicity distributions are measured in increasing bins of pseudorapidity.

The statistical error is checked by varying the raw spectrum according to the Poisson distribution around the center value of each bin to study the effect of statistical fluctuation. Each generated raw spectrum is unfolded with 50 iterations because in the large iteration limit, the unfolded result will be approaching the exact solution from matrix inversion method. The statistical errors are determined by a Gaussian fit on the pull distributions obtained from the pseudo-experiments.

The fully corrected results from 0.9, 2.36, 7.0 TeV samples are shown in Fig. 7.5. The error bar shown in the plots included the statistical and systematical uncertainty which will be discussed in the next section.

7.4. Systematic Check

7.4.1. Uncertainty due to the algorithmic efficiency and acceptance corrections

The uncertainties associated to the algorithmic efficiency and acceptance corrections are summarized in table 7.1. The total systematic error from reconstruction efficiency

correction is found to be 2.6%(2.9%) with (without) magnetic field.

In order to check the effect of the efficiency uncertainty to the multiplicity distribution measurement, a Toy MC study is performed by varying the reconstruction efficiency by 2.6%. The differences of the reconstructed results are quoted as the systematic errors. The systematic uncertainty as a function of N_{ch} is shown in Fig. 7.6 and obtain the final uncertainty in the multiplicity distribution.

Source	7 TeV (%)
Algorithmic efficiency	1.6
P_T extrapolation	0.3
Pixel hit reconstruction efficiency	1.0
Pixel hit splitting	0.4
Acceptance uncertainty	1.0
Correction of secondary contribution	1.0
Tracklet selection and background subtraction	0.5
Misalignment	1.0
Random hit from beam halo	0.2
Total	2.6

Table 7.1.: Summary of systematic uncertainties related to the efficiency and acceptance correction.

7.4.2. Uncertainty due to the unfolding procedure

The unfolding procedure is checked by varying the number of iterations. The effect is found to be 0 - 5% level which is much smaller than the other uncertainty. The effect of the prior assumption is also checked by using a flat prior distribution, the effect is found to be in 0 - 5% level.

7.4.3. Uncertainty due to the event selection and SD fraction correction

The uncertainty due to the event selection efficiency and SD fraction correction is studied by comparing the corrected result with PHOJET MC and with PYTHIA MC because these two models have pretty different SD definitions. We quote the difference as the systematic error. The systematic uncertainty as a function of N_{ch} is shown in Fig. 7.6 for 7 TeV and $|\eta| < 2.0$. This uncertainty is the dominant systematics in the low multiplicity region.

7.4.4. Cross-checks between different layers

The results from 1st+2nd, 1st+3rd and 2nd+3rd pixel layers are obtained independently by different response matrices and are compared to each other. This check helps to understand the uncertainty due to the algorithmic efficiency, p_T extrapolation and the correction of the secondary produced particles. Fig. 7.7 shows the results from 7 TeV sample. The agreement is found to be within 10-20% in the high multiplicity region which is well covered by the total systematic uncertainty.

7.4.5. Cross-checks between magnetic field on / off sample

In order to check the effect of looper hits and magnetic field, results with and without magnetic field are checked. The unfolded distributions from the two samples at 7 TeV in the high multiplicity region are consistent within 25 % level which is covered by the total systematic uncertainty.

7.4.6. Uncertainty due to event pile-up

The systematics due to the event pile-up is studied by randomly merging two event with a probability of 2%. The contribution from the pile-up event is largely rejected in the tracklet reconstruction procedure. The uncertainty due to the event pile-up is found to be negligible compared to other systematics.

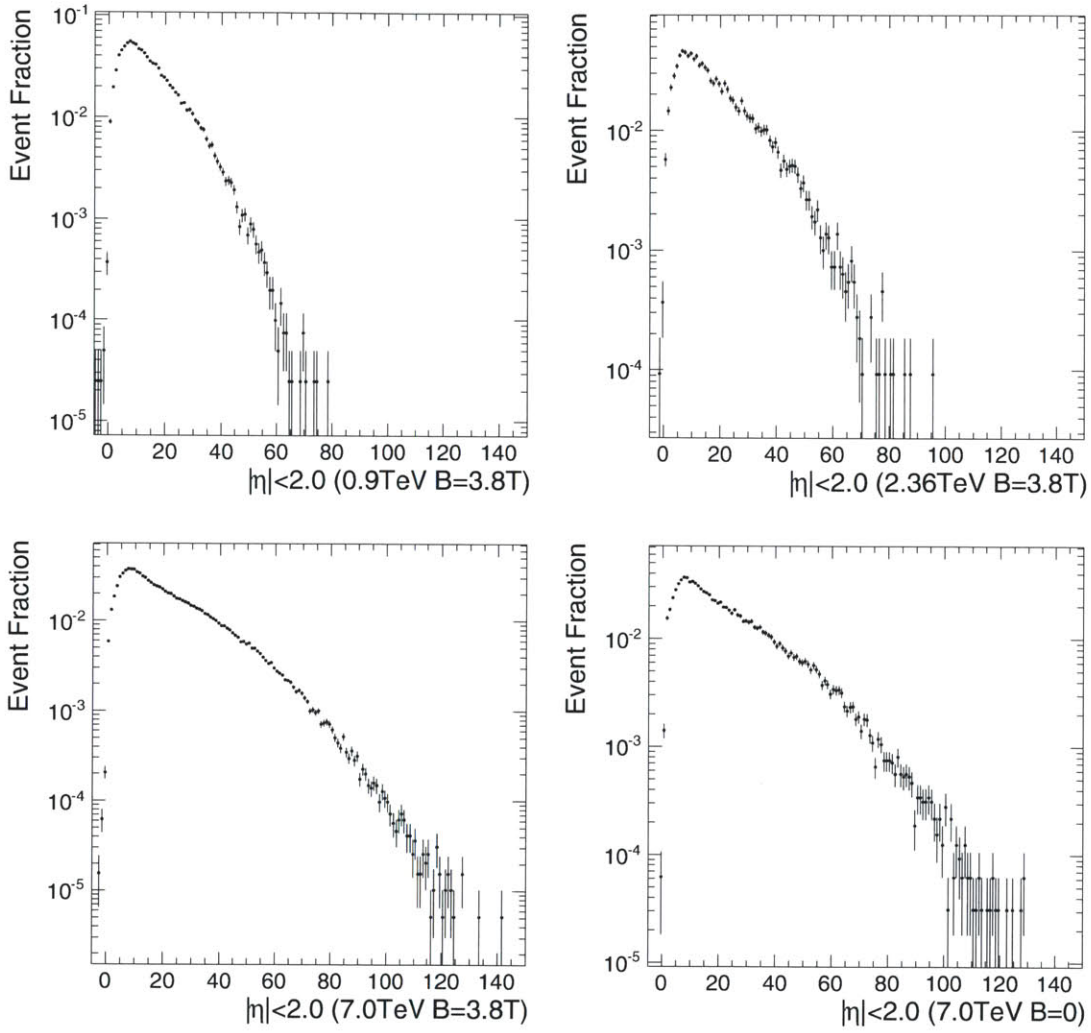

Figure 7.1.: Raw multiplicity distributions from 0.9, 2.36, 7.0 TeV samples taken with or without magnetic field.

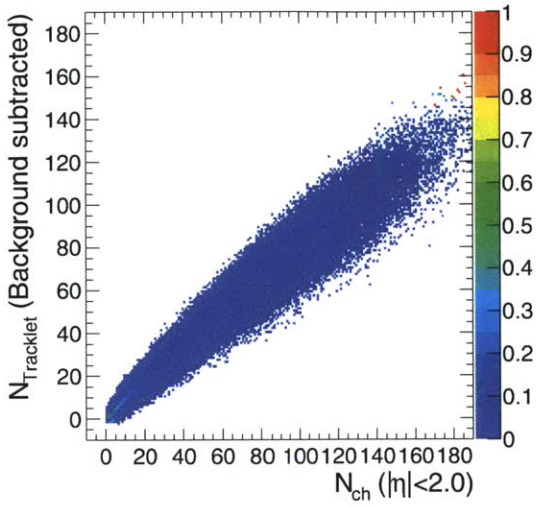

Figure 7.2.: The response matrix obtained from PYTHIA 7 TeV MC.

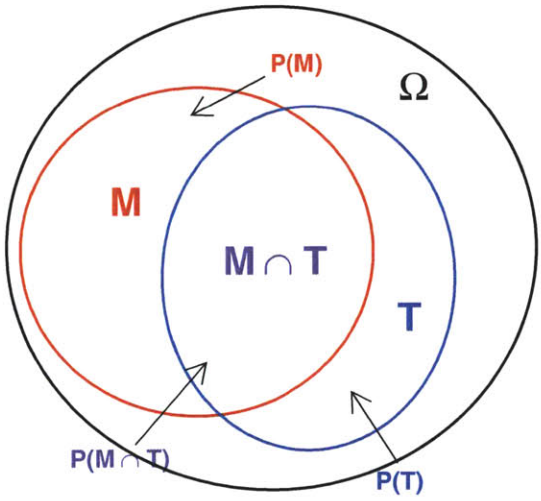

Figure 7.3.: Venn diagram of the measurement(M) and physics input(T) in the probability space (Ω))

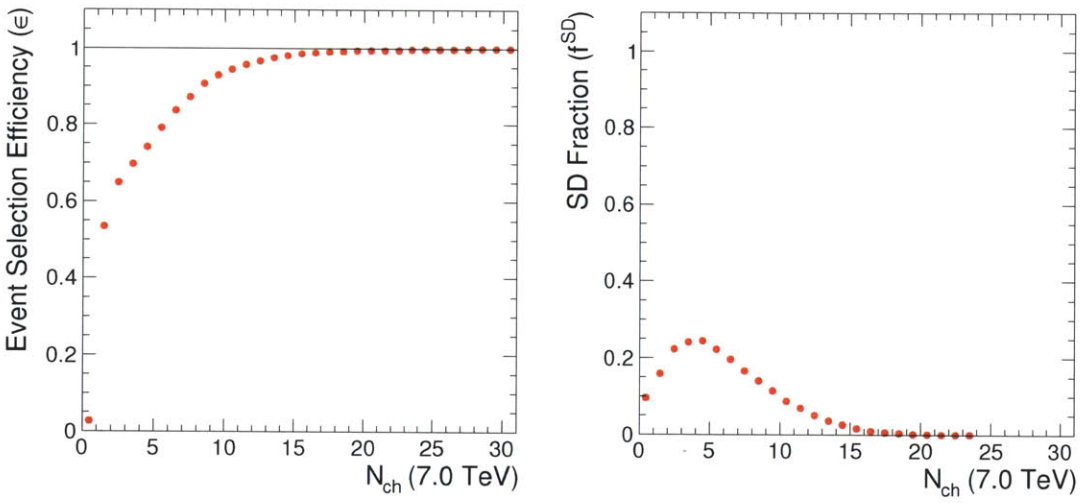

Figure 7.4.: (Left Panel) The event selection efficiency (ϵ) as a function of N_{ch} with $|\eta|$<2.0. (Right Panel) The single-diffractive fraction (f^{SD}) as a function of N_{ch} with $|\eta|$<2.0.

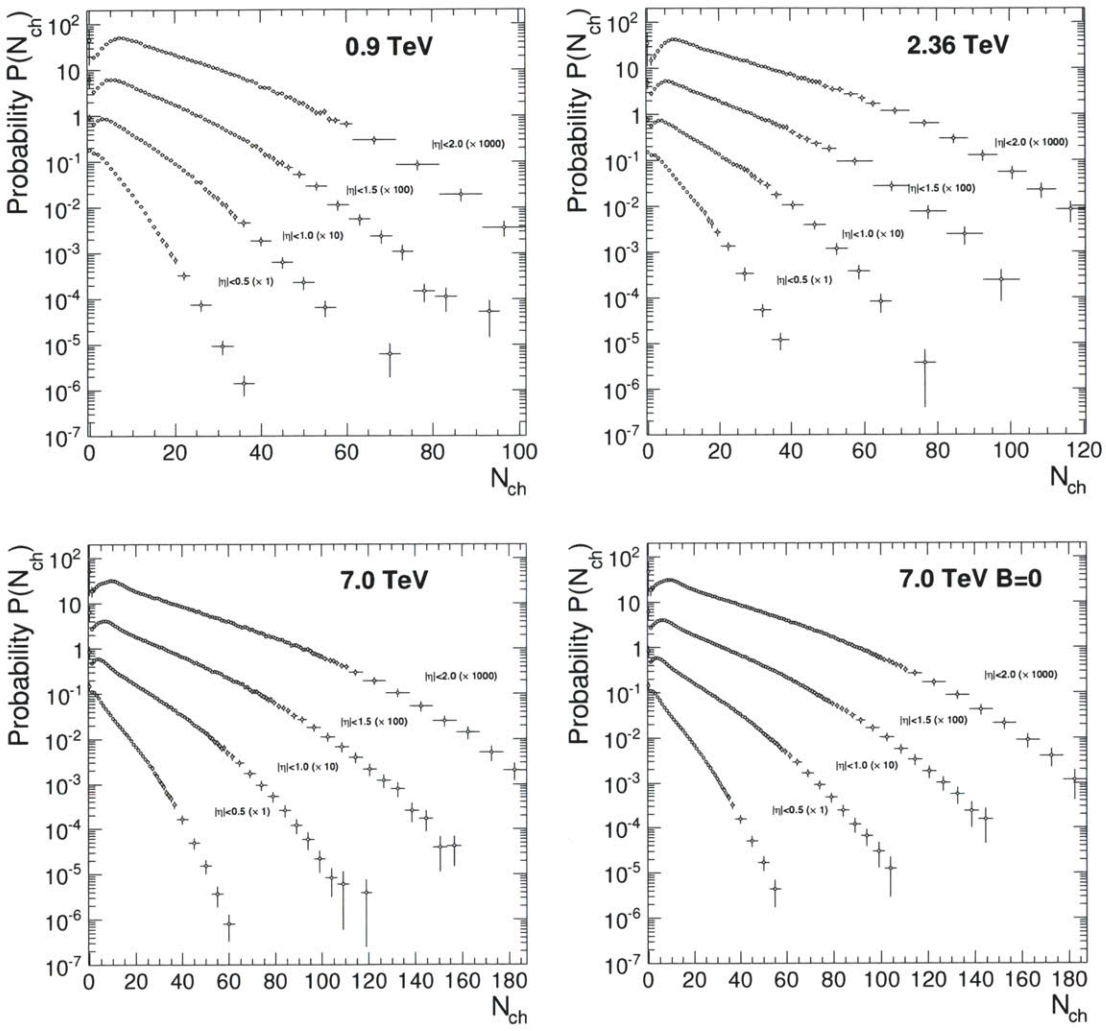

Figure 7.5.: Corrected multiplicity distributions from 0.9, 2.36, 7.0 TeV samples taken with or without magnetic field.

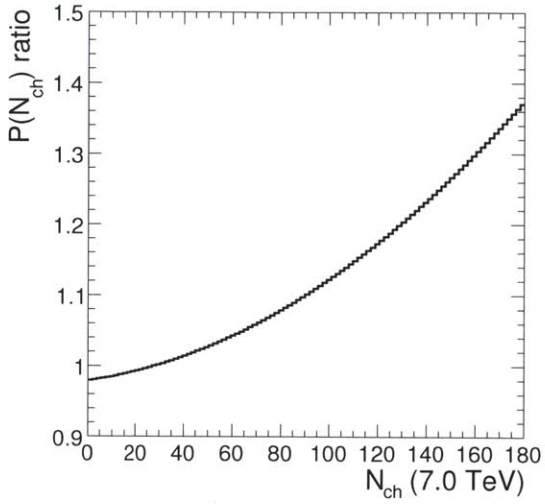

Figure 7.6.: The ratio of $P(N_{ch})$ with $|\eta|$<2.0 before and after varying the reconstruction efficiency by 2.6%.

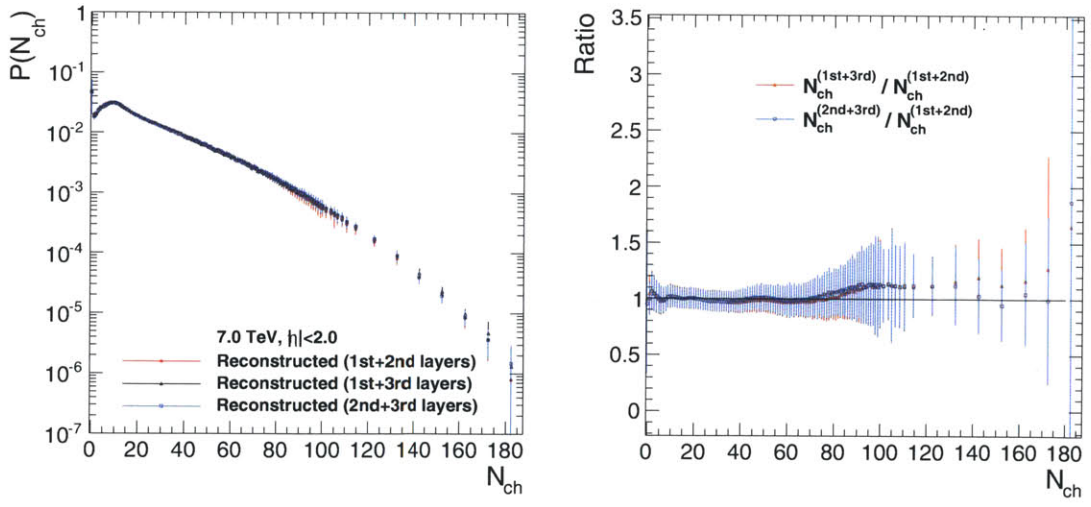

Figure 7.7.: (Left Panel) Reconstructed N_{ch} from three different combinations with 7 TeV data sample. (Right Panel) Ratios of reconstructed N_{ch}.

8. Results

In this chapter, the final measurements discussed in this thesis are summarized and compared with measurements in CMS obtained using other methods. A short summary of related measurements from the other LHC experiments will be given in Sec. 8.2. This is then followed by discussions of the results and their implications.

8.1. Comparison between different methods

8.1.1. Pseudorapidity distributions

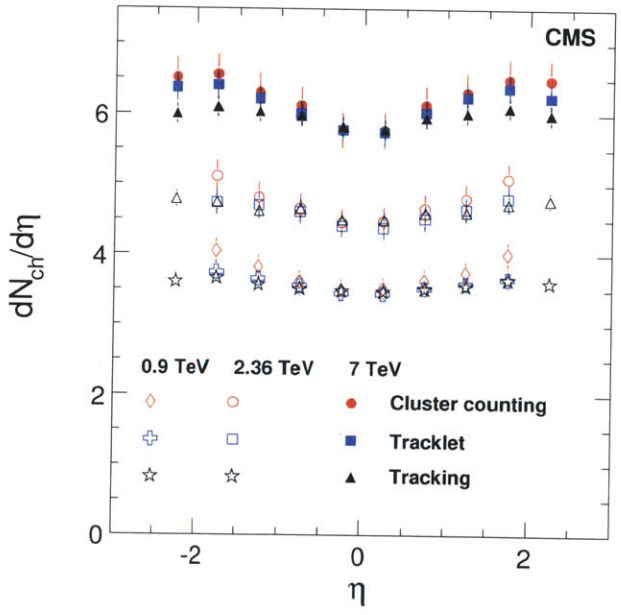

Figure 8.1.: Reconstructed $dN_{ch}/d\eta$ distributions obtained from the tracklet (squares with error bars), cluster counting (dots) [76, 77], and tracking (triangles) methods [76, 77], in p+p collisions at 0.9, 2.36 and 7.0 TeV. The error bars shown in the figure are uncorrelated systematic errors.

The measured $dN_{ch}/d\eta$ from the tracklet method in this thesis are compared with the pixel cluster counting method [76] and tracking method [76]. The strengths and weaknesses of each method are discussed in Chapter. 6. Fig. 8.1 shows the summary of results on pseudorapidity density distributions. The three methods are consistent within 4%. There is a trend of increasing discrepancy as a function of pseudorapidity. This may come from the increasing fraction of the background hits in the forward region and the acceptance correction.

To minimize the systematic uncertainties, results from the three methods are averaged to produce the final result in the publication [76, 77]. The averaged CMS results are shown in Fig. 8.2 and compare with other experiments.

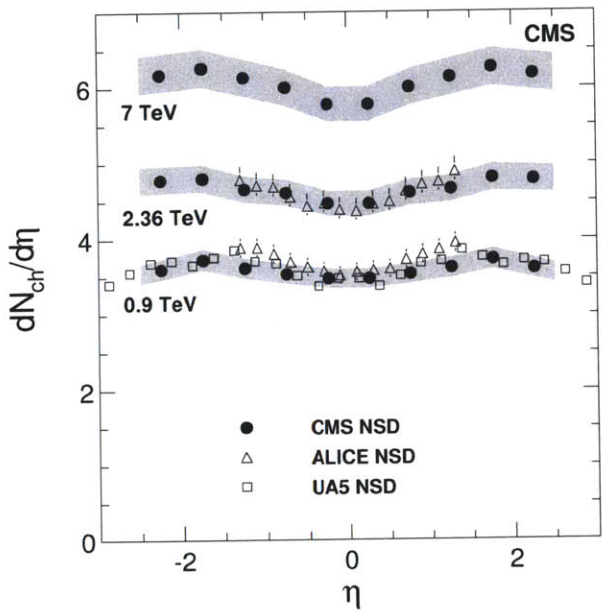

Figure 8.2.: Distributions of $dN_{ch}/d\eta$, averaged over the three measurement methods and compared with data from UA5 [24] (p+$\bar{p}$, with statistical errors only) and ALICE [81] (with statistical and systematic uncertainties). The shaded band shows systematic uncertainties of the CMS data. The CMS and UA5 data are averaged over negative and positive values of η.

8.1.2. Multiplicity distributions

In Fig. 8.3, the measured multiplicity distributions from the tracklet method is compared to the tracking method [78]. At $\sqrt{s} = 7$ TeV, the tracklet measurement are higher than the tracking results in the high multiplicity region at $\sqrt{s} = 7$ TeV, but the difference

between the two methods is within the quoted systematic uncertainty. The tracklet results are used for later discussions.

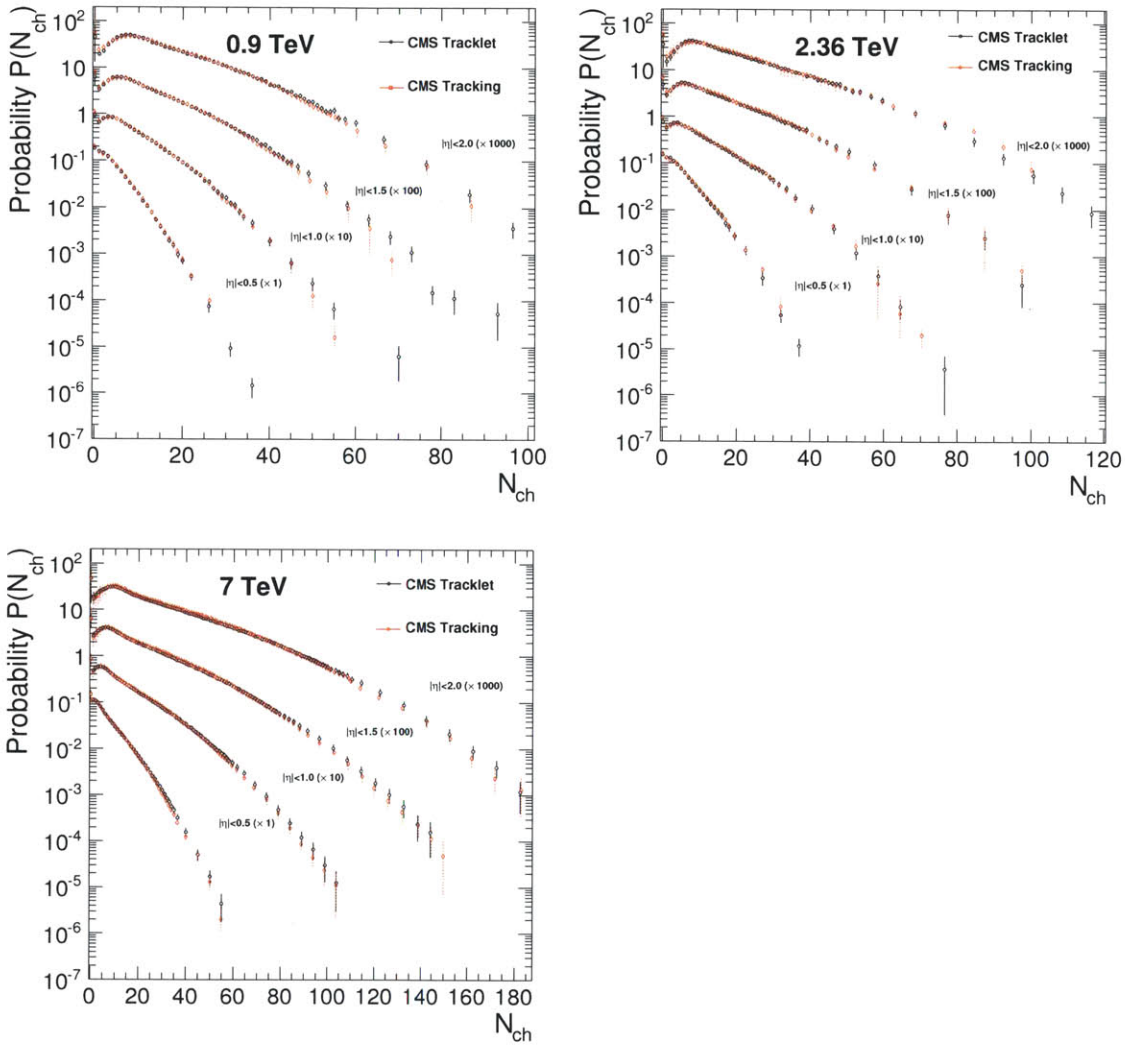

Figure 8.3.: The measured multiplicity distributions at $\sqrt{s}$ = 0.9, 2.36 and 7.0 TeV. The tracklet results (black circle) are compared with the measurement from tracking method (red circle).

From the comparisons above, we see that the experimental results are in a good state and different methods are in reasonable agreement. In the following sections, the results will be compared with other experiments and with low energy data, and the physics implications from these results will be discussed.

8.2. Comparison with other experiments

8.2.1. Results from other LHC experiments

The ALICE (A Large Ion Collider Experiment) detector measured inclusive and NSD charged hadron multiplicity distributions and $dN_{ch}/d\eta$ from p+p collisions at $\sqrt{s}$ = 0.9 and 2.36 TeV during the commissioning of the LHC [81]. The main detector used in the analysis was the Silicon Pixel Detector (SPD), which covered a range of $|\eta| < 1.4$, and the two scintillation hodoscopes (VZERO), which covered the region $2.8 < \eta < 5.1$ and $-3.7 < \eta < -1.7$. The minimum-bias trigger used in ALICE was at least 1 hit in the SPD or VZERO and in coincidence with the signals from the two beam pick-up counters indicating the presence of two passing proton bunches. During the 2.36 TeV data taking, the VZERO detector was not turned on. Therefore, the trigger conditions and uncertainties differ slightly from the 0.9 TeV analysis [81]. For the NSD measurement at $\sqrt{s} = 0.9$ TeV, a subset of the sample were selected by requiring a coincidence between the two sides of the VZEROs to minimize the contamination from the SD events.

The charged particle multiplicity was reconstructed with a tracklet method, which is similar to the technique used in the PHOBOS experiment and in this thesis. This also limited the pseudorapidity reach to the acceptance range of the SPD. The results were corrected for tracking efficiency, detector acceptance, and secondaries. The multiplicity distributions were measured by an unfolding technique based on a regularized χ^2 fit. The results were cross-checked by a Bayesian unfolding method.

The ATLAS (A Toroidal LHC Apparatus) detector measured charged hadron multiplicity distribution and $dN_{ch}/d\eta$ from p+p collisions at $\sqrt{s} = 900$ GeV during the commissioning of the LHC [82]. The events were triggered by a single-arm trigger and a total of 455,593 events were collected. The measurement was done with the inner tracking system. However, the measurement was mainly for PYTHIA model tunning. Only charged particles with $p_T > 500$ MeV/c were included in the measurement in order to minimize the model dependence of the event classification, diffractive component and p_T extrapolation. The results were compared with calculation from several PYTHIA tunes and the PHOJET generator [82]. This choice made comparison to previous experiments and analytical models impossible. The results from ATLAS are not further discussed.

Table 8.1.: Summary of the LHC experiments. The symbol ∘ indices that measurements of $dN_{ch}/d\eta$ (or multiplicity distributions) is available in this experiment.

Exp.	$\sqrt{s}$ (GeV)	Type	$dN_{ch}/d\eta$	Multi.	Trigger	N_{ev}	p_T reach	Ref.
CMS	900,2360(p+p)	NSD	∘		incl./2-arm	40k, 11k	30 MeV	[76]
	7000(p+p)	NSD	∘		incl./2-arm	55k	30 MeV	[77]
	900,2360,7000(p+p)	NSD		∘	incl./2-arm		100 MeV	[78]
ALICE	900,2360(p+p)	INEL/NSD	∘	∘	incl./2-arm	150k,40k		[81]
ATLAS	900(p+p)	other	∘	∘	1-arm	456k	500 MeV	[82]

8.2.2. Comparison between experiments

Fig. 8.4 shows the comparison between the CMS NSD $dN_{\rm ch}/d\eta$ and previous experiments as well as the ALICE measurement. Our result on p+p collisions at $\sqrt{s} = 0.9$ TeV agrees with UA5 measurement (p+$\bar{\rm p}$) at the 1-3% level. This shows that the averaged charged hadron production is similar in p+p and p+$\bar{\rm p}$ collisions.

The ALICE collaboration also measured the inelastic and NSD p+p collisions at $\sqrt{s} =$ 0.9 and 2.36 TeV. The 0.9 TeV results are slightly higher than our results, while the two experiments are in good agreement at $\sqrt{s} = 2.36$ TeV. It has to be noted that different trigger conditions were used in the two ALICE measurements. Overall, the $dN_{\rm ch}/d\eta$ results from ALICE are consistent with our results at the 1-5% level and the differences are within the quoted systematic uncertainties.

We also compared the multiplicity distribution measurements with results from UA5 and ALICE, which are shown in Fig. 8.5. Generally the results are consistent between different experiments. The results from CMS and ALICE have a peak at $N_{ch} = 0$ which is different from the UA5 results. This is because of the different treatment of the diffractive component, i.e., CMS and ALICE used the PYTHIA definition for the correction, while UA5 used their own event generator. At $\sqrt{s} = 2.36$TeV, there are wavy structures at $N_{ch}(|\eta| < 1.0) \sim 30$ and $N_{ch}(|\eta| < 0.5) \sim 30$ which are due to statistical fluctuations. There is no wavy structure found in the 7 TeV result.

8.3. Discussions

8.3.1. $dN_{\rm ch}/d\eta$ structure and the central platau

The $dN_{\rm ch}/d\eta$ results from 0.9, 2.36 and 7.0 TeV shows a dip at the mid-rapidity ($|\eta| \sim 0$), which is similar to the behavior in lower energy measurements. The only $dN_{\rm ch}/d\eta$ measurements which show a flat pseudorapidity distribution without a dip are the results from UA5 at $\sqrt{s} = 53$ GeV. From a PYTHIA generator study (Fig. 1.2), it is found that the width of the $dN_{\rm ch}/dy$ is narrow such that the transformation from $dN_{\rm ch}/dy$ to $dN_{\rm ch}/d\eta$ accidentally flattened the distribution. The ratio between $dN/d\eta$ at $|\eta| = 2$ and 0 is similar to the previous measurements from 0.2 - 0.9 TeV, unlike the large dip seen in CDF results at $\sqrt{s} = 0.63$ and 1.8 TeV.

The ratio between $dN_{\rm ch}/d\eta$ at $|\eta| = 0$ and $|\eta| = 2$ is ~ 0.92 at $\sqrt{s} = 7.0$ TeV. The PYTHIA and PHOJET generator (See Sec. 1.3) studies give ratios between 0.82 and 0.84 if the $dN_{\rm ch}/dy$ is flat as a function of y. It implies that the $dN_{\rm ch}/dy$ at $|y| \sim 0$ is

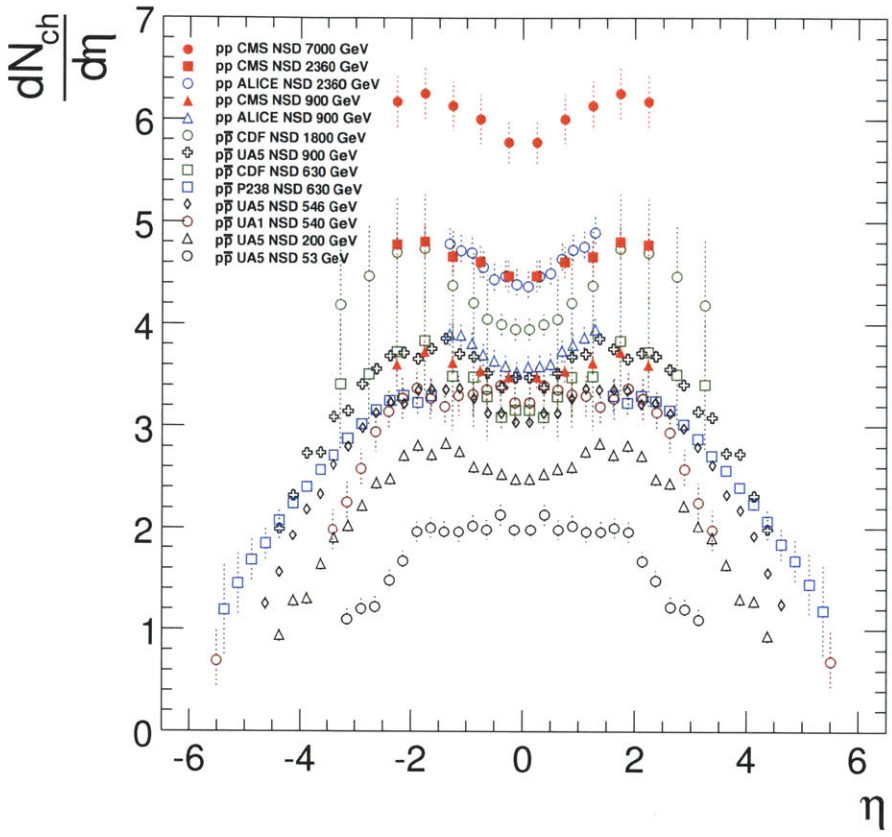

Figure 8.4.: $dN_{\mathrm{ch}}/d\eta$ distribution compared with lower energy data

roughly 10% higher than at $|y| \sim 2$. There is no evidence of a *flat platau* in dN_{ch}/dy in p+p collisions at $\sqrt{s} = 7$ TeV.

8.3.2. $\sqrt{s}$ dependence

From Fig. 8.4, it is evident that the $dN_{\mathrm{ch}}/d\eta$ in the CM frame is increasing in all pseudorapidity ranges as a function of centre-of-mass energy of the collision. Also the distribution becomes wider because of the increasing rapidity difference between the two protons.

Fig. 8.6 shows the $dN_{\mathrm{ch}}/d\eta\ |_{|\eta|\sim 0}$ as a function of $\sqrt{s}$. Clearly, Feynman scaling is violated. At 0.9 TeV, the p+p result from this thesis can be compared with UA5 measurement on p+$\bar{\mathrm{p}}$ collisions. At 2.36 and 7.0 TeV, the raising $dN_{\mathrm{ch}}/d\eta$ continues and deviates from the linear parameterization $a + b \ln s$ significantly. The second order

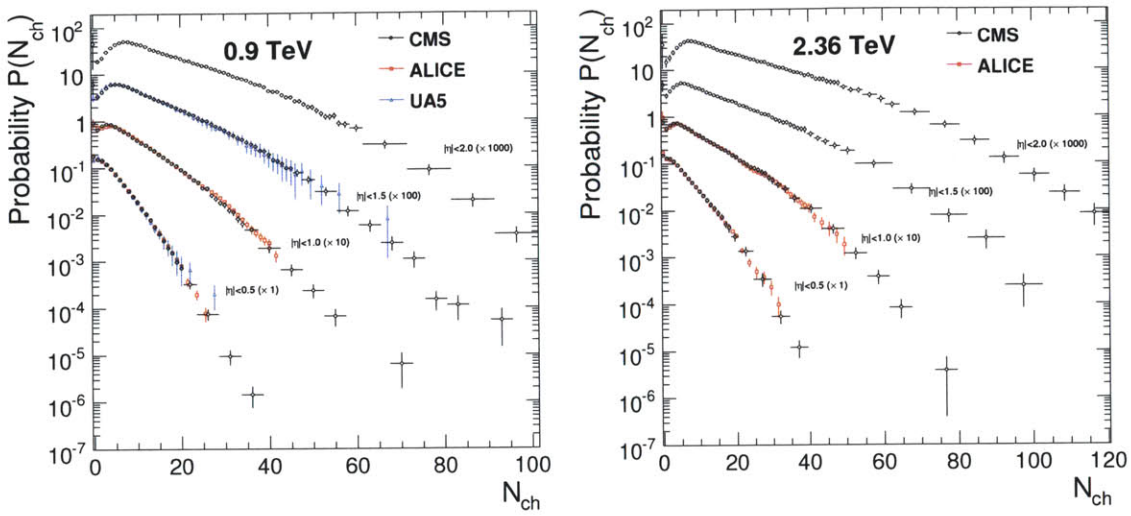

Figure 8.5.: The measured multiplicity distributions at $\sqrt{s} = 0.9$ and 2.36 TeV. The results are compared with the data from ALICE (pp) [81] and UA5 (p+$\bar{\text{p}}$) [44, 45] at the same energy.

parametrization $a + b \ln s + c \ln s^2$ describes the observed data reasonable well.

In the figure we also included the fit with $a \times s^{\frac{\lambda}{2}}$, which was motivated by the Saturation Model described in Sec. 1.4.6. More details can be found in [33].The dashed blue line is the result from a fit to all available NSD data, while the green solid line is from a fit to CMS NSD data only in order to check the validity of the extrapolation from high energies to lower energies. The blue line shows nice description of the experimental data and the extrapolated value at $\sqrt{s}$ =14 TeV is close to the result from second order $\ln s$. The green line which uses only CMS data also gives reasonable description to the low energy data, but starts to under-predict the $dN_{\text{ch}}/d\eta$ at $\sqrt{s} \sim 100$ GeV. The extracted λ value, which describes the energy dependence of the saturation scale $Q_{sat} \sim 1/x^{\lambda}$, is $\sim 0.23 - 0.25$ which is slightly lower than the value (0.288) determinated by the HERA data.

The successful description of the existing data from $a + b \ln s + c \ln s^2$ and Saturation model motivated parametrization also strengthen the extrapolation to p+p at $\sqrt{s} = 14$TeV ($dN_{\text{ch}}/d\eta \sim 6.5-6.8$) and interpolation at $\sqrt{s} = 2.76$ TeV ($dN_{\text{ch}}/d\eta \sim 4.54$) and $\sqrt{s} = 5.5$ TeV ($dN_{\text{ch}}/d\eta \sim 5.3$). The agreement between data and Saturation models also gives us more confidence to the prediction (extrapolation) of the $dN_{\text{ch}}/d\eta$ of Pb+Pb collisions at $\sqrt{s} = 2.76$ and 5.5 TeV.

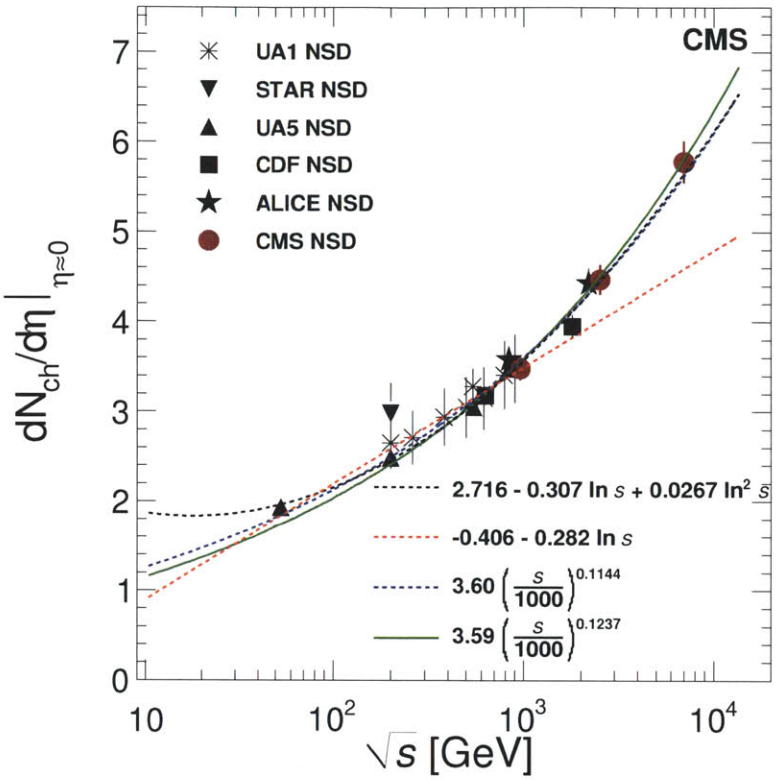

Figure 8.6.: $dN_{\mathrm{ch}}/d\eta\,|_{|\eta|\sim 0}$ as a function of $\sqrt{s}$.

8.3.3. Limiting fragmentation and extended longitudinal scaling

Fig. 8.7 shows the $dN_{\mathrm{ch}}/d\eta$ distributions plotted in the rest frame of one of the proton beams. Although the pseudorapidity range in this measurement is limited in $|\eta| < 2.5$ and can not probe the fragmentation region directly, it is clear that if the *Extended Longitudinal Scaling* still holds, the the limiting curve is not a straight line.

8.3.4. KNO violation

The results from 0.9 and 7 TeV are plotted in the KNO variables. Fig. 8.8 shows the comparison between the multiplicity distributions in three different pseudorapidity ranges from UA5 data at $\sqrt{s} = 0.2$ TeV [45] and CMS measurements. The KNO scaling seems to hold between the three energies if we limit ourselves in $|\eta| < 0.5$.

Strong KNO violation is observed in the pseudorapidity ranges of $|\eta| < 1.5$ and 2.0. With increasing energy, the peak of the distribution moves closer to 0 while the tail part

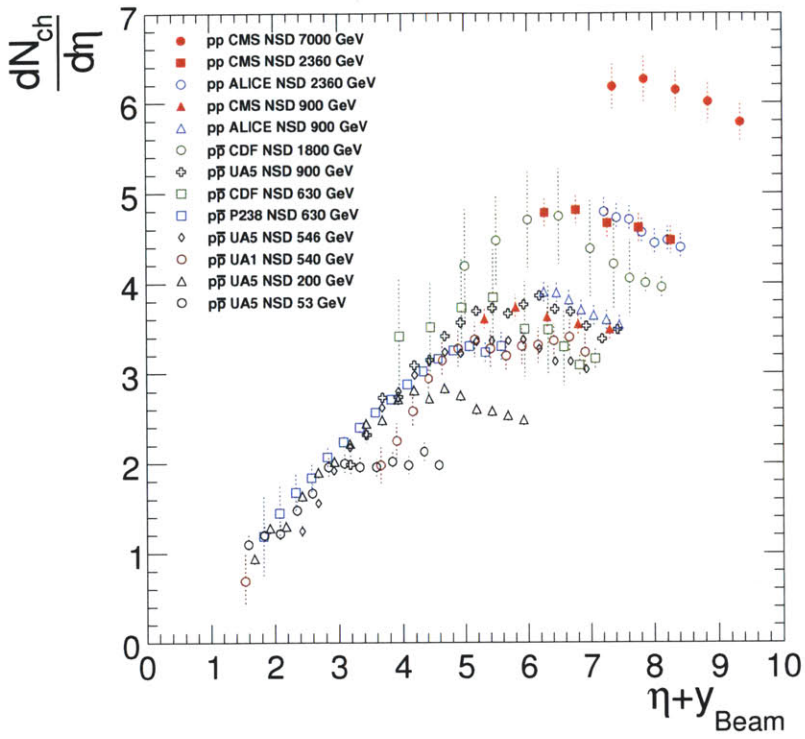

Figure 8.7.: $dN_{\mathrm{ch}}/d\eta$ distribution in the lab frame of the proton beam.

becomes wider. Also the distribution at 7 TeV shows a kink structure at $z \sim 1$. Apparently, the distribution at 7 TeV can not be described by two NBD fit. More NBD components may be needed to describe the extended tail, which may correspond to event classes with large number of multiple parton interactions. More detailed studies are needed to understand the extended tail.

It's not obvious why the physics near $|\eta| \sim 0$ should be different from $0.5 < |\eta| < 1.5$ in high energy p+p collisions. One possible explanation of the KNO scaling in $|\eta| < 0.5$ is the following: In case of limited acceptance range, the mean of the multiplicity distribution is closer to zero. There will be limited separation power to distinguish two NBDs from a single NBD such that it's hard to extract information about the dynamics from it. In the limit of zero acceptance, the multiplicity distribution will always look similar no matter how many event classes are present in the data.

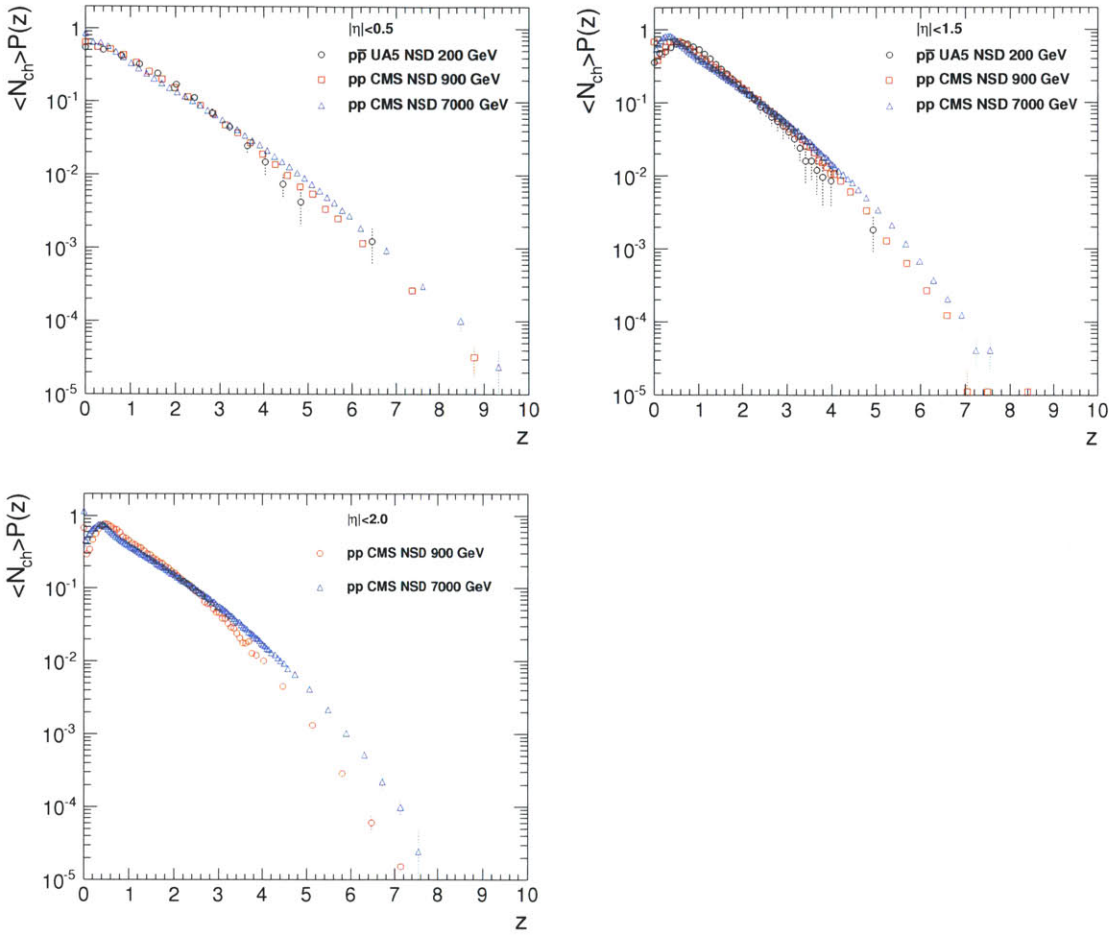

Figure 8.8.: The measured multiplicity distributions in KNO variable. The results from CMS are compared with the measurement from UA5 at $\sqrt{s}$ =0.2 TeV [45].

8.3.5. Comparison with event generators

Fig. 8.9 shows the comparison between the CMS measurements and the model predictions. A summary of the predictions (posdictions) from extrapolations, generators, and analytical models is given in Fig. 8.10. The extrapolation by a second order polynomial of $\log s$ gives good description of the data, while the extrapolation from $a + b \log s$ under-predict the pseudorapidity density and the ratio of the $dN_{\mathrm{ch}}/d\eta$ at $\sqrt{s} = 0.9$ and 7.0 TeV.

The commonly used PYTHIA D6T [10] and Perugia-0 [83] tunes, which was tuned with CDF data, predicted a much lower $dN_{\mathrm{ch}}/d\eta$ than the experimental data at $\sqrt{s} =$ 0.9, 2.36 and 7.0 TeV. The PYTHIA ATLAS tune [84] and PYTHIA8 (default) describe the

observed $dN_{ch}/d\eta$ and the ratio reasonably well from 0.9 to 7.0 TeV, but underestimate the $dN_{ch}/d\eta$ for p+p collisions at $\sqrt{s} < 0.9$ TeV. The $dN_{ch}/d\eta$ from PHOJET roughly increases linearly as a function of $logs$ which follows the raising of the $dN_{ch}/d\eta$ from 53 GeV to 0.9 TeV, but doesn't describe the rapid raising from 0.9 TeV to 7.0 TeV.

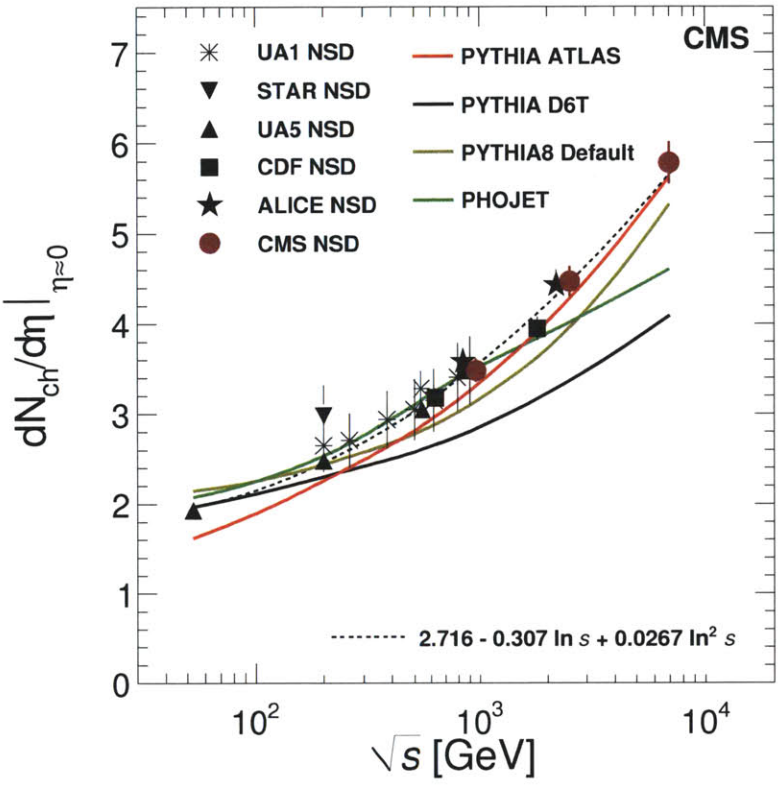

Figure 8.9.: $dN_{ch}/d\eta\,|_{|\eta|\sim 0}$ as a function of $\sqrt{s}$ compared to PYTHIA and PHOJET.

The multiplicity distribution in PYTHIA is controlled by the infrared cutoff (Q_0) of the parton-parton scattering cross sections and the shape of the proton. Those factors are closely related to the average number of the multiple parton interaction(MPI) and its fluctuations. Changing the parton distribution function from CTEQ5L to CTEQ6L has little effect on the multiplicity distribution.

To characterize the parton spatial distribution inside the proton, the PYTHIA Perugia-0 chooses a exponential form, while the D6T, ATLAS, Z2 and PYTHIA8 use a double-Gaussian. The parton spatial distribution in Perugia-0 and D6T features a narrower parton spatial distribution, while ATLAS and Z2 tune are wider. The infrared cutoff(Q_0) in Perugia-0 and D6T are higher and describe the multiplicity fluctuation measured in

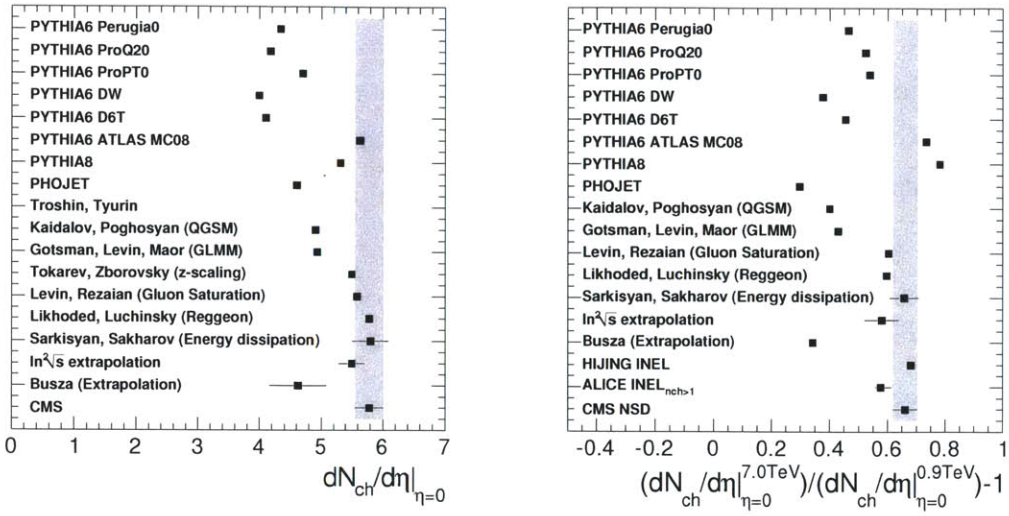

Figure 8.10.: (Left Panel) $dN_{\rm ch}/d\eta\ |_{|\eta|\sim 0}$ at $\sqrt{s}$ = 7.0 TeV compared to theoretical and phenomenological calculation. (Right Panel) The increase of $dN_{\rm ch}/d\eta$ from $\sqrt{s}$ = 0.9 TeV to 7.0 TeV compared to theoretical and phenomenological calculation [85–89].

CDF [10, 83], while the cutoff in ATLAS, Z2 and PYTHIA8 are lower which allows more MPIs.

Fig. 8.11 shows the multiplicity distributions at $\sqrt{s} = 7$ TeV compared with the predictions from PYTHIA and PHOJET generators. The PYTHIA D6T, Perugia-0, and PHOJET predicted smaller multiplicity fluctuation than data which is due to the higher infrared cutoff. The ATLAS tune over-estimates the multiplicity fluctuation. The PYTHIA8, which contains new diffraction model and lower infrared cutoff, describes the high multiplicity tail reasonably well. The Z2 tune, which is created after the 7 TeV measurement was made, also features a lower Q_0 and reproduce the observed multiplicity fluctuation. The PYTHIA D6T and Perugia-0 tunes also under-predict the $dN_{\rm ch}/d\eta$ by $\sim 40\%$ at $\sqrt{s} = 7$ TeV.

Fig. 8.12 shows the zoom-in of the multiplicity distributions at low N_{ch} region. The region contains contributions from the double-diffractive process. The PYTHIA6 tunes used a simple model for the diffractive processes which doesn't include central diffraction and hard diffractive events, while the PYTHIA8 generator used a improved diffraction model which is closer to the implementation in PHOJET. It is found that the D6T tune has the best agreement with the data. The predictions from PYTHIA8 and PHOJET are similar at low N_{ch} region, under-predict the $N_{ch} < 3$ region.

In summary, the observed multiplicity distributions feature large MPI fluctuation, which can be reproduced by lowering the infrared cutoff. However, those tunes (ie. ATLAS and PYTHIA8) usually under-estimate the $dN_{\mathrm{ch}}/d\eta$ of the p+p collision with $\sqrt{s} < 0.9$ TeV. More detailed tuning are needed to reproduce the distribution at low multiplicity region.

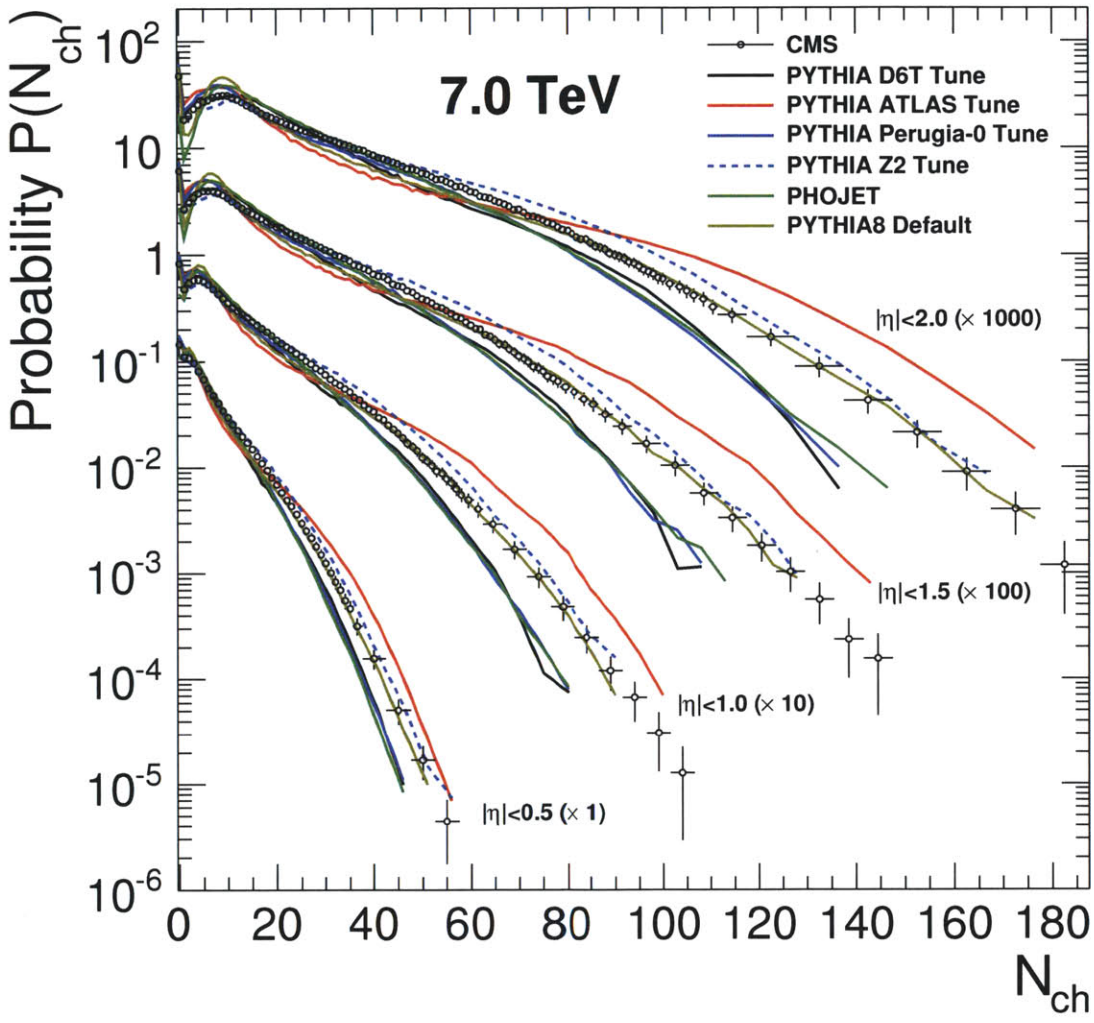

Figure 8.11.: The measured multiplicity distributions at $\sqrt{s} = 7$ TeV. The results are compared with predictions from different event generators and tunes.

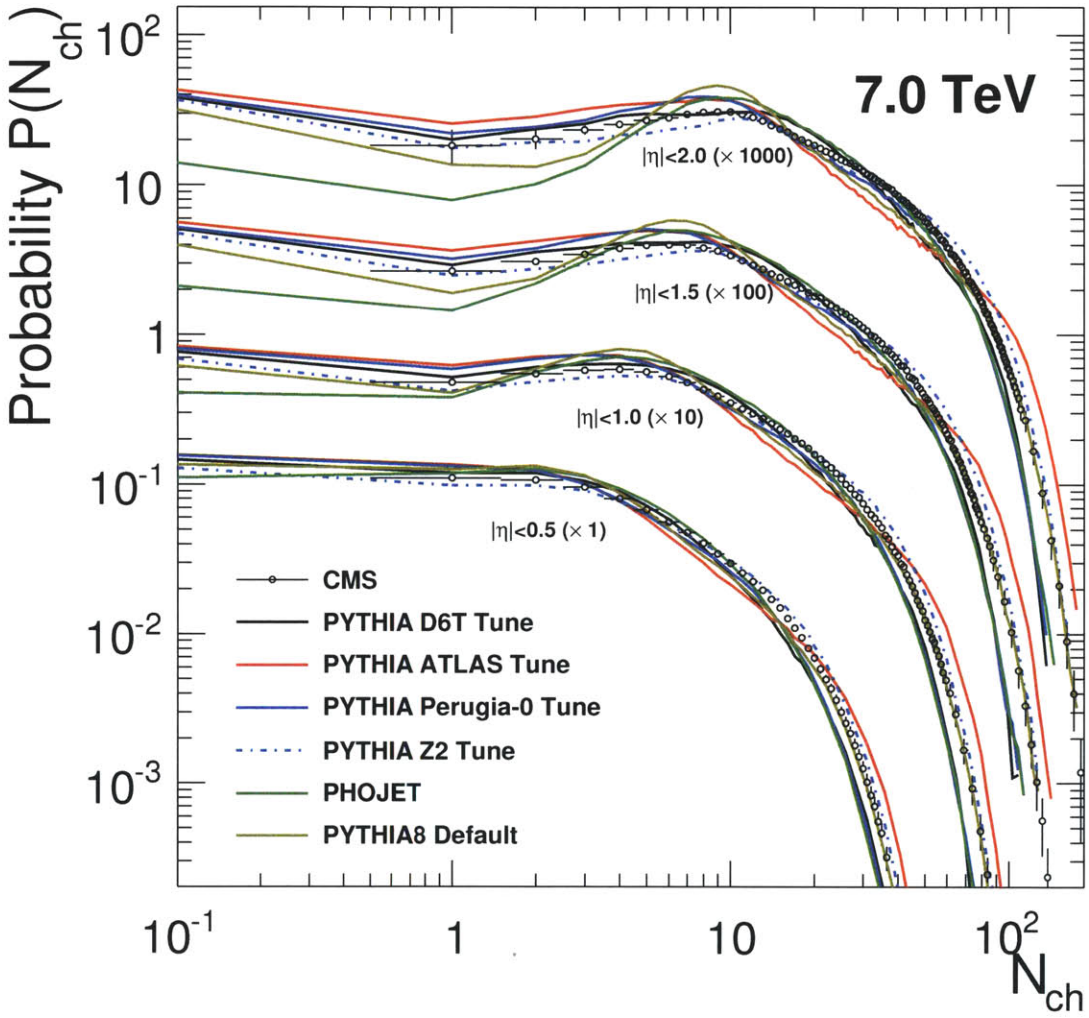

Figure 8.12.: The measured multiplicity distributions at $\sqrt{s} = 7$ TeV. The results are compared with predictions from different event generators and tunes (the x-axis in log scale).

9. Conclusion

In this thesis, the theoretical background of the particle production in p+p(p+$\bar{p}$) collisions is briefed to give the picture of the charged hadron multiplicity studies. In order to compare experimental results to theoretical descriptions, a complete data review on the pseudorapidity density and multiplicity distribution measurements in p+p(p+$\bar{p}$) collisions from fixed target and collider experiments is presented. Since the trigger strategies and detector capabilities affect the measurement significantly, experimental methods and analysis procedures from those experiments are summarized and compared. We measured the pseudorapidity densities and multiplicity distributions in p+p collisions at $\sqrt{s} = 0.9$, 2.36 and 7.0 TeV, which are the first results from the world highest energy p+p collisions. The analysis techniques developed and used in this thesis can be applied in the future studies of the p+p and Pb+Pb collisions.

The observed $dN_{\rm ch}/d\eta$ is different from Fermi-Landau's picture, which predicts a much narrower η distribution if the system is completely thermalized and particles are radiated isotropically. This suggests the interaction between the protons is weak.

The important features of the $dN_{\rm ch}/dy$ distributions predicted by Feynman are the flat platau near the mid-rapidity in the CM frame and scaling of $dN_{\rm ch}/dy$ at mid-rapidity in different collisional energies. The $dN_{\rm ch}/d\eta$ distributions measured in the three different energies shows a central-dip around $\eta \sim 0$. This structure is understood to be from the effect of the transformation from $dN_{\rm ch}/dy$ to $dN_{\rm ch}/d\eta$ from generator studies. However, the size of the dip is small which implies that the $dN_{\rm ch}/dy$ at $|y| \sim 0$ is actually 10% higher than $dN_{\rm ch}/dy$ at $|y| \sim 2$ (as discussed in Sec. 8.3.1). We conclude that there is no central platau in $dN_{\rm ch}/dy$. It is also evident that the $dN_{\rm ch}/dy$ ($dN_{\rm ch}/d\eta$)is growing as a function of $\sqrt{s}$, which violated the Feynman scaling.

The measurements are also compared with low energy data and plotted in the center-of-mass frame of the incoming proton. Although the measurement is limited by the detector acceptance, we can still extract some information about the *Extended Longitudinal Scaling*. If the extended longitudinal scaling still holds, the universal curve of this

scaling will no longer be a straight line.

The $dN_{ch}/d\eta$ at $|\eta| \sim 0$ is clearly rising faster than $\log s$ and also exceeds the expectations of the commonly used event generators. This implies that the current models of the multiple parton interaction are not accurate and tunings are needed in order to describe the experimental data. The rising $dN_{ch}/d\eta$ can be describe by an empirical parameterization $a + b\log s + c\log^2 s$ or $a \times s^{\lambda/2}$ which was motivated by the Saturation Model. The extracted λ value is close to the extracted value from the e+p deep inelastic scattering data from HERA and supports the picture of gluon saturation in the limit of low x. It will be very interesting to measure the $dN_{ch}/d\eta$ in p+p collisions at 14 TeV to check the validity of the Saturation Model.

The multiplicity distribution at the three energies are measured in different pseudorapidity intervals and compared with low energy measurements in KNO variables. The data shows a violation of KNO scaling in the pseudorapidity interval of $|\eta| < 1.5$. The observed data deviates from the Poisson distribution and can not be described by a single negative binomial distribution (NBD) or a two-NBD. This implies more independent event classes in the collisions. The distributions were compared with PYTHIA and PHOJET generator. The generator tunes with larger number of multiple parton interaction are closer to the observed large event-by-event fluctuation in data, but none of the tunes give a complete description of the multiplicity distributions. Detailed studies on the moments of the multiplicity distribution are ongoing in CMS and will be published soon. Those results will provide valuable inputs to the parameter tunings in the models. More studies on the high multiplicity tails may provide more information about the event class and the physics of collisions with large number of multiple parton interactions.

Since the increase of the multiplicity is faster than extrapolation from the existing models, empirical parameterizations are used to fit the rising $dN_{ch}/d\eta$, which provide reliable interpolations and extrapolations at $\sqrt{s} = 2.76$, 5.5 and 14 TeV. The extrapolated values will be compared with the measurements in Pb+Pb collisions at the LHC and help with the interpretation of the heavy ion collisions. The extrapolation to $\sqrt{s} = 14$ TeV also helps the preparation of the data taking. Furthermore, those measurements give constraints on the phenomenological models which is used to simulate the ultra-high energy cosmic showers [90].

Although it will be hard experimentally, measurement of $dN_{ch}/d\eta$ at forward region will be interesting to check the validity of the extended longitudinal scaling. It is also interesting to identify the charged particles and perform multiplicity measurement on

π, k and p to provide more detailed information of the hadron production.

A. Kinematic Variables

In this appendix the kinematic variables used in this thesis are introduced.

A.1. The CMS coordinate system

The origin of the CMS coordinate sytem is the CMS collision point. The x axis is horizontal, pointing south to the LHC center, the y axis is vertical pointing upwards and the z axis is horizontal poing west. The beam axis is parallel to the z axis.

A.2. Momentum

The momentum of a particle can be expressed as $\overrightarrow{p} = (p_x, p_y, p_z)$, where p_x, p_y and p_z are the momentum in the x, y, z direction.

The momentum can be divided into two components, the logitudinal momentum (p_L) and transverse momentum (p_T) which can be written as:

$$p_l = p_z \tag{A.1}$$

$$p_t = \sqrt{p_x^2 + p_y^2} \tag{A.2}$$

A.3. Four-momentum

A particle with momentum $\overrightarrow{p}$ and energy E can be expressed as

$$P = (\frac{E}{c}, p_x, p_y, p_z) \tag{A.3}$$

where P is a four-momentum in spacetime and c is the speed of light. Four-momentum is a Lorentz vector in the spacetime and follow the Lorentz transformations.

The particle's proper mass (m) can be expressed by

$$m^2 = \frac{|P|^2}{c^2} = E^2 - |\overrightarrow{p}|^2 \tag{A.4}$$

which is invariant under Lorentz transform.

A.4. Mandelstam variables

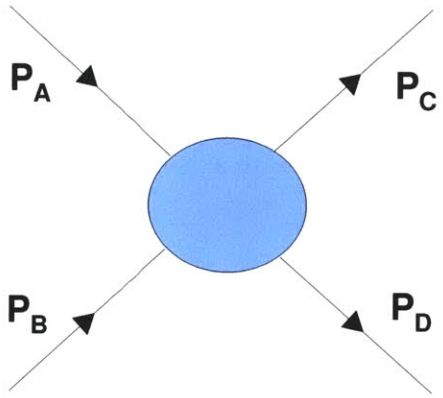

Figure A.1.: Two particles with incoming momenta P_A and P_B interact and then produce two particles with outgoing momenta P_C and P_D

In a $2 \rightarrow 2$ process, such as AB→CD shown in Fig. A.1, the Mandelstam variables are introduced by Stanley Mandelstam in 1958 in order to describe the scattering process. The variables s,t,u are defined by:

$$s = (P_A + P_B)^2 = (P_C + P_D)^2 \tag{A.5}$$

$$t = (P_A - P_C)^2 = (P_B - P_D)^2 \tag{A.6}$$

$$u = (P_A - P_D)^2 = (P_B - P_C)^2 \tag{A.7}$$

where $\sqrt{s}$ is usually known as the center-of-mass energy and $\sqrt{t}$ is known as the momentum-transfer.

A.5. Rapidity and Pseudorapidity

The rapidity y is an alternative to speed in relativity which is defined by:

$$y = \frac{1}{2} \ln \frac{E + p_l c}{E - p_l c} \tag{A.8}$$

In one-dimensional space, rapidities are additive. Experimentally, the energy of the unidentified particle is usually not measured. Alternatively, the pseudorapidity η is defined by:

$$\eta = \frac{1}{2} \ln \frac{p + p_l}{p - p_l} \tag{A.9}$$

$$= -\ln \left[\tan \left(\frac{\theta}{2} \right) \right] \tag{A.10}$$

which can be determined by the measurement of the particle trajectory and can be used to characterize the emission angle (θ, with respect to the beam pipe) of the particle. In the relativistic limit, pseudorapidity is approximately the same as rapidity.

B. Negative binomial distribution

The negative binomial distribution (NBD) is a discrete distribution of the number of fails n in a sequence of independent Bernoulli trials before a specified number k success occurs. For instance, the number of exams that a student can fail before he passes.

If the probability of success is p in each Bernoulli trails, the probability density function of the negative binomial distribution is:

$$f(n) = \begin{pmatrix} k+n-1 \\ k-1 \end{pmatrix} p^n (1-p)^k \tag{B.1}$$

$$= \frac{\Gamma(k+n)}{\Gamma(n+1)\Gamma(k)} p^k (1-p)^n \tag{B.2}$$

In the description of the multiplicity distribution, the NBD is expressed in the two independent parameters: The average multiplicity ($\bar{n} = k/p - 1$) of the distribution and a parameter k which describe the shape of the distribution. Replacing p by $k/(\bar{n}+1)$, the functional form becomes:

$$f(n) = \frac{\Gamma(k+n)}{\Gamma(n+1)\Gamma(k)} \left(\frac{\bar{n}}{k}\right)^n \left(1+\frac{\bar{n}}{k}\right)^{-n-k} \tag{B.3}$$

If k is a negative integer, the distribution become a binomial distribution. In the limit $k \to \infty$, the negative binomial distirbution reduces to the Poisson distribution.

C. Pomeron and Reggeon

In this appendix, the optical theorem and reggeon theory are briefly discussed in order to provide necessary theoretical background to the inclusive cross-section of the proton proton collisions.

C.1. S-Matrix and optical theorem

Before the development of QCD, the scattering of hadrons involved in the strong interaction were studied by S-matrix approach. Since the strength of the strong force is much greater than the other forces, the electromagnetic and weak interactions are neglected. In a $2 \rightarrow 2$ scattering, for instance, $A+B \rightarrow C+D$, the *in*-state $|a>$ $(t \rightarrow -\infty)$ and *out*-state $<b|$ $(t \rightarrow +\infty)$ are assumed to be free particle states The S-matrix is defined as

$$S_{ab} = < a|b > \tag{C.1}$$

The scattering amplitude $A_{ab}(s,t)$ from $|a>$ to $|b>$ is related to the S-matrix by

$$S_{ab}(s,t) = \delta_{ab} + i(2\pi)^4 \delta^4 \left(\sum_i p_a - \sum_f p_b \right) A_{ab}(s,t) \tag{C.2}$$

The δ function ensure the conservation of 4-momentum. From the unitarity of the S-matrix, one get

$$2\mathrm{Im}A_{ab}(s,t) = (2\pi)^4 \delta^4 \left(\sum_a p_a - \sum_b p_b \right) \sum_c A_{ac}(s,t) A^{\dagger}_{cb}(s,t) \tag{C.3}$$

where c is an *intermediate* state. The Eq. C.3 relate the imaginary part of the amplitude $a \rightarrow b$ to the sum of all amplitudes of $a \rightarrow c$ and $c \rightarrow b$. This is known as Cutkosky rules. One important special case of the Cutkosky rules is the *optical theorem.* If the initial

state and the final state are the same ($a \to a$), Eq. C.3 becomes:

$$2\mathrm{Im}A_{aa}(s,0) = (2\pi)^4 \delta^4 \left(\sum_a p_a - \sum_f p_f \right) \sum_n |A_{a\to n}(s,0)|^2 = F\sigma_{tot}(s) \tag{C.4}$$

where F is the flux factor. The optical theorem relates the imaginary part of the amplitude to the total cross-section. In the limit of high energy scattering ($\sqrt{s} >> m$), F is shown to be $\sim 2s$. The Eq. C.4 becomes

$$\sigma_{tot}(s) \sim \frac{2\mathrm{Im}A_{aa}(s,0)}{2s} \tag{C.5}$$

C.2. Reggeon and Pomeron

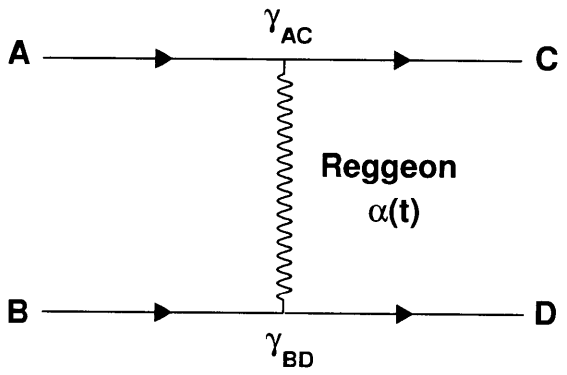

Figure C.1.: Diagram of $A + B \to C + D$ in the language of Reggeon theory.

Regge theory was based by the S-matrix approach and partial wave expansion. The amplitudes are expressed as combinations of partial waves with complex angular momentum (J). The final scattering amplitudes in the $s \to \infty$ limit can be related to the singularities in the J-plane ($\alpha(t)$), which is called *Regge-poles.*

In the language of Regge theory, the scattering amplitude of the reaction $A+B \to C+D$ can be viewed as the exchange in the t-channel of an object with angular momentum equal to $\alpha(t)$ with couplings of $\gamma(t)$. This object is call a *Reggeon.* Fig. C.1 shows

a Reggeon exchange diagram. The scattering amplitude is expressed as:

$$A(s,t) = \frac{\eta + e^{-i\pi\alpha(t)}}{2\sin\pi\alpha(t)} \frac{\gamma_{AC}(t)\gamma_{BD}(t)}{\Gamma(\alpha(t))} s^{\alpha(t)} \tag{C.6}$$

where η is -1 or -1. When $\alpha(t)$ takes an integer value for some value of t, then the amplitude in Eq. C.6 has a pole. For positive integers (J_i), the corresponse to the exchange of a resonance particle (m_i) with integer spin. In this case, $\alpha(m_i^2) = J_i$. For negative integers, it is cancelled by the factor $1/\Gamma(\alpha(t))$ which is vanishing.

In 1961, Chew and Frautschi plotted the square of mass of the mesons as a function of the J_i. The data points lie in a straight line. This means that the *Reggeon trajectories* $\alpha(t)$ a linear function of t:

$$\alpha(t) = \alpha_0 + \alpha' t \tag{C.7}$$

If we insert the trajectories $\alpha(t)$ into Eq. C.6, the differential cross in the large s limit is given by:

$$\frac{d\sigma(s,t)}{dt} \propto s^{2\alpha_0 - 2\alpha' t - 2} \tag{C.8}$$

From the optical theorem (Eq. C.5), the total cross-section σ_{tot} in the large s limit can be written as:

$$\sigma_{tot}(s) \propto s^{(\alpha_0 - 1)} \tag{C.9}$$

In the Regge theory, the p+p collisions are exchanges of Reggeon trajectories, or the mesons on the trajectories and the total cross-section is an exponential function of s. From the linear fit to the Chew-Frautschi diagrams, the α_0 is found to be smaller than 1 and the total cross-section is expected to vanish in the limit of $s \to \infty$. Indeed, the total cross-section of the p+p collision is found to be falling at the region $\sqrt{s} < 20$ GeV.

However, it was found that the p+p total cross-section reach a minimum around $\sqrt{s} =$ 20 GeV and rise slowly as s increases. We can attribute this rise to the exchange of a single Regge pole with α_0>1. This trajectory is called the Pomeron, which carries the quantum number of the vacuum. The functional form [91] of the total cross-section is

$$\sigma = c_1 s^{(\alpha_{R0} - 1)} + c_2 s^{(\alpha_{P0} - 1)} \tag{C.10}$$

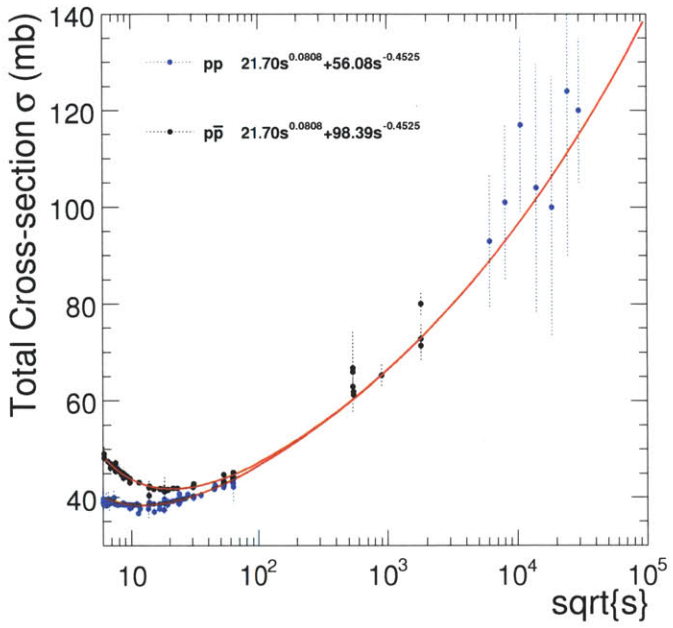

Figure C.2.: The total cross-sections of p+p and p+$\bar{p}$ collisions. The fits shown in the plot are taken from [91].

The two terms in Eq. C.10 characterize the contribution from the Reggeon and Pomeron. Fig. C.2 shows the rising total cross-section of the p+p (p+$\bar{p}$) collision and the quality of the fits of Eq. C.10 [91].

D. BSC MIP Efficiency Measurement

The siganl from BSC scintillation counter served as one of the most important minimum-bias trigger of the CMS experiment. It is important to understand the MIP detection efficiency of the BSC. In this appendix, the method which is used to commission the BSC scintillation counter is briefed. The averaged MIP efficiency of the BSC segments is found to be 95.7%. This study also provide important input to the MC simulation tuning.

D.1. Circulating beam sample

The efficiency of the BSC scintillator segments was measured based on the measurement of the MIP peak in the scintillators. The measurement was done on the 26th and 29th of March, with circulating proton beams, just before the first collision data taking on 30th of March, 2010. The BSC has a standalone readout based on CAEN VME V1721 8-bit digitizers (called ADC-s in this section). These can measure the pulse shape in 2 ns steps. All the ADC's are calibrated with a known pulse shape, so the ADC counts and the voltage is related to each other with $< 1\%$ precision. The ADC's use 6dB attenuators as well, and those are also calibrated using pulse generators and measuring them with oscilloscope, also with $< 1\%$ precision.

In this measurement, self-triggering was used with 5 ADC unit threshold. The pedestal of the readout signal is estimated event by event. After pedestal subtraction, the pulse (-to pedestal) height was measured for each pulse. Part of these pulses are from MIPs crossing the scintillator layer, while other part is from noise (including ambient gamma radiation and cosmic rays).

To eliminate the noise contribution, a correlation method is used to estimation the background shape. The ADC's have the BPTX signal connected, so events can be selected off-line where BPTX was firing, giving the MIP distribution. The random coincidences from noise were subtracted carefully (small contribution), using off-time signals with respect to the BPTX signal. The result of the MIP measurement for a typical seg-

ment is plotted in Fig. D.1.

The final, subtracted MIP peak was fitted with a convolution of the Landau and Gaussian distribution, see Fig. D.1, and the relative fraction of its area above the hardware discriminator threshold set for triggering, which was 31 ± 1 mV (that was converted to ADC units for each channel separately using the calibration, and the fit function was integrated above this ADC value corresponding to the threshold).

D.2. MIP efficiency

The resulting segment efficiencies are given in Table D.1. The measured MIP efficiency were included in the Monte Carlo simulation to estimate the impact of the MIP inefficiency. The difference of the reconstructed $dN/d\eta$ between the Monte Carlo with 95% and 100% MIP efficiencies is found to be smaller than 1%.

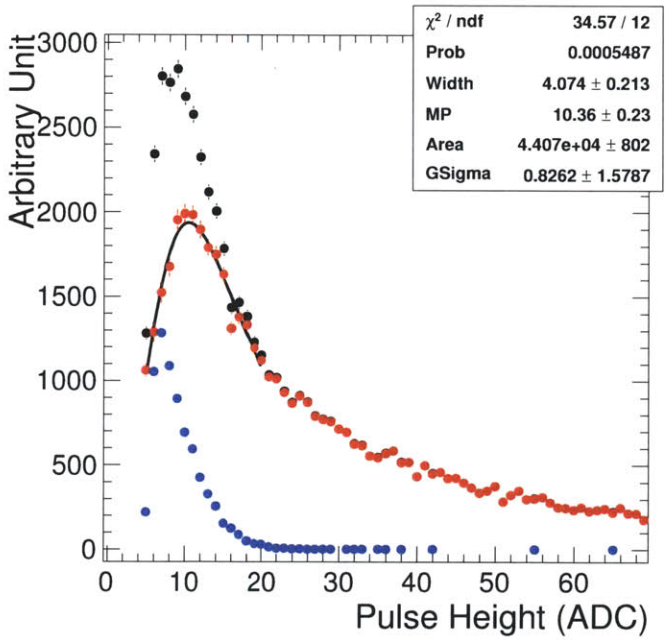

Figure D.1.: MIP peak in the BSC. Black: all signals, blue: background (out-of-time), red: subtracted spectrum, line: Landau*Gaussian fit.

Table D.1.: Measured efficiencies of the BSC segments. Mean: 95.7%. + and − stands for positive and negative z side from the IP. D and P mean disk (inner ring) and paddles (outer segments).

segment	eff. (%)	segment	eff. (%)	segment	eff. (%)	segment	eff. (%)
+D1	98	-D1	92	+P1	92	-P1	90
+D2	98	-D2	98	+P2	92	-P2	96
+D3	98	-D3	95	+P3	98	-P3	97
+D4	96	-D4	94	+P4	96	-P4	96
+D5	99	-D5	92	+P5	94	-P5	91
+D6	98	-D6	99	+P6	92	-P6	98
+D7	99	-D7	96	+P7	95	-P7	94
+D8	98	-D8	96	+P8	98	-P8	98

E. List of Acronyms

Facilities:

CERN European Organization for Nuclear Research – *Conseil Européen pour la Recherche Nucléaire* (http://public.web.cern.ch/public/)

HERA Hadron Elektron Ring Anlage

ISR Intersecting Storage Rings

LHC Large Hadron Collider (http://lhc.web.cern.ch/lhc/)

RHIC Relativistic Heavy Ion Collider (http://www.bnl.gov/RHIC/)

SPS Super Proton Synchrotron (http://ab-dep-op-sps.web.cern.ch/ab-dep-op-sps/)

Physics Terminology:

KNO Koba-Nielsen-Olesen

NLO Next-to-leading Order

NNLO Next-to-next-to-leading Order

pQCD perturbative Quantum Chromodynamics (QCD)

QCD Quantum Chromodynamics

QED Quantum Electrodynamics

QGP Quark Gluon Plasma

Hardware:

ADC Analog-to-Digital Converter

DAQ Data Acquisition

Experimental Terminology:

MC Monte Carlo

MinBias Minimum Bias

MIP Minimum Ionizing Particle

NSD Non-Sigle-Diffractive

RMS Root Mean Square

Bibliography

[1] Lyndon Evans, (ed.) and Philip Bryant, (ed.). LHC Machine. *JINST*, 3:S08001, 2008. doi: 10.1088/1748-0221/3/08/S08001.

[2] The TriDAS Project Technical Design Report, Volume 1: The Trigger Systems. *CERN-LHCC*, 2000-038, 2000.

[3] B. B. Back et al. Charged-particle multiplicity near midrapidity in central $au + au$ collisions at $\sqrt{s_{NN}} = 56$ and $130 gev$. *Phys. Rev. Lett.*, 85(15):3100–3104, Oct 2000. doi: 10.1103/PhysRevLett.85.3100.

[4] Fritz W. Bopp, R. Engel, and J. Ranft. Rapidity gaps and the PHOJET Monte Carlo, version 1.12-35. 1998.

[5] R. Engel, J. Ranft, and S. Roesler. Hard diffraction in hadron-hadron interactions and in photoproduction. *Phys. Rev.*, D52:1459, 1995. doi: 10.1103/PhysRevD.52.1459.

[6] Torbjorn Sjöstrand, Stephen Mrenna, and Peter Skands. PYTHIA 6.4 Physics and Manual; v6.420, tune ATLAS. *JHEP*, 05:026, 2006.

[7] K. Namura et al. Review of Particle Physics . *J. Phys.*, G37:075021, 2010. doi: 10.1088/0954-3899/37/7A/075021.

[8] R. W. McAllister and R. Hofstadter. Elastic scattering of 188-mev electrons from the proton and the alpha particle. *Phys. Rev.*, 102(3):851–856, May 1956. doi: 10.1103/PhysRev.102.851.

[9] E. D. Bloom, D. H. Coward, H. DeStaebler, J. Drees, G. Miller, L. W. Mo, R. E. Taylor, M. Breidenbach, J. I. Friedman, G. C. Hartmann, and H. W. Kendall. High-energy inelastic $e - p$ scattering at 6° and 10°. *Phys. Rev. Lett.*, 23(16):930–934, Oct 1969. doi: 10.1103/PhysRevLett.23.930.

[10] Paolo Bartalini, (ed.) et al. Proceedings of the First International Workshop on Multiple Partonic Interactions at the LHC (MPI08). 2010.

[11] M. L. Good and W. D. Walker. Diffraction dissociation of beam particles. *Phys. Rev.*, 120(5):1857–1860, Dec 1960. doi: 10.1103/PhysRev.120.1857.

[12] Enrico Fermi. High-energy nuclear events. *Prog. Theor. Phys.*, 5:570–583, 1950.

[13] L. D. Landau. On the multiparticle production in high-energy collisions. *Izv. Akad. Nauk SSSR Ser. Fiz.*, 17:51–64, 1953.

[14] Richard P. Feynman. Very high-energy collisions of hadrons. *Phys. Rev. Lett.*, 23: 1415–1417, 1969. doi: 10.1103/PhysRevLett.23.1415.

[15] C. Halliwell, J. E. Elias, W. Busza, D. Luckey, L. Votta, and C. Young. Energy dependence of the pseudorapidity distributions in proton-nucleus collisions between 50 and 200 gev/c. *Phys. Rev. Lett.*, 39(24):1499–1502, Dec 1977. doi: 10.1103/PhysRevLett.39.1499.

[16] I. Otterlund et al. Nuclear interactions of 400 gev protons in emulsion. *Nuclear Physics B*, 142(4):445 – 462, 1978. ISSN 0550-3213. doi: DOI:10.1016/0550-3213(78)90223-7. URL http://www.sciencedirect.com/science/article/B6TVC-4719JKC-RF/2/d6994f55f04776f83f3f57bb2627c4cc.

[17] B.B. Back et al. The phobos perspective on discoveries at rhic. *Nuclear Physics A*, 757(1-2):28 – 101, 2005. ISSN 0375-9474. doi: DOI:10.1016/j.nuclphysa.2005.03.084. URL http://www.sciencedirect.com/science/article/B6TVB-4FY28CF-1/2/9b988946dbeeb263171a46b2044b94dc. First Three Years of Operation of RHIC.

[18] Wit Busza. Extended longitudinal scaling: Direct evidence of saturation. *Nuclear Physics A*, In Press, Corrected Proof:–, 2011. ISSN 0375-9474. doi: DOI:10.1016/j.nuclphysa.2010.12.015. URL http://www.sciencedirect.com/science/article/B6TVB-51XH97B-1/2/a98e0efc7c091b2c7c378998da360098.

[19] Z. Koba, Holger Bech Nielsen, and P. Olesen. Scaling of multiplicity distributions in high-energy hadron collisions. *Nucl. Phys.*, B40:317–334, 1972. doi: 10.1016/0550-3213(72)90551-2.

[20] C.P. Ward, D.R. Ward, R.E. Ansorge, J.R. Carter, W.W. Neal e, J.G. Rushbrooke, B.Y. Oh, M. Pratap, G.A. Smith, J. Whitmore a nd R. Raja, and L. Voyvodic. General features of charged particle production in p interactions at 10 0 gev/c. *Nuclear Physics B*, 153:299 – 333, 1979. ISSN 0550-3213. doi: DOI:10.1016/0550-3213(79)90603-5. URL http://www.sciencedirect.com/science/article/B6TVC-4968W15-J/2/7be45437a4c0add32829141fd4e41551.

[21] Charged Particle Multiplicity Distributions in pp Collisions at ISR Energies. *Nucl. Phys.*, B129:365, 1977. doi: 10.1016/0550-3213(77)90122-5.

[22] A. Breakstone et al. Charged Multiplicity Distribution in p p Interactions at ISR Energies. *Phys. Rev.*, D30:528, 1984. doi: 10.1103/PhysRevD.30.528.

[23] G. J. Alner et al. UA5: A general study of proton-antiproton physics at $\sqrt{s} = 546$-GeV. *Phys. Rept.*, 154:247–383, 1987. doi: 10.1016/0370-1573(87)90130-X.

[24] G. J. Alner et al. Scaling of Pseudorapidity Distributions at c.m. Energies Up to 0.9-TeV. *Z. Phys.*, C33:1–6, 1986. doi: 10.1007/BF01410446.

[25] Alberto Giovannini and L. Van Hove. Negative binomial multiplicity distributions in high energy hadron collisions. *Z. Phys.*, C30:391, 1986. doi: 10.1007/BF01557602.

[26] Alberto Giovannini and Roberto Ugoccioni. On signals of new physics in global event properties in pp collisions in the TeV energy domain. *Phys. Rev.*, D68:034009, 2003. doi: 10.1103/PhysRevD.68.034009.

[27] Darin E. Acosta et al. Soft and hard interactions in $p\bar{p}$ collisions at $\sqrt{s} = 1800$-GeV and 630-GeV. *Phys. Rev.*, D65:072005, 2002. doi: 10.1103/PhysRevD.65.072005.

[28] Dmitri Kharzeev and Eugene Levin. Manifestations of high density QCD in the first RHIC data. *Phys. Lett.*, B523:79–87, 2001. doi: 10.1016/S0370-2693(01)01309-0.

[29] Nestor Armesto, Carlos A. Salgado, and Urs Achim Wiedemann. Relating high-energy lepton hadron, proton nucleus and nucleus nucleus collisions through geometric scaling. *Phys. Rev. Lett.*, 94:022002, 2005. doi: 10.1103/PhysRevLett.94.022002.

[30] Krzysztof J. Golec-Biernat and M. Wusthoff. Saturation effects in deep inelastic scattering at low Q**2 and its implications on diffraction. *Phys. Rev.*, D59:014017, 1998. doi: 10.1103/PhysRevD.59.014017.

[31] Krzysztof J. Golec-Biernat and M. Wusthoff. Saturation in diffractive deep inelastic scattering. *Phys. Rev.*, D60:114023, 1999. doi: 10.1103/PhysRevD.60.114023.

[32] A. M. Stasto, Krzysztof J. Golec-Biernat, and J. Kwiecinski. Geometric scaling for the total gamma* p cross-section in the low x region. *Phys. Rev. Lett.*, 86:596–599, 2001. doi: 10.1103/PhysRevLett.86.596.

[33] Larry McLerran and Michal Praszalowicz. Saturation and Scaling of Multiplicity, Mean p_T and p_T Distributions from 200 GeV < sqrts < 7 TeV - Addendum. *Acta Phys. Polon.*, B42:99, 2011. doi: 10.5506/APhysPolB.42.99.

[34] Gerhard A. Schuler and Torbjorn Sjostrand. Towards a complete description of high-energy photoproduction. *Nucl. Phys.*, B407:539–605, 1993. doi: 10.1016/0550-3213(93)90091-3.

[35] G. J. Alner et al. Scaling Violation Favoring High Multiplicity Events at 540-GeV CMS Energy. *Phys. Lett.*, B138:304, 1984. doi: 10.1016/0370-2693(84)91666-6.

[36] V. N. Gribov and L. N. Lipatov. Deep inelastic e p scattering in perturbation theory. *Sov. J. Nucl. Phys.*, 15:438–450, 1972.

[37] Guido Altarelli and G. Parisi. Asymptotic Freedom in Parton Language. *Nucl. Phys.*, B126:298, 1977. doi: 10.1016/0550-3213(77)90384-4.

[38] Bo Andersson, G. Gustafson, G. Ingelman, and T. Sjostrand. Parton Fragmentation and String Dynamics. *Phys. Rept.*, 97:31–145, 1983. doi: 10.1016/0370-1573(83)90080-7.

[39] A. Capella, U. Sukhatme, C-I Tan, and J. Tran Thanh Van. Dual parton model. *Phys. Rept.*, 236:225–329, 1994. doi: 10.1016/0370-1573(94)90064-7.

[40] C. M. G. Lattes, Y. Fujimoto, and S. Hasegawa. Hadronic interactions of high energy cosmic-ray observed by emulsion chambers. *Physics Reports*, 65(3): 151 – 229, 1980. ISSN 0370-1573. doi: DOI:10.1016/0370-1573(80)90165-9. URL http://www.sciencedirect.com/science/article/B6TVP-46TY0GN-N/2/baf60d087fb5aa47f39282729c7870a3.

[41] C. Albajar et al. A Study of the General Characteristics of $p\bar{p}$ Collisions at $\sqrt{s} = 0.2$-TeV to 0.9-TeV. *Nucl. Phys.*, B335:261, 1990. doi: 10.1016/0550-3213(90)90493-W.

[42] G. Arnison et al. CHARGED PARTICLE MULTIPLICITY DISTRIBUTIONS IN PROTON ANTI-PROTON COLLISIONS AT 540-GeV CENTER-OF-MASS ENERGY. *Phys. Lett.*, B123:108, 1983. doi: 10.1016/0370-2693(83)90969-3.

[43] K. Alpgard et al. COMPARISON OF p anti-p and p p INTERACTIONS AT s**(1/2) = 53-GeV. *Phys. Lett.*, B112:183, 1982. doi: 10.1016/0370-2693(82)90325-2.

[44] G. J. Alner et al. Scaling Violations in Multiplicity Distributions at 200- GeV and 900-GeV. *Phys. Lett.*, B167:476–480, 1986. doi: 10.1016/0370-2693(86)91304-3.

[45] R. E. Ansorge et al. Charged Particle Multiplicity Distributions at 200-GeV and 900-GeV Center-Of-Mass Energy. *Z. Phys.*, C43:357, 1989. doi: 10.1007/BF01506531.

[46] R. Harr et al. Pseudorapidity distribution of charged particles in $\bar{p}p$ collisions at $\sqrt{s}$ = 630-GeV. *Phys. Lett.*, B401:176–180, 1997. doi: 10.1016/S0370-2693(97)00385-7.

[47] Pseudorapidity distributions of charged particles produced in $p\bar{p}$ interactions at $\sqrt{s} = 630$ GeV and 1800 GeV. *Phys. Rev.*, D41:2330, 1990. doi: 10.1103/PhysRevD.41.2330.

[48] F. Rimondi. Multiplicity distributions in $\bar{p}p$ interactions at $\sqrt{s}$ = 1800-GeV. To be published in the proceedings of 23rd International Symposium on Ultra-High Energy Multiparticle Phenomena, Aspen, CO, 12-17 Sep 1993.

[49] T. Alexopoulos et al. The role of double parton collisions in soft hadron interactions. *Phys. Lett.*, B435:453–457, 1998. doi: 10.1016/S0370-2693(98)00921-6.

[50] J. Whitmore. Experimental Results on Strong Interactions in the NAL Hydrogen Bubble Chamber. *Phys. Rept.*, 10:273, 1974. doi: 10.1016/0370-1573(74)90046-5.

[51] Clark S. Lindsey et al. Results from E735 at the tevatron $p\bar{p}$ collider with $\sqrt{s}$ = 1.8-TeV. *Nucl. Phys.*, A544:343–356, 1992. doi: 10.1016/0375-9474(92)90585-8.

[52] Joseph F. Sagerer. Proton-Proton multiplicity distributions at the relativistic heavy ion collider. 2008.

[53] Systematic measurements of identified particle spectra in pp, d-Au and Au-Au collisions at the STAR detector. *Phys. Rev.*, C79:034909, 2009. doi: 10.1103/PhysRevC.79.034909.

[54] CMS, the Compact Muon Solenoid: Technical proposal. . CERN-LHCC-94-38.

[55] W. W. Armstrong et al. ATLAS: Technical proposal for a general-purpose p p experiment at the Large Hadron Collider at CERN. CERN-LHCC-94-43.

[56] ALICE: Technical proposal for a large ion collider experiment at the CERN LHC. CERN-LHCC-95-71.

[57] S. Amato et al. LHCb technical proposal. CERN-LHCC-98-04.

[58] V. Berardi et al. TOTEM: Technical design report. Total cross section, elastic scattering and diffraction dissociation at the Large Hadron Collider at CERN. CERN-LHCC-2004-002.

[59] O. Adriani et al. Technnical proposal for the CERN LHCf experiment: Measurement of photons and neutral pions in the very forward region of LHC. CERN-LHCC-2005-032.

[60] R. Adolphi et al. The CMS experiment at the CERN LHC. *JINST*, 3:S08004, 2008. doi: 10.1088/1748-0221/3/08/S08004.

[61] Alan James Bell. Design and Construction of the Beam Scintillation Counter for CMS. Master's thesis, University of Canterbury, Christchurch, New Zealand, 2008.

[62] Thomas Aumeyr. Beam Phase and Intensity Monitoring for the Compact Muon Solenoid Experiment. Master's thesis, Vienna University of Technology, Austria, 2008.

[63] CMS Physics TDR: Volume I, Detector Performance and Software. *CERN-LHCC*, 2006-001, 2006.

[64] G. Acquistapace et al. CMS, the magnet project: Technical design report. CERN-LHCC-97-10, CMS TDR1.

[65] CMS, tracker technical design report. . CERN-LHCC-98-06, CMS TDR5, Addendum CERN/LHCC 2000-016.

[66] Commissioning and Performance of the CMS Pixel Tracker with Cosmic Ray Muons. *to be published in JINST*, 2009.

[67] Alignment of the cms silicon tracker during commissioning with cosmic rays. *to appear in JINST*, 2009.

[68] CMS, the Compact Muon Solenoid. Muon technical design report. . CERN-LHCC-97-32, CMS TDR3.

[69] CMS: The electromagnetic calorimeter. Technical design report. . CERN-LHCC-97-33, CMS TDR4, Addendum CERN/LHCC 2002-027.

[70] CMS: The hadron calorimeter technical design report. . CERN-LHCC-97-31, CMS TDR2.

[71] L. Agostino, G. Bauer, B. Beccati, U. Behrens, J. Berryhil, K. Biery, T. Bose, A. Brett, J. Branson, E. Cano, H. Cheung, M. Ciganek, S. Cittolin, J. A. Coarasa, B. Dahmes, C. Deldicque, E. Dusinberre, S. Erhan, D. Gigi, F. Glege, R. Gomez-Reino, J. Gutleber, D. Hatton, J. Laurens, C. Loizides, F. Ma, F. Meijers, E. Meschi, A. Meyer, R. K. Mommsen, R. Moser, V. O'Dell, A. Oh, L. Orsini, V. Patras, C. Paus, A. Petrucci, M. Pieri, A. Racz, H. Sakulin, M. Sani, P. Schieferdecker, C. Schwick, J. F. S. Margaleff, D. Shpakov, S. Simon, K. Sumorok, A. S. Yoon, P. Wittich, and M. Zanetti. Commissioning of the CMS High Level Trigger. *Journal of Instrumentation*, 4:10005–+, October 2009. doi: 10.1088/1748-0221/4/10/P10005.

[72] Serguei Chatrchyan et al. Commissioning of the CMS High-Level Trigger with Cosmic Rays. *JINST*, 5:T03005, 2010. doi: 10.1088/1748-0221/5/03/T03005.

[73] Geant4: a simulation toolkit. *Nucl. Instrum. and Methods*, A506:250, 2003. doi: 10.1016/S0168-9002(03)01368-8.

[74] Ferenc Siklér. Study of clustering methods to improve primary vertex finding for collider detectors. 2009. doi: 10.1016/j.nima.2010.04.058.

[75] S. Agostinelli et al. G4–a simulation toolkit. *Nucl. Instrum. Meth. A*, 506(3): 250 – 303, 2003. ISSN 0168-9002. doi: DOI:10.1016/S0168-9002(03)01368-8. URL http://www.sciencedirect.com/science/article/B6TJM-48TJFY8-5/2/23ea98096ce11c1be446850c04cfa498.

[76] Transverse-momentum and pseudorapidity distributions of charged hadrons in pp collisions at $\sqrt{s} = 0.9$ and 2.36 TeV. *JHEP*, 02:041, 2010. doi: 10.1007/JHEP02(2010)041.

[77] Vardan Khachatryan et al. Transverse-momentum and pseudorapidity distributions of charged hadrons in pp collisions at sqrt(s) = 7 TeV. *Phys. Rev. Lett.*, 105: 022002, 2010. doi: 10.1103/PhysRevLett.105.022002.

[78] Vardan Khachatryan et al. Charged particle multiplicities in pp interactions at sqrt(s) = 0.9, 2.36, and 7 TeV. *JHEP*, 01:079, 2011. doi: 10.1007/JHEP01(2011)079.

[79] G. D'Agostini. A multidimensional unfolding method based on bayes' theorem. *Nucl. Instrum. Meth. A*, 362(2-3):487 - 498, 1995. ISSN 0168-9002. doi: DOI:10.1016/0168-9002(95)00274-X. URL `http://www.sciencedirect.com/science/article/B6TJM-3YRNX0H-5K/2/3e3a92555a7955c7f4ab989fa99baef7`.

[80] G. D'Agostini. Bayesian reasoning in high-energy physics: Principles and applications. *CERN Yellow Report*, CERN-YELLOW-99-03, 1999.

[81] Charged-particle multiplicity measurement in proton-proton collisions at $\sqrt{s}$ = 0.9 and 2.36 TeV with ALICE at LHC. 2010.

[82] Charged-particle multiplicities in pp interactions at $\sqrt{s} = 900$ GeV measured with the ATLAS detector at the LHC. *Phys. Lett.*, B688:21, 2010. doi: 10.1016/j.physletb.2010.03.064.

[83] Peter Z. Skands. The Perugia Tunes. 2009.

[84] A. Moraes, C. Buttar, and I. Dawson. Prediction for minimum bias and the underlying event at LHC energies. *Eur. Phys. J.*, C50:435, 2007. doi: 10.1140/epjc/s10052-007-0239-1.

[85] A. B. Kaidalov and M. G. Poghosyan. Predictions of Quark-Gluon String Model for pp at LHC. *Eur. Phys. J.*, C67:397–404, 2010. doi: 10.1140/epjc/s10052-010-1301-y.

[86] E. Gotsman, E. Levin, and U. Maor. QCD motivated approach to soft interactions at high energy: inclusive production. *Phys. Rev.*, D81:051501, 2010. doi: 10.1103/PhysRevD.81.051501.

[87] A. K. Likhoded, A. V. Luchinsky, and A. A. Novoselov. Light hadron production in inclusive pp-scattering at LHC. *Phys. Rev.*, D82:114006, 2010. doi: 10.1103/PhysRevD.82.114006.

[88] Edward K. G. Sarkisyan and Alexander S. Sakharov. Relating multihadron production in hadronic and nuclear collisions. *Eur. Phys. J.*, C70:533–541, 2010. doi: 10.1140/epjc/s10052-010-1493-1.

[89] Wit Busza. Trends in multiparticle production and some 'predictions' for pp and PbPb collisions at LHC. *J. Phys.*, G35:044040, 2008. doi: 10.1088/0954-3899/35/4/044040.

[90] David d'Enterria, Ralph Engel, Tanguy Pierog, Sergey Ostapchenko, and Klaus Werner. Constraints from the first LHC data on hadronic event generators for ultra-high energy cosmic-ray physics. 2011.

[91] A. Donnachie and P. V. Landshoff. Total cross-sections. *Phys. Lett.*, B296:227–232, 1992. doi: 10.1016/0370-2693(92)90832-O.

List of Figures

List of Tables

Acknowledgments

This thesis would not have been possible without generous assistances and supports of many people.

First and foremost, I would like to express my deep and sincere gratitude to my advisor, Professor Wit Busza, who helped me through my graduate studies. Wit guided me through all the difficulties I faced in the research and when I needed to make choices. He was always patient and good at explaining complicated physics concepts. What I learned from him changed my way of thinking about physics questions. He also encouraged me to take some time to think about the available measurements and theory to enjoy and understand the physics implications of the data. That was proven to be one of the most important thing I learned in my graduate studies. I also learned a lot from him about the philosophy of life.

I would like to thank my thesis committee, Professor Gunther Roland and Professor Janet Conrad for their comments and suggestions. Janet is helpful and kind. I would like to thank to her comments and suggestions on my thesis. As the leader of the CMS Heavy Ion program, Gunther has been very helpful on all fronts and he always points out the most important task to be done in order to finish the analysis. Due to Gunther's organization and planning, we started a very ambitious program to study the particle production and aimed for the first physics publication on collision data. The plan worked out really nicely and this is a unforgettable experience I have during my life.

I would like to thank my academic advisor, Professor Bolek Wyslouch. He made sure that the fractions of time I spent on courses, service works and thesis works were nicely balanced. He also gave me the first culture shock of the MIT standard. Bolek always played the key role in the leadership and ensured good communication between various of CMS detector groups.

It is my pleasure to be educated at MIT and work with talented people in the heavy ion group. Constantin Loizides was always helpful and due to his high standard, my programming skill improved significantly. From him, I learned how to organize the analysis and the philosophy that one should try to solve problems nicely to save time. Christof

Roland was the trigger expert and ensured the useful data was collected. From him, I learned how to plan the data samples we want to use, and how to design and understand the complicated trigger paths. Ivan Cali was the expert of the silicon tracker that I can consult with. George Stephans was my source of knowledge about the heavy ion physics. I would like to thank my senior fellow students, Edward Wenger, Wei Li, Burak Alver and Siarhei Vaurynovich. Edward and Wei were already Postdoc researcher in our group. Edward was the soul of the reconstruction of the heavy ion events. Under his organization, the heavy ion analysis framework worked beautifully. Wei ensured the MIT Tier2 was working nicely to make the analysis possible. Burak and Siarhei were always helpful on the discussions and improved my knowledge of the heavy ion physics. My friends and colleagues, Yetkin Yilmaz, Andre Yoon, and Frank Ma have been working closely with me. We moved to CERN together and had a new life here. We also successfully survived through the first p+p data taking, the first analysis of p+p data, and the first Pb+Pb data taking. It was really a pleasure to work with them. I also want to thank my younger fellow students, Yongsun Kim, Yi Chen, Yongsoo Park, Arya Tafvizi, and Dragos Velicanu who helped me and made our office at CERN full of fun. In the end, I would like to thank to Anna Maria Convertino, our secretary, for elegantly arranging all our administrative affairs. It is hard to imagine how we could survive without your help.

I had the great privilege of working in the CMS collaboration. First of all, I would like to thank to Gabor Veres, Krisztian Krajczar, Ferenc Sikler and Alan Bell who I worked closely with on the first p+p analysis. I worked on the Beam Scintillation Counter with Gabor and Alan. It was my first hardware project and I learned a lot from them. Gabor was also the source of knowledge and his suggestions were always to the right point. He was full of nice ideas and I learned how to think from him. Alan helped me on English and he always made the work of a lot of fun. I worked closely with Krisztian and Ferenc on the multiplicity analysis. Krisztian was always calm and accurate. Ferenc's experience and knowledge also broadened my view. I will never forget the time I worked with them during the first p+p data taking. I would like to thank Xavier Janssen and Romain Rougny. We worked on the multiplicity distribution analysis together and the discussions and cross-checks were very useful.

I want to thank the CMS heavy ion group convenors David d'Enterria, Raphael Granier De Cassagnac, Olga Kodolova for their guidence, and all my collaborators in the CMS Heavy Ion group, Catherline Silvestre, Marguerite Tonjes, Victoria Zhukova, Dong-Ho Moon, Eric Appelt and many others for their encouragements and supports.

I also would like to express my gratitude to Vivian O'dell, Albert De Roeck, Gigi Rolandi and Joe Incandela for their help and management, and all the heroes who built and maintained the CMS detector.

I would like to thank my friends from Taiwan: Professor Chia-Ming Kuo, Shin-Shan Yu, Rong-Shyang Lu, Yeng-Ming Tzeng, Syue-Wei Li who helped me though the difficult time. My life in CERN would have been intolerable without so many great friends I met here, Yeong-Jyi Lei, Kai-Yi Kao, Yun-Ju Lu, Yu-Wei Chang, Gianni Pucciani, Karolin Kokaz, Daniele Kruse made living in Geneva great fun.

Finally, I owe everything to my family. My parents, Chien-Kun Lee and Ruoh-Pyng Wu, have been constantly providing me selfless love, support and guidance that could not be expected more by any other child, and my brother Yen-Fu Lee who have been encouraged me and provide essential supports from Taiwan. I would like to appreciate all the sacrifices made by my girl friend, Hui-Jing Lai. Although being apart thousands of miles away and a 6-hour difference in time-zone, she had been my the most important support. She had to wake up very early in the morning in Taiwan and I had to sleep very late in Geneva in order to meet on the internet and to share our life. I will never forget about it. None of this work would have been possible without them.

Published papers

JHEP

Published for SISSA by Springer

Received: *February 4, 2010*
Accepted: *February 7, 2010*
Published: *February 10, 2010*

Transverse-momentum and pseudorapidity distributions of charged hadrons in pp collisions at $\sqrt{s} = 0.9$ and 2.36 TeV

CMS Collaboration

Abstract: Measurements of inclusive charged-hadron transverse-momentum and pseudorapidity distributions are presented for proton-proton collisions at $\sqrt{s} = 0.9$ and 2.36 TeV. The data were collected with the CMS detector during the LHC commissioning in December 2009. For non-single-diffractive interactions, the average charged-hadron transverse momentum is measured to be 0.46 ± 0.01 (stat.) $\pm$ 0.01 (syst.) GeV/c at 0.9 TeV and 0.50 ± 0.01 (stat.) $\pm$ 0.01 (syst.) GeV/c at 2.36 TeV, for pseudorapidities between -2.4 and $+2.4$. At these energies, the measured pseudorapidity densities in the central region, $dN_{\mathrm{ch}}/d\eta|_{|\eta|<0.5}$, are 3.48 ± 0.02 (stat.) $\pm$ 0.13 (syst.) and 4.47 ± 0.04 (stat.) $\pm$ 0.16 (syst.), respectively. The results at 0.9 TeV are in agreement with previous measurements and confirm the expectation of near equal hadron production in $\mathrm{p\bar{p}}$ and pp collisions. The results at 2.36 TeV represent the highest-energy measurements at a particle collider to date.

Keywords: Hadron-Hadron Scattering

ArXiv ePrint: 1002.0621

doi:10.1007/JHEP02(2010)041

JHEP02(2010)041

The CMS Collaboration

Yerevan Physics Institute, Yerevan, Armenia
V. Khachatryan, A.M. Sirunyan, A. Tumasyan

Institut für Hochenergiephysik der OeAW, Wien, Austria
W. Adam, T. Bergauer, M. Dragicevic, J. Erö, M. Friedl, R. Frühwirth, V.M. Ghete, J. Hammer,[1] S. Hänsel, M. Hoch, N. Hörmann, J. Hrubec, M. Jeitler, G. Kasieczka, M. Krammer, D. Liko, I. Mikulec, M. Pernicka, H. Rohringer, R. Schöfbeck, J. Strauss, A. Taurok, F. Teischinger, W. Waltenberger, G. Walzel, E. Widl, C.-E. Wulz

National Centre for Particle and High Energy Physics, Minsk, Belarus
V. Mossolov, N. Shumeiko, J. Suarez Gonzalez

Universiteit Antwerpen, Antwerpen, Belgium
L. Benucci, E.A. De Wolf, M. Hashemi, X. Janssen, T. Maes, L. Mucibello, S. Ochesanu, R. Rougny, M. Selvaggi, H. Van Haevermaet, P. Van Mechelen, N. Van Remortel

Vrije Universiteit Brussel, Brussel, Belgium
V. Adler, S. Beauceron, J. D'Hondt, O. Devroede, A. Kalogeropoulos, J. Maes, M.U. Mozer, S. Tavernier, W. Van Doninck, P. Van Mulders, I. Villella

Université Libre de Bruxelles, Bruxelles, Belgium
E.C. Chabert, O. Charaf, B. Clerbaux, G. De Lentdecker, V. Dero, A.P.R. Gay, G.H. Hammad, P.E. Marage, C. Vander Velde, P. Vanlaer, J. Wickens

Ghent University, Ghent, Belgium
M. Grunewald, B. Klein, A. Marinov, D. Ryckbosch, F. Thyssen, M. Tytgat, L. Vanelderen, P. Verwilligen, S. Walsh

Université Catholique de Louvain, Louvain-la-Neuve, Belgium
S. Basegmez, G. Bruno, J. Caudron, E. Cortina Gil, J. De Favereau De Jeneret, C. Delaere, P. Demin, D. Favart, A. Giammanco, G. Grégoire, J. Hollar, V. Lemaitre, F. Maltoni, O. Militaru, S. Ovyn, K. Piotrzkowski,[1] L. Quertenmont, N. Schul

Université de Mons, Mons, Belgium
N. Beliy, T. Caebergs, E. Daubie, P. Herquet

Centro Brasileiro de Pesquisas Fisicas, Rio de Janeiro, Brazil
G.A. Alves, M.E. Pol, M.H.G. Souza

Universidade do Estado do Rio de Janeiro, Rio de Janeiro, Brazil
W. Carvalho, E.M. Da Costa, D. De Jesus Damiao, C. De Oliveira Martins, S. Fonseca De Souza, L. Mundim, V. Oguri, A. Santoro, S.M. Silva Do Amaral, A. Sznajder, F. Torres Da Silva De Araujo

Instituto de Fisica Teorica, Universidade Estadual Paulista, Sao Paulo, Brazil
F.A. Dias, M.A.F. Dias, T.R. Fernandez Perez Tomei, E. M. Gregores,[2] F. Marinho, S.F. Novaes, Sandra S. Padula

Institute for Nuclear Research and Nuclear Energy, Sofia, Bulgaria
J. Damgov, N. Darmenov,[1] L. Dimitrov, V. Genchev,[1] P. Iaydjiev, S. Piperov, S. Stoykova, G. Sultanov, R. Trayanov, I. Vankov

University of Sofia, Sofia, Bulgaria
R. Hadjiiska, V. Kozhuharov, L. Litov, M. Mateev, B. Pavlov, P. Petkov

Institute of High Energy Physics, Beijing, China
G.M. Chen, H.S. Chen, C.H. Jiang, D. Liang, S. Liang, X. Meng, J. Tao, J. Wang, J. Wang, X. Wang, Z. Wang, J. Zang, Z. Zhang

State Key Lab. of Nucl. Phys. and Tech., Peking University, Beijing, China
Y. Ban, S. Guo, Z. Hu, Y. Mao, S.J. Qian, H. Teng, B. Zhu

Universidad de Los Andes, Bogota, Colombia
C.A. Carrillo Montoya, B. Gomez Moreno, A.A. Ocampo Rios, J.C. Sanabria

Technical University of Split, Split, Croatia
N. Godinovic, K. Lelas, R. Plestina, D. Polic, I. Puljak

University of Split, Split, Croatia
Z. Antunovic, M. Dzelalija

Institute Rudjer Boskovic, Zagreb, Croatia
V. Brigljevic, S. Duric, K. Kadija, S. Morovic

University of Cyprus, Nicosia, Cyprus
A. Attikis, R. Fereos, M. Galanti, J. Mousa, A. Papadakis, F. Ptochos, P.A. Razis, D. Tsiakkouri, Z. Zinonos

National Institute of Chemical Physics and Biophysics, Tallinn, Estonia
A. Hektor, M. Kadastik, K. Kannike, M. Müntel, M. Raidal, L. Rebane

Department of Physics, University of Helsinki, Helsinki, Finland
P. Eerola

Helsinki Institute of Physics, Helsinki, Finland
S. Czellar, J. Härkönen, A. Heikkinen, V. Karimäki, R. Kinnunen, J. Klem, M.J. Kortelainen, T. Lampén, K. Lassila-Perini, S. Lehti, T. Lindén, P. Luukka, T. Mäenpää, E. Tuominen, J. Tuominiemi, E. Tuovinen, D. Ungaro, L. Wendland

Lappeenranta University of Technology, Lappeenranta, Finland
K. Banzuzi, A. Korpela, T. Tuuva

Laboratoire d'Annecy-le-Vieux de Physique des Particules, IN2P3-CNRS, Annecy-le-Vieux, France
D. Sillou

DSM/IRFU, CEA/Saclay, Gif-sur-Yvette, France
M. Besancon, M. Dejardin, D. Denegri, J. Descamps, B. Fabbro, J.L. Faure, F. Ferri, S. Ganjour, F.X. Gentit, A. Givernaud, P. Gras, G. Hamel de Monchenault, P. Jarry,

E. Locci, J. Malcles, M. Marionneau, L. Millischer, J. Rander, A. Rosowsky, D. Rousseau, M. Titov, P. Verrecchia

Laboratoire Leprince-Ringuet, Ecole Polytechnique, IN2P3-CNRS, Palaiseau, France
S. Baffioni, L. Bianchini, C. Broutin, P. Busson, C. Charlot, L. Dobrzynski, S. Elgammal, R. Granier de Cassagnac, M. Haguenauer, P. Miné, P. Paganini, Y. Sirois, C. Thiebaux, A. Zabi

Institut Pluridisciplinaire Hubert Curien, Université de Strasbourg, Université de Haute Alsace Mulhouse, CNRS/IN2P3, Strasbourg, France
J.-L. Agram,[3] A. Besson, D. Bloch, D. Bodin, J.-M. Brom, M. Cardaci, E. Conte,[3] F. Drouhin,[3] C. Ferro, J.-C. Fontaine,[3] D. Gelé, U. Goerlach, S. Greder, P. Juillot, A.-C. Le Bihan, Y. Mikami, I. Ripp-Baudot, J. Speck, P. Van Hove

Université de Lyon, Université Claude Bernard Lyon 1, CNRS-IN2P3, Institut de Physique Nucléaire de Lyon, Villeurbanne, France
C. Baty, M. Bedjidian, O. Bondu, G. Boudoul, D. Boumediene, H. Brun, N. Chanon, R. Chierici, D. Contardo, P. Depasse, H. El Mamouni, F. Fassi,[4] J. Fay, S. Gascon, B. Ille, T. Kurca, T. Le Grand, M. Lethuillier, L. Mirabito, S. Perries, S. Tosi, Y. Tschudi, P. Verdier, H. Xiao

E. Andronikashvili Institute of Physics, Academy of Science, Tbilisi, Georgia
V. Roinishvili

RWTH Aachen University, I. Physikalisches Institut, Aachen, Germany
G. Anagnostou, M. Edelhoff, L. Feld, N. Heracleous, O. Hindrichs, R. Jussen, K. Klein, J. Merz, N. Mohr, A. Ostapchuk, D. Pandoulas, A. Perieanu, F. Raupach, J. Sammet, S. Schael, D. Sprenger, H. Weber, M. Weber, B. Wittmer

RWTH Aachen University, III. Physikalisches Institut A, Aachen, Germany
O. Actis, W. Bender, P. Biallass, M. Erdmann, J. Frangenheim, T. Hebbeker, A. Hinzmann, K. Hoepfner, C. Hof, M. Kirsch, T. Klimkovich, P. Kreuzer,[1] D. Lanske,[†] M. Merschmeyer, A. Meyer, H. Pieta, H. Reithler, S.A. Schmitz, M. Sowa, J. Steggemann, D. Teyssier, C. Zeidler

RWTH Aachen University, III. Physikalisches Institut B, Aachen, Germany
M. Bontenackels, M. Davids, M. Duda, G. Flügge, H. Geenen, M. Giffels, W. Haj Ahmad, D. Heydhausen, T. Kress, Y. Kuessel, A. Linn, A. Nowack, L. Perchalla, O. Pooth, P. Sauerland, A. Stahl, M. Thomas, D. Tornier, M.H. Zoeller

Deutsches Elektronen-Synchrotron, Hamburg, Germany
M. Aldaya Martin, U. Behrens, K. Borras, A. Campbell, E. Castro, D. Dammann, G. Eckerlin, A. Flossdorf, G. Flucke, A. Geiser, J. Hauk, H. Jung, M. Kasemann, I. Katkov, C. Kleinwort, H. Kluge, A. Knutsson, E. Kuznetsova, W. Lange, W. Lohmann, R. Mankel,[1] M. Marienfeld, A.B. Meyer, J. Mnich, J. Olzem, A. Parenti, R. Schmidt, T. Schoerner-Sadenius, N. Sen, M. Stein, D. Volyanskyy, C. Wissing

University of Hamburg, Hamburg, Germany
C. Autermann, J. Draeger, D. Eckstein, H. Enderle, U. Gebbert, K. Kaschube, G. Kaussen, R. Klanner, B. Mura, S. Naumann-Emme, F. Nowak, C. Sander, P. Schleper, M. Schröder, T. Schum, H. Stadie, G. Steinbrück, J. Thomsen, R. Wolf

Institut für Experimentelle Kernphysik, Karlsruhe, Germany
J. Bauer, P. Blüm, V. Buege, A. Cakir, T. Chwalek, D. Daeuwel, W. De Boer, A. Dierlamm, G. Dirkes, M. Feindt, M. Frey, J. Gruschke, C. Hackstein, F. Hartmann, M. Heinrich, K.H. Hoffmann, S. Honc, T. Kuhr, D. Martschei, S. Mueller, Th. Müller, M. Niegel, O. Oberst, A. Oehler, J. Ott, T. Peiffer, D. Piparo, G. Quast, K. Rabbertz, M. Renz, A. Sabellek, C. Saout,[1] A. Scheurer, P. Schieferdecker, F.-P. Schilling, G. Schott, H.J. Simonis, F.M. Stober, J. Wagner-Kuhr, M. Zeise, V. Zhukov,[5] E.B. Ziebarth

Institute of Nuclear Physics "Demokritos", Aghia Paraskevi, Greece
G. Daskalakis, T. Geralis, K. Karafasoulis, A. Kyriakis, D. Loukas, A. Markou, C. Markou, C. Mavrommatis, E. Petrakou, A. Zachariadou

University of Athens, Athens, Greece
A. Agapitos, L. Gouskos, P. Katsas, A. Panagiotou, K. Saganis, E. Xaxiris

University of Ioánnina, Ioánnina, Greece
I. Evangelou, P. Kokkas, N. Manthos, I. Papadopoulos, F.A. Triantis

KFKI Research Institute for Particle and Nuclear Physics, Budapest, Hungary
A. Aranyi, G. Bencze, L. Boldizsar, G. Debreczeni, C. Hajdu,[1] D. Horvath,[6] A. Kapusi, K. Krajczar, A. Laszlo, F. Sikler, G. Vesztergombi

Institute of Nuclear Research ATOMKI, Debrecen, Hungary
N. Beni, J. Molnar, J. Palinkas, Z. Szillasi,[1] V. Veszpremi

University of Debrecen, Debrecen, Hungary
P. Raics, Z.L. Trocsanyi, B. Ujvari

Panjab University, Chandigarh, India
S. Bansal, S.B. Beri, V. Bhatnagar, M. Jindal, M. Kaur, J.M. Kohli, M.Z. Mehta, N. Nishu, L.K. Saini, A. Sharma, R. Sharma, A.P. Singh, J.B. Singh, S.P. Singh

University of Delhi, Delhi, India
S. Ahuja, S. Bhattacharya,[7] S. Chauhan, B.C. Choudhary, P. Gupta, S. Jain, S. Jain, A. Kumar, K. Ranjan, R.K. Shivpuri

Bhabha Atomic Research Centre, Mumbai, India
R.K. Choudhury, D. Dutta, S. Kailas, S.K. Kataria, A.K. Mohanty, L.M. Pant, P. Shukla, P. Suggisetti

Tata Institute of Fundamental Research - EHEP, Mumbai, India
T. Aziz, M. Guchait,[8] A. Gurtu, M. Maity,[9] D. Majumder, G. Majumder, K. Mazumdar, A. Nayak, A. Saha, K. Sudhakar, N. Wickramage

Tata Institute of Fundamental Research - HECR, Mumbai, India
S. Banerjee, S. Dugad, N.K. Mondal

Institute for Studies in Theoretical Physics & Mathematics (IPM), Tehran, Iran
H. Arfaei, H. Bakhshiansohi, A. Fahim, A. Jafari, M. Mohammadi Najafabadi, A. Moshaii, S. Paktinat Mehdiabadi, M. Zeinali

University College Dublin, Dublin, Ireland
M. Felcini

INFN Sezione di Bari,[a] Università di Bari,[b] Politecnico di Bari,[c] Bari, Italy
M. Abbrescia,[a,b] L. Barbone,[a] A. Colaleo,[a] D. Creanza,[a,c] N. De Filippis,[a] M. De Palma,[a,b] A. Dimitrov, F. Fedele,[a] L. Fiore,[a] G. Iaselli,[a,c] L. Lusito,[a,b,1] G. Maggi,[a,c] M. Maggi,[a] N. Manna,[a,b] B. Marangelli,[a,b] S. My,[a,c] S. Nuzzo,[a,b] G.A. Pierro,[a] G. Polese, A. Pompili,[a,b] G. Pugliese,[a,c] F. Romano,[a,c] G. Roselli,[a,b] G. Selvaggi,[a,b] L. Silvestris,[a] S. Tupputi,[a,b] G. Zito[a]

INFN Sezione di Bologna,[a] Università di Bologna,[b] Bologna, Italy
G. Abbiendi,[a] D. Bonacorsi,[a] S. Braibant-Giacomelli,[a,b] P. Capiluppi,[a,b] F.R. Cavallo,[a] G. Codispoti,[a,b] M. Cuffiani,[a,b] G.M. Dallavalle[a,1] F. Fabbri,[a] A. Fanfani,[a,b] D. Fasanella,[a] P. Giacomelli,[a] M. Giunta[a,1] C. Grandi,[a] S. Marcellini,[a] G. Masetti,[a,b] A. Montanari,[a] F.L. Navarria,[a,b] F. Odorici,[a] A. Perrotta,[a] A.M. Rossi,[a,b] T. Rovelli,[a,b] G. Siroli,[a,b] R. Travaglini[a,b]

INFN Sezione di Catania,[a] Università di Catania,[b] Catania, Italy
S. Albergo,[a,b] M. Chiorboli,[a,b] S. Costa,[a,b] R. Potenza,[a,b] A. Tricomi,[a,b] C. Tuve[a]

INFN Sezione di Firenze,[a] Università di Firenze,[b] Firenze, Italy
G. Barbagli,[a] G. Broccolo,[a,b] V. Ciulli,[a,b] C. Civinini,[a] R. D'Alessandro,[a,b] E. Focardi,[a,b] S. Frosali,[a,b] E. Gallo,[a] C. Genta,[a,b] G. Landi,[a,b] P. Lenzi[a,b,1] M. Meschini,[a] S. Paoletti,[a] G. Sguazzoni,[a] A. Tropiano[a]

INFN Laboratori Nazionali di Frascati, Frascati, Italy
S. Bianco, S. Colafranceschi,[10] F. Fabbri, D. Piccolo

INFN Sezione di Genova, Genova, Italy
P. Fabbricatore, R. Musenich

INFN Sezione di Milano-Biccoca,[a] Università di Milano-Bicocca,[b] Milano, Italy
A. Benaglia,[a] G.B. Cerati[a,b,1] F. De Guio,[a] A. Ghezzi[a,1] P. Govoni,[a,b] M. Malberti[a,b,1] S. Malvezzi,[a] A. Martelli,[a] D. Menasce,[a] V. Miccio,[a,b] L. Moroni,[a] P. Negri,[a,b] M. Paganoni,[a,b] D. Pedrini,[a] A. Pullia,[a,b] S. Ragazzi,[a,b] N. Redaelli,[a] S. Sala,[a] R. Salerno,[a,b] T. Tabarelli de Fatis,[a,b] V. Tancini,[a,b] S. Taroni[a,b]

INFN Sezione di Napoli,[a] Università di Napoli "Federico II",[b] Napoli, Italy
A. Cimmino[a,b,1] M. De Gruttola[a,b,1] F. Fabozzi[a,11] A.O.M. Iorio,[a] L. Lista,[a] P. Noli,[a,b] P. Paolucci[a]

INFN Sezione di Padova,[a] Università di Padova,[b] Università di Trento (Trento),[c] Padova, Italy
P. Azzi,[a] N. Bacchetta,[a] P. Bellan[a,b,1] M. Biasotto[a,12] R. Carlin,[a,b] P. Checchia,[a] M. De Mattia,[a,b] T. Dorigo,[a] F. Fanzago,[a] F. Gasparini,[a,b] P. Giubilato,[a,b] F. Gonella,[a]

A. Gresele,[a,c] M. Gulmini[a,12] S. Lacaprara[a,12] I. Lazzizzera,[a,c] G. Maron[a,12] S. Mattiazzo,[a,b] A.T. Meneguzzo,[a,b] M. Passaseo,[a] M. Pegoraro,[a] N. Pozzobon,[a,b] P. Ronchese,[a,b] E. Torassa,[a] M. Tosi,[a,b] S. Vanini,[a,b] S. Ventura,[a] P. Zotto[a,b]

INFN Sezione di Pavia,[a] Università di Pavia,[b] Pavia, Italy
P. Baesso,[a,b] U. Berzano,[a] D. Pagano,[a,b] S.P. Ratti,[a,b] C. Riccardi,[a,b] P. Torre,[a,b] P. Vitulo,[a,b] C. Viviani[a,b]

INFN Sezione di Perugia,[a] Università di Perugia,[b] Perugia, Italy
M. Biasini,[a,b] G.M. Bilei,[a] B. Caponeri,[a,b] L. Fanò,[a] P. Lariccia,[a,b] A. Lucaroni,[a,b] G. Mantovani,[a,b] A. Nappi,[a,b] A. Santocchia,[a,b] L. Servoli,[a] R. Volpe[a,b,1]

INFN Sezione di Pisa,[a] Università di Pisa,[b] Scuola Normale Superiore di Pisa,[c] Pisa, Italy
P. Azzurri,[a,c] G. Bagliesi,[a] J. Bernardini,[a,b] T. Boccali,[a] A. Bocci,[a,c] R. Castaldi,[a] R. Dell'Orso,[a] S. Dutta,[a] F. Fiori,[a,b] L. Foà,[a,c] S. Gennai,[a,c] A. Giassi,[a] A. Kraan,[a] F. Ligabue,[a,c] T. Lomtadze,[a] L. Martini,[a] A. Messineo,[a,b] F. Palla,[a] F. Palmonari,[a] S. Sarkar,[a] G. Segneri,[a] A.T. Serban,[a] P. Spagnolo[a,1] R. Tenchini[a,1] G. Tonelli[a,b,1] A. Venturi,[a] P.G. Verdini[a]

INFN Sezione di Roma,[a] Università di Roma "La Sapienza",[b] Roma, Italy
L. Barone,[a,b] F. Cavallari[a,1] D. Del Re,[a,b] E. Di Marco,[a,b] M. Diemoz,[a] D. Franci,[a,b] M. Grassi,[a] E. Longo,[a,b] G. Organtini,[a,b] A. Palma,[a,b] F. Pandolfi,[a,b] R. Paramatti[a,1] S. Rahatlou,[a,b] C. Rovelli[a]

INFN Sezione di Torino,[a] Università di Torino,[b] Università del Piemonte Orientale (Novara),[c] Torino, Italy
N. Amapane,[a,b] R. Arcidiacono,[a,b] S. Argiro,[a,b] M. Arneodo,[a,c] C. Biino,[a] M.A. Borgia,[a,b] C. Botta,[a,b] N. Cartiglia,[a] R. Castello,[a,b] M. Costa,[a,b] G. Dellacasa,[a] N. Demaria,[a] A. Graziano,[a,b] C. Mariotti,[a] M. Marone,[a,b] S. Maselli,[a] E. Migliore,[a,b] G. Mila,[a,b] V. Monaco,[a,b] M. Musich,[a,b] M.M. Obertino,[a,c] N. Pastrone,[a] A. Romero,[a,b] M. Ruspa,[a,c] R. Sacchi,[a,b] A. Solano,[a,b] A. Staiano,[a] D. Trocino,[a,b] A. Vilela Pereira[a,b,1]

INFN Sezione di Trieste,[a] Università di Trieste,[b] Trieste, Italy
F. Ambroglini,[a,b] S. Belforte,[a] F. Cossutti,[a] G. Della Ricca,[a,b] B. Gobbo,[a] A. Penzo[a]

Kyungpook National University, Daegu, Korea
S. Chang, J. Chung, D.H. Kim, G.N. Kim, D.J. Kong, H. Park, D.C. Son

Chonnam National University, Kwangju, Korea
Zero Kim, S. Song

Konkuk University, Seoul, Korea
S.Y. Jung

Korea University, Seoul, Korea
B. Hong, H. Kim, J.H. Kim, K.S. Lee, D.H. Moon, S.K. Park, H.B. Rhee, K.S. Sim

Seoul National University, Seoul, Korea
J. Kim

University of Seoul, Seoul, Korea
M. Choi, I.C. Park

Sungkyunkwan University, Suwon, Korea
S. Choi, Y. Choi, Y.K. Choi, J. Goh, Y. Jo, J. Kwon, J. Lee, S. Lee

Vilnius University, Vilnius, Lithuania
M. Janulis, D. Martisiute, P. Petrov, T. Sabonis

Centro de Investigacion y de Estudios Avanzados del IPN, Mexico City, Mexico
H. Castilla Valdez,[1] A. Sánchez Hernández

Universidad Iberoamericana, Mexico City, Mexico
S. Carrillo Moreno

Benemerita Universidad Autonoma de Puebla, Puebla, Mexico
H.A. Salazar Ibarguen

Universidad Autónoma de San Luis Potosí, San Luis Potosí, Mexico
E. Casimiro Linares, A. Morelos Pineda

University of Auckland, Auckland, New Zealand
P. Allfrey, D. Krofcheck

University of Canterbury, Christchurch, New Zealand
T. Aumeyr, P.H. Butler, T. Signal, J.C. Williams

National Centre for Physics, Quaid-I-Azam University, Islamabad, Pakistan
M. Ahmad, I. Ahmed, M.I. Asghar, H.R. Hoorani, W.A. Khan, T. Khurshid, S. Qazi

Institute of Experimental Physics, Warsaw, Poland
M. Cwiok, W. Dominik, K. Doroba, M. Konecki, J. Krolikowski

Soltan Institute for Nuclear Studies, Warsaw, Poland
T. Frueboes, R. Gokieli, M. Górski, M. Kazana, K. Nawrocki, M. Szleper, G. Wrochna, P. Zalewski

Laboratório de Instrumentação e Física Experimental de Partículas, Lisboa, Portugal
N. Almeida, P. Bargassa, A. David, P. Faccioli, P.G. Ferreira Parracho, M. Gallinaro, P. Musella, P.Q. Ribeiro, J. Seixas, P. Silva, J. Varela,[1] H.K. Wöhri

Joint Institute for Nuclear Research, Dubna, Russia
I. Altsybeev, I. Belotelov, P. Bunin, M. Finger, M. Finger Jr., I. Golutvin, A. Kamenev, V. Karjavin, G. Kozlov, A. Lanev, P. Moisenz, V. Palichik, V. Perelygin, S. Shmatov, V. Smirnov, A. Vishnevskiy, A. Volodko, A. Zarubin

Petersburg Nuclear Physics Institute, Gatchina (St Petersburg), Russia
Y. Ivanov, V. Kim, P. Levchenko, G. Obrant, Y. Shcheglov, A. Shchetkovskiy, I. Smirnov, V. Sulimov, S. Vavilov, A. Vorobyev

Institute for Nuclear Research, Moscow, Russia
Yu. Andreev, S. Gninenko, N. Golubev, A. Karneyeu, M. Kirsanov, N. Krasnikov, V. Matveev, A. Pashenkov, A. Toropin, S. Troitsky

Institute for Theoretical and Experimental Physics, Moscow, Russia
V. Epshteyn, V. Gavrilov, N. Ilina, V. Kaftanov,[†] M. Kossov,[1] A. Krokhotin, S. Kuleshov, A. Oulianov, G. Safronov, S. Semenov, I. Shreyber, V. Stolin, E. Vlasov, A. Zhokin

Moscow State University, Moscow, Russia
E. Boos, M. Dubinin,[13] L. Dudko, A. Ershov, A. Gribushin, O. Kodolova, I. Lokhtin, S. Petrushanko, L. Sarycheva, V. Savrin, I. Vardanyan

P.N. Lebedev Physical Institute, Moscow, Russia
I. Dremin, M. Kirakosyan, N. Konovalova, S.V. Rusakov, A. Vinogradov

State Research Center of Russian Federation, Institute for High Energy Physics, Protvino, Russia
I. Azhgirey, S. Bitioukov, K. Datsko, V. Kachanov, D. Konstantinov, V. Krychkine, V. Petrov, R. Ryutin, S. Slabospitsky, A. Sobol, A. Sytine, L. Tourtchanovitch, S. Troshin, N. Tyurin, A. Uzunian, A. Volkov

Vinca Institute of Nuclear Sciences, Belgrade, Serbia
P. Adzic, M. Djordjevic, D. Maletic, J. Puzovic[14]

Centro de Investigaciones Energéticas Medioambientales y Tecnológicas (CIEMAT), Madrid, Spain
M. Aguilar-Benitez, J. Alcaraz Maestre, P. Arce, C. Battilana, E. Calvo, M. Cepeda, M. Cerrada, M. Chamizo Llatas, N. Colino, B. De La Cruz, C. Diez Pardos, C. Fernandez Bedoya, J.P. Fernández Ramos, A. Ferrando, J. Flix, M.C. Fouz, P. Garcia-Abia, O. Gonzalez Lopez, S. Goy Lopez, J.M. Hernandez, M.I. Josa, G. Merino, J. Puerta Pelayo, L. Romero, J. Santaolalla, C. Willmott

Universidad Autónoma de Madrid, Madrid, Spain
C. Albajar, J.F. de Trocóniz

Universidad de Oviedo, Oviedo, Spain
J. Cuevas, J. Fernandez Menendez, I. Gonzalez Caballero, L. Lloret Iglesias, J.M. Vizan Garcia

Instituto de Física de Cantabria (IFCA), CSIC-Universidad de Cantabria, Santander, Spain
I.J. Cabrillo, A. Calderon, S.H. Chuang, I. Diaz Merino, C. Diez Gonzalez, J. Duarte Campderros, M. Fernandez, G. Gomez, J. Gonzalez Sanchez, R. Gonzalez Suarez, C. Jorda, P. Lobelle Pardo, A. Lopez Virto, J. Marco, R. Marco, C. Martinez Rivero, P. Martinez Ruiz del Arbol, F. Matorras, T. Rodrigo, A. Ruiz Jimeno, L. Scodellaro, M. Sobron Sanudo, I. Vila, R. Vilar Cortabitarte

CERN, European Organization for Nuclear Research, Geneva, Switzerland
D. Abbaneo, E. Auffray, P. Baillon, A.H. Ball, D. Barney, F. Beaudette,[15] B. Beccati,

A.J. Bell,[16] R. Bellan, D. Benedetti, C. Bernet, W. Bialas, P. Bloch, S. Bolognesi, M. Bona, H. Breuker, K. Bunkowski, T. Camporesi, E. Cano, A. Cattai, G. Cerminara, T. Christiansen, J.A. Coarasa Perez, R. Covarelli, B. Curé, T. Dahms, A. De Roeck, A. Elliott-Peisert, W. Funk, A. Gaddi, H. Gerwig, D. Gigi, K. Gill, D. Giordano, F. Glege, S. Gowdy, L. Guiducci, J. Gutleber, C. Hartl, J. Harvey, B. Hegner, C. Henderson, H.F. Hoffmann, A. Honma, M. Huhtinen, V. Innocente, P. Janot, P. Lecoq, C. Leonidopoulos, C. Lourenço, A. Macpherson, T. Mäki, L. Malgeri, M. Mannelli, L. Masetti, F. Meijers, P. Meridiani, S. Mersi, E. Meschi, R. Moser, M. Mulders, M. Noy, T. Orimoto, L. Orsini, E. Perez, A. Petrilli, A. Pfeiffer, M. Pierini, M. Pimiä, A. Racz, G. Rolandi,[17] M. Rovere, V. Ryjov, H. Sakulin, C. Schäfer, W.D. Schlatter, C. Schwick, I. Segoni, A. Sharma, P. Siegrist, M. Simon, P. Sphicas,[18] D. Spiga, M. Spiropulu,[13] F. Stöckli, P. Traczyk, P. Tropea, A. Tsirou, G.I. Veres,[19] P. Vichoudis, M. Voutilainen, W.D. Zeuner

Paul Scherrer Institut, Villigen, Switzerland
W. Bertl, K. Deiters, W. Erdmann, K. Gabathuler, R. Horisberger, Q. Ingram, H.C. Kaestli, S. König, D. Kotlinski, U. Langenegger, F. Meier, D. Renker, T. Rohe, J. Sibille,[20] A. Starodumov[21]

Institute for Particle Physics, ETH Zurich, Zurich, Switzerland
L. Caminada,[22] M.C. Casella, Z. Chen, S. Cittolin, S. Dambach,[22] G. Dissertori, M. Dittmar, C. Eggel,[22] J. Eugster, K. Freudenreich, C. Grab, A. Hervé, W. Hintz, P. Lecomte, W. Lustermann, C. Marchica,[22] P. Milenovic,[23] F. Moortgat, A. Nardulli, F. Nessi-Tedaldi, L. Pape, F. Pauss, T. Punz, A. Rizzi, F.J. Ronga, L. Sala, A.K. Sanchez, M.-C. Sawley, D. Schinzel, V. Sordini, B. Stieger, L. Tauscher†, A. Thea, K. Theofilatos, D. Treille, P. Trüb,[22] M. Weber, L. Wehrli, J. Weng

Universität Zürich, Zurich, Switzerland
C. Amsler, V. Chiochia, S. De Visscher, M. Ivova Rikova, C. Regenfus, P. Robmann, T. Rommerskirchen, A. Schmidt, H. Snoek, D. Tsirigkas, L. Wilke

National Central University, Chung-Li, Taiwan
Y.H. Chang, E.A. Chen, W.T. Chen, A. Go, C.M. Kuo, S.W. Li, W. Lin, M.H. Liu, J.H. Wu

National Taiwan University (NTU), Taipei, Taiwan
P. Bartalini, P. Chang, Y.H. Chang, Y. Chao, K.F. Chen, W.-S. Hou, Y. Hsiung, Y.J. Lei, S.W. Lin, R.-S. Lu, J.G. Shiu, Y.M. Tzeng, K. Ueno, C.C. Wang, M. Wang

Cukurova University, Adana, Turkey
A. Adiguzel, A. Ayhan, M.N. Bakirci, S. Cerci, Z. Demir, C. Dozen, I. Dumanoglu, E. Eskut, S. Girgis, E. Gurpinar, T. Karaman, A. Kayis Topaksu, G. Önengüt, K. Ozdemir, S. Ozturk, A. Polatöz, O. Sahin, O. Sengul, K. Sogut,[24] B. Tali, H. Topakli, D. Uzun, L.N. Vergili, M. Vergili

Middle East Technical University, Physics Department, Ankara, Turkey
I.V. Akin, T. Aliev, S. Bilmis, M. Deniz, H. Gamsizkan, A.M. Guler, K. Öcalan, M. Serin, R. Sever, U.E. Surat, M. Zeyrek

Bogaziçi University, Department of Physics, Istanbul, Turkey
M. Deliomeroglu, D. Demir,[25] E. Gülmez, A. Halu, B. Isildak, M. Kaya,[26] O. Kaya,[26] S. Ozkorucuklu,[27] N. Sonmez[28]

National Scientific Center, Kharkov Institute of Physics and Technology, Kharkov, Ukraine
L. Levchuk

University of Bristol, Bristol, United Kingdom
P. Bell, F. Bostock, J.J. Brooke, T.L. Cheng, D. Cussans, R. Frazier, J. Goldstein, M. Hansen, G.P. Heath, H.F. Heath, C. Hill, B. Huckvale, J. Jackson, L. Kreczko, C.K. Mackay, S. Metson, D.M. Newbold,[29] K. Nirunpong, V.J. Smith, S. Ward

Rutherford Appleton Laboratory, Didcot, United Kingdom
L. Basso, K.W. Bell, C. Brew, R.M. Brown, B. Camanzi, D.J.A. Cockerill, J.A. Coughlan, K. Harder, S. Harper, B.W. Kennedy, C.H. Shepherd-Themistocleous, I.R. Tomalin, W.J. Womersley, S.D. Worm

Imperial College, University of London, London, United Kingdom
R. Bainbridge, G. Ball, J. Ballin, R. Beuselinck, O. Buchmuller, D. Colling, N. Cripps, G. Davies, M. Della Negra, C. Foudas, J. Fulcher, D. Futyan, G. Hall, J. Hays, G. Iles, G. Karapostoli, L. Lyons, B.C. MacEvoy, A.-M. Magnan, J. Marrouche, J. Nash, A. Nikitenko,[21] A. Papageorgiou, M. Pesaresi, K. Petridis, M. Pioppi,[30] D.M. Raymond, N. Rompotis, A. Rose, M.J. Ryan, C. Seez, P. Sharp, M. Stoye, A. Tapper, S. Tourneur, M. Vazquez Acosta, T. Virdee,[1] S. Wakefield, D. Wardrope, T. Whyntie

Brunel University, Uxbridge, United Kingdom
M. Barrett, M. Chadwick, J.E. Cole, P.R. Hobson, A. Khan, P. Kyberd, D. Leslie, I.D. Reid, L. Teodorescu

Boston University, Boston, U.S.A.
T. Bose, A. Clough, A. Heister, J. St. John, P. Lawson, D. Lazic, J. Rohlf, L. Sulak

Brown University, Providence, U.S.A.
J. Andrea, A. Avetisyan, S. Bhattacharya, J.P. Chou, D. Cutts, S. Esen, G. Kukartsev, G. Landsberg, M. Narain, D. Nguyen, T. Speer, K.V. Tsang

University of California, Davis, Davis, U.S.A.
R. Breedon, M. Calderon De La Barca Sanchez, D. Cebra, M. Chertok, J. Conway, P.T. Cox, J. Dolen, R. Erbacher, E. Friis, W. Ko, A. Kopecky, R. Lander, H. Liu, S. Maruyama, T. Miceli, M. Nikolic, D. Pellett, J. Robles, M. Searle, J. Smith, M. Squires, M. Tripathi, R. Vasquez Sierra, C. Veelken

University of California, Los Angeles, Los Angeles, U.S.A.
V. Andreev, K. Arisaka, D. Cline, R. Cousins, S. Erhan,[1] C. Farrell, J. Hauser, M. Ignatenko, C. Jarvis, G. Rakness, P. Schlein†, J. Tucker, V. Valuev, R. Wallny

University of California, Riverside, Riverside, U.S.A.
J. Babb, A. Chandra, R. Clare, J.A. Ellison, J.W. Gary, G. Hanson, G.Y. Jeng, S.C. Kao,

F. Liu, H. Liu, A. Luthra, H. Nguyen, B.C. Shen[†], R. Stringer, J. Sturdy, R. Wilken, S. Wimpenny

University of California, San Diego, La Jolla, U.S.A.
W. Andrews, J.G. Branson, E. Dusinberre, D. Evans, F. Golf, A. Holzner, R. Kelley, M. Lebourgeois, J. Letts, B. Mangano, J. Muelmenstaedt, M. Norman, S. Padhi, G. Petrucciani, H. Pi, M. Pieri, R. Ranieri, M. Sani, V. Sharma,[1] S. Simon, A. Vartak, F. Würthwein, A. Yagil

University of California, Santa Barbara, Santa Barbara, U.S.A.
D. Barge, M. Blume, C. Campagnari, M. D'Alfonso, T. Danielson, J. Garberson, J. Incandela, C. Justus, P. Kalavase, S.A. Koay, D. Kovalskyi, V. Krutelyov, J. Lamb, S. Lowette, V. Pavlunin, F. Rebassoo, J. Ribnik, J. Richman, R. Rossin, D. Stuart, W. To, J.R. Vlimant, M. Witherell

California Institute of Technology, Pasadena, U.S.A.
A. Apresyan, A. Bornheim, J. Bunn, M. Gataullin, V. Litvine, Y. Ma, H.B. Newman, C. Rogan, V. Timciuc, J. Veverka, R. Wilkinson, Y. Yang, R.Y. Zhu

Carnegie Mellon University, Pittsburgh, U.S.A.
B. Akgun, R. Carroll, T. Ferguson, D.W. Jang, S.Y. Jun, M. Paulini, J. Russ, N. Terentyev, H. Vogel, I. Vorobiev

University of Colorado at Boulder, Boulder, U.S.A.
J.P. Cumalat, M.E. Dinardo, B.R. Drell, W.T. Ford, B. Heyburn, E. Luiggi Lopez, U. Nauenberg, K. Stenson, K. Ulmer, S.R. Wagner, S.L. Zang

Cornell University, Ithaca, U.S.A.
L. Agostino, J. Alexander, F. Blekman, D. Cassel, A. Chatterjee, S. Das, N. Eggert, L.K. Gibbons, B. Heltsley, W. Hopkins, A. Khukhunaishvili, B. Kreis, J.R. Patterson, D. Puigh, A. Ryd, X. Shi, W. Sun, W.D. Teo, J. Thom, J. Vaughan, Y. Weng, P. Wittich

Fairfield University, Fairfield, U.S.A.
A. Biselli, G. Cirino, D. Winn

Fermi National Accelerator Laboratory, Batavia, U.S.A.
M. Albrow, G. Apollinari, M. Atac, J.A. Bakken, S. Banerjee, L.A.T. Bauerdick, A. Beretvas, J. Berryhill, P.C. Bhat, M. Binkley[†], I. Bloch, F. Borcherding, K. Burkett, J.N. Butler, V. Chetluru, H.W.K. Cheung, F. Chlebana, S. Cihangir, M. Demarteau, D.P. Eartly, V.D. Elvira, I. Fisk, J. Freeman, E. Gottschalk, D. Green, O. Gutsche, A. Hahn, J. Hanlon, R.M. Harris, E. James, H. Jensen, M. Johnson, U. Joshi, B. Klima, K. Kousouris, S. Kunori, S. Kwan, P. Limon, L. Lueking, J. Lykken, K. Maeshima, J.M. Marraffino, D. Mason, P. McBride, T. McCauley, T. Miao, K. Mishra, S. Mrenna, Y. Musienko,[31] C. Newman-Holmes, V. O'Dell, S. Popescu, O. Prokofyev, E. Sexton-Kennedy, S. Sharma, R.P. Smith[†], A. Soha, W.J. Spalding, L. Spiegel, P. Tan, L. Taylor, S. Tkaczyk, L. Uplegger, E.W. Vaandering, R. Vidal, J. Whitmore, W. Wu, F. Yumiceva, J.C. Yun

University of Florida, Gainesville, U.S.A.
D. Acosta, P. Avery, D. Bourilkov, M. Chen, G.P. Di Giovanni, D. Dobur, A. Drozdetskiy, R.D. Field, Y. Fu, I.K. Furic, J. Gartner, B. Kim, S. Klimenko, J. Konigsberg, A. Korytov, K. Kotov, A. Kropivnitskaya, T. Kypreos, K. Matchev, G. Mitselmakher, Y. Pakhotin, J. Piedra Gomez, C. Prescott, V. Rapsevicius, R. Remington, M. Schmitt, B. Scurlock, D. Wang, J. Yelton, M. Zakaria

Florida International University, Miami, U.S.A.
C. Ceron, V. Gaultney, L. Kramer, L.M. Lebolo, S. Linn, P. Markowitz, G. Martinez, J.L. Rodriguez

Florida State University, Tallahassee, U.S.A.
T. Adams, A. Askew, J. Chen, W.G.D. Dharmaratna, B. Diamond, S.V. Gleyzer, J. Haas, S. Hagopian, V. Hagopian, M. Jenkins, K.F. Johnson, H. Prosper, S. Sekmen

Florida Institute of Technology, Melbourne, U.S.A.
M.M. Baarmand,[32] S. Guragain, M. Hohlmann, H. Kalakhety, H. Mermerkaya, R. Ralich, I. Vodopiyanov

University of Illinois at Chicago (UIC), Chicago, U.S.A.
M.R. Adams, I.M. Anghel, L. Apanasevich, V.E. Bazterra, R.R. Betts, J. Callner, R. Cavanaugh, C. Dragoiu, E.J. Garcia-Solis, C.E. Gerber, D.J. Hofman, S. Khalatian, C. Mironov, E. Shabalina, A. Smoron, N. Varelas

The University of Iowa, Iowa City, U.S.A.
U. Akgun, E.A. Albayrak, B. Bilki, K. Cankocak,[33] K. Chung, W. Clarida, F. Duru, C.K. Lae, E. McCliment, J.-P. Merlo, A. Mestvirishvili, A. Moeller, J. Nachtman, C.R. Newsom, E. Norbeck, J. Olson, Y. Onel, F. Ozok, S. Sen, J. Wetzel, T. Yetkin, K. Yi

Johns Hopkins University, Baltimore, U.S.A.
B.A. Barnett, B. Blumenfeld, A. Bonato, C. Eskew, D. Fehling, G. Giurgiu, A.V. Gritsan, Z.J. Guo, G. Hu, P. Maksimovic, S. Rappoccio, M. Swartz, N.V. Tran

The University of Kansas, Lawrence, U.S.A.
P. Baringer, A. Bean, G. Benelli, O. Grachov, M. Murray, V. Radicci, S. Sanders, J.S. Wood, V. Zhukova

Kansas State University, Manhattan, U.S.A.
D. Bandurin, A.F. Barfuss, T. Bolton, I. Chakaberia, K. Kaadze, Y. Maravin, S. Shrestha, I. Svintradze, Z. Wan

Lawrence Livermore National Laboratory, Livermore, U.S.A.
J. Gronberg, D. Lange, D. Wright

University of Maryland, College Park, U.S.A.
D. Baden, M. Boutemeur, S.C. Eno, D. Ferencek, N.J. Hadley, R.G. Kellogg, M. Kirn, K. Rossato, P. Rumerio, F. Santanastasio, A. Skuja, J. Temple, M.B. Tonjes, S.C. Tonwar, E. Twedt

Massachusetts Institute of Technology, Cambridge, U.S.A.
B. Alver, G. Bauer, J. Bendavid, W. Busza, E. Butz, I.A. Cali, M. Chan, D. D'Enterria, P. Everaerts, G. Gomez Ceballos, M. Goncharov, K.A. Hahn, P. Harris, Y. Kim, M. Klute, Y.-J. Lee, W. Li, C. Loizides, P.D. Luckey, T. Ma, S. Nahn, C. Paus, C. Roland, G. Roland, M. Rudolph, G.S.F. Stephans, K. Sumorok, K. Sung, E.A. Wenger, B. Wyslouch, S. Xie, Y. Yilmaz, A.S. Yoon, M. Zanetti

University of Minnesota, Minneapolis, U.S.A.
P. Cole, S.I. Cooper, P. Cushman, B. Dahmes, A. De Benedetti, P.R. Dudero, G. Franzoni, J. Haupt, K. Klapoetke, Y. Kubota, J. Mans, D. Petyt, V. Rekovic, R. Rusack, M. Sasseville, A. Singovsky

University of Mississippi, University, U.S.A.
L.M. Cremaldi, R. Godang, R. Kroeger, L. Perera, R. Rahmat, D.A. Sanders, P. Sonnek, D. Summers

University of Nebraska-Lincoln, Lincoln, U.S.A.
K. Bloom, S. Bose, J. Butt, D.R. Claes, A. Dominguez, M. Eads, J. Keller, T. Kelly, I. Kravchenko, J. Lazo-Flores, C. Lundstedt, H. Malbouisson, S. Malik, G.R. Snow

State University of New York at Buffalo, Buffalo, U.S.A.
U. Baur, I. Iashvili, A. Kharchilava, A. Kumar, K. Smith, M. Strang

Northeastern University, Boston, U.S.A.
G. Alverson, E. Barberis, D. Baumgartel, O. Boeriu, S. Reucroft, J. Swain, D. Wood

Northwestern University, Evanston, U.S.A.
A. Anastassov, A. Kubik, R.A. Ofierzynski, A. Pozdnyakov, M. Schmitt, S. Stoynev, M. Velasco, S. Won

University of Notre Dame, Notre Dame, U.S.A.
L. Antonelli, D. Berry, M. Hildreth, C. Jessop, D.J. Karmgard, J. Kolb, T. Kolberg, K. Lannon, S. Lynch, N. Marinelli, D.M. Morse, R. Ruchti, N. Valls, J. Warchol, M. Wayne, J. Ziegler

The Ohio State University, Columbus, U.S.A.
B. Bylsma, L.S. Durkin, J. Gu, P. Killewald, T.Y. Ling, G. Williams

Princeton University, Princeton, U.S.A.
N. Adam, E. Berry, P. Elmer, D. Gerbaudo, V. Halyo, A. Hunt, J. Jones, E. Laird, D. Lopes Pegna, D. Marlow, T. Medvedeva, M. Mooney, J. Olsen, P. Piroué, D. Stickland, C. Tully, J.S. Werner, A. Zuranski

University of Puerto Rico, Mayaguez, U.S.A.
J.G. Acosta, X.T. Huang, A. Lopez, H. Mendez, S. Oliveros, J.E. Ramirez Vargas, A. Zatzerklyaniy

Purdue University, West Lafayette, U.S.A.
E. Alagoz, V.E. Barnes, G. Bolla, L. Borrello, D. Bortoletto, A. Everett, A.F. Garfinkel, Z. Gecse, L. Gutay, M. Jones, O. Koybasi, A.T. Laasanen, N. Leonardo, C. Liu,

V. Maroussov, P. Merkel, D.H. Miller, N. Neumeister, K. Potamianos, A. Sedov, I. Shipsey, D. Silvers, H.D. Yoo, Y. Zheng

Purdue University Calumet, Hammond, U.S.A.
P. Jindal, N. Parashar

Rice University, Houston, U.S.A.
V. Cuplov, K.M. Ecklund, F.J.M. Geurts, J.H. Liu, M. Matveev, J. Morales, B.P. Padley, R. Redjimi, J. Roberts

University of Rochester, Rochester, U.S.A.
B. Betchart, A. Bodek, Y.S. Chung, P. de Barbaro, R. Demina, H. Flacher, A. Garcia-Bellido, Y. Gotra, J. Han, A. Harel, S. Korjenevski, D.C. Miner, D. Orbaker, G. Petrillo, D. Vishnevskiy, M. Zielinski

The Rockefeller University, New York, U.S.A.
A. Bhatti, L. Demortier, K. Goulianos, K. Hatakeyama,[34] G. Lungu, C. Mesropian, M. Yan

Rutgers, the State University of New Jersey, Piscataway, U.S.A.
O. Atramentov, Y. Gershtein, E. Halkiadakis, D. Hits, A. Lath, K. Rose, S. Schnetzer, S. Somalwar, R. Stone, S. Thomas

University of Tennessee, Knoxville, U.S.A.
G. Cerizza, M. Hollingsworth, S. Spanier, Z.C. Yang, A. York

Texas A&M University, College Station, U.S.A.
J. Asaadi, R. Eusebi, J. Gilmore, A. Gurrola, T. Kamon, V. Khotilovich, C.N. Nguyen, J. Pivarski, A. Safonov, S. Sengupta, D. Toback, M. Weinberger

Texas Tech University, Lubbock, U.S.A.
N. Akchurin, C. Jeong, S.W. Lee, Y. Roh, A. Sill, I. Volobouev, R. Wigmans, E. Yazgan

Vanderbilt University, Nashville, U.S.A.
E. Brownson, D. Engh, C. Florez, W. Johns, P. Kurt, P. Sheldon

University of Virginia, Charlottesville, U.S.A.
M.W. Arenton, M. Balazs, M. Buehler, S. Conetti, B. Cox, R. Hirosky, A. Ledovskoy, C. Neu, R. Yohay

Wayne State University, Detroit, U.S.A.
S. Gollapinni, K. Gunthoti, R. Harr, P.E. Karchin, M. Mattson

University of Wisconsin, Madison, U.S.A.
M. Anderson, M. Bachtis, J.N. Bellinger, D. Carlsmith, S. Dasu, J. Efron, K. Flood, L. Gray, K.S. Grogg, M. Grothe, R. Hall-Wilton,[1] P. Klabbers, J. Klukas, A. Lanaro, C. Lazaridis, J. Leonard, D. Lomidze, R. Loveless, A. Mohapatra, D. Reeder, A. Savin, W.H. Smith, J. Swanson, M. Weinberg

†: Deceased
1: Also at CERN, European Organization for Nuclear Research, Geneva, Switzerland
2: Also at Universidade Federal do ABC, Santo Andre, Brazil
3: Also at Université de Haute-Alsace, Mulhouse, France
4: Also at Centre de Calcul de l'Institut National de Physique Nucleaire et de Physique des Particules (IN2P3), Villeurbanne, France
5: Also at Moscow State University, Moscow, Russia
6: Also at Institute of Nuclear Research ATOMKI, Debrecen, Hungary
7: Also at University of California, San Diego, La Jolla, U.S.A.
8: Also at Tata Institute of Fundamental Research - HECR, Mumbai, India
9: Also at University of Visva-Bharati, Santiniketan, India
10: Also at Facoltà Ingegneria Università di Roma "La Sapienza", Roma, Italy
11: Also at Università della Basilicata, Potenza, Italy
12: Also at Laboratori Nazionali di Legnaro dell' INFN, Legnaro, Italy
13: Also at California Institute of Technology, Pasadena, U.S.A.
14: Also at Faculty of Physics of University of Belgrade, Belgrade, Serbia
15: Also at Laboratoire Leprince-Ringuet, Ecole Polytechnique, IN2P3-CNRS, Palaiseau, France
16: Also at Université de Genève, Geneva, Switzerland
17: Also at Scuola Normale e Sezione dell' INFN, Pisa, Italy
18: Also at University of Athens, Athens, Greece
19: Also at Eötvös Loránd University, Budapest, Hungary
20: Also at The University of Kansas, Lawrence, U.S.A.
21: Also at Institute for Theoretical and Experimental Physics, Moscow, Russia
22: Also at Paul Scherrer Institut, Villigen, Switzerland
23: Also at Vinca Institute of Nuclear Sciences, Belgrade, Serbia
24: Also at Mersin University, Mersin, Turkey
25: Also at Izmir Institute of Technology, Izmir, Turkey
26: Also at Kafkas University, Kars, Turkey
27: Also at Suleyman Demirel University, Isparta, Turkey
28: Also at Ege University, Izmir, Turkey
29: Also at Rutherford Appleton Laboratory, Didcot, United Kingdom
30: Also at INFN Sezione di Perugia; Università di Perugia, Perugia, Italy
31: Also at Institute for Nuclear Research, Moscow, Russia
32: Also at Institute for Studies in Theoretical Physics & Mathematics (IPM), Tehran, Iran
33: Also at Istanbul Technical University, Istanbul, Turkey
34: Also at Baylor University, Waco, U.S.A.

Contents

1 Introduction

Measurements of transverse-momentum (p_{T}) and pseudorapidity (η) distributions are reported for charged hadrons produced in proton-proton (pp) collisions at centre-of-mass energies ($\sqrt{s}$) of 0.9 and 2.36 TeV at the CERN Large Hadron Collider (LHC) [1]. The data were recorded with the Compact Muon Solenoid (CMS) experiment in December 2009 during two 2-hour periods of the LHC commissioning, demonstrating the readiness of CMS in the early phase of LHC operations. The results at $\sqrt{s} = 2.36$ TeV represent the highest-energy measurements at a particle collider to date.

The majority of pp collisions are soft, i.e., without any hard scattering of the partonic constituents of the proton. In contrast to the higher-p_{T} regime, well described by perturbative QCD, particle production in soft collisions is generally modelled phenomenologically to describe the different pp scattering processes: elastic scattering, single-diffractive and double-diffractive dissociation, and inelastic non-diffractive scattering [2].

The measurements presented in this paper are the inclusive primary charged-hadron multiplicity densities ($dN_{\mathrm{ch}}/dp_{\mathrm{T}}$ and $dN_{\mathrm{ch}}/d\eta$) in the pseudorapidity range $|\eta| < 2.4$, where p_{T} is the momentum of the particle transverse to the beam axis, and where N_{ch} is the number of charged hadrons in any given η or p_{T} interval. The pseudorapidity η is defined as $-\ln[\tan(\theta/2)]$, where θ is the polar angle of the particle with respect to the anti-clockwise beam direction.

Primary charged hadrons are defined as all charged hadrons produced in the interactions, including the products of strong and electromagnetic decays, but excluding products of weak decays and hadrons originating from secondary interactions. In this paper, the multiplicity densities are measured for inelastic non-single-diffractive (NSD) interactions to minimize the model dependence of the necessary corrections for the event selection, and to enable a comparison with earlier experiments. The event selection was therefore designed to retain a large fraction of inelastic double-diffractive (DD) and non-diffractive (ND) events, while rejecting all elastic and most single-diffractive dissociation (SD) events.

Measurements of $dN_{\mathrm{ch}}/dp_{\mathrm{T}}$ and $dN_{\mathrm{ch}}/d\eta$ distributions and their $\sqrt{s}$ dependence are important for understanding the mechanisms of hadron production and the relative roles of soft and hard scattering contributions in the LHC energy regime. Furthermore, the measurements at the highest collision energy of 2.36 TeV are a first step towards understanding inclusive particle production at a new energy frontier. These measurements will be particularly relevant for the LHC as, when it is operated at design luminosity, rare signal events will be embedded in a background of more than 20 near-simultaneous minimum-bias collisions. These results will also serve as a reference in the measurement of nuclear-medium effects in PbPb collisions at the LHC. The differences in these distributions between pp and $\mathrm{p\bar{p}}$ collisions are expected to be smaller than the attainable precision of these measurements [3]. The results reported here at $\sqrt{s} = 0.9$ TeV can therefore be directly compared to those previously obtained in $\mathrm{p\bar{p}}$ collisions.

This paper is organized as follows. In section 2, the elements of the CMS detector relevant to this analysis are outlined. In sections 3 and 4, the event selection and reconstruction algorithms are described. Results on $dN_{\mathrm{ch}}/dp_{\mathrm{T}}$ and $dN_{\mathrm{ch}}/d\eta$ are presented in section 5 and compared with previous $\mathrm{p\bar{p}}$ and pp measurements in section 6.

2 The CMS detector

A detailed description of the CMS experiment can be found in ref. [4]. The central feature of the CMS apparatus is a superconducting solenoid of 6 m internal diameter, providing a uniform magnetic field of 3.8 T. Immersed in the magnetic field are the pixel tracker, the silicon-strip tracker (SST), the lead-tungstate crystal electromagnetic calorimeter (ECAL) and the brass/scintillator hadron calorimeter (HCAL). In addition to barrel and end-cap detectors for ECAL and HCAL, the steel/quartz-fibre forward calorimeter (HF) covers the region of $|\eta|$ between 2.9 and 5.2. The HF tower segmentation in η and azimuthal angle ϕ (expressed in radians) is 0.175×0.175, except for $|\eta|$ above 4.7 where the segmentation is 0.175×0.35. Muons are measured in gas-ionization detectors embedded in the steel return yoke.

The tracker consists of 1440 silicon-pixel and 15 148 silicon-strip detector modules and measures charged particle trajectories within the nominal pseudorapidity range $|\eta| < 2.5$. The pixel tracker consists of three 53.3 cm long barrel layers and two end-cap disks on each side of the barrel section. The innermost barrel layer has a radius of 4.4 cm, while for the second and third layers the radii are 7.3 cm and 10.2 cm, respectively. The tracker is designed to provide an impact-parameter resolution of about 100 μm and a transverse-momentum resolution of about 0.7 % for 1 GeV/c charged particles at normal incidence (η=0) [5].

During the data-taking period addressed by this analysis, 98.4% of the pixel and 97.2% of the SST channels were operational. The fraction of noisy pixel channels was less than 10^{-5}. The signal-to-noise ratio in the SST depends on the sensor thickness and was measured to be between 28 and 36, consistent with the design expectations and cosmic-ray measurements [5, 6]. The tracker was aligned as described in ref. [7] using cosmic ray data prior to the LHC commissioning. The precision achieved for the positions of the detector modules with respect to particle trajectories is 3-4 μm in the barrel for the coordinate in the bending plane.

Two elements of the CMS detector monitoring system, the Beam Scintillator Counters (BSCs) [4, 8] and the Beam Pick-up Timing for the eXperiments (BPTX) devices [4, 9], were used to trigger the detector readout. The two BSCs are located at a distance of $\pm$10.86 m from the nominal interaction point (IP) and are sensitive in the $|\eta|$ range from 3.23 to 4.65. Each BSC is a set of 16 scintillator tiles. The BSC elements have a time resolution of 3 ns and an average minimum-ionizing-particle detection efficiency of 96.3%, and are designed to provide hit and coincidence rates. The two BPTX devices, located around the beam pipe at a distance of $\pm$175 m from the IP on either side, are designed to provide precise information on the bunch structure and timing of the incoming beam, with better than 0.2 ns time resolution.

The CMS experiment uses a right-handed coordinate system, with the origin at the nominal interaction point, the x axis pointing to the centre of the LHC, the y axis pointing up (perpendicular to the LHC plane) and the z axis along the anticlockwise-beam direction. The azimuthal angle, ϕ, is measured in the (x,y) plane, where $\phi = 0$ is the $+x$ and $\phi = \pi/2$ is the $+y$ direction.

The detailed Monte Carlo (MC) simulation of the CMS detector response is based on Geant4 [10]. The position and width of the beam spot in the simulation were adjusted to that determined from the data. Simulated events were processed and reconstructed in the same manner as collision data.

3 Event selection

This analysis uses two LHC collision data sets collected with pp interaction rates of about 11 and 3 Hz at $\sqrt{s} = 0.9$ and 2.36 TeV, respectively. At these rates, the probability for more than one inelastic collision to occur in the same proton bunch crossing is less than 2×10^{-4} at both collision energies.

Centre-of-mass Energy	0.9 TeV	2.36 TeV
Selection	Number of Events	
BPTX Coincidence + one BSC Signal	72 637	18 074
One Pixel Track	51 308	13 029
HF Coincidence	40 781	10 948
Beam Halo Rejection	40 741	10 939
Beam Background Rejection	40 647	10 905
Valid Event Vertex	40 320	10 837

Table 1. Numbers of events per data sample used in this analysis. The offline event selection criteria are applied in sequence, i.e., each line includes the selection of the lines above.

Events were selected by a trigger signal in any of the BSC scintillators, coincident with a signal from either of the two BPTX detectors indicating the presence of at least one proton bunch crossing the IP. From these samples, collision events were selected offline by requiring BPTX signals from both beams passing the IP and at least one reconstructed charged particle trajectory in the pixel detector originating from within 0.2 cm of the beam position in the transverse direction (section 4.1). The total number of collision events and the numbers of collision events passing each requirement are listed in table 1.

To select NSD events, a coincidence of at least one HF calorimeter tower with more than 3 GeV total energy on each of the positive and negative sides of the HF was required. Events containing beam-halo muons crossing the detector were identified by requiring the time difference between any two hits from the BSC stations on opposite sides of the IP to be within 73 ± 20 ns. Such events were removed from the data sample. Beam-induced background events producing an anomalously large number of pixel hits were excluded by rejecting events with pixel clusters (section 4.2) inconsistent with a pp collision vertex. This rejection algorithm was only applied for events with more than 150 pixel clusters, providing a clean separation between collision events and beam background events. Finally, events were required to contain at least one reconstructed primary vertex, as described in section 4.

To study beam-induced background, the event selection criteria were also applied to a data sample obtained by selecting events with only a single unpaired bunch crossing the IP. The contamination of background events in the colliding-bunch data sample was estimated by taking into account the total unpaired and paired bunch intensities and was found to be negligible (<0.1%). The total number of cosmic-ray muons in the selected data sample was estimated to be less than one event, and was also neglected.

The event selection criteria are expected to have high efficiency for the NSD part of the pp cross section, while rejecting a large fraction of the SD component of pp interactions. The efficiency of the event selection for the different processes and centre-of-mass energies was determined using simulated events obtained from the PYTHIA [11] (version 6.420, tune D6T, [12]) and PHOJET [13, 14] (version 1.12-35) event generators processed with a MC simulation of the CMS detector response (hereafter simply called PYTHIA and PHOJET). In the case of PHOJET, the discussion and numerical values concerning the DD process given

	PYTHIA				PHOJET			
Energy	0.9 TeV		2.36 TeV		0.9 TeV		2.36 TeV	
	Frac.	Sel. Eff.	Frac.	Sel. Eff.	Frac.	Sel. Eff.	Frac.	Sel. Eff.
SD	22.5%	16.1%	21.0%	21.8%	18.9%	20.1%	16.2%	25.1%
DD	12.3%	35.0%	12.8%	33.8%	8.4%	53.8%	7.3%	50.0%
ND	65.2%	95.2%	66.2%	96.4%	72.7%	94.7%	76.5%	96.5%
NSD	77.5%	85.6%	79.0%	86.2%	81.1%	90.5%	83.8%	92.4%

Table 2. Expected fractions of SD, DD, ND and NSD processes ("Frac.") obtained from the PYTHIA and PHOJET event generators before any selection and the corresponding selection efficiencies ("Sel. Eff.") determined from the MC simulation.

in this paper contain both the DD and the Double-Pomeron-Exchange (DPE) processes. The relative event fractions of SD, DD and ND processes and event selection efficiencies at $\sqrt{s} = 0.9$ and 2.36 TeV are listed in table 2 for these two samples.

The measurements were corrected for the selection efficiency of NSD processes and for the fraction of SD events contained in the data sample after the event selection. Based on the PYTHIA (PHOJET) event generator, the fractions of SD events contained in the selected data samples were estimated to be 5.2% (4.9%) at 0.9 TeV and 6.3% (5.0%) at 2.36 TeV.

The generated charged-hadron multiplicity distribution is shown in figure 1a in the range $|\eta| < 2.5$ for all inelastic events after event selection. The event selection efficiency for NSD events is shown in figure 1b as a function of generated charged-hadron multiplicity in the region $|\eta| < 2.5$. The correction for the event selection efficiency was applied as a function of number of reconstructed charged particles per event, as illustrated at generator level in figures 1a and 1b.

The sum of the corrections to the $dN_{\rm ch}/d\eta$ measurements due to the NSD event selection efficiency and the SD event contamination typically amounts to 8%. The corrections applied in the analysis are based on PYTHIA using the default SD and DD process fractions as listed in table 2.

The PYTHIA predictions for the SD and DD fractions differ from those of PHOJET, and are not fully consistent with existing measurements, as explained in section 5. These differences propagate to a systematic uncertainty of 2% in the $dN_{\rm ch}/d\eta$ measurement. To estimate the additional systematic uncertainty on the event selection efficiency correction resulting from the possible inaccuracies in the detector simulation, the analysis was repeated after replacing the HF event-selection criterion with a two-sided hit coincidence of signals in the BSC detectors. Based on this comparison, an additional 1% systematic uncertainty was assigned to the $dN_{\rm ch}/d\eta$ measurements.

4 Reconstruction algorithms

The analysis presented in this paper measures the $dN_{\rm ch}/d\eta$ and $dN_{\rm ch}/dp_{\rm T}$ distributions of primary charged hadrons. The $dN_{\rm ch}/d\eta$ distributions were obtained using three methods based on counting of (i) reconstructed clusters in the pixel barrel detector; (ii) pixel

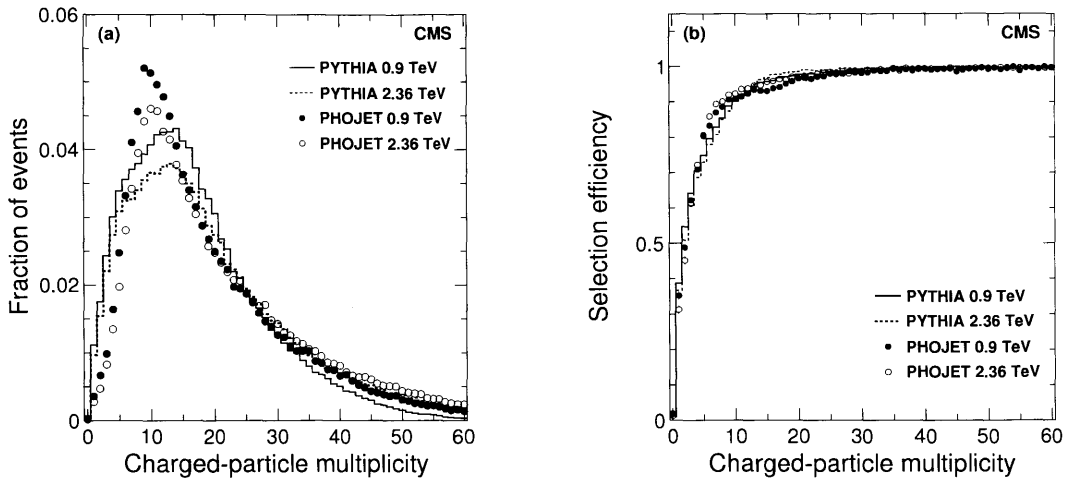

Figure 1. (a) Generated multiplicity distributions of primary charged hadrons in the range $|\eta| < 2.5$ for $\sqrt{s} = 0.9$ TeV (solid dots and histogram) and 2.36 TeV (open circles and dashed histogram) after the event selection is applied to the reconstructed events, using inelastic events from the PYTHIA (histograms) and PHOJET (symbols) event generators. (b) The event selection efficiency expected for NSD events from the PYTHIA (histograms) and PHOJET (symbols) event generators as a function of generated charged hadron multiplicity in the region $|\eta| < 2.5$.

tracklets composed of pairs of clusters in different pixel barrel layers; and (iii) tracks reconstructed in the full tracker volume, combining the pixel and strip hits. The cluster counting method provides an independent measurement for each pixel barrel layer, and the tracklet method for each pair of layers. The third method also allows a measurement of the $dN_{\mathrm{ch}}/dp_{\mathrm{T}}$ distribution. All three methods rely on the reconstruction of the primary vertex (PV) described in section 4.1.

The pixel-cluster-counting method has the advantage of having the largest p_T acceptance down to small transverse momentum (30 MeV/c), is insensitive to geometrical misalignment of the detector and does not require detailed knowledge of the primary vertex position resolution. A potential disadvantage is the sensitivity to backgrounds from collisions with residual gas in the beam pipe (beam-gas collisions), from secondary particles produced in the detector material and from low-p_{T} particles curling in the axial magnetic field (loopers). The pixel-tracklet method is capable of measuring and correcting for the combinatorial background and has a p_{T} threshold of 50 MeV/c. The third method uses the tracker (pixel and SST) to build tracks. It requires at least two pixel hits in different layers, has the largest p_{T} threshold ($\approx$100 MeV/c) and algorithmic complexity, but is the most robust against background hits produced by particles not originating from the collision. The charged-particle multiplicity was corrected in all three methods for the small contamination ($< 1\%$) of primary charged leptons. The measured $dN_{\mathrm{ch}}/d\eta$ values were evaluated by extrapolating or correcting to $p_{\mathrm{T}} = 0$ for all the three analysis methods.

The three reconstruction methods are described in sections 4.2–4.4.

4.1 Primary vertex reconstruction

The x, y and z positions of the luminous region where protons of both beams interact, hereafter referred to as beam spot, are obtained for each data set from three-dimensional vertex fits based on tracks reconstructed with $p_{\mathrm{T}} > 0.9$ GeV/c, using the full event sample. The RMS of the beam spot in the transverse directions was found to be less than 0.05 cm. The beam spot position and dimensions were found to be stable within a given data set.

To reconstruct the z coordinate of the PV for each event, tracks consisting of triplets of pixel hits were formed. The minimum transverse momentum of these tracks is ≈ 75 MeV/c. The tracks were required to originate from the vicinity of the beam spot with a transverse impact parameter (d_{T}) smaller than 0.2 cm. Of these tracks, only those with $d_{\mathrm{T}} < 4\,\sigma_{\mathrm{T}}$, where σ_{T} is the quadratic sum of the uncertainty in d_{T} and the RMS of the beam spot in the transverse direction, were used in the vertex reconstruction.

The vertex-reconstruction algorithm uses the z coordinate of the tracks at the point of closest approach to the beam axis and the corresponding estimated measurement uncertainty (σ_z). It performs an agglomerative clustering by adding tracks to form groups. These groups (denoted the i^{th} and j^{th} group) are then merged based on their normalized distance, $d_{ij}^2 = (z_i - z_j)^2/(\sigma_i^2 + \sigma_j^2)$ where σ_i and σ_j are the uncertainties of the z_i and z_j positions, with a fast nearest-neighbour search algorithm [15]. The z position and its uncertainty σ_z for the newly joined group are calculated using a weighted average. The clustering process stops when the smallest normalized distance between the remaining groups gets larger than 8.0, where the stopping condition was optimized using simulated events. Only vertices formed from at least two tracks were considered except when only one track was reconstructed in the event. In the latter case the PV position was defined as the point of the closest approach of the track to the beam axis. The fraction of single-track vertices in the selected data sample is 1.7% (1.3%) at 0.9 TeV (2.36 TeV). The overall PV reconstruction efficiency, evaluated from the data after all other event selection cuts, is in excess of 99% and the fraction of events with more than one primary vertex candidate is 5.0% (7.4%) at 0.9 TeV (2.36 TeV). In the rare case of multiple PV candidates, the vertex composed of the largest set of tracks was chosen.

The reconstructed primary vertex resolution in the z direction is a function of the associated track multiplicity (N) and was found to be parameterized adequately as $0.087\ \mathrm{cm}\ /N^{0.6}$ using simulated events.

The distribution of the reconstructed z position of the PV is shown in figure 2a. Overlaid is the PV distribution in simulated events, the position and RMS of which were adjusted to reproduce the beam spot measured in data.

4.2 Pixel cluster counting method

The pseudorapidity distribution of primary charged hadrons produced in a pp collision can be measured by counting the number of clusters they create when traversing each of the three pixel barrel layers and applying appropriate corrections, as described in this section.

The energy deposited by charged particles traversing a pixel detector layer is spread over multiple pixels. Adjacent pixels with a charge measurement above a readout threshold

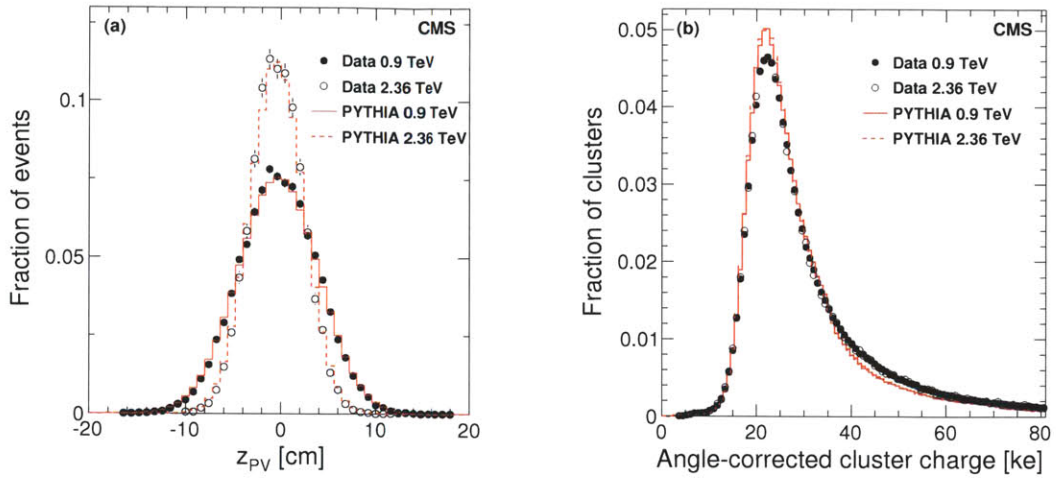

Figure 2. (a) The distribution of the reconstructed z position of the primary vertex in the data (dots), compared to that from the PYTHIA simulation (histogram). (b) Distribution of the cluster charge multiplied by $|\sin\theta|$ in the data (dots) and the simulation (histogram), for the clusters selected for analysis.

of typically 2740 electrons are combined into pixel clusters to integrate the total charge deposit [6]. The cluster size and charge depend on the incident angle of the particle with respect to the active detector surface. The cluster length along the z axis ranges from 1-2 pixels at normal incident angle up to 14-16 pixels at shallow crossing angles. Figure 2b shows the measured distribution of cluster charge multiplied by $|\sin\theta|$ (or $1/\cosh\eta$) after the cluster selection discussed below, compared to the simulation. Here, θ is the polar angle of the straight line connecting the PV to the cluster.

The peak position is consistent with the expected charge of 22 ke, while the width of the distribution is slightly larger in the data than in the simulation due to gain calibration non-uniformities.

The cluster counting method correlates the observed pixel-cluster length in the z direction, expressed in number of pixels, with the expected path length traveled by a primary particle at a given η value. For primary particles the cluster length in z is proportional to $|\cot\theta|$ (or $|\sinh\eta|$) as displayed in figure 3a. Small clusters at large $|\eta|$ are due to loopers, secondary particles and daughters of long-lived hadrons. Clusters from these background particles were efficiently removed by the cluster-length cut represented by the solid line in figure 3a. To allow for an efficient background rejection, only the barrel part of the pixel detector was used, where the detector units are parallel to the beam axis, as opposed to the pixel end-caps. Furthermore, the η range for the cluster counting was restricted to $|\eta| < 2$ to avoid acceptance problems due to the slightly off-centred position of the luminous region.

The event selection efficiency and the SD contribution for a given total multiplicity of selected clusters (M) for each pixel barrel layer can be determined from Monte Carlo simulation. The overall change of the $dN_{\rm ch}/d\eta$ value due to this correction is 9% for both collision energies.

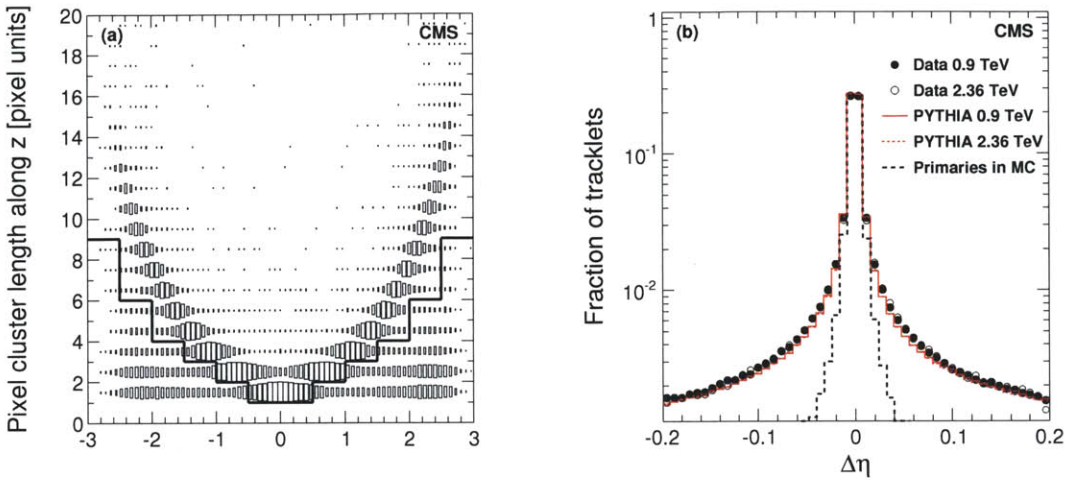

Figure 3. (a) Pixel cluster length along z as a function of η for the 900 GeV data. The solid line illustrates the cut applied in the cluster counting method. (b) The $\Delta\eta$ distribution of clusters on tracklets in the data (dots and circles), together with the distribution obtained from the PYTHIA simulation (solid and dotted lines), for both 0.9 and 2.36 TeV collision energy. The dashed line shows the $\Delta\eta$ distribution of clusters for primary charged-particle tracks in the Monte Carlo simulation at 0.9 TeV. The tail of the $\Delta\eta$ distribution comes from the combinatorial background.

The fraction of clusters created by loopers above the cluster-length cut (1% and 5% for $\eta = 2$ and $\eta = 0.5$, respectively) can be estimated by measuring the total number of clusters below the cut in data, corrected by the ratio of looper clusters below and above the cut in simulated events. The number of clusters eliminated by the cluster-length cut was found to be higher in data than in simulated events by 10-20% due to a slightly larger abundance of secondary particles and loopers, while the observed number and length distributions of clusters above the cut was found to agree with the simulation.

The corrections for absorption in the beam pipe and detector material, secondary particles, daughters of long-lived hadrons, delta-ray electrons and double hits caused by geometrically overlapping detector units were all evaluated, in bins of η and M, with simulated data. The size of these corrections is 10%, 23% and 41% for the first, second and third detector layer, respectively. Varying the charged-particle multiplicity in the event generator by 50% only causes a $\pm 3\%$ relative change in these corrections. Their dependence on η and pixel-cluster multiplicity is similarly small.

4.3 Pixel-tracklet method

This method was first used to measure charged-hadron multiplicities by the PHOBOS experiment at RHIC [16]. Pixel tracklets are constructed from combinations of two pixel hits in any two pixel barrel layers. The difference in the angular positions of the two clusters with respect to the PV, $\Delta\eta$ and $\Delta\phi$, are calculated for each tracklet. If two tracklets share a hit, the tracklet with the larger $\Delta\eta$ is discarded. The $\Delta\eta$ distribution of reconstructed

JHEP02(2010)041

tracklets is shown in figure 3b, together with the corresponding distribution from simulated data and a separate distribution for simulated primary particles only. Tracklets from primary particles display a sharp peak at $\Delta\eta = 0$, while the tracklets from the combinatorial background have an extended tail. The simulated $\Delta\eta$ distributions are in good agreement with data.

To suppress the combinatorial background, only tracklets with $|\Delta\eta| < 0.1$ and $|\Delta\phi| < 1.0$ were selected. Since the combinatorial background is flat in $\Delta\phi$, the remaining fraction of background tracklets in the signal region $|\Delta\phi| < 1.0$ can be estimated from tracklets with $1.0 < |\Delta\phi| < 2.0$. This data-driven estimate of the background accurately describes the raw $\Delta\eta$ distribution of tracklets for $|\Delta\eta| > 2$, where no signal from primary particles is expected from the MC simulation. Typical values of this estimated background fraction in the signal region increase with $|\eta|$ from 2% to 30%. The η range for the tracklet method was restricted to $|\eta| < 2$ to avoid a large acceptance correction.

The contribution from secondary particles, reconstruction efficiency and geometrical acceptance needs to be accounted for to determine the number of primary charged hadrons. These correction factors were calculated using PYTHIA simulations for background-subtracted tracklets in bins of z position of the PV, pseudorapidity, and tracklet multiplicity. The magnitude of the correction varies with $|\eta|$ from 0 to 20%. The correction factors were also cross-checked by PHOJET simulations and only cause a 2-3% change in the $dN_{\rm ch}/d\eta$ result.

The correction for the event selection efficiency and the SD contribution was determined for each tracklet multiplicity bin. The overall change in the $dN_{\rm ch}/d\eta$ value due to this correction is about 8% at $\eta = 0$.

4.4 Tracking method

Pixel and SST detectors were used to reconstruct tracks, including both barrel and endcap layers. The acceptance was limited to $|\eta| < 2.4$ to avoid edge effects. The iterative reconstruction procedure described below follows refs. [17, 18], but was further optimized for primary-track reconstruction in minimum bias events.

In the first step of track reconstruction, tracks with three pixel hits (triplets) are built using the x and y positions of the beam spot and the z coordinate of the primary vertex as constraints. These clean pixel tracks are used as seeds for the Kalman-filter-based trajectory-building algorithm in the SST. The resulting trajectories are stored. Before the second tracking step, the pixel and strip hits associated with the tracks found in the first step are removed from further consideration. The second step uses pixel triplet seeds as well, but does not require a vertex constraint and has a looser transverse impact parameter requirement than in the first step. After removal of hits associated with tracks found in the second step, the third tracking step finds primary tracks seeded by two hits in the pixel detector. At least three hits were required for a track to be accepted.

Tracks found during the three iterative steps were collected and a second iteration of the PV reconstruction, as described in section 4.1, was performed to refine primary vertex position determination. Finally, the tracks were refit with the corresponding vertex constraint, thus improving their η and $p_{\rm T}$ resolution.

In this analysis, a reconstructed track was considered as a primary-track candidate if it is compatible with originating from the PV ($d_{\mathrm{T}} < \min(4\sigma_{\mathrm{T}}, 0.2\ \mathrm{cm})$ and $d_z < 4\sigma_z$, where d_z is the distance between the point of the closest approach of the track to the beam axis and the PV along the z direction).

Studies with simulated events showed that the combined geometrical acceptance and reconstruction efficiency for the tracking method exceeds 50% around $p_{\mathrm{T}} \approx 0.1$, 0.2 and 0.3 GeV/$c$ for pions, kaons and protons, respectively. The efficiency is about 96% in the $|\eta| < 1$ region for $p_{\mathrm{T}} > 0.25$ GeV/c, and is above 80% for pions at $p_{\mathrm{T}} = 0.15$ GeV/c. By requiring the geometrical shapes of the pixel clusters to be consistent with the crossing angle and direction of the track, the fraction of fake tracks was kept below 1%. The fraction of duplicated tracks (e.g., from loopers) was estimated to be about 0.1% in the central region, rising to 0.5% at large $|\eta|$.

The measured yield in data was corrected, based on MC simulation and comparisons with data, for geometrical acceptance (2% correction for $p_T > 200$ MeV/c), efficiency of the reconstruction algorithm (5-10% for $p_T > 300$ MeV/c), fake and duplicate tracks (<1% each). The contamination of less than 2% from decay products of long-lived hadrons, photon conversions and inelastic hadronic interactions with the detector material was also subtracted. To obtain the $dN_{\mathrm{ch}}/d\eta$ result from the p_{T} spectrum, an extrapolation to $p_{\mathrm{T}} = 0$ was necessary, resulting in an increase of 5% in the estimated number of charged hadrons.

Corrections based on the average hit efficiency of pixel layers, size of the beam spot, longitudinal and transverse impact-parameter resolutions of pixel tracks were validated with data. As an example, the average number of pixel and strip hits found on tracks in the range $|\eta| < 1$ is shown in figures 4a and 4b, together with the expectation from PYTHIA. Somewhat fewer particles are predicted with $p_T < 500$ MeV/c than seen in the data, which results in the small difference in the number of tracks with few SST hits in figure 4b. This small difference, which originates from limitations of the PYTHIA generator, does not affect the final measurement. The correction for the event selection efficiency and the SD contribution was determined for each track multiplicity bin, and has an overall magnitude of 8.3%.

5 Results

5.1 Systematic uncertainties

Various corrections and their event-selection and model dependence contribute to the systematic uncertainties of the measured quantities. A summary of these systematic uncertainties averaged over η and p_{T} is given in table 3 and discussed below.

The uncertainties related to the trigger bias and to the event selection are common to all the analysis methods. The efficiency of the trigger and event-selection was corrected for by the prediction of the PYTHIA D6T event generator combined with the full Geant4 simulation of the CMS detector. The material description relevant for this analysis was verified by studies of photon conversion probabilities in the data, found to be in agreement with those obtained from the simulation.

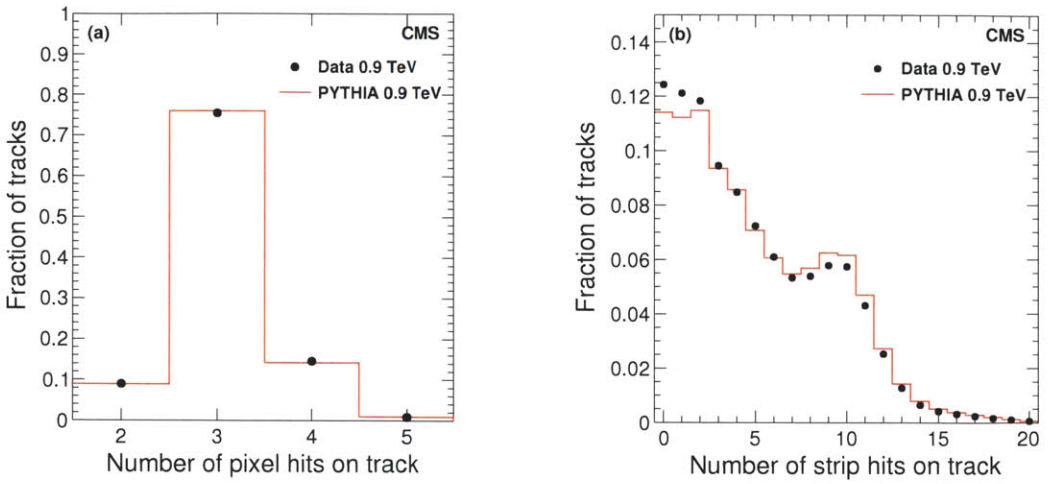

Figure 4. (a) The distribution of the number of pixel hits attached to reconstructed tracks in the region of $|\eta| < 1$ (closed circles), compared to the CMS detector simulation (histogram). (b) The distribution of the number of hits in the SST detector attached to reconstructed tracks in the region of $|\eta| < 1$ (closed circles), compared to the CMS detector simulation (histogram).

Because single- and double-diffractive pp collisions have much smaller charged-hadron multiplicities per event than non-diffractive events, they contribute to the uncertainty in the measured $dN_{\mathrm{ch}}/d\eta$ mostly through the uncertainty in the fraction of SD and DD events passing the event selection criteria. The fractions of SD events for $\sqrt{s} = 0.9$ TeV in PYTHIA and PHOJET (table 2) are 23% and 19%, respectively. The UA5 experiment measured 15.5% for this fraction [19]. Based on the simulated trigger efficiencies for the different event types, only 5.5% of events passing the analysis event selection are expected to be single-diffractive events. From the aforementioned variations of SD fractions, an uncertainty of $\pm 1\%$ is attributed to this correction. The contribution of the uncertainty of the fraction of DD events was estimated similarly to be $\pm 1\%$. Since underestimated DD and SD fractions both lead to an underestimated $dN_{\mathrm{ch}}/d\eta$ result, a conservative linear sum of 2% was assigned to the above systematic uncertainty. The trigger efficiency of the BSC is more than 98% for events with a valid vertex, and even a 5% uncertainty in single-particle detection efficiency of its individual segments results in a negligible uncertainty in the final result. The trigger efficiency of the BSC and the event selection efficiency of the HF detector were both measured from data and found to be consistent within 1% with the MC simulation. The total systematic uncertainty from propagating all event selection and trigger related uncertainties is 3%. The measurement of the average transverse momentum is less sensitive to the trigger selection efficiency. A smaller, 1% uncertainty was therefore assigned to that result.

The geometrical acceptance was studied by comparing the hit occupancy of the pixel barrel with the predictions from the simulation. The efficiency of the pixel hit reconstruction was estimated using tracks propagated from the SST to the pixel detector and

by extrapolating pixel tracklets to the unused pixel barrel layer. The measured pixel hit efficiency was found to exceed 99% with a 0.5% uncertainty from both methods, which propagates into 0.5% uncertainty in the pixel-counting-based, 1% in the tracklet-based, and 0.3% in the track-based results. If the collected charge in one or more pixels in a cluster remains below the threshold, the cluster may be split. The splitting rate was estimated from the geometrical distance distributions of close-by pixel clusters found in the data and in the Monte Carlo simulation and found to be 0.5-0.9% in the simulation and 1.0-1.5% in data.

The uncertainty related to the cluster and tracklet selections was estimated by varying the selection cuts. An additional 3% and 2% uncertainty was assigned to the tracklet and track reconstruction algorithm efficiencies, respectively. Corrections for loopers and secondary particles are simulation dependent; the tracklet- and pixel-counting-based methods have low rejection power compared to the tracking method, thus carry a larger systematic uncertainty (as shown in table 3).

The effects of the geometrical misalignment of the pixel barrel detector were simulated and a 1% uncertainty was assigned to the results from the tracklet-based method. Hits from beam-induced backgrounds coinciding with the collision were estimated to be very rare, and a conservative 1% random hit contribution was propagated to obtain the uncertainty of the results. The corrections for multiple track counting and fake track rate were estimated from the Monte Carlo simulation and found to be less than 1%. The uncertainty of the extrapolation to the full p_T-range depends on the low-p_T reach of the three methods and varies between 0.2 and 0.5%. While the sources of uncertainties are largely independent from each other, they are correlated among all the data points.

5.2 Charged hadron transverse-momentum distributions

Tracks with $|\eta| < 2.4$ and $p_{\mathrm{T}} > 0.1$ GeV/c were used for the measurement of $dN_{\mathrm{ch}}/dp_{\mathrm{T}}$. The measured average charged-hadron yields per NSD event are shown in figure 5a, as a function of p_{T} in bins of $|\eta|$. The yields were fit by the Tsallis function (eq. (5.1)), which empirically describes both the low-p_{T} exponential and the high-p_{T} power-law behaviours [20, 21]:

$$E\frac{d^3N_{\mathrm{ch}}}{dp^3} = \frac{1}{2\pi p_T}\frac{E}{p}\frac{d^2N_{\mathrm{ch}}}{d\eta dp_T} = C(n,T,m)\frac{dN_{\mathrm{ch}}}{dy}\left(1+\frac{E_T}{nT}\right)^{-n}, \tag{5.1}$$

where $y = 0.5\ln[(E+p_z)/(E-p_z)]$ is the rapidity; $C(n,T,m)$ is a normalization constant that depends on n, T and m; $E_{\mathrm{T}} = \sqrt{m^2+p_{\mathrm{T}}^2} - m$ and m is the charged pion mass. This function provides both the inverse slope parameter T, characteristic for low p_{T}, and the exponent n, which parameterizes the high-p_{T} power-law tail. These fit parameters change by less than 5% with η, thus a fit to the whole region $|\eta| < 2.4$ was performed. The p_{T} spectrum of charged hadrons, $1/(2\pi p_{\mathrm{T}})d^2N_{\mathrm{ch}}/d\eta dp_{\mathrm{T}}$, in the region $|\eta| < 2.4$, was also fit with the empirical function (eq. (5.1)) and is shown in figure 5b. The p_{T} resolution of the CMS tracker was found to have a negligible effect on the measured spectral shape and was therefore ignored in the fit function. For the 0.9 TeV data, the inverse slope parameter and the exponent were found to be $T = 0.13 \pm 0.01$ GeV and $n = 7.7 \pm 0.2$. For the 2.36 TeV data, the values were $T = 0.14 \pm 0.01$ GeV and $n = 6.7 \pm 0.2$. The average transverse momentum, calculated from the measured data points adding the low-

Source	Pixel Counting [%]	Tracklet [%]	Tracking [%]
Correction on event selection	3.0	3.0	3.0 (1.0)
Acceptance uncertainty	1.0	1.0	1.0
Pixel hit efficiency	0.5	1.0	0.3
Pixel cluster splitting	1.0	0.4	0.2
Tracklet and cluster selection	3.0	0.5	-
Efficiency of the reconstruction	-	3.0	2.0
Correction of looper hits	2.0	1.0	-
Correction of secondary particles	2.0	1.0	1.0
Misalignment, different scenarios	-	1.0	0.1
Random hits from beam halo	1.0	0.2	0.1
Multiple track counting	-	-	0.1
Fake track rate	-	-	0.5
p_{T} extrapolation	0.2	0.3	0.5
Total, excl. common uncertainties	4.4	3.7	2.4
Total, incl. common uncert. of 3.2%	5.4	4.9	4.0 (2.8)

Table 3. Summary of systematic uncertainties. While the various sources of uncertainties are largely independent, most of the uncertainties are correlated between data points and between the analysis methods. The event selection and acceptance uncertainty is common to the three methods and affects them in the same way. The values in parentheses apply to the $\langle p_T \rangle$ measurement.

and high-p_{T} extrapolations from the fit is $\langle p_{\mathrm{T}} \rangle = 0.46 \pm 0.01$ (stat.) $\pm$ 0.01 (syst.) GeV/c for the 0.9 TeV and 0.50 ± 0.01 (stat.) $\pm$ 0.01 (syst.) GeV/c for the 2.36 TeV data.

The $dN_{\mathrm{ch}}/d\eta$ spectrum was obtained by summing the measured differential yields for $0.1 < p_{\mathrm{T}} < 3.5$ GeV/c and adding the result to the integral of the fit function for $p_{\mathrm{T}} < 0.1$ GeV/c and $p_{\mathrm{T}} > 3.5$ GeV/c. The latter term amounts to 5% of the total.

5.3 Charged hadron pseudorapidity density

The summary of results on the pseudorapidity density distribution of charged hadrons is shown in figure 6. The $dN_{\mathrm{ch}}/d\eta$ results for the three layers in the cluster-counting method and the three layer-pairs in the pixel-tracklet method are consistent within 3%. These results from the various layers and from the different layer pairs were combined to provide one set of data from each analysis method, as shown in figure 6a. The error bars include the systematic uncertainties of about 2.4–4.4% specific to each method, estimated from the variations of model parameters in the simulation used for corrections and the uncertainties in the data-driven corrections. The systematic uncertainties common to all the three methods, which amount to 3.2%, are not shown. The results from the three analysis methods are in agreement. The larger fraction of background hits in the data compared to simulation affects the cluster-counting method differently from the other two, which results in a small difference at high η, well accounted for by the systematic uncertainty of the measurement.

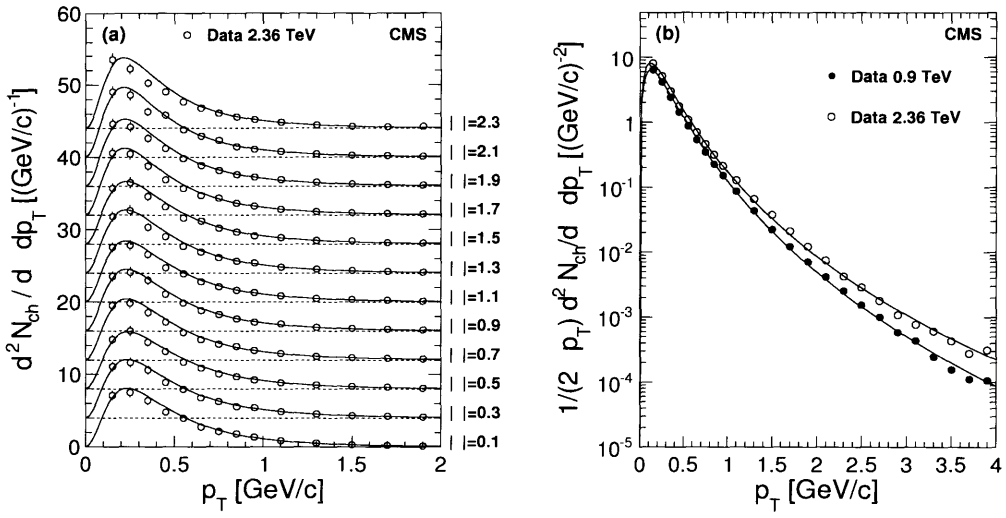

Figure 5. (a) Measured differential yield of charged hadrons in the range $|\eta| < 2.4$ in 0.2-unit-wide bins of $|\eta|$ for the 2.36 TeV data. The measured values with systematic uncertainties (symbols) and the fit functions (eq. (5.1)) are displayed. The values with increasing η are successively shifted by four units along the vertical axis. (b) Measured yield of charged hadrons for $|\eta| < 2.4$ with systematic uncertainties (symbols), fit with the empirical function (eq. (5.1)).

6 Discussion

The average transverse-momentum and pseudorapidity densities of charged hadrons derived from the measured data can be compared to results from earlier experiments as a function of the collision energy. The average transverse momentum of charged hadrons was obtained from the fits (eq. (5.1)) to the transverse-momentum spectrum (figure 5b). At low energies the energy dependence of $\langle p_{\mathrm{T}} \rangle$ can be described by a quadratic function of $\ln s$. The $\langle p_{\mathrm{T}} \rangle$ from this measurement, shown in figure 7a, follows the general trend. At 0.9 TeV it is similar to the results from $\mathrm{p\bar{p}}$ collisions at the same energy [22].

The $dN_{\mathrm{ch}}/d\eta$ distribution was calculated as the weighted average of the data from the three reconstruction methods, taking into account their systematic uncertainties, excluding the common ones, as listed in table 3. The averaged result is shown in figure 6b and compared to measurements at the same accelerator (ALICE, pp [23]) and to previous measurements at the same energy but with different colliding particles (UA5, $\mathrm{p\bar{p}}$ [24]). The shaded error band on the CMS data indicates systematic uncertainties, while the error bars on the data from UA5 and ALICE display statistical uncertainties only. No significant difference is observed between the $dN_{\mathrm{ch}}/d\eta$ distributions measured in pp and $\mathrm{p\bar{p}}$ collisions at $\sqrt{s} = 0.9$ TeV.

The $dN_{\mathrm{ch}}/d\eta$ distribution is weakly η-dependent, with a slow increase towards higher η values, and an indication of a decrease at $|\eta| > 2$ for the 0.9 TeV data. At 2.36 TeV, the entire distribution is wider due to the increased collision energy hence the larger η range

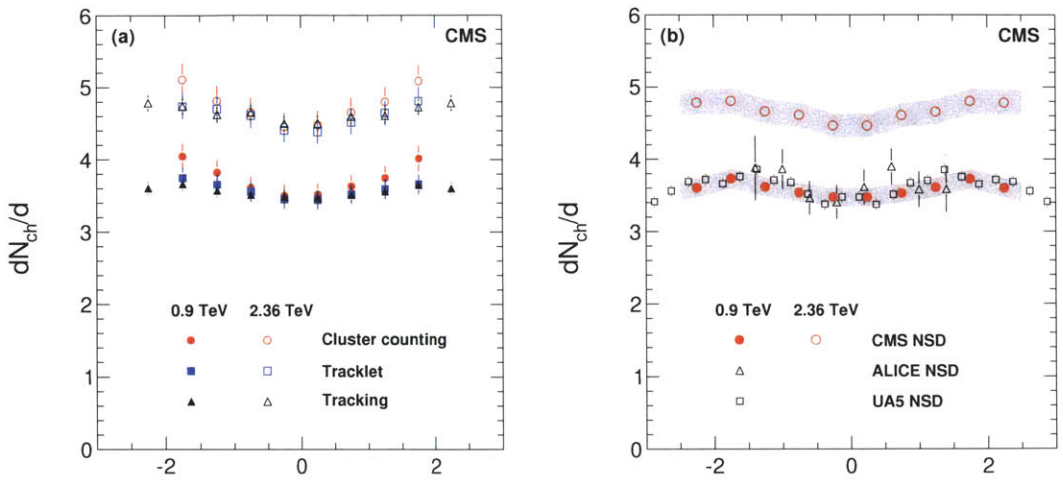

Figure 6. (a) Reconstructed $dN_{\mathrm{ch}}/d\eta$ distributions obtained from the cluster counting (dots with error bars), tracklet (squares) and tracking (triangles) methods, in pp collisions at 0.9 TeV (filled symbols) and 2.36 TeV (open symbols). The error bars include systematic uncertainties (as discussed in the text), excluding those common to all the methods. (b) Reconstructed $dN_{\mathrm{ch}}/d\eta$ distributions averaged over the cluster counting, tracklet and tracking methods (circles), compared to data from the UA5 [24] (open squares) and from the ALICE [23] (open triangles) experiments at 0.9 TeV, and the averaged result over the three methods at 2.36 TeV (open circles). The CMS and UA5 data points are symmetrized in η. The shaded band represents systematic uncertainties of this measurement, which are largely correlated point-to-point. The error bars on the UA5 and ALICE data points are statistical only.

available for inclusive particle production. For $|\eta| < 0.5$, the corrected results average to $dN_{\mathrm{ch}}/d\eta = 3.48 \pm 0.02$ (stat.) $\pm$ 0.13 (syst.) and $dN_{\mathrm{ch}}/d\eta = 4.47 \pm 0.04$ (stat.) $\pm$ 0.16 (syst.) for NSD events at $\sqrt{s}$ = 0.9 and 2.36 TeV. The increase of (28.4 $\pm$ 1.4 $\pm$ 2.6)% from 0.9 to 2.36 TeV is significantly larger than the 18.5% (14.5%) increase predicted by the PYTHIA (PHOJET) model tunes used in this analysis. The collision energy dependence of the measured $dN_{\mathrm{ch}}/d\eta|_{\eta\approx 0}$ is shown in figure 7b, which includes data from the NAL Bubble Chamber [25], the ISR [26], and UA1 [22], UA5 [24], CDF [27], STAR [28], PHOBOS [29] and ALICE [23]. The $dN_{\mathrm{ch}}/d\eta$ measurement reported here is consistent with the previously observed trend.

7 Summary

Inclusive measurements of charged-hadron densities, $dN_{\mathrm{ch}}/dp_{\mathrm{T}}$ and $dN_{\mathrm{ch}}/d\eta$, have been presented based on the first pp collisions recorded at $\sqrt{s}$ = 0.9 and 2.36 TeV by the CMS experiment during LHC commissioning in December 2009. The numerical values of the data presented in this paper can be found in ref. [30]. For NSD interac-

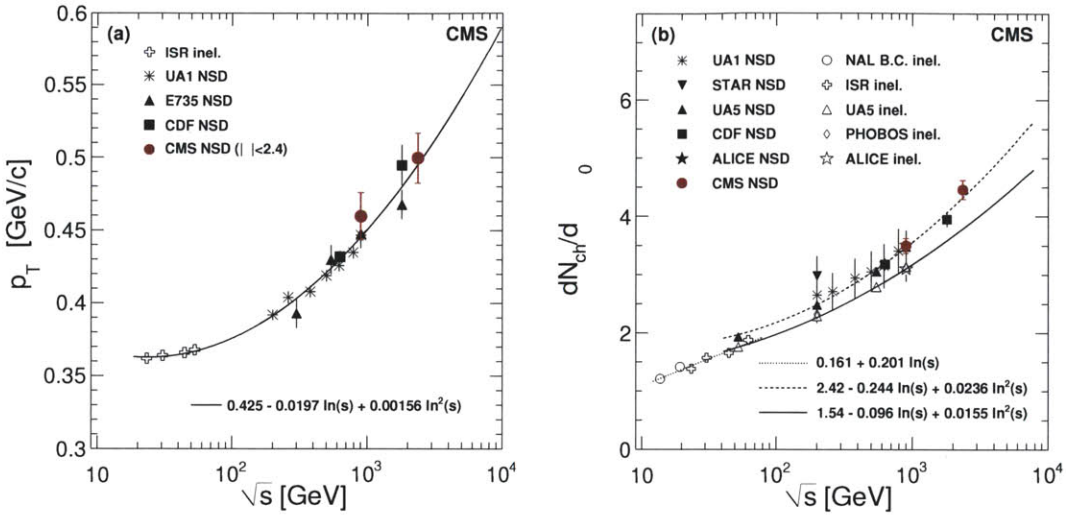

Figure 7. (a) Energy dependence of the average transverse momentum of charged hadrons. The CMS data points are evaluated for the range $|\eta| < 2.4$. Data of other experiments are taken from refs. [22, 31–33]. The curve shows the fit to the data points of the form $\langle p_{\mathrm{T}} \rangle = 0.425 - 0.0197 \ln(s) + 0.00156 \ln^2(s)$ with $\langle p_{\mathrm{T}} \rangle$ in GeV/c and s in GeV^2. The error bars on the CMS data points include systematic uncertainties. (b) Charged-hadron pseudorapidity density in the central region as a function of centre-of-mass energy in pp and p$\bar{\mathrm{p}}$ collisions including lower energy data from refs. [22–29], together with various empirical parameterizations fit to the data corresponding to the inelastic (solid and dotted curves with open symbols) and to the NSD (dashed curve with solid symbols) event selection. The error bars indicate systematic uncertainties, when available.

tions, the average charged-hadron transverse momentum has been measured to be 0.46 ± 0.01 (stat.) $\pm$ 0.01 (syst.) GeV/c at 0.9 TeV and 0.50 ± 0.01 (stat.) $\pm$ 0.01 (syst.) GeV/c at 2.36 TeV. The three reconstruction methods employed for the $dN_{\mathrm{ch}}/d\eta$ measurement have yielded consistent results, demonstrating the excellent performance and detailed understanding of the CMS tracker. The pseudorapidity density in the central region, $dN_{\mathrm{ch}}/d\eta|_{|\eta|<0.5}$, has been measured to be 3.48 ± 0.02 (stat.) $\pm$ 0.13 (syst.) at 0.9 TeV and 4.47 ± 0.04 (stat.) $\pm$ 0.16 (syst.) at 2.36 TeV. The results at 0.9 TeV have been found to be in agreement with previous measurements in p$\bar{\mathrm{p}}$ and pp collisions. With the new measurements at 2.36 TeV, which show a steeper-than-expected increase of charged-hadron multiplicity density with collision energy, the study of particle production in pp collisions has been extended into a new energy regime.

Acknowledgments

We congratulate and express our gratitude to our colleagues in the CERN accelerator departments for the excellent performance of the LHC. We thank the technical and administrative staff at CERN and other CMS Institutes, and acknowledge support from: FMSR

JHEP02(2010)041

(Austria); FNRS and FWO (Belgium); CNPq, CAPES, FAPERJ, and FAPESP (Brazil); MES (Bulgaria); CERN; CAS, MoST, and NSFC (China); COLCIENCIAS (Colombia); MSES (Croatia); RPF (Cyprus); Academy of Sciences and NICPB (Estonia); Academy of Finland, ME, and HIP (Finland); CEA and CNRS/IN2P3 (France); BMBF, DFG, and HGF (Germany); GSRT (Greece); OTKA and NKTH (Hungary); DAE and DST (India); IPM (Iran); SFI (Ireland); INFN (Italy); NRF (Korea); LAS (Lithuania); CINVESTAV, CONACYT, SEP, and UASLP-FAI (Mexico); PAEC (Pakistan); SCSR (Poland); FCT (Portugal); JINR (Armenia, Belarus, Georgia, Ukraine, Uzbekistan); MST and MAE (Russia); MSTDS (Serbia); MICINN and CPAN (Spain); Swiss Funding Agencies (Switzerland); NSC (Taipei); TUBITAK and TAEK (Turkey); STFC (United Kingdom); DOE and NSF (USA). Individuals have received support from the Marie-Curie IEF program (European Union); the Leventis Foundation; the A. P. Sloan Foundation; and the Alexander von Humboldt Foundation.

References

[1] L. Evans and P. Bryant eds., *LHC Machine*, 2008 *JINST* **3** S08001 [SPIRES].

[2] W. Kittel and E.A. De Wolf, *Soft Multihadron Dynamics*, World Scientific, Singapore (2005).

[3] J.G. Rushbrooke and B.R. Webber, *High energy anti-particle-particle reaction differences and annihilations*, *Phys. Rept.* **44** (1978) 1 [SPIRES].

[4] CMS collaboration, R. Adolphi et al., *The CMS experiment at the CERN LHC*, 2008 *JINST* **3** S08004 [SPIRES].

[5] CMS collaboration, *CMS Physics TDR: Volume I, Detector Performance and Software*, *CERN-LHCC* 2006-001 (2006).

[6] CMS collaboration, *Commissioning and Performance of the CMS Pixel Tracker with Cosmic Ray Muons*, arXiv:0911.5434 [SPIRES].

[7] CMS collaboration, *Alignment of the CMS Silicon Tracker during Commissioning with Cosmic Rays*, arXiv:0910.2505 [SPIRES].

[8] A.J. Bell, *Design and Construction of the Beam Scintillation Counter for CMS*, Master's thesis, University of Canterbury, Christchurch, New Zealand, (2008).

[9] T. Aumeyr, *Beam Phase and Intensity Monitoring for the Compact Muon Solenoid Experiment*, Master's thesis, Vienna University of Technology, Austria, (2008).

[10] GEANT4 collaboration, S. Agostinelli et al., *Geant4: a simulation toolkit*, *Nucl. Instrum. Meth.* **A506** (2003) 250.

[11] T. Sjöstrand, S. Mrenna and P.Z. Skands, *PYTHIA 6.4 Physics and Manual*, *JHEP* **05** (2006) 026 [hep-ph/0603175] [SPIRES].

[12] Proceedings of *Multiple Parton Interactions at the LHC*, 1st Workshop, Perugia, Italy, October 27–31, 2008 [DESY-PROC-2009-06].

[13] F.W. Bopp, R. Engel and J. Ranft, *Rapidity gaps and the PHOJET Monte Carlo*, hep-ph/9803437 [SPIRES].

[14] R. Engel, J. Ranft and S. Roesler, *Hard diffraction in hadron-hadron interactions and in photoproduction*, *Phys. Rev.* **D 52** (1995) 1459 [hep-ph/9502319] [SPIRES].

[15] F. Sikler, *Improved primary vertex finding for collider detectors*, arXiv:0911.2767 [SPIRES].

[16] PHOBOS collaboration, B.B. Back et al., *Charged particle multiplicity near mid-rapidity in central Au + Au collisions at $\sqrt{s}$ = 56 and 130 A/GeV*, *Phys. Rev. Lett.* **85** (2000) 3100 [hep-ex/0007036] [SPIRES].

[17] S. Cucciarelli et al., *Track reconstruction, primary vertex finding and seed generation with the pixel detector*, *CMS Note* 2006/026 (2006).

[18] T. Speer et al., *Track reconstruction in the CMS tracker*, *Nucl. Instrum. Meth.* **A559** (2006) 143.

[19] UA5 collaboration, R.E. Ansorge et al., *Diffraction Dissociation at the CERN Pulsed p p-bar Collider at c.m. Energies of 900 and 200 GeV*, *Z. Phys.* **C 33** (1986) 175 [SPIRES].

[20] C. Tsallis, *Possible generalization of Boltzmann-Gibbs statistics*, *J. Stat. Phys.* **52** (1988) 479 [SPIRES].

[21] G. Wilk and Z. Wlodarczyk, *Power laws in elementary and heavy-ion collisions: A Story of fluctuations and nonextensivity?*, *Eur. Phys. J.* **A 40** (2009) 299 [arXiv:0810.2939] [SPIRES].

[22] UA1 collaboration, C. Albajar et al., *A Study of the General Characteristics of Proton-Antiproton Collisions at 0.2 to 0.9 TeV*, *Nucl. Phys.* **B 335** (1990) 261 [SPIRES].

[23] ALICE collaboration, K. Aamod et al., *First proton–proton collisions at the LHC as observed with the ALICE detector: measurement of the charged-particle pseudorapidity density at $\sqrt{s}$ = 900 GeV*, *Eur. Phys. J.* **C 65** (2010) 111 [arXiv:0911.5430] [SPIRES].

[24] UA5 collaboration, G.J. Alner et al., *Scaling of pseudorapidity distributions at c.m. energies up to 0.9 TeV*, *Z. Phys.* **C 33** (1986) 1 [SPIRES].

[25] J. Whitmore, *Experimental Results on Strong Interactions in the NAL Hydrogen Bubble Chamber*, *Phys. Rept.* **10** (1974) 273 [SPIRES].

[26] Aachen-CERN-Heidelberg-Munich collaboration, W. Thome et al., *Charged Particle Multiplicity Distributions in p p Collisions at ISR Energies*, *Nucl. Phys.* **B 129** (1977) 365 [SPIRES].

[27] CDF collaboration, F. Abe et al., *Pseudorapidity distributions of charged particles produced in $\bar{p}p$ interactions at $\sqrt{s}$ = 630 GeV and 1800 GeV*, *Phys. Rev.* **D 41** (1990) 2330 [SPIRES].

[28] STAR collaboration, B.I. Abelev et al., *Systematic measurements of identified particle spectra in p+p, d+Au and Au+Au collisions at the STAR detector*, *Phys. Rev.* **C 79** (2009) 034909 [arXiv:0808.2041] [SPIRES].

[29] PHOBOS collaboration, R. Nouicer et al., *Pseudorapidity distributions of charged particles in d+Au and p+p collisions at $\sqrt{s_{\rm NN}}$ = 200 GeV*, *J. Phys.* **G 30** (2004) S1133 [nucl-ex/0403033] [SPIRES].

[30] CMS collaboration, *Numerical values of the data presented in this paper*, available at *JHEP* **02** (2010) 041 as supplemental material.

[31] A.M. Rossi et al., *Experimental Study of the Energy Dependence in Proton Proton Inclusive Reactions*, *Nucl. Phys.* **B 84** (1975) 269 [SPIRES].

[32] T. Alexopoulos et al., *Multiplicity dependence of the transverse momentum spectrum for centrally produced hadrons in antiproton - proton collisions at $\sqrt{s}$ = 1.8 TeV*, *Phys. Rev. Lett.* **60** (1988) 1622 [SPIRES].

[33] CDF collaboration, F. Abe et al., *Transverse momentum distributions of charged particles produced in $\bar{p}p$ interactions at $\sqrt{s}$ = 630 GeV and 1800 GeV*, *Phys. Rev. Lett.* **61** (1988) 1819 [SPIRES].

Transverse-Momentum and Pseudorapidity Distributions of Charged Hadrons in pp Collisions at $\sqrt{s} = 7$ TeV

V. Khachatryan *et al.**
(CMS Collaboration)

(Received 18 May 2010; published 6 July 2010)

Charged-hadron transverse-momentum and pseudorapidity distributions in proton-proton collisions at $\sqrt{s} = 7$ TeV are measured with the inner tracking system of the CMS detector at the LHC. The charged-hadron yield is obtained by counting the number of reconstructed hits, hit pairs, and fully reconstructed charged-particle tracks. The combination of the three methods gives a charged-particle multiplicity per unit of pseudorapidity $dN_{\rm ch}/d\eta|_{|\eta|<0.5} = 5.78 \pm 0.01(\text{stat}) \pm 0.23(\text{syst})$ for non-single-diffractive events, higher than predicted by commonly used models. The relative increase in charged-particle multiplicity from $\sqrt{s} = 0.9$ to 7 TeV is $[66.1 \pm 1.0(\text{stat}) \pm 4.2(\text{syst})]\%$. The mean transverse momentum is measured to be $0.545 \pm 0.005(\text{stat}) \pm 0.015(\text{syst})$ GeV/c. The results are compared with similar measurements at lower energies.

DOI: 10.1103/PhysRevLett.105.022002 PACS numbers: 13.85.Ni

Introduction.—Measurements of particle yields and kinematic distributions are an essential first step in exploring a new energy regime of particle collisions. Such studies contribute to our understanding of the physics of hadron production, including the relative roles of soft and hard scattering contributions, and help construct a solid foundation for other investigations. In the complicated environment of LHC pp collisions [1], firm knowledge of the rates and distributions of inclusive particle production is needed to distinguish rare signal events from the much larger backgrounds of soft hadronic interactions. They will also serve as points of reference for the measurement of nuclear-medium effects in Pb-Pb collisions in the LHC heavy ion program.

The bulk of the particles produced in pp collisions arise from soft interactions, which are modeled only phenomenologically. Experimental results provide the critical guidance for tuning these widely used models and event generators. Soft collisions are commonly classified as elastic scattering, inelastic single-diffractive (SD) dissociation, double-diffractive (DD) dissociation, and inelastic nondiffractive (ND) scattering [2]. (Double-Pomeron exchange is treated as DD in this Letter.) All results presented here refer to inelastic non-single-diffractive (NSD) interactions, and are based on an event selection that retains a large fraction of the ND and DD events, while disfavoring SD events.

The measurements focus on transverse-momentum p_T and pseudorapidity η distributions. The pseudorapidity, commonly used to characterize the direction of particle emission, is defined as $\eta = -\ln\tan(\theta/2)$, where θ is the polar angle of the direction of the particle with respect to the anticlockwise beam direction. The count of primary charged hadrons $N_{\rm ch}$ is defined to include decay products of particles with proper lifetimes less than 1 cm. Products of secondary interactions are excluded, and a percent-level correction is applied for prompt leptons. The measurements reported here are of $dN_{\rm ch}/d\eta$ and $dN_{\rm ch}/dp_T$ in the pseudorapidity range $|\eta| < 2.4$ and closely follow our previous analysis of minimum-bias data at lower center-of-mass energies of $\sqrt{s} = 0.9$ and 2.36 TeV as reported in Ref. [3].

The data for this study are drawn from an integrated luminosity of 1.1 μb^{-1} recorded with the Compact Muon Solenoid (CMS) experiment [4] on 30 March 2010, during the first hour of the LHC operation at $\sqrt{s} = 7$ TeV. These results are the highest center-of-mass energy measurements of the $dN_{\rm ch}/d\eta$ and $dN_{\rm ch}/dp_T$ distributions conducted at a particle collider so far and complement the other recent measurements of the ALICE experiment at 7 TeV [5].

Experimental methods.—A detailed description of the CMS experiment can be found in Ref. [4]. The detectors used for the present analysis are the pixel and silicon-strip tracker, covering the region $|\eta| < 2.5$ and immersed in a 3.8 T axial magnetic field. The pixel tracker consists of three barrel layers and two end-cap disks at each barrel end. The forward calorimeter (HF), which covers the region $2.9 < |\eta| < 5.2$, was also used for event selection. The detailed Monte Carlo (MC) simulation of the CMS detector response is based on GEANT4 [6].

The event selection and analysis methods in this Letter are identical to those used in Ref. [3], where more details can be found. The inelastic pp collision rate was about 50 Hz. At these rates, the fraction of events in the data,

*Full author list given at the end of the article.

TABLE I. Numbers of events passing the selection cuts. The selection criteria are applied in sequence, i.e., each line includes the selection from the previous ones.

Selection	Number of events
Colliding bunches + one BSC signal	68 512
Reconstructed PV	61 551
HF coincidence	55 113
Beam-halo rejection	55 104
Other beam-background rejection	55 100

where two or more minimum-bias collisions occurred in the same bunch crossing, is estimated to be less than 0.3% and was neglected. Any hit in the beam scintillator counters (BSC, $3.23 < |\eta| < 4.65$) coinciding with colliding proton bunches was used for triggering the data acquisition. A sample mostly populated with NSD events was selected by requiring a primary vertex (PV) to be reconstructed with the tracker, together with at least one HF tower in each end with more than 3 GeV total energy. Beam-halo and other beam-background events were rejected as described in Ref. [3]. The remaining fraction of background events in the data was found to be less than 2×10^{-5}. The numbers of events satisfying the selection criteria are listed in Table I.

The event selection efficiency was estimated with simulated events using the PYTHIA [7,8] and PHOJET [9,10] event generators. The relative event fractions of SD, DD, and ND processes and their respective event selection efficiencies are listed in Table II. The fraction of diffractive events is predicted by the models to decrease as a function of collision energy, while the selection efficiency increases. At $\sqrt{s} = 7$ TeV, the fraction of SD (DD) events in the selected data sample, estimated with PYTHIA and PHOJET, are 6.8% (5.8%) and 5.0% (3.8%), respectively, somewhat higher than at $\sqrt{s} = 0.9$ and 2.36 TeV [3]. With PYTHIA, the overall correction for the selection efficiency of NSD processes and for the fraction of SD events remaining in the data sample lowers the measured charged-particle multiplicity by 6% compared with the uncorrected distribution.

The $dN_{\rm ch}/d\eta$ distributions were obtained, as in Ref. [3], with three methods, based on counting the following quantities: (i) reconstructed clusters in the barrel part of the pixel detector; (ii) pixel tracklets composed of pairs of clusters in different pixel barrel layers; and (iii) tracks reconstructed in the full tracker volume. The third method also allows a measurement of the $dN_{\rm ch}/dp_T$ distribution. All three methods rely on the reconstruction of a PV [11]. The PV reconstruction efficiency was found to be 98.3% (98.0%) in data (MC), evaluated after all other event selection cuts. In case of multiple PV candidates, the vertex with the largest track multiplicity was chosen. The three methods are sensitive to the measurement of particles down to p_T values of about 30, 50, and 100 MeV/c, respectively. Only 0.5, 1.5, and 5% of all charged particles are estimated to be produced below these p_T values, respectively, and these fractions were corrected for.

The measurements were corrected for the geometrical acceptance ($\approx$2%), efficiency ($\approx$5%–10%), fake (<1%) and duplicate tracks (<0.5%), low-p_T particles curling in the axial magnetic field (<1%), decay products of long-lived hadrons (<2%) and photon conversions (<1%), and inelastic hadronic interactions in the detector material ($\approx$1%–2%), where the size of the corrections in parentheses refers to the tracking method. The PYTHIA parameter set from Ref. [8] was chosen to determine the corrections, because it reproduces the $dN_{\rm ch}/d\eta$ and charged-particle multiplicity distributions, as well as other control distributions at 7 TeV, better than other available tuning parameter sets. Although the corrections do not depend significantly on the model used, it is indeed important that the simulated data set contains a sufficient number of high-multiplicity events to determine these corrections with the desired accuracy.

Results.—For the measurement of the $dN_{\rm ch}/dp_T$ distribution, charged-particle tracks with p_T in excess of 0.1 GeV/c were used in 12 different $|\eta|$ bins, from 0 to 2.4. The average charged-hadron yields in NSD events are shown in Fig. 1 as a function of p_T and $|\eta|$. The Tsallis parametrization [12–14],

$$E\frac{d^3N_{\rm ch}}{dp^3} = \frac{1}{2\pi p_T}\frac{E}{p}\frac{d^2N_{\rm ch}}{d\eta\, dp_T} = C\frac{dN_{\rm ch}}{dy}\left(1+\frac{E_T}{nT}\right)^{-n}, \quad (1)$$

where $y = 0.5\ln[(E+p_z)/(E-p_z)]$, $E_T = \sqrt{m^2+p_T^2} - m$, and m is the charged pion mass, was fitted to the data. The p_T spectrum of charged hadrons, $1/(2\pi p_T)d^2N_{\rm ch}/d\eta\, dp_T$, measured in the range $|\eta| < 2.4$, is shown in Fig. 2 for data

TABLE II. Fractions of SD, DD, ND, and NSD processes obtained from the PYTHIA and PHOJET event generators before any selection, and the corresponding selection efficiencies determined from the MC simulation.

	PYTHIA		PHOJET	
	Fractions	Selection efficiencies	Fractions	Selection efficiencies
SD	19.2%	26.7%	13.8%	30.7%
DD	12.9%	33.6%	6.6%	48.3%
ND	67.9%	96.4%	79.6%	97.1%
NSD	80.8%	86.3%	86.2%	93.4%

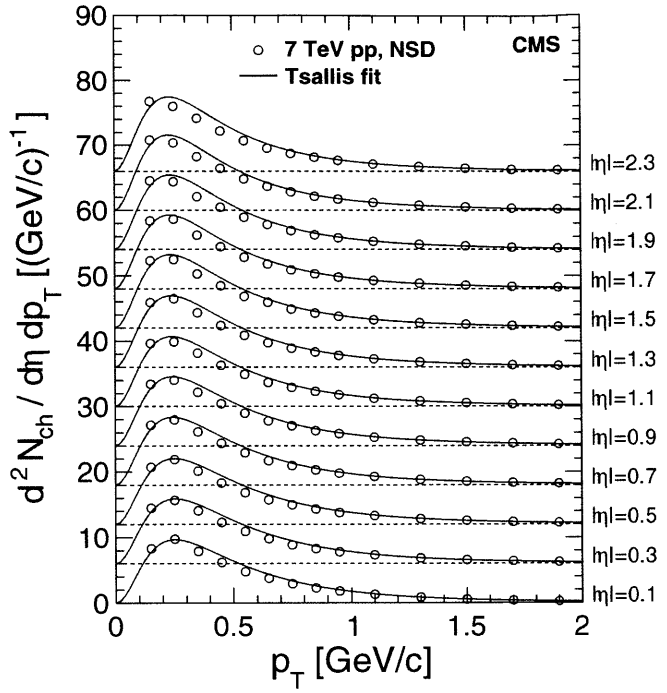

FIG. 1. Differential yield of charged hadrons in the range $|\eta| < 2.4$ in 0.2-unit-wide bins of $|\eta|$ in NSD events. The solid curves represent fits of Eq. (1) to the data. The measurements with increasing η are successively shifted by six units along the vertical axis.

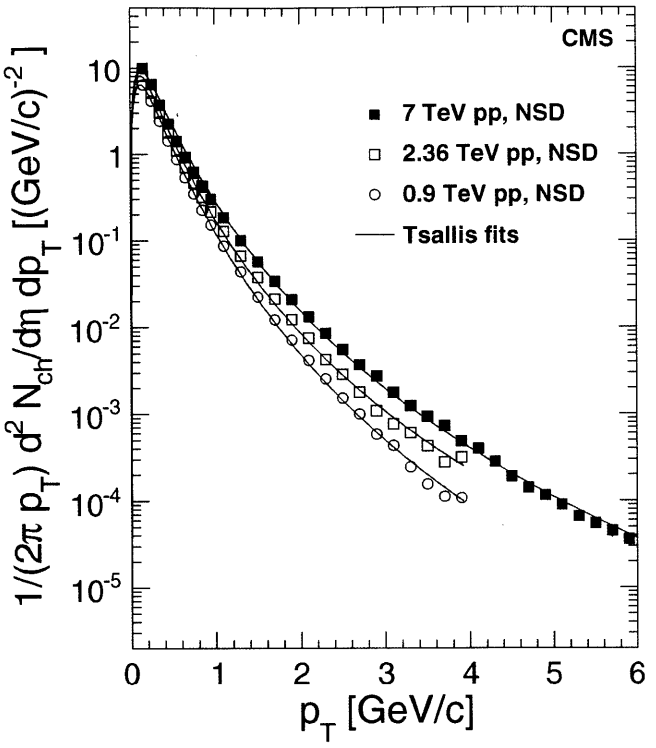

FIG. 2. Charged-hadron yield in the range $|\eta| < 2.4$ in NSD events as a function of p_T; the systematic uncertainties are smaller than the symbols. The measurements at $\sqrt{s} = 0.9$ and 2.36 TeV [3] are also shown. The solid lines represent fits of Eq. (1) to the data.

at 0.9, 2.36, and 7 TeV. The high-p_T reach of the data is limited by the increase of systematic uncertainties with p_T. The fit to the data [Eq. (1)] is mainly used for extrapolations to $p_T = 0$, but is not expected to give a good description of the data in all η bins with only two parameters. The parameter T and the exponent n were found to be $T = 0.145 \pm 0.005(\text{syst})$ GeV and $n = 6.6 \pm 0.2(\text{syst})$. The average p_T, calculated from a combination of the measured data points and the low- and high-p_T contributions as determined from the fit, is $\langle p_T \rangle = 0.545 \pm 0.005(\text{stat}) \pm 0.015(\text{syst})$ GeV/c.

Experimental uncertainties related to the trigger and event selection are common to all the analysis methods. The uncertainty related to the presence of SD (DD) events in the final sample was estimated to be 1.4% (1.1%), based on consistency checks between data and simulation for diffractive event candidates. The total event selection uncertainty, which also includes the selection efficiency of the BSC and HF, was found to be 3.5%. Based on studies similar to those presented in Ref. [3], additional 3% and 2% uncertainties were assigned to the tracklet and track reconstruction algorithm efficiencies, respectively. Corrections at the percent level were applied to the final results to extrapolate to $p_T = 0$. The uncertainty on these extrapolation corrections was found to be less than 1%. All other uncertainties are identical to those listed in Ref. [3]. The $dN_{\text{ch}}/d\eta$ measurements were repeated on a separate data sample without any magnetic field, for which almost no p_T extrapolation is needed, and gave results consistent within 1.5%. The final systematic uncertainties for the pixel counting, tracklet, and track methods were found to be 5.7%, 4.6%, and 4.3%, respectively, and are strongly correlated.

For the $dN_{\text{ch}}/d\eta$ measurements, the results for the three individual layers within the cluster-counting method were found to be consistent within 1.2% and were combined. The three layer pairs in the pixel-tracklet method provided results that agreed within 0.6% and were also combined. Finally, the results from the three different measurement methods, which agree with the combined result within 1% to 4% depending on η, were averaged. The final $dN_{\text{ch}}/d\eta$ distributions are shown in Fig. 3 for $\sqrt{s} = 0.9$, 2.36, and 7 TeV. The CMS results are compared with measurements made by other experiments. In the ATLAS Collaboration analysis [15], events and particles were selected in a different region of phase space, which makes a direct comparison difficult. Their results are therefore not included in the figure.

The results can also be compared to earlier experiments as a function of $\sqrt{s}$. The energy dependence of the average charged hadron p_T can be described by a quadratic function of $\ln s$ [16]. As shown in Fig. 4, the present measure-

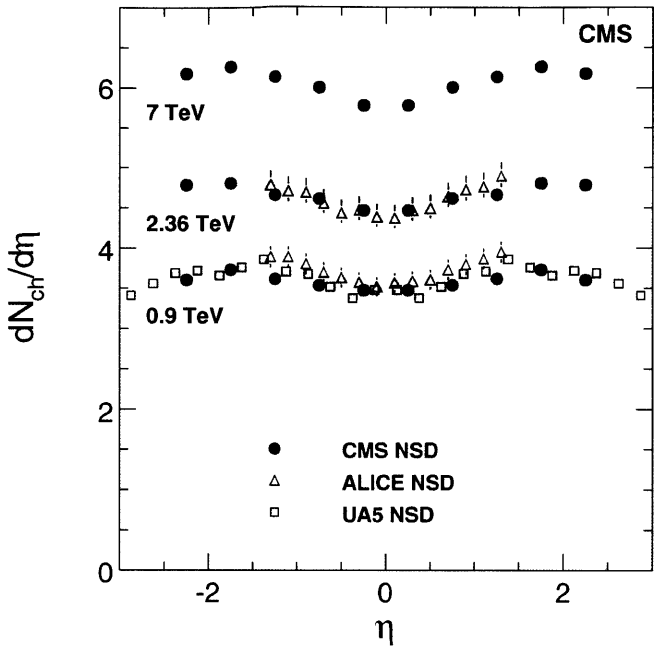

FIG. 3. Distributions of $dN_{ch}/d\eta$, averaged over the three measurement methods and compared with data from UA5 [23] ($p\bar{p}$, with statistical errors only) and ALICE [24] (with systematic uncertainties). The shaded band shows systematic uncertainties of the CMS data. The CMS and UA5 data are averaged over negative and positive values of η.

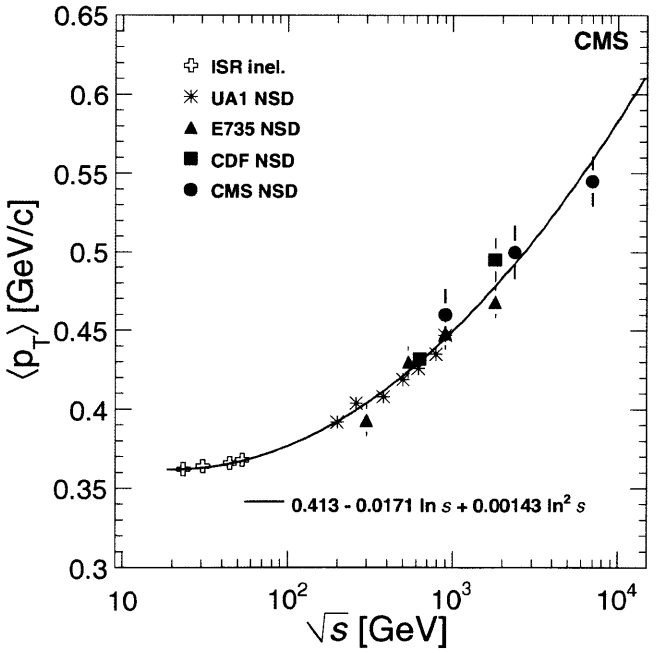

FIG. 4. Average p_T of charged hadrons as a function of the center-of-mass energy. The CMS measurements are for $|\eta| < 2.4$. Also shown are measurements from the ISR [25] (pp), E735 [26] ($p\bar{p}$), and CDF [27] ($p\bar{p}$) for $|\eta| < 0.5$, and from UA1 [16] ($p\bar{p}$) for $|\eta| < 2.5$. The solid line is a fit of the functional form $\langle p_T \rangle = 0.413 - 0.0171 \ln s + 0.00143 \ln^2 s$ to the data. The error bars on the CMS data include the systematic uncertainties.

ment follows this trend. The choice of the $|\eta|$ interval can influence the average p_T value by a few percent.

For $|\eta| < 0.5$, the average charged multiplicity density is $dN_{ch}/d\eta = 5.78 \pm 0.01(\text{stat}) \pm 0.23(\text{syst})$ for NSD events. The $\sqrt{s}$ dependence of the measured $dN_{ch}/d\eta|_{\eta\approx 0}$ is shown in Fig. 5, which includes data from various other experiments. The $dN_{ch}/d\eta$ results reported here show a rather steep increase between 0.9 and 7 TeV, which is measured to be $[66.1 \pm 1.0(\text{stat}) \pm 4.2(\text{syst})]\%$. Using a somewhat different event selection, the ALICE Collaboration has found a similar increase of $[57.6 \pm 0.4(\text{stat})^{+3.6}_{-1.8}(\text{syst})]\%$ [5]. The measured charged-particle multiplicity is accurate enough to distinguish among most sets of event-generator tuning parameter values and various models. The measured value at 7 TeV significantly exceeds the prediction of 4.57 from PHOJET [9,10], and the predictions of 3.99, 4.18, and 4.34 from the DW [17], PROQ20 [18], and Perugia0 [19] tuning parameter values of PYTHIA, respectively, while it is closer to the prediction of 5.48 from the PYTHIA parameter set from Ref. [8] and to the recent model predictions of 5.58 and 5.78 from Refs. [20,21]. The measured excess of the number of charged hadrons with respect to the event generators is independent of η and concentrated in the $p_T < 1$ GeV/c

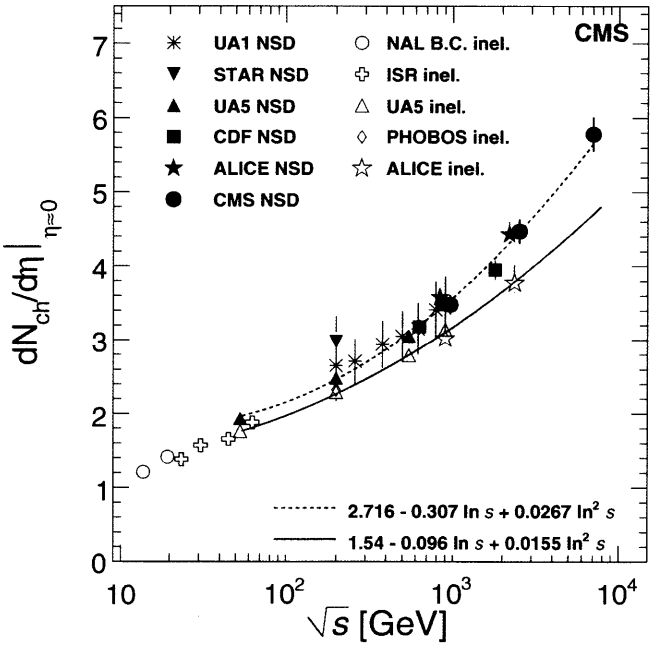

FIG. 5. Average value of $dN_{ch}/d\eta$ in the central η region as a function of center-of-mass energy in pp and $p\bar{p}$ collisions. Also shown are NSD and inelastic measurements from the NAL Bubble Chamber [28] ($p\bar{p}$), ISR [29] (pp), UA1 [16] ($p\bar{p}$), UA5 [23] ($p\bar{p}$), CDF [30] ($p\bar{p}$), STAR [31] (pp), PHOBOS [32] (pp), and ALICE [24] (pp). The curves are second-order polynomial fits for the inelastic (solid) and NSD event selections (dashed). The error bars include systematic uncertainties, when available. Data points at 0.9 and 2.36 TeV are slightly displaced horizontally for visibility.

range. These differences indicate the need for a continued model development and simulation tuning. Work on updated event generators based on LHC data is currently under way.

Summary.—Charged-hadron transverse-momentum and pseudorapidity distributions have been measured in proton-proton collisions at $\sqrt{s} = 7$ TeV. The numerical values of the data presented in this Letter can be found in the HEPDATA database [22]. The combined result for the central pseudorapidity density, from three mutually consistent methods of measurement, is $dN_{\mathrm{ch}}/d\eta|_{|\eta|<0.5} = 5.78 \pm 0.01(\mathrm{stat}) \pm 0.23(\mathrm{syst})$ for non-single-diffractive events. This value is higher than most predictions and provides new information to constrain ongoing improvements of soft particle production models and event generators. The mean transverse momentum has been measured to be $0.545 \pm 0.005(\mathrm{stat}) \pm 0.015(\mathrm{syst})$ GeV/c. These studies are the first steps in the exploration of particle production at the new center-of-mass energy frontier, and contribute to the understanding of the dynamics in soft hadronic interactions.

We congratulate and express our gratitude to our colleagues in the CERN accelerator departments for the excellent performance of the LHC. We thank the technical and administrative staff at CERN and other CMS institutes, and acknowledge support from the following: FMSR (Austria); FNRS and FWO (Belgium); CNPq, CAPES, FAPERJ, and FAPESP (Brazil); MES (Bulgaria); CERN; CAS, MoST, and NSFC (China); COLCIENCIAS (Colombia); MSES (Croatia); RPF (Cyprus); Academy of Sciences and NICPB (Estonia); Academy of Finland, ME, and HIP (Finland); CEA and CNRS/IN2P3 (France); BMBF, DFG, and HGF (Germany); GSRT (Greece); OTKA and NKTH (Hungary); DAE and DST (India); IPM (Iran); SFI (Ireland); INFN (Italy); NRF and WCU (Korea); LAS (Lithuania); CINVESTAV, CONACYT, SEP, and UASLP-FAI (Mexico); PAEC (Pakistan); SCSR (Poland); FCT (Portugal); JINR (Armenia, Belarus, Georgia, Ukraine, Uzbekistan); MST and MAE (Russia); MSTDS (Serbia); MICINN and CPAN (Spain); Swiss Funding Agencies (Switzerland); NSC (Taipei); TUBITAK and TAEK (Turkey); STFC (U.K.); DOE and NSF (U.S.).

[1] L. Evans and P. Bryant, JINST **3**, S08001 (2008).
[2] W. Kittel and E. A. DeWolf, *Soft Multihadron Dynamics* (World Scientic, Singapore, 2005), ISBN 981-256-295-8.
[3] V. Khachatryan *et al.* (CMS Collaboration), J. High Energy Phys. 02 (2010) 041.
[4] S. Chatrchyan *et al.* (CMS Collaboration), JINST **3**, S08004 (2008).
[5] K. Aamodt *et al.* (ALICE Collaboration), arXiv:1004.3514.
[6] S. Agostinelli *et al.* (GEANT4 Collaboration), Nucl. Instrum. Methods Phys. Res., Sect. A **506**, 250 (2003).
[7] T. Sjöstrand, S. Mrenna, and P. Skands, J. High Energy Phys. 05 (2006) 026.
[8] A. Moraes, C. Buttar, and I. Dawson, Eur. Phys. J. C **50**, 435 (2007).
[9] F. W. Bopp, R. Engel, and J. Ranft, arXiv:hepph/9803437.
[10] R. Engel, J. Ranft, and S. Roesler, Phys. Rev. D **52**, 1459 (1995).
[11] F. Siklér, Nucl. Instrum. Methods Phys. Res., Sect. A (in press).
[12] C. Tsallis, J. Stat. Phys. **52**, 479 (1988).
[13] G. Wilk and Z. Włodarczyk, Eur. Phys. J. A **40**, 299 (2009).
[14] T. S. Biró, G. Purcsel, and K. Ürmössy, Eur. Phys. J. A **40**, 325 (2009).
[15] G. Aad *et al.* (ATLAS Collaboration), Phys. Lett. B **688**, 21 (2010).
[16] C. Albajar *et al.* (UA1 Collaboration), Nucl. Phys. **B335**, 261 (1990).
[17] R. Bernhard *et al.*, in Proceedings of the First International Workshop on Multiple Partonic Interactions at the LHC MPI'08, Perugia, Italy, 2008, edited by P. Bartalini and L. Fanó (arXiv:1003.4220).
[18] A. Buckley *et al.*, Eur. Phys. J. C **65**, 331 (2010).
[19] P. Z. Skands, arXiv:0905.3418.
[20] E. Levin and A. H. Rezaeian, arXiv:1005.0631.
[21] A. K. Likhoded, A. V. Luchinsky, and A. A. Novoselov, arXiv:1005.1827.
[22] Available at HEPDATA, http://hepdata.cedar.ac.uk/view/irn8656010.
[23] G. J. Alner *et al.* (UA5 Collaboration), Z. Phys. C **33**, 1 (1986).
[24] K. Aamodt *et al.* (ALICE Collaboration), arXiv:1004.3034 [Eur. Phys. J. C (to be published)].
[25] A. M. Rossi *et al.*, Nucl. Phys. **B84**, 269 (1975).
[26] T. Alexopoulos *et al.* (E735 Collaboration), Phys. Rev. Lett. **60**, 1622 (1988).
[27] F. Abe *et al.* (CDF Collaboration), Phys. Rev. Lett. **61**, 1819 (1988).
[28] J. Whitmore, Phys. Rep. **10**, 273 (1974).
[29] W. Thomé *et al.* (Aachen-CERN-Heidelberg-Munich Collaboration), Nucl. Phys. **B129**, 365 (1977).
[30] F. Abe *et al.* (CDF Collaboration), Phys. Rev. D **41**, 2330 (1990).
[31] B. I. Abelev *et al.* (STAR Collaboration), Phys. Rev. C **79**, 034909 (2009).
[32] R. Nouicer *et al.* (PHOBOS Collaboration), J. Phys. G **30**, S1133 (2004).

V. Khachatryan,[1] A. M. Sirunyan,[1] A. Tumasyan,[1] W. Adam,[2] T. Bergauer,[2] M. Dragicevic,[2] J. Erö,[2] C. Fabjan,[2] M. Friedl,[2] R. Frühwirth,[2] V. M. Ghete,[2] J. Hammer,[2,b] S. Hänsel,[2] M. Hoch,[2] N. Hörmann,[2] J. Hrubec,[2] M. Jeitler,[2] G. Kasieczka,[2] W. Kiesenhofer,[2] M. Krammer,[2] D. Liko,[2] I. Mikulec,[2] M. Pernicka,[2] H. Rohringer,[2] R. Schöfbeck,[2]

J. Strauss,[2] A. Taurok,[2] F. Teischinger,[2] W. Waltenberger,[2] G. Walzel,[2] E. Widl,[2] C.-E. Wulz,[2] V. Mossolov,[3] N. Shumeiko,[3] J. Suarez Gonzalez,[3] L. Benucci,[4] L. Ceard,[4] E. A. De Wolf,[4] M. Hashemi,[4] X. Janssen,[4] T. Maes,[4] L. Mucibello,[4] S. Ochesanu,[4] B. Roland,[4] R. Rougny,[4] M. Selvaggi,[4] H. Van Haevermaet,[4] P. Van Mechelen,[4] N. Van Remortel,[4] V. Adler,[5] S. Beauceron,[5] S. Blyweert,[5] J. D'Hondt,[5] O. Devroede,[5] A. Kalogeropoulos,[5] J. Maes,[5] M. Maes,[5] S. Tavernier,[5] W. Van Doninck,[5] P. Van Mulders,[5] I. Villella,[5] E. C. Chabert,[6] O. Charaf,[6] B. Clerbaux,[6] G. De Lentdecker,[6] V. Dero,[6] A. P. R. Gay,[6] G. H. Hammad,[6] P. E. Marage,[6] C. Vander Velde,[6] P. Vanlaer,[6] J. Wickens,[6] S. Costantini,[7] M. Grunewald,[7] B. Klein,[7] A. Marinov,[7] D. Ryckbosch,[7] F. Thyssen,[7] M. Tytgat,[7] L. Vanelderen,[7] P. Verwilligen,[7] S. Walsh,[7] N. Zaganidis,[7] S. Basegmez,[8] G. Bruno,[8] J. Caudron,[8] J. De Favereau De Jeneret,[8] C. Delaere,[8] P. Demin,[8] D. Favart,[8] A. Giammanco,[8] G. Grégoire,[8] J. Hollar,[8] V. Lemaitre,[8] O. Militaru,[8] S. Ovyn,[8] D. Pagano,[8] A. Pin,[8] K. Piotrzkowski,[8,b] L. Quertenmont,[8] N. Schul,[8] N. Beliy,[9] T. Caebergs,[9] E. Daubie,[9] G. A. Alves,[10] M. E. Pol,[10] M. H. G. Souza,[10] W. Carvalho,[11] E. M. Da Costa,[11] D. De Jesus Damiao,[11] C. De Oliveira Martins,[11] S. Fonseca De Souza,[11] L. Mundim,[11] V. Oguri,[11] A. Santoro,[11] S. M. Silva Do Amaral,[11] A. Sznajder,[11] F. Torres Da Silva De Araujo,[11] F. A. Dias,[12] M. A. F. Dias,[12] T. R. Fernandez Perez Tomei,[12] E. M. Gregores,[12] F. Marinho,[12] S. F. Novaes,[12] Sandra S. Padula,[12] N. Darmenov,[13,b] L. Dimitrov,[13] V. Genchev,[13,b] P. Iaydjiev,[13] S. Piperov,[13] S. Stoykova,[13] G. Sultanov,[13] R. Trayanov,[13] I. Vankov,[13] M. Dyulendarova,[14] R. Hadjiiska,[14] V. Kozhuharov,[14] L. Litov,[14] E. Marinova,[14] M. Mateev,[14] B. Pavlov,[14] P. Petkov,[14] J. G. Bian,[15] G. M. Chen,[15] H. S. Chen,[15] C. H. Jiang,[15] D. Liang,[15] S. Liang,[15] J. Wang,[15] J. Wang,[15] X. Wang,[15] Z. Wang,[15] M. Yang,[15] J. Zang,[15] Z. Zhang,[15] Y. Ban,[16] S. Guo,[16] Z. Hu,[16] Y. Mao,[16] S. J. Qian,[16] H. Teng,[16] B. Zhu,[16] A. Cabrera,[17] C. A. Carrillo Montoya,[17] B. Gomez Moreno,[17] A. A. Ocampo Rios,[17] A. F. Osorio Oliveros,[17] J. C. Sanabria,[17] N. Godinovic,[18] D. Lelas,[18] K. Lelas,[18] R. Plestina,[18,c] D. Polic,[18] I. Puljak,[18] Z. Antunovic,[19] M. Dzelalija,[19] V. Brigljevic,[20] S. Duric,[20] K. Kadija,[20] S. Morovic,[20] A. Attikis,[21] R. Fereos,[21] M. Galanti,[21] J. Mousa,[21] C. Nicolaou,[21] A. Papadakis,[21] F. Ptochos,[21] P. A. Razis,[21] H. Rykaczewski,[21] D. Tsiakkouri,[21] Z. Zinonos,[21] M. Mahmoud,[22] A. Hektor,[23] M. Kadastik,[23] K. Kannike,[23] M. Müntel,[23] M. Raidal,[23] L. Rebane,[23] V. Azzolini,[24] P. Eerola,[24] S. Czellar,[25] J. Härkönen,[25] A. Heikkinen,[25] V. Karimäki,[25] R. Kinnunen,[25] J. Klem,[25] M. J. Kortelainen,[25] T. Lampén,[25] K. Lassila-Perini,[25] S. Lehti,[25] T. Lindén,[25] P. Luukka,[25] T. Mäenpää,[25] E. Tuominen,[25] J. Tuominiemi,[25] E. Tuovinen,[25] D. Ungaro,[25] L. Wendland,[25] K. Banzuzi,[26] A. Korpela,[26] T. Tuuva,[26] D. Sillou,[27] M. Besancon,[28] M. Dejardin,[28] D. Denegri,[28] J. Descamps,[28] B. Fabbro,[28] J. L. Faure,[28] F. Ferri,[28] S. Ganjour,[28] F. X. Gentit,[28] A. Givernaud,[28] P. Gras,[28] G. Hamel de Monchenault,[28] P. Jarry,[28] E. Locci,[28] J. Malcles,[28] M. Marionneau,[28] L. Millischer,[28] J. Rander,[28] A. Rosowsky,[28] D. Rousseau,[28] M. Titov,[28] P. Verrecchia,[28] S. Baffioni,[29] L. Bianchini,[29] M. Bluj,[29,d] C. Broutin,[29] P. Busson,[29] C. Charlot,[29] L. Dobrzynski,[29] S. Elgammal,[29] R. Granier de Cassagnac,[29] M. Haguenauer,[29] A. Kalinowski,[29] P. Miné,[29] P. Paganini,[29] D. Sabes,[29] Y. Sirois,[29] C. Thiebaux,[29] A. Zabi,[29] J.-L. Agram,[30] A. Besson,[30] D. Bloch,[30] D. Bodin,[30] J.-M. Brom,[30] M. Cardaci,[30] E. Conte,[30] F. Drouhin,[30] C. Ferro,[30] J.-C. Fontaine,[30] D. Gelé,[30] U. Goerlach,[30] S. Greder,[30] P. Juillot,[30] M. Karim,[30] A.-C. Le Bihan,[30] Y. Mikami,[30] J. Speck,[30] P. Van Hove,[30] F. Fassi,[31] D. Mercier,[31] C. Baty,[32] N. Beaupere,[32] M. Bedjidian,[32] O. Bondu,[32] G. Boudoul,[32] D. Boumediene,[32] H. Brun,[32] N. Chanon,[32] R. Chierici,[32] D. Contardo,[32] P. Depasse,[32] H. El Mamouni,[32] J. Fay,[32] S. Gascon,[32] B. Ille,[32] T. Kurca,[32] T. Le Grand,[32] M. Lethuillier,[32] L. Mirabito,[32] S. Perries,[32] S. Tosi,[32] Y. Tschudi,[32] P. Verdier,[32] H. Xiao,[32] V. Roinishvili,[33] G. Anagnostou,[34] M. Edelhoff,[34] L. Feld,[34] N. Heracleous,[34] O. Hindrichs,[34] R. Jussen,[34] K. Klein,[34] J. Merz,[34] N. Mohr,[34] A. Ostapchuk,[34] A. Perieanu,[34] F. Raupach,[34] J. Sammet,[34] S. Schael,[34] D. Sprenger,[34] H. Weber,[34] M. Weber,[34] B. Wittmer,[34] O. Actis,[35] M. Ata,[35] W. Bender,[35] P. Biallass,[35] M. Erdmann,[35] J. Frangenheim,[35] T. Hebbeker,[35] A. Hinzmann,[35] K. Hoepfner,[35] C. Hof,[35] M. Kirsch,[35] T. Klimkovich,[35] P. Kreuzer,[35,b] D. Lanske,[35,a] C. Magass,[35] M. Merschmeyer,[35] A. Meyer,[35] P. Papacz,[35] H. Pieta,[35] H. Reithler,[35] S. A. Schmitz,[35] L. Sonnenschein,[35] M. Sowa,[35] J. Steggemann,[35] D. Teyssier,[35] C. Zeidler,[35] M. Bontenackels,[36] M. Davids,[36] M. Duda,[36] G. Flügge,[36] H. Geenen,[36] M. Giffels,[36] W. Haj Ahmad,[36] D. Heydhausen,[36] T. Kress,[36] Y. Kuessel,[36] A. Linn,[36] A. Nowack,[36] L. Perchalla,[36] O. Pooth,[36] P. Sauerland,[36] A. Stahl,[36] M. Thomas,[36] D. Tornier,[36] M. H. Zoeller,[36] M. Aldaya Martin,[37] W. Behrenhoff,[37] U. Behrens,[37] M. Bergholz,[37] K. Borras,[37] A. Campbell,[37] E. Castro,[37] D. Dammann,[37] G. Eckerlin,[37] A. Flossdorf,[37] G. Flucke,[37] A. Geiser,[37] J. Hauk,[37] H. Jung,[37] M. Kasemann,[37] I. Katkov,[37] C. Kleinwort,[37] H. Kluge,[37] A. Knutsson,[37] E. Kuznetsova,[37] W. Lange,[37] W. Lohmann,[37] R. Mankel,[37] M. Marienfeld,[37] I.-A. Melzer-Pellmann,[37] A. B. Meyer,[37] J. Mnich,[37] A. Mussgiller,[37] J. Olzem,[37] A. Parenti,[37] A. Raspereza,[37] R. Schmidt,[37] T. Schoerner-Sadenius,[37] N. Sen,[37] M. Stein,[37] J. Tomaszewska,[37] D. Volyanskyy,[37] C. Wissing,[37] C. Autermann,[38]

J. Draeger,[38] D. Eckstein,[38] H. Enderle,[38] U. Gebbert,[38] K. Kaschube,[38] G. Kaussen,[38] R. Klanner,[38] B. Mura,[38] S. Naumann-Emme,[38] F. Nowak,[38] C. Sander,[38] H. Schettler,[38] P. Schleper,[38] M. Schröder,[38] T. Schum,[38] J. Schwandt,[38] H. Stadie,[38] G. Steinbrück,[38] J. Thomsen,[38] R. Wolf,[38] J. Bauer,[39] V. Buege,[39] A. Cakir,[39] T. Chwalek,[39] D. Daeuwel,[39] W. De Boer,[39] A. Dierlamm,[39] G. Dirkes,[39] M. Feindt,[39] J. Gruschke,[39] C. Hackstein,[39] F. Hartmann,[39] M. Heinrich,[39] H. Held,[39] K.H. Hoffmann,[39] S. Honc,[39] T. Kuhr,[39] D. Martschei,[39] S. Mueller,[39] Th. Müller,[39] M. Niegel,[39] O. Oberst,[39] A. Oehler,[39] J. Ott,[39] T. Peiffer,[39] D. Piparo,[39] G. Quast,[39] K. Rabbertz,[39] F. Ratnikov,[39] M. Renz,[39] A. Sabellek,[39] C. Saout,[39,b] A. Scheurer,[39] P. Schieferdecker,[39] F.-P. Schilling,[39] G. Schott,[39] H.J. Simonis,[39] F.M. Stober,[39] D. Troendle,[39] J. Wagner-Kuhr,[39] M. Zeise,[39] V. Zhukov,[39,e] E.B. Ziebarth,[39] G. Daskalakis,[40] T. Geralis,[40] A. Kyriakis,[40] D. Loukas,[40] I. Manolakos,[40] A. Markou,[40] C. Markou,[40] C. Mavrommatis,[40] E. Petrakou,[40] L. Gouskos,[41] P. Katsas,[41] A. Panagiotou,[41,b] I. Evangelou,[42] P. Kokkas,[42] N. Manthos,[42] I. Papadopoulos,[42] V. Patras,[42] F.A. Triantis,[42] A. Aranyi,[43] G. Bencze,[43] L. Boldizsar,[43] G. Debreczeni,[43] C. Hajdu,[43,b] D. Horvath,[43,f] A. Kapusi,[43] K. Krajczar,[43] A. Laszlo,[43] F. Sikler,[43] G. Vesztergombi,[43] N. Beni,[44] J. Molnar,[44] J. Palinkas,[44] Z. Szillasi,[44,b] V. Veszpremi,[44] P. Raics,[45] Z.L. Trocsanyi,[45] B. Ujvari,[45] S. Bansal,[46] S.B. Beri,[46] V. Bhatnagar,[46] M. Jindal,[46] M. Kaur,[46] J.M. Kohli,[46] M.Z. Mehta,[46] N. Nishu,[46] L.K. Saini,[46] A. Sharma,[46] R. Sharma,[46] A.P. Singh,[46] J.B. Singh,[46] S.P. Singh,[46] S. Ahuja,[47] S. Bhattacharya,[47,g] S. Chauhan,[47] B.C. Choudhary,[47] P. Gupta,[47] S. Jain,[47] S. Jain,[47] A. Kumar,[47] K. Ranjan,[47] R.K. Shivpuri,[47] R.K. Choudhury,[48] D. Dutta,[48] S. Kailas,[48] S.K. Kataria,[48] A.K. Mohanty,[48] L.M. Pant,[48] P. Shukla,[48] P. Suggisetti,[48] T. Aziz,[49] M. Guchait,[49,h] A. Gurtu,[49] M. Maity,[49] D. Majumder,[49] G. Majumder,[49] K. Mazumdar,[49] G.B. Mohanty,[49] A. Saha,[49] K. Sudhakar,[49] N. Wickramage,[49] S. Banerjee,[50] S. Dugad,[50] N.K. Mondal,[50] H. Arfaei,[51] H. Bakhshiansohi,[51] A. Fahim,[51] A. Jafari,[51] M. Mohammadi Najafabadi,[51] S. Paktinat Mehdiabadi,[51] B. Safarzadeh,[51] M. Zeinali,[51] M. Abbrescia,[52a,52b] L. Barbone,[52a] A. Colaleo,[52a] D. Creanza,[52a,52c] N. De Filippis,[52a] M. De Palma,[52a,52b] A. Dimitrov,[52a] F. Fedele,[52a] L. Fiore,[52a] G. Iaselli,[52a,52c] L. Lusito,[52a,52b,b] G. Maggi,[52a,52c] M. Maggi,[52a] N. Manna,[52a,52b] B. Marangelli,[52a,52b] S. My,[52a,52c] S. Nuzzo,[52a,52b] G.A. Pierro,[52a] A. Pompili,[52a,52b] G. Pugliese,[52a,52c] F. Romano,[52a,52c] G. Roselli,[52a,52b] G. Selvaggi,[52a,52b] L. Silvestris,[52a] R. Trentadue,[52a] S. Tupputi,[52a,52b] G. Zito,[52a] G. Abbiendi,[53a] A.C. Benvenuti,[53a] D. Bonacorsi,[53a] S. Braibant-Giacomelli,[53a,53b] A. Castro,[53a,53b] F.R. Cavallo,[53a] G. Codispoti,[53a,53b] G.M. Dallavalle,[53a,b] F. Fabbri,[53a] A. Fanfani,[53a,53b] D. Fasanella,[53a] P. Giacomelli,[53a] M. Giunta,[53a,b] C. Grandi,[53a] S. Marcellini,[53a] G. Masetti,[53a,53b] A. Montanari,[53a] F.L. Navarria,[53a,53b] F. Odorici,[53a] A. Perrotta,[53a] A.M. Rossi,[53a,53b] T. Rovelli,[53a,53b] G. Siroli,[53a,53b] R. Travaglini,[53a,53b] S. Albergo,[54a,54b] G. Cappello,[54a,54b] M. Chiorboli,[54a,54b] S. Costa,[54a,54b] A. Tricomi,[54a,54b] C. Tuve,[54a] G. Barbagli,[55a] G. Broccolo,[55a,55b] V. Ciulli,[55a,55b] C. Civinini,[55a] R. D'Alessandro,[55a,55b] E. Focardi,[55a,55b] S. Frosali,[55a,55b] E. Gallo,[55a] C. Genta,[55a,55b] P. Lenzi,[55a,55b,b] M. Meschini,[55a] S. Paoletti,[55a] G. Sguazzoni,[55a] A. Tropiano,[55a] L. Benussi,[56] S. Bianco,[56] S. Colafranceschi,[56] F. Fabbri,[56] D. Piccolo,[56] P. Fabbricatore,[57] R. Musenich,[57] A. Benaglia,[58a,58b] G.B. Cerati,[58a,58b,b] F. De Guio,[58a,58b] L. Di Matteo,[58a,58b] A. Ghezzi,[58a,58b,b] P. Govoni,[58a,58b] M. Malberti,[58a,58b,b] S. Malvezzi,[58a] A. Martelli,[58a,58b,c] A. Massironi,[58a,58b] D. Menasce,[58a] V. Miccio,[58a,58b] L. Moroni,[58a] P. Negri,[58a,58b] M. Paganoni,[58a,58b] D. Pedrini,[58a] S. Ragazzi,[58a,58b] N. Redaelli,[58a] S. Sala,[58a] R. Salerno,[58a,58b] T. Tabarelli de Fatis,[58a,58b] V. Tancini,[58a,58b] S. Taroni,[58a,58b] S. Buontempo,[59a] A. Cimmino,[59a,59b] A. De Cosa,[59a,59b,b] M. De Gruttola,[59a,59b,b] F. Fabozzi,[59a] A.O.M. Iorio,[59a] L. Lista,[59a] P. Noli,[59a,59b] P. Paolucci,[59a] P. Azzi,[60a] N. Bacchetta,[60a] P. Bellan,[60a,60b,b] M. Bellato,[60a] M. Biasotto,[60a] D. Bisello,[60a,60b] R. Carlin,[60a,60b] P. Checchia,[60a] M. De Mattia,[60a,60b] T. Dorigo,[60a] F. Fanzago,[60a] F. Gasparini,[60a,60b] P. Giubilato,[60a,60b] A. Gresele,[60a,60c] S. Lacaprara,[60a] I. Lazzizzera,[60a,60c] M. Margoni,[60a,60b] G. Maron,[60a] A.T. Meneguzzo,[60a,60b] M. Nespolo,[60a] L. Perrozzi,[60a] N. Pozzobon,[60a,60b] P. Ronchese,[60a,60b] F. Simonetto,[60a,60b] E. Torassa,[60a] M. Tosi,[60a,60b] A. Triossi,[60a] S. Vanini,[60a,60b] G. Zumerle,[60a,60b] P. Baesso,[61a,61b] U. Berzano,[61a] C. Riccardi,[61a,61b] P. Torre,[61a,61b] P. Vitulo,[61a,61b] C. Viviani,[61a,61b] M. Biasini,[62a,62b] G.M. Bilei,[62a] B. Caponeri,[62a,62b] L. Fanò,[62a] P. Lariccia,[62a,62b] A. Lucaroni,[62a,62b] G. Mantovani,[62a,62b] M. Menichelli,[62a] A. Nappi,[62a,62b] A. Santocchia,[62a,62b] L. Servoli,[62a] M. Valdata,[62a] R. Volpe,[62a,62b,b] P. Azzurri,[63a,63c] G. Bagliesi,[63a] J. Bernardini,[63a,63b,b] T. Boccali,[63a] R. Castaldi,[63a] R.T. Dagnolo,[63a,63c] R. Dell'Orso,[63a] F. Fiori,[63a,63b] L. Foà,[63a,63c] A. Giassi,[63a] A. Kraan,[63a] F. Ligabue,[63a,63c] T. Lomtadze,[63a] L. Martini,[63a] A. Messineo,[63a,63b] F. Palla,[63a] F. Palmonari,[63a] G. Segneri,[63a] A.T. Serban,[63a] P. Spagnolo,[63a,b] R. Tenchini,[63a,b] G. Tonelli,[63a,63b,b] A. Venturi,[63a] P.G. Verdini,[63a] L. Barone,[64a,64b] F. Cavallari,[64a,b] D. Del Re,[64a,64b] E. Di Marco,[64a,64b] M. Diemoz,[64a] D. Franci,[64a,64b] M. Grassi,[64a] E. Longo,[64a,64b] G. Organtini,[64a,64b] A. Palma,[64a,64b] F. Pandolfi,[64a,64b] R. Paramatti,[64a,b] S. Rahatlou,[64a,64b,b] N. Amapane,[65a,65b]

R. Arcidiacono,[65a,65b] S. Argiro,[65a,65b] M. Arneodo,[65a,65c] C. Biino,[65a] C. Botta,[65a,65b] N. Cartiglia,[65a] R. Castello,[65a,65b] M. Costa,[65a,65b] N. Demaria,[65a] A. Graziano,[65a,65b] C. Mariotti,[65a] M. Marone,[65a,65b] S. Maselli,[65a] E. Migliore,[65a,65b] G. Mila,[65a,65b] V. Monaco,[65a,65b] M. Musich,[65a,65b] M. M. Obertino,[65a,65c] N. Pastrone,[65a] M. Pelliccioni,[65a,65b,b] A. Romero,[65a,65b] M. Ruspa,[65a,65c] R. Sacchi,[65a,65b] A. Solano,[65a,65b] A. Staiano,[65a] D. Trocino,[65a,65b] A. Vilela Pereira,[65a,65b,b] F. Ambroglini,[66a,66b] S. Belforte,[66a] F. Cossutti,[66a] G. Della Ricca,[66a,66b] B. Gobbo,[66a] D. Montanino,[66a] A. Penzo,[66a] S. Chang,[67] J. Chung,[67] D. H. Kim,[67] G. N. Kim,[67] J. E. Kim,[67] D. J. Kong,[67] H. Park,[67] D. C. Son,[67] Zero Kim,[68] J. Y. Kim,[68] S. Song,[68] B. Hong,[69] H. Kim,[69] J. H. Kim,[69] T. J. Kim,[69] K. S. Lee,[69] D. H. Moon,[69] S. K. Park,[69] H. B. Rhee,[69] K. S. Sim,[69] M. Choi,[70] S. Kang,[70] H. Kim,[70] C. Park,[70] I. C. Park,[70] S. Park,[70] S. Choi,[71] Y. Choi,[71] Y. K. Choi,[71] J. Goh,[71] J. Lee,[71] S. Lee,[71] H. Seo,[71] I. Yu,[71] M. Janulis,[72] D. Martisiute,[72] P. Petrov,[72] T. Sabonis,[72] H. Castilla Valdez,[73,b] E. De La Cruz Burelo,[73] R. Lopez-Fernandez,[73] A. Sánchez Hernández,[73] L. M. Villaseñor-Cendejas,[73] S. Carrillo Moreno,[74] H. A. Salazar Ibarguen,[75] E. Casimiro Linares,[76] A. Morelos Pineda,[76] M. A. Reyes-Santos,[76] P. Allfrey,[77] D. Krofcheck,[77] J. Tam,[77] T. Aumeyr,[78] P. H. Butler,[78] T. Signal,[78] J. C. Williams,[78] M. Ahmad,[79] I. Ahmed,[79] M. I. Asghar,[79] H. R. Hoorani,[79] W. A. Khan,[79] T. Khurshid,[79] S. Qazi,[79] M. Cwiok,[80] W. Dominik,[80] K. Doroba,[80] M. Konecki,[80] J. Krolikowski,[80] T. Frueboes,[81] R. Gokieli,[81] M. Górski,[81] M. Kazana,[81] K. Nawrocki,[81] M. Szleper,[81] G. Wrochna,[81] P. Zalewski,[81] N. Almeida,[82] A. David,[82] P. Faccioli,[82] P. G. Ferreira Parracho,[82] M. Gallinaro,[82] G. Mini,[82] P. Musella,[82] A. Nayak,[82] L. Raposo,[82] P. Q. Ribeiro,[82] J. Seixas,[82] P. Silva,[82] D. Soares,[82] J. Varela,[82,b] H. K. Wöhri,[82] I. Altsybeev,[83] I. Belotelov,[83] P. Bunin,[83] M. Finger,[83] M. Finger, Jr.,[83] I. Golutvin,[83] A. Kamenev,[83] V. Karjavin,[83] G. Kozlov,[83] A. Lanev,[83] P. Moisenz,[83] V. Palichik,[83] V. Perelygin,[83] S. Shmatov,[83] V. Smirnov,[83] A. Volodko,[83] A. Zarubin,[83] N. Bondar,[84] V. Golovtsov,[84] Y. Ivanov,[84] V. Kim,[84] P. Levchenko,[84] I. Smirnov,[84] V. Sulimov,[84] L. Uvarov,[84] S. Vavilov,[84] A. Vorobyev,[84] Yu. Andreev,[85] S. Gninenko,[85] N. Golubev,[85] M. Kirsanov,[85] N. Krasnikov,[85] V. Matveev,[85] A. Pashenkov,[85] A. Toropin,[85] S. Troitsky,[85] V. Epshteyn,[86] V. Gavrilov,[86] N. Ilina,[86] V. Kaftanov,[86,a] M. Kossov,[86,b] A. Krokhotin,[86] S. Kuleshov,[86] A. Oulianov,[86] G. Safronov,[86] S. Semenov,[86] I. Shreyber,[86] V. Stolin,[86] E. Vlasov,[86] A. Zhokin,[86] E. Boos,[87] M. Dubinin,[87,i] L. Dudko,[87] A. Ershov,[87] A. Gribushin,[87] O. Kodolova,[87] I. Lokhtin,[87] S. Obraztsov,[87] S. Petrushanko,[87] L. Sarycheva,[87] V. Savrin,[87] A. Snigirev,[87] V. Andreev,[88] I. Dremin,[88] M. Kirakosyan,[88] S. V. Rusakov,[88] A. Vinogradov,[88] I. Azhgirey,[89] S. Bitioukov,[89] K. Datsko,[89] V. Grishin,[89,b] V. Kachanov,[89] D. Konstantinov,[89] V. Krychkine,[89] V. Petrov,[89] R. Ryutin,[89] S. Slabospitsky,[89] A. Sobol,[89] A. Sytine,[89] L. Tourtchanovitch,[89] S. Troshin,[89] N. Tyurin,[89] A. Uzunian,[89] A. Volkov,[89] P. Adzic,[90] M. Djordjevic,[90] D. Krpic,[90] D. Maletic,[90] J. Milosevic,[90] J. Puzovic,[90] M. Aguilar-Benitez,[91] J. Alcaraz Maestre,[91] P. Arce,[91] C. Battilana,[91] E. Calvo,[91] M. Cepeda,[91] M. Cerrada,[91] M. Chamizo Llatas,[91] N. Colino,[91] B. De La Cruz,[91] C. Diez Pardos,[91] C. Fernandez Bedoya,[91] J. P. Fernández Ramos,[91] A. Ferrando,[91] J. Flix,[91] M. C. Fouz,[91] P. Garcia-Abia,[91] O. Gonzalez Lopez,[91] S. Goy Lopez,[91] J. M. Hernandez,[91] M. I. Josa,[91] G. Merino,[91] J. Puerta Pelayo,[91] I. Redondo,[91] L. Romero,[91] J. Santaolalla,[91] C. Willmott,[91] C. Albajar,[92] J. F. de Trocóniz,[92] J. Cuevas,[93] J. Fernandez Menendez,[93] I. Gonzalez Caballero,[93] L. Lloret Iglesias,[93] J. M. Vizan Garcia,[93] I. J. Cabrillo,[94] A. Calderon,[94] S. H. Chuang,[94] I. Diaz Merino,[94] C. Diez Gonzalez,[94] J. Duarte Campderros,[94] M. Fernandez,[94] G. Gomez,[94] J. Gonzalez Sanchez,[94] R. Gonzalez Suarez,[94] C. Jorda,[94] P. Lobelle Pardo,[94] A. Lopez Virto,[94] J. Marco,[94] R. Marco,[94] C. Martinez Rivero,[94] P. Martinez Ruiz del Arbol,[94] F. Matorras,[94] T. Rodrigo,[94] A. Ruiz Jimeno,[94] L. Scodellaro,[94] M. Sobron Sanudo,[94] I. Vila,[94] R. Vilar Cortabitarte,[94] D. Abbaneo,[95] E. Auffray,[95] P. Baillon,[95] A. H. Ball,[95] D. Barney,[95] F. Beaudette,[95,c] A. J. Bell,[95] R. Bellan,[95] D. Benedetti,[95] C. Bernet,[95,c] W. Bialas,[95] P. Bloch,[95] A. Bocci,[95] S. Bolognesi,[95] H. Breuker,[95] G. Brona,[95] K. Bunkowski,[95] T. Camporesi,[95] E. Cano,[95] A. Cattai,[95] G. Cerminara,[95] T. Christiansen,[95] J. A. Coarasa Perez,[95] R. Covarelli,[95] B. Curé,[95] T. Dahms,[95] A. De Roeck,[95] A. Elliott-Peisert,[95] W. Funk,[95] A. Gaddi,[95] S. Gennai,[95] H. Gerwig,[95] D. Gigi,[95] K. Gill,[95] D. Giordano,[95] F. Glege,[95] R. Gomez-Reino Garrido,[95] S. Gowdy,[95] L. Guiducci,[95] M. Hansen,[95] C. Hartl,[95] J. Harvey,[95] B. Hegner,[95] C. Henderson,[95] H. F. Hoffmann,[95] A. Honma,[95] V. Innocente,[95] P. Janot,[95] P. Lecoq,[95] C. Leonidopoulos,[95] C. Lourenço,[95] A. Macpherson,[95] T. Mäki,[95] L. Malgeri,[95] M. Mannelli,[95] L. Masetti,[95] G. Mavromanolakis,[95] F. Meijers,[95] S. Mersi,[95] E. Meschi,[95] R. Moser,[95] M. U. Mozer,[95] M. Mulders,[95] E. Nesvold,[95,b] L. Orsini,[95] E. Perez,[95] A. Petrilli,[95] A. Pfeiffer,[95] M. Pierini,[95] M. Pimiä,[95] A. Racz,[95] G. Rolandi,[95] C. Rovelli,[95,j] M. Rovere,[95] V. Ryjov,[95] H. Sakulin,[95] C. Schäfer,[95] C. Schwick,[95] I. Segoni,[95] A. Sharma,[95] P. Siegrist,[95] M. Simon,[95] P. Sphicas,[95,k] D. Spiga,[95] M. Spiropulu,[95,i] F. Stöckli,[95] P. Traczyk,[95] P. Tropea,[95] A. Tsirou,[95] G. I. Veres,[95] P. Vichoudis,[95] M. Voutilainen,[95] W. D. Zeuner,[95] W. Bertl,[96] K. Deiters,[96] W. Erdmann,[96]

K. Gabathuler,[96] R. Horisberger,[96] Q. Ingram,[96] H. C. Kaestli,[96] S. König,[96] D. Kotlinski,[96] U. Langenegger,[96] F. Meier,[96] D. Renker,[96] T. Rohe,[96] J. Sibille,[96,l] A. Starodumov,[96,m] L. Caminada,[97,n] Z. Chen,[97] S. Cittolin,[97] G. Dissertori,[97] M. Dittmar,[97] J. Eugster,[97] K. Freudenreich,[97] C. Grab,[97] A. Hervé,[97] W. Hintz,[97] P. Lecomte,[97] W. Lustermann,[97] C. Marchica,[97,n] P. Meridiani,[97] P. Milenovic,[97,o] F. Moortgat,[97] A. Nardulli,[97] F. Nessi-Tedaldi,[97] L. Pape,[97] F. Pauss,[97] T. Punz,[97] A. Rizzi,[97] F. J. Ronga,[97] L. Sala,[97] A. K. Sanchez,[97] M.-C. Sawley,[97] D. Schinzel,[97] V. Sordini,[97] B. Stieger,[97] L. Tauscher,[97,a] A. Thea,[97] K. Theofilatos,[97] D. Treille,[97] M. Weber,[97] L. Wehrli,[97] J. Weng,[97] C. Amsler,[98] V. Chiochia,[98] S. De Visscher,[98] M. Ivova Rikova,[98] B. Millan Mejias,[98] C. Regenfus,[98] P. Robmann,[98] T. Rommerskirchen,[98] A. Schmidt,[98] D. Tsirigkas,[98] L. Wilke,[98] Y. H. Chang,[99] K. H. Chen,[99] W. T. Chen,[99] A. Go,[99] C. M. Kuo,[99] S. W. Li,[99] W. Lin,[99] M. H. Liu,[99] Y. J. Lu,[99] J. H. Wu,[99] S. S. Yu,[99] P. Bartalini,[100] P. Chang,[100] Y. H. Chang,[100] Y. W. Chang,[100] Y. Chao,[100] K. F. Chen,[100] W.-S. Hou,[100] Y. Hsiung,[100] K. Y. Kao,[100] Y. J. Lei,[100] S. W. Lin,[100] R.-S. Lu,[100] J. G. Shiu,[100] Y. M. Tzeng,[100] K. Ueno,[100] C. C. Wang,[100] M. Wang,[100] J. T. Wei,[100] A. Adiguzel,[101] A. Ayhan,[101] M. N. Bakirci,[101] S. Cerci,[101] Z. Demir,[101] C. Dozen,[101] I. Dumanoglu,[101] E. Eskut,[101] S. Girgis,[101] G. Gökbulut,[101] Y. Güler,[101] E. Gurpinar,[101] I. Hos,[101] E. E. Kangal,[101] T. Karaman,[101] A. Kayis Topaksu,[101] A. Nart,[101] G. Önengüt,[101] K. Ozdemir,[101] S. Ozturk,[101] A. Polatöz,[101] O. Sahin,[101] O. Sengul,[101] K. Sogut,[101] B. Tali,[101] H. Topakli,[101] D. Uzun,[101] L. N. Vergili,[101] M. Vergili,[101] C. Zorbilmez,[101] I. V. Akin,[102] T. Aliev,[102] S. Bilmis,[102] M. Deniz,[102] H. Gamsizkan,[102] A. M. Guler,[102] K. Ocalan,[102] A. Ozpineci,[102] M. Serin,[102] R. Sever,[102] U. E. Surat,[102] M. Zeyrek,[102] M. Deliomeroglu,[103] D. Demir,[103] E. Gülmez,[103] A. Halu,[103] B. Isildak,[103] M. Kaya,[103] O. Kaya,[103] M. Özbek,[103] S. Ozkorucuklu,[103] N. Sonmez,[103] L. Levchuk,[104] P. Bell,[105] F. Bostock,[105] J. J. Brooke,[105] T. L. Cheng,[105] D. Cussans,[105] R. Frazier,[105] J. Goldstein,[105] M. Hansen,[105] G. P. Heath,[105] H. F. Heath,[105] C. Hill,[105] B. Huckvale,[105] J. Jackson,[105] L. Kreczko,[105] C. K. Mackay,[105] S. Metson,[105] D. M. Newbold,[105,p] K. Nirunpong,[105] V. J. Smith,[105] S. Ward,[105] L. Basso,[106] K. W. Bell,[106] A. Belyaev,[106] C. Brew,[106] R. M. Brown,[106] B. Camanzi,[106] D. J. A. Cockerill,[106] J. A. Coughlan,[106] K. Harder,[106] S. Harper,[106] B. W. Kennedy,[106] E. Olaiya,[106] B. C. Radburn-Smith,[106] C. H. Shepherd-Themistocleous,[106] I. R. Tomalin,[106] W. J. Womersley,[106] S. D. Worm,[106] R. Bainbridge,[107] G. Ball,[107] J. Ballin,[107] R. Beuselinck,[107] O. Buchmuller,[107] D. Colling,[107] N. Cripps,[107] M. Cutajar,[107] G. Davies,[107] M. Della Negra,[107] C. Foudas,[107] J. Fulcher,[107] D. Futyan,[107] A. Guneratne Bryer,[107] G. Hall,[107] Z. Hatherell,[107] J. Hays,[107] G. Iles,[107] G. Karapostoli,[107] L. Lyons,[107] A.-M. Magnan,[107] J. Marrouche,[107] R. Nandi,[107] J. Nash,[107] A. Nikitenko,[107,m] A. Papageorgiou,[107] M. Pesaresi,[107] K. Petridis,[107] M. Pioppi,[107,q] D. M. Raymond,[107] N. Rompotis,[107] A. Rose,[107] M. J. Ryan,[107] C. Seez,[107] P. Sharp,[107] A. Sparrow,[107] M. Stoye,[107] A. Tapper,[107] S. Tourneur,[107] M. Vazquez Acosta,[107] T. Virdee,[107,b] S. Wakefield,[107] D. Wardrope,[107] T. Whyntie,[107] M. Barrett,[108] M. Chadwick,[108] J. E. Cole,[108] P. R. Hobson,[108] A. Khan,[108] P. Kyberd,[108] D. Leslie,[108] I. D. Reid,[108] L. Teodorescu,[108] T. Bose,[109] A. Clough,[109] A. Heister,[109] J. St. John,[109] P. Lawson,[109] D. Lazic,[109] J. Rohlf,[109] L. Sulak,[109] J. Andrea,[110] A. Avetisyan,[110] S. Bhattacharya,[110] J. P. Chou,[110] D. Cutts,[110] S. Esen,[110] U. Heintz,[110] S. Jabeen,[110] G. Kukartsev,[110] G. Landsberg,[110] M. Narain,[110] D. Nguyen,[110] T. Speer,[110] K. V. Tsang,[110] M. A. Borgia,[111] R. Breedon,[111] M. Calderon De La Barca Sanchez,[111] D. Cebra,[111] M. Chertok,[111] J. Conway,[111] P. T. Cox,[111] J. Dolen,[111] R. Erbacher,[111] E. Friis,[111] W. Ko,[111] A. Kopecky,[111] R. Lander,[111] H. Liu,[111] S. Maruyama,[111] T. Miceli,[111] M. Nikolic,[111] D. Pellett,[111] J. Robles,[111] T. Schwarz,[111] M. Searle,[111] J. Smith,[111] M. Squires,[111] M. Tripathi,[111] R. Vasquez Sierra,[111] C. Veelken,[111] V. Andreev,[112] K. Arisaka,[112] D. Cline,[112] R. Cousins,[112] A. Deisher,[112] S. Erhan,[112,b] C. Farrell,[112] M. Felcini,[112] J. Hauser,[112] M. Ignatenko,[112] C. Jarvis,[112] C. Plager,[112] G. Rakness,[112] P. Schlein,[112,a] J. Tucker,[112] V. Valuev,[112] R. Wallny,[112] J. Babb,[113] R. Clare,[113] J. Ellison,[113] J. W. Gary,[113] G. Hanson,[113] G. Y. Jeng,[113] S. C. Kao,[113] F. Liu,[113] H. Liu,[113] A. Luthra,[113] H. Nguyen,[113] G. Pasztor,[113,r] A. Satpathy,[113] B. C. Shen,[113,a] R. Stringer,[113] J. Sturdy,[113] S. Sumowidagdo,[113] R. Wilken,[113] S. Wimpenny,[113] W. Andrews,[114] J. G. Branson,[114] E. Dusinberre,[114] D. Evans,[114] F. Golf,[114] A. Holzner,[114] R. Kelley,[114] M. Lebourgeois,[114] J. Letts,[114] B. Mangano,[114] J. Muelmenstaedt,[114] S. Padhi,[114] C. Palmer,[114] G. Petrucciani,[114] H. Pi,[114] M. Pieri,[114] R. Ranieri,[114] M. Sani,[114] V. Sharma,[114,b] S. Simon,[114] Y. Tu,[114] A. Vartak,[114] F. Würthwein,[114] A. Yagil,[114] D. Barge,[115] M. Blume,[115] C. Campagnari,[115] M. D'Alfonso,[115] T. Danielson,[115] J. Garberson,[115] J. Incandela,[115] C. Justus,[115] P. Kalavase,[115] S. A. Koay,[115] D. Kovalskyi,[115] V. Krutelyov,[115] J. Lamb,[115] S. Lowette,[115] V. Pavlunin,[115] F. Rebassoo,[115] J. Ribnik,[115] J. Richman,[115] R. Rossin,[115] D. Stuart,[115] W. To,[115] J. R. Vlimant,[115] M. Witherell,[115] A. Bornheim,[116] J. Bunn,[116] M. Gataullin,[116] D. Kcira,[116] V. Litvine,[116] Y. Ma,[116] H. B. Newman,[116] C. Rogan,[116] K. Shin,[116] V. Timciuc,[116] J. Veverka,[116] R. Wilkinson,[116] Y. Yang,[116] R. Y. Zhu,[116] B. Akgun,[117] R. Carroll,[117] T. Ferguson,[117] D. W. Jang,[117] S. Y. Jun,[117] M. Paulini,[117]

J. Russ,[117] N. Terentyev,[117] H. Vogel,[117] I. Vorobiev,[117] J. P. Cumalat,[118] M. E. Dinardo,[118] B. R. Drell,[118] W. T. Ford,[118] B. Heyburn,[118] E. Luiggi Lopez,[118] U. Nauenberg,[118] J. G. Smith,[118] K. Stenson,[118] K. A. Ulmer,[118] S. R. Wagner,[118] S. L. Zang,[118] L. Agostino,[119] J. Alexander,[119] F. Blekman,[119] A. Chatterjee,[119] S. Das,[119] N. Eggert,[119] L. J. Fields,[119] L. K. Gibbons,[119] B. Heltsley,[119] W. Hopkins,[119] A. Khukhunaishvili,[119] B. Kreis,[119] V. Kuznetsov,[119] G. Nicolas Kaufman,[119] J. R. Patterson,[119] D. Puigh,[119] D. Riley,[119] A. Ryd,[119] X. Shi,[119] W. Sun,[119] W. D. Teo,[119] J. Thom,[119] J. Thompson,[119] J. Vaughan,[119] Y. Weng,[119] P. Wittich,[119] A. Biselli,[120] G. Cirino,[120] D. Winn,[120] S. Abdullin,[121] M. Albrow,[121] J. Anderson,[121] G. Apollinari,[121] M. Atac,[121] J. A. Bakken,[121] S. Banerjee,[121] L. A. T. Bauerdick,[121] A. Beretvas,[121] J. Berryhill,[121] P. C. Bhat,[121] I. Bloch,[121] F. Borcherding,[121] K. Burkett,[121] J. N. Butler,[121] V. Chetluru,[121] H. W. K. Cheung,[121] F. Chlebana,[121] S. Cihangir,[121] M. Demarteau,[121] D. P. Eartly,[121] V. D. Elvira,[121] I. Fisk,[121] J. Freeman,[121] Y. Gao,[121] E. Gottschalk,[121] D. Green,[121] O. Gutsche,[121] A. Hahn,[121] J. Hanlon,[121] R. M. Harris,[121] E. James,[121] H. Jensen,[121] M. Johnson,[121] U. Joshi,[121] R. Khatiwada,[121] B. Kilminster,[121] B. Klima,[121] K. Kousouris,[121] S. Kunori,[121] S. Kwan,[121] P. Limon,[121] R. Lipton,[121] J. Lykken,[121] K. Maeshima,[121] J. M. Marraffino,[121] D. Mason,[121] P. McBride,[121] T. McCauley,[121] T. Miao,[121] K. Mishra,[121] S. Mrenna,[121] Y. Musienko,[121,s] C. Newman-Holmes,[121] V. O'Dell,[121] S. Popescu,[121] R. Pordes,[121] O. Prokofyev,[121] N. Saoulidou,[121] E. Sexton-Kennedy,[121] S. Sharma,[121] R. P. Smith,[121,a] A. Soha,[121] W. J. Spalding,[121] L. Spiegel,[121] P. Tan,[121] L. Taylor,[121] S. Tkaczyk,[121] L. Uplegger,[121] E. W. Vaandering,[121] R. Vidal,[121] J. Whitmore,[121] W. Wu,[121] F. Yumiceva,[121] J. C. Yun,[121] D. Acosta,[122] P. Avery,[122] D. Bourilkov,[122] M. Chen,[122] G. P. Di Giovanni,[122] D. Dobur,[122] A. Drozdetskiy,[122] R. D. Field,[122] Y. Fu,[122] I. K. Furic,[122] J. Gartner,[122] B. Kim,[122] S. Klimenko,[122] J. Konigsberg,[122] A. Korytov,[122] K. Kotov,[122] A. Kropivnitskaya,[122] T. Kypreos,[122] K. Matchev,[122] G. Mitselmakher,[122] Y. Pakhotin,[122] J. Piedra Gomez,[122] C. Prescott,[122] R. Remington,[122] M. Schmitt,[122] B. Scurlock,[122] P. Sellers,[122] D. Wang,[122] J. Yelton,[122] M. Zakaria,[122] C. Ceron,[123] V. Gaultney,[123] L. Kramer,[123] L. M. Lebolo,[123] S. Linn,[123] P. Markowitz,[123] G. Martinez,[123] D. Mesa,[123] J. L. Rodriguez,[123] T. Adams,[124] A. Askew,[124] J. Chen,[124] B. Diamond,[124] S. V. Gleyzer,[124] J. Haas,[124] S. Hagopian,[124] V. Hagopian,[124] M. Jenkins,[124] K. F. Johnson,[124] H. Prosper,[124] S. Sekmen,[124] V. Veeraraghavan,[124] M. M. Baarmand,[125] S. Guragain,[125] M. Hohlmann,[125] H. Kalakhety,[125] H. Mermerkaya,[125] R. Ralich,[125] I. Vodopiyanov,[125] M. R. Adams,[126] I. M. Anghel,[126] L. Apanasevich,[126] V. E. Bazterra,[126] R. R. Betts,[126] J. Callner,[126] R. Cavanaugh,[126] C. Dragoiu,[126] E. J. Garcia-Solis,[126] C. E. Gerber,[126] D. J. Hofman,[126] S. Khalatian,[126] F. Lacroix,[126] E. Shabalina,[126] A. Smoron,[126] D. Strom,[126] N. Varelas,[126] U. Akgun,[127] E. A. Albayrak,[127] B. Bilki,[127] K. Cankocak,[127] W. Clarida,[127] F. Duru,[127] C. K. Lae,[127] E. McCliment,[127] J.-P. Merlo,[127] A. Mestvirishvili,[127] A. Moeller,[127] J. Nachtman,[127] C. R. Newsom,[127] E. Norbeck,[127] J. Olson,[127] Y. Onel,[127] F. Ozok,[127] S. Sen,[127] J. Wetzel,[127] T. Yetkin,[127] K. Yi,[127] B. A. Barnett,[128] B. Blumenfeld,[128] A. Bonato,[128] C. Eskew,[128] D. Fehling,[128] G. Giurgiu,[128] A. V. Gritsan,[128] Z. J. Guo,[128] G. Hu,[128] P. Maksimovic,[128] S. Rappoccio,[128] M. Swartz,[128] N. V. Tran,[128] A. Whitbeck,[128] P. Baringer,[129] A. Bean,[129] G. Benelli,[129] O. Grachov,[129] M. Murray,[129] V. Radicci,[129] S. Sanders,[129] J. S. Wood,[129] V. Zhukova,[129] D. Bandurin,[130] T. Bolton,[130] I. Chakaberia,[130] A. Ivanov,[130] K. Kaadze,[130] Y. Maravin,[130] S. Shrestha,[130] I. Svintradze,[130] Z. Wan,[130] J. Gronberg,[131] D. Lange,[131] D. Wright,[131] D. Baden,[132] M. Boutemeur,[132] S. C. Eno,[132] D. Ferencek,[132] N. J. Hadley,[132] R. G. Kellogg,[132] M. Kirn,[132] A. Mignerey,[132] K. Rossato,[132] P. Rumerio,[132] F. Santanastasio,[132] A. Skuja,[132] J. Temple,[132] M. B. Tonjes,[132] S. C. Tonwar,[132] E. Twedt,[132] B. Alver,[133] G. Bauer,[133] J. Bendavid,[133] W. Busza,[133] E. Butz,[133] I. A. Cali,[133] M. Chan,[133] D. D'Enterria,[133] P. Everaerts,[133] G. Gomez Ceballos,[133] M. Goncharov,[133] K. A. Hahn,[133] P. Harris,[133] Y. Kim,[133] M. Klute,[133] Y.-J. Lee,[133] W. Li,[133] C. Loizides,[133] P. D. Luckey,[133] T. Ma,[133] S. Nahn,[133] C. Paus,[133] C. Roland,[133] G. Roland,[133] M. Rudolph,[133] G. S. F. Stephans,[133] K. Sumorok,[133] K. Sung,[133] E. A. Wenger,[133] B. Wyslouch,[133] S. Xie,[133] Y. Yilmaz,[133] A. S. Yoon,[133] M. Zanetti,[133] P. Cole,[134] S. I. Cooper,[134] P. Cushman,[134] B. Dahmes,[134] A. De Benedetti,[134] P. R. Dudero,[134] G. Franzoni,[134] J. Haupt,[134] K. Klapoetke,[134] Y. Kubota,[134] J. Mans,[134] D. Petyt,[134] V. Rekovic,[134] R. Rusack,[134] M. Sasseville,[134] A. Singovsky,[134] L. M. Cremaldi,[135] R. Godang,[135] R. Kroeger,[135] L. Perera,[135] R. Rahmat,[135] D. A. Sanders,[135] P. Sonnek,[135] D. Summers,[135] K. Bloom,[136] S. Bose,[136] J. Butt,[136] D. R. Claes,[136] A. Dominguez,[136] M. Eads,[136] J. Keller,[136] T. Kelly,[136] I. Kravchenko,[136] J. Lazo-Flores,[136] C. Lundstedt,[136] H. Malbouisson,[136] S. Malik,[136] G. R. Snow,[136] U. Baur,[137] I. Iashvili,[137] A. Kharchilava,[137] A. Kumar,[137] K. Smith,[137] M. Strang,[137] J. Zennamo,[137] G. Alverson,[138] E. Barberis,[138] D. Baumgartel,[138] O. Boeriu,[138] S. Reucroft,[138] J. Swain,[138] D. Wood,[138] J. Zhang,[138] A. Anastassov,[139] A. Kubik,[139] R. A. Ofierzynski,[139] A. Pozdnyakov,[139] M. Schmitt,[139] S. Stoynev,[139] M. Velasco,[139] S. Won,[139] L. Antonelli,[140] D. Berry,[140] M. Hildreth,[140] C. Jessop,[140] D. J. Karmgard,[140] J. Kolb,[140] T. Kolberg,[140]

K. Lannon,[140] S. Lynch,[140] N. Marinelli,[140] D. M. Morse,[140] R. Ruchti,[140] J. Slaunwhite,[140] N. Valls,[140] J. Warchol,[140] M. Wayne,[140] J. Ziegler,[140] B. Bylsma,[141] L. S. Durkin,[141] J. Gu,[141] P. Killewald,[141] T. Y. Ling,[141] G. Williams,[141] N. Adam,[142] E. Berry,[142] P. Elmer,[142] D. Gerbaudo,[142] V. Halyo,[142] A. Hunt,[142] J. Jones,[142] E. Laird,[142] D. Lopes Pegna,[142] D. Marlow,[142] T. Medvedeva,[142] M. Mooney,[142] J. Olsen,[142] P. Piroué,[142] D. Stickland,[142] C. Tully,[142] J. S. Werner,[142] A. Zuranski,[142] J. G. Acosta,[143] X. T. Huang,[143] A. Lopez,[143] H. Mendez,[143] S. Oliveros,[143] J. E. Ramirez Vargas,[143] A. Zatzerklyaniy,[143] E. Alagoz,[144] V. E. Barnes,[144] G. Bolla,[144] L. Borrello,[144] D. Bortoletto,[144] A. Everett,[144] A. F. Garfinkel,[144] Z. Gecse,[144] L. Gutay,[144] M. Jones,[144] O. Koybasi,[144] A. T. Laasanen,[144] N. Leonardo,[144] C. Liu,[144] V. Maroussov,[144] P. Merkel,[144] D. H. Miller,[144] N. Neumeister,[144] K. Potamianos,[144] I. Shipsey,[144] D. Silvers,[144] H. D. Yoo,[144] J. Zablocki,[144] Y. Zheng,[144] P. Jindal,[145] N. Parashar,[145] V. Cuplov,[146] K. M. Ecklund,[146] F. J. M. Geurts,[146] J. H. Liu,[146] J. Morales,[146] B. P. Padley,[146] R. Redjimi,[146] J. Roberts,[146] B. Betchart,[147] A. Bodek,[147] Y. S. Chung,[147] P. de Barbaro,[147] R. Demina,[147] H. Flacher,[147] A. Garcia-Bellido,[147] Y. Gotra,[147] J. Han,[147] A. Harel,[147] D. C. Miner,[147] D. Orbaker,[147] G. Petrillo,[147] D. Vishnevskiy,[147] M. Zielinski,[147] A. Bhatti,[148] L. Demortier,[148] K. Goulianos,[148] K. Hatakeyama,[148] G. Lungu,[148] C. Mesropian,[148] M. Yan,[148] O. Atramentov,[149] Y. Gershtein,[149] R. Gray,[149] E. Halkiadakis,[149] D. Hidas,[149] D. Hits,[149] A. Lath,[149] K. Rose,[149] S. Schnetzer,[149] S. Somalwar,[149] R. Stone,[149] S. Thomas,[149] G. Cerizza,[150] M. Hollingsworth,[150] S. Spanier,[150] Z. C. Yang,[150] A. York,[150] J. Asaadi,[151] R. Eusebi,[151] J. Gilmore,[151] A. Gurrola,[151] T. Kamon,[151] V. Khotilovich,[151] R. Montalvo,[151] C. N. Nguyen,[151] J. Pivarski,[151] A. Safonov,[151] S. Sengupta,[151] D. Toback,[151] M. Weinberger,[151] N. Akchurin,[152] C. Bardak,[152] J. Damgov,[152] C. Jeong,[152] K. Kovitanggoon,[152] S. W. Lee,[152] P. Mane,[152] Y. Roh,[152] A. Sill,[152] I. Volobouev,[152] R. Wigmans,[152] E. Yazgan,[152] E. Appelt,[153] E. Brownson,[153] D. Engh,[153] C. Florez,[153] W. Gabella,[153] W. Johns,[153] P. Kurt,[153] C. Maguire,[153] A. Melo,[153] P. Sheldon,[153] J. Velkovska,[153] M. W. Arenton,[154] M. Balazs,[154] M. Buehler,[154] S. Conetti,[154] B. Cox,[154] R. Hirosky,[154] A. Ledovskoy,[154] C. Neu,[154] R. Yohay,[154] S. Gollapinni,[155] K. Gunthoti,[155] R. Harr,[155] P. E. Karchin,[155] M. Mattson,[155] C. Milstène,[155] A. Sakharov,[155] M. Anderson,[156] M. Bachtis,[156] J. N. Bellinger,[156] D. Carlsmith,[156] S. Dasu,[156] S. Dutta,[156] J. Efron,[156] L. Gray,[156] K. S. Grogg,[156] M. Grothe,[156] R. Hall-Wilton,[156,b] M. Herndon,[156] P. Klabbers,[156] J. Klukas,[156] A. Lanaro,[156] C. Lazaridis,[156] J. Leonard,[156] D. Lomidze,[156] R. Loveless,[156] A. Mohapatra,[156] G. Polese,[156] D. Reeder,[156] A. Savin,[156] W. H. Smith,[156] J. Swanson,[156] and M. Weinberg[156]

(CMS Collaboration)

[1]*Yerevan Physics Institute, Yerevan, Armenia*
[2]*Institut für Hochenergiephysik der OeAW, Wien, Austria*
[3]*National Centre for Particle and High Energy Physics, Minsk, Belarus*
[4]*Universiteit Antwerpen, Antwerpen, Belgium*
[5]*Vrije Universiteit Brussel, Brussel, Belgium*
[6]*Université Libre de Bruxelles, Bruxelles, Belgium*
[7]*Ghent University, Ghent, Belgium*
[8]*Université Catholique de Louvain, Louvain-la-Neuve, Belgium*
[9]*Université de Mons, Mons, Belgium*
[10]*Centro Brasileiro de Pesquisas Fisicas, Rio de Janeiro, Brazil*
[11]*Universidade do Estado do Rio de Janeiro, Rio de Janeiro, Brazil*
[12]*Instituto de Fisica Teorica, Universidade Estadual Paulista, Sao Paulo, Brazil*
[13]*Institute for Nuclear Research and Nuclear Energy, Sofia, Bulgaria*
[14]*University of Sofia, Sofia, Bulgaria*
[15]*Institute of High Energy Physics, Beijing, China*
[16]*State Key Laboratory of Nuclear Physics and Technology, Peking University, Beijing, China*
[17]*Universidad de Los Andes, Bogota, Colombia*
[18]*Technical University of Split, Split, Croatia*
[19]*University of Split, Split, Croatia*
[20]*Institute Rudjer Boskovic, Zagreb, Croatia*
[21]*University of Cyprus, Nicosia, Cyprus*
[22]*Academy of Scientific Research and Technology of the Arab Republic of Egypt, Egyptian Network of High Energy Physics, Cairo, Egypt*
[23]*National Institute of Chemical Physics and Biophysics, Tallinn, Estonia*
[24]*Department of Physics, University of Helsinki, Helsinki, Finland*

[25]Helsinki Institute of Physics, Helsinki, Finland
[26]Lappeenranta University of Technology, Lappeenranta, Finland
[27]Laboratoire d'Annecy-le-Vieux de Physique des Particules, IN2P3-CNRS, Annecy-le-Vieux, France
[28]DSM/IRFU, CEA/Saclay, Gif-sur-Yvette, France
[29]Laboratoire Leprince-Ringuet, Ecole Polytechnique, IN2P3-CNRS, Palaiseau, France
[30]Institut Pluridisciplinaire Hubert Curien, Université de Strasbourg, Université de Haute Alsace Mulhouse, CNRS/IN2P3, Strasbourg, France
[31]Centre de Calcul de l'Institut National de Physique Nucleaire et de Physique des Particules (IN2P3), Villeurbanne, France
[32]Université de Lyon, Université Claude Bernard Lyon 1, CNRS-IN2P3, Institut de Physique Nucléaire de Lyon, Villeurbanne, France
[33]E. Andronikashvili Institute of Physics, Academy of Science, Tbilisi, Georgia
[34]RWTH Aachen University, I. Physikalisches Institut, Aachen, Germany
[35]RWTH Aachen University, III. Physikalisches Institut A, Aachen, Germany
[36]RWTH Aachen University, III. Physikalisches Institut B, Aachen, Germany
[37]Deutsches Elektronen-Synchrotron, Hamburg, Germany
[38]University of Hamburg, Hamburg, Germany
[39]Institut für Experimentelle Kernphysik, Karlsruhe, Germany
[40]Institute of Nuclear Physics "Demokritos," Aghia Paraskevi, Greece
[41]University of Athens, Athens, Greece
[42]University of Ioánnina, Ioánnina, Greece
[43]KFKI Research Institute for Particle and Nuclear Physics, Budapest, Hungary
[44]Institute of Nuclear Research ATOMKI, Debrecen, Hungary
[45]University of Debrecen, Debrecen, Hungary
[46]Panjab University, Chandigarh, India
[47]University of Delhi, Delhi, India
[48]Bhabha Atomic Research Centre, Mumbai, India
[49]Tata Institute of Fundamental Research–EHEP, Mumbai, India
[50]Tata Institute of Fundamental Research–HECR, Mumbai, India
[51]Institute for Studies in Theoretical Physics & Mathematics (IPM), Tehran, Iran
[52a]INFN Sezione di Bari, Bari, Italy
[52b]Università di Bari, Bari, Italy
[52c]Politecnico di Bari, Bari, Italy
[53a]INFN Sezione di Bologna, Bologna, Italy
[53b]Università di Bologna, Bologna, Italy
[54a]INFN Sezione di Catania, Catania, Italy
[54b]Università di Catania, Catania, Italy
[55a]INFN Sezione di Firenze, Firenze, Italy
[55b]Università di Firenze, Firenze, Italy
[56]INFN Laboratori Nazionali di Frascati, Frascati, Italy
[57]INFN Sezione di Genova, Genova, Italy
[58a]INFN Sezione di Milano-Biccoca, Milano, Italy
[58b]Università di Milano-Bicocca, Milano, Italy
[59a]INFN Sezione di Napoli, Napoli, Italy
[59b]Università di Napoli "Federico II," Napoli, Italy
[60a]INFN Sezione di Padova, Padova, Italy
[60b]IUniversità di Padova, Padova, Italy
[60c]Università di Trento (Trento), Padova, Italy
[61a]INFN Sezione di Pavia, Pavia, Italy
[61b]Università di Pavia, Pavia, Italy
[62a]INFN Sezione di Perugia, Perugia, Italy
[62b]Università di Perugia, Perugia, Italy
[63a]INFN Sezione di Pisa, Pisa, Italy
[63b]Università di Pisa, Pisa, Italy
[63c]Scuola Normale Superiore di Pisa, Pisa, Italy
[64a]INFN Sezione di Roma, Roma, Italy
[64b]Università di Roma "La Sapienza,", Roma, Italy
[65a]INFN Sezione di Torino, Torino, Italy
[65b]Università di Torino, Torino, Italy
[65c]Università del Piemonte Orientale (Novara), Torino, Italy
[66a]INFN Sezione di Trieste, Trieste, Italy
[66b]Università di Trieste, Trieste, Italy
[67]Kyungpook National University, Daegu, Korea

[68]Chonnam National University, Institute for Universe and Elementary Particles, Kwangju, Korea
[69]Korea University, Seoul, Korea
[70]University of Seoul, Seoul, Korea
[71]Sungkyunkwan University, Suwon, Korea
[72]Vilnius University, Vilnius, Lithuania
[73]Centro de Investigacion y de Estudios Avanzados del IPN, Mexico City, Mexico
[74]Universidad Iberoamericana, Mexico City, Mexico
[75]Benemerita Universidad Autonoma de Puebla, Puebla, Mexico
[76]Universidad Autónoma de San Luis Potosí, San Luis Potosí, Mexico
[77]University of Auckland, Auckland, New Zealand
[78]University of Canterbury, Christchurch, New Zealand
[79]National Centre for Physics, Quaid-I-Azam University, Islamabad, Pakistan
[80]Institute of Experimental Physics, Warsaw, Poland
[81]Soltan Institute for Nuclear Studies, Warsaw, Poland
[82]Laboratório de Instrumentação e Física Experimental de Partículas, Lisboa, Portugal
[83]Joint Institute for Nuclear Research, Dubna, Russia
[84]Petersburg Nuclear Physics Institute, Gatchina (St. Petersburg), Russia
[85]Institute for Nuclear Research, Moscow, Russia
[86]Institute for Theoretical and Experimental Physics, Moscow, Russia
[87]Moscow State University, Moscow, Russia
[88]P. N. Lebedev Physical Institute, Moscow, Russia
[89]State Research Center of Russian Federation, Institute for High Energy Physics, Protvino, Russia
[90]Vinca Institute of Nuclear Sciences, Belgrade, Serbia
[91]Centro de Investigaciones Energéticas Medioambientales y Tecnológicas (CIEMAT), Madrid, Spain
[92]Universidad Autónoma de Madrid, Madrid, Spain
[93]Universidad de Oviedo, Oviedo, Spain
[94]Instituto de Física de Cantabria (IFCA), CSIC-Universidad de Cantabria, Santander, Spain
[95]CERN, European Organization for Nuclear Research, Geneva, Switzerland
[96]Paul Scherrer Institut, Villigen, Switzerland
[97]Institute for Particle Physics, ETH Zurich, Zurich, Switzerland
[98]Universität Zürich, Zurich, Switzerland
[99]National Central University, Chung-Li, Taiwan
[100]National Taiwan University (NTU), Taipei, Taiwan
[101]Cukurova University, Adana, Turkey
[102]Physics Department, Middle East Technical University, Ankara, Turkey
[103]Department of Physics, Bogaziçi University, Istanbul, Turkey
[104]National Scientific Center, Kharkov Institute of Physics and Technology, Kharkov, Ukraine
[105]University of Bristol, Bristol, United Kingdom
[106]Rutherford Appleton Laboratory, Didcot, United Kingdom
[107]Imperial College, University of London, London, United Kingdom
[108]Brunel University, Uxbridge, United Kingdom
[109]Boston University, Boston, Massachusetts 02215, USA
[110]Brown University, Providence, Rhode Island 02912, USA
[111]University of California, Davis, Davis, California 95616, USA
[112]University of California, Los Angeles, Los Angeles, California 90095, USA
[113]University of California, Riverside, Riverside, California 92521, USA
[114]University of California, San Diego, La Jolla, California 92093, USA
[115]University of California, Santa Barbara, Santa Barbara, California 93106, USA
[116]California Institute of Technology, Pasadena, California 91125, USA
[117]Carnegie Mellon University, Pittsburgh, Pennsylvania 15213, USA
[118]University of Colorado at Boulder, Boulder, Colorado 80309, USA
[119]Cornell University, Ithaca, New York 14853-5001, USA
[120]Fairfield University, Fairfield, Connecticut 06824, USA
[121]Fermi National Accelerator Laboratory, Batavia, Illinois 60510-0500, USA
[122]University of Florida, Gainesville, Florida 32611-8440, USA
[123]Florida International University, Miami, Florida 33199, USA
[124]Florida State University, Tallahassee, Florida 32306-4350, USA
[125]Florida Institute of Technology, Melbourne, Florida 32901, USA
[126]University of Illinois at Chicago (UIC), Chicago, Illinois 60607-7059, USA
[127]The University of Iowa, Iowa City, Iowa 52242-1479, USA
[128]Johns Hopkins University, Baltimore, Maryland 21218, USA

[129]*The University of Kansas, Lawrence, Kansas 66045, USA*
[130]*Kansas State University, Manhattan, Kansas 66506, USA*
[131]*Lawrence Livermore National Laboratory, Livermore, California 94720, USA*
[132]*University of Maryland, College Park, Maryland 20742, USA*
[133]*Massachusetts Institute of Technology, Cambridge, Massachusetts 02139, USA*
[134]*University of Minnesota, Minneapolis, Minnesota 55455, USA*
[135]*University of Mississippi, University, Mississippi 38677, USA*
[136]*University of Nebraska–Lincoln, Lincoln, Nebraska 68588-0111, USA*
[137]*State University of New York at Buffalo, Buffalo, New York 14260-1500, USA*
[138]*Northeastern University, Boston, Massachusetts 02115, USA*
[139]*Northwestern University, Evanston, Illinois 60208-3112, USA*
[140]*University of Notre Dame, Notre Dame, Indiana 46556, USA*
[141]*The Ohio State University, Columbus, Ohio 43210, USA*
[142]*Princeton University, Princeton, New Jersey 08544-0708, USA*
[143]*University of Puerto Rico, Mayaguez, Puerto Rico 00680*
[144]*Purdue University, West Lafayette, Indiana 47907-1396, USA*
[145]*Purdue University Calumet, Hammond, Indiana 46323, USA*
[146]*Rice University, Houston, Texas 77251-1892, USA*
[147]*University of Rochester, Rochester, New York 14627-0171, USA*
[148]*The Rockefeller University, New York, New York 10021-6399, USA*
[149]*Rutgers, The State University of New Jersey, Piscataway, New Jersey 08854-8019, USA*
[150]*University of Tennessee, Knoxville, Tennessee 37996-1200, USA*
[151]*Texas A&M University, College Station, Texas 77843-4242, USA*
[152]*Texas Tech University, Lubbock, Texas 79409-1051, USA*
[153]*Vanderbilt University, Nashville, Tennessee 37235, USA*
[154]*University of Virginia, Charlottesville, Virginia 22901, USA*
[155]*Wayne State University, Detroit, Michigan 48202, USA*
[156]*University of Wisconsin, Madison, Wisconsin 53706, USA*

[a]Deceased.
[b]Also at CERN, European Organization for Nuclear Research, Geneva, Switzerland.
[c]Also at Laboratoire Leprince-Ringuet, Ecole Polytechnique, IN2P3-CNRS, Palaiseau, France.
[d]Also at Soltan Institute for Nuclear Studies, Warsaw, Poland.
[e]Also at Moscow State University, Moscow, Russia.
[f]Also at Institute of Nuclear Research ATOMKI, Debrecen, Hungary.
[g]Also at University of California, San Diego, La Jolla, CA, USA.
[h]Also at Tata Institute of Fundamental Research–HECR, Mumbai, India.
[i]Also at California Institute of Technology, Pasadena, CA, USA.
[j]Also at INFN Sezione di Roma, Università di Roma "La Sapienza," Roma, Italy.
[k]Also at University of Athens, Athens, Greece.
[l]Also at The University of Kansas, Lawrence, KS, USA.
[m]Also at Institute for Theoretical and Experimental Physics, Moscow, Russia.
[n]Also at Paul Scherrer Institut, Villigen, Switzerland.
[o]Also at Vinca Institute of Nuclear Sciences, Belgrade, Serbia.
[p]Also at Rutherford Appleton Laboratory, Didcot, United Kingdom.
[q]Also at INFN Sezione di Perugia, Università di Perugia, Perugia, Italy.
[r]Also at KFKI Research Institute for Particle and Nuclear Physics, Budapest, Hungary.
[s]Also at Institute for Nuclear Research, Moscow, Russia.